Relatório científico - FAPESP

Vivian de A. D. Nunes

Processo: 2020/04751-4
Título: Formação de padrões em recifes de coral
Beneficiário: Vivian de Araujo Dornelas Nunes
Responsável: Nathan Jacob Berkovits
Vínculo Institucional: IFT-UNESP
Vigência: 01/08/2020 à 30/11/2022
Período do relatório: 01/12/2021 à 30/11/2022

1 Resumo do projeto proposto

Nas últimas décadas muitos pesquisadores têm usado do advento da computação para, através de modelagens matemáticas, entender problemas que não eram tradicionalmente estudados na física. Dentre eles podemos citar a correlação entre uma população e o seu habitat, ou ainda, como diferentes tipos de interações afetam a distribuição espacial e a persistência de populações em um habitat. Essas interações podem ser do tipo cooperativa, competitiva ou mutualistíca, e podem ser intraespecíficas ou entre diferentes espécies. Estudos como estes são temas fundamentais no estudo da ecologia, e vêm sendo abordado por diferentes campos de estudos, como biologia, matemática e física.

A fim de descrever como evolui a distribuição espacial e temporal de uma população em um meio, pode-se utilizar um modelo matemático. Tal modelo deve ser capas de predizer comportamentos nesse sistema, incorporando os elementos principais presentes nesta população, tais como nascimento e morte, competição por recursos e difusão.

Além disso, o modelo escolhido deve ser tal que seja capaz de descrever e de fazer predições do que vai acontecer nesses sistemas, da forma mais sucinta possível, seja por meio de soluções analíticas, numéricas ou ambas.

O projeto tem como objetivo principal estudar a formação de diferentes tipos de padrões em recifes de corais por meio de modelagem matemática. Ele pode ser desenvolvido levando-se em consideração que os recifes de corais da mesma espécie podem formar diferentes padrões, dependendo das condições ambientais, como fluxo de nutrientes e disponibilidade de luz e água. No decorrer do projeto o tema foi adaptado (devido à oportunidades de colaborações), e veremos a seguir o que foi estudado.

2 Resultados do projeto

Durante o período de vigência deste relatório, dois principais trabalhos foram desenvolvidos, que descreveremos nesta seção.

2.1 O dilema do bem público em populações microbianas sob um fluxo

Este estudo vem sendo desenvolvido desde o início do projeto e se encontra em fase final de escrita. Todos os resultados já foram obtidos e apresentados em congressos, como serão listados adiante.

Colaboração:

- Enrico Ser-Giacomi (Department of Earth, Atmospheric and Planetary Sciences, MIT, USA);
- Ricardo Martinez-Garcia (IFT-UNESP / ICTP-SAIFR, Brazil / CASUS - HZDR Görlitz, Germany).

Motivação:

Bens públicos (PG - Public good) são moléculas produzidas por certos micróbios, que são liberadas no meio ambiente e fornecem um benefício reprodutivo não apenas para os próprios produtores, mas também para outros indivíduos (caronas). Um exemplo de PGs são as enzimas digestivas secretadas por certas bactérias para quebrar polímeros complexos em fontes de carbono mais simples que podem ser importadas e catabolizadas mais facilmente pelas células.

Os ambientes aquosos fornecem um contexto ambiental muito interessante para estudar a produção de PG, pois o fluxo externo propaga microrganismos e as substâncias que eles liberam, e pode gerar dinâmicas muito complexas e inexploradas. O objetivo é entender quais são os mecanismos que tornam a cooperação estável evolutivamente e que explicam por que alguns indivíduos investem parte de sua aptidão individual para fornecer benefícios de aptidão ao coletivo (conhecido como dilema do bem público).

Resumo:

Visto que muitos habitats microbianos estão presentes em ambientes aquosos sujeitos a correntes de fluxos existentes no meio em que estão inseridos (rios, lagos, intestinos, pulmões, cavidade nasal...), estudamos como diferentes tipos de fluxos afetam a sobrevivência e coexistência entre diferentes tipos de fenótipos na população microbiana.

Para tal consideramos uma população bacteriana composta de células produtoras de PG e não produtoras em um biofilme (imerso em um meio aquoso) que modelamos usando um processo estocástico de nascimento-morte. Tal população, fixa em uma superfície, é modelada por um processo de nascimento-morte em uma rede regular. Os bens públicos em nosso modelo são liberados em nós da rede ocupados por células produtoras. Por serem moléculas muito menores que o tamanho das células, estão sujeitas à advecção devido ao fluido, além do processo de difusão e, portanto, modelamos o transporte das moléculas (PGs) em todo o sistema por uma equação de reação-advecção-difusão.

Analisamos este modelo para diferentes fluxos a fim de investigar se, e como, a interação entre os fluxos ambientais e os parâmetros fisiológicos poderia tornar a produção de bem público evolutivamente estável. Nossos resultados mostram que os fluxos podem remodelar a distribuição espacial dos bens públicos e fazer com que os produtores de PG e não produtores coexistam em condições nas quais o transporte unicamente difusivo resultaria na extinção das células produtoras. Observamos também que fluxos de baixa velocidade são mais importantes para sobrevivência de células produtoras de que a caoticidade do fluxo.

2.2 O efeito de locais preferenciais na persistência e espalhamento de uma população

Este estudo foi realizado durante o ano de 2022 e se encontra em fase final de revisão de escrita para ser submetido, ver Seção 5.

Colaborações:

- Pablo de Castro (IFT-UNESP / ICTP-SAIFR);
- William F. Fagan (Department of Biology, University of Maryland, College Park, MD, USA);
- Justin M. Calabrese (Center for Advanced Systems Understanding (CASUS), Görlitz, Germany);
- Ricardo Martinez-Garcia (IFT-UNESP / ICTP-SAIFR, Brazil / CASUS - HZDR Görlitz, Germany).

Motivação:

O tamanho crítico de um habitat que causa a extinção de uma população é um problema central na ecologia, além de como uma população biológica se espalha no espaço.

Assumindo modelos simples de difusão browniana para os indivíduos, bem como uma matriz ambiental mortal, completamente inviável, em torno do habitat, a dispersão e a persistência da população são bem compreendidas no nível teórico. No entanto, avanços em dispositivos de rastreamento e métodos estatísticos nos permitem entender melhor como os animais se movem. Em particular, foi demonstrado usando dados de rastreamento por GPS, que os animais usam o espaço de maneira não uniforme.

A razão pela qual os animais podem apresentar esse tipo de comportamento tem a ver com a existência de centros atrativos localizados em locais com propriedades ou recursos especiais (incluindo lagoas, ninhos e abrigos), que geralmente assumem uma posição fixa no tempo.

Resumo:

Uma questão central em ecologia é como os parâmetros de uma população, tanto demográficos quanto de movimentos, determinam sua distribuição espacial e temporal, bem como o tamanho crítico do habitat que pode sustentar essa população. No entanto, a maioria dos estudos simplifica demais as suposições sobre o comportamento do movimento individual, o que pode resultar em previsões imprecisas.

Estudamos a persistência e espalhamento de uma população de indivíduos que experimentam uma atração efetiva para um local preferido no espaço. Usando modelos explícitos de crescimento-dispersão com termos advectivos e mostramos como as populações biológicas podem se ajustar à destruição do habitat dependendo de quão longe do local preferido o habitat é destruído.

Também incorporamos uma resposta de fuga da matriz ativando a atração em direção às bordas do habitat, para indivíduos localizados em um ambiente hostil ao redor do habitat. Em particular, nossos resultados mostram que aumentar as forças de atração nem sempre é benéfico. Quando o centro de atração está localizado perto das bordas do habitat, os animais podem passar muito tempo expostos a taxas de mortalidade mais altas, o que diminui a população total.

Além disso, para forças intermediárias de resposta de fuga da matriz

hostil, a morte por competição dentro do habitat pode conquistar o benefício individual de escapar mais cedo da matriz, levando a menores populações em geral. Nossos resultados constituem um primeiro passo importante para uma compreensão mais realista dos efeitos de localização preferencial no nível populacional.

3 Participação em eventos científicos

3.1 Conferências internacionais

1. Conference on Complex Systems (CCS2022), (October 17-21, 2022), Palma de Mallorca, Spain. Ver trabalho apresentado na Seção 4.1.
   Oral presentation: *Public good dilemma for a microbial population under the flow.*
   Poster presentation: *Critical patch size reduction by heterogeneous diffusion.*

2. Models in Population Dynamics, Ecology and Evolution (MPDEE), (June 13-17, 2022), Turin, Italy. . Ver trabalho apresentado na Seção 4.2.
   Oral presentation: *Public good dilemma for a microbial population under the flow.*

3.2 Conferências nacionais

Encontro de Outono da Sociedade Brasileira de Física (EOSBF) 2022, São Paulo, Brazil.
Oral presentation: *Public good dilemma for a microbial population under the flow.*

3.3 Mesa redonda

Escola de Verão ICTP-SAIFR para Jovens Físicos (22 a 29 de janeiro, 2022).
Tema: *Carreira científica.*

3.4 Bancas de trabalhos de conclusão

Anteneodo, C.; Dornelas, V.; Martinez, A. S.; Oliveira, F. A.; Stariolo, D.. Participação em banca de Gabriel Gomides Piva. *Organização espacial de uma populações de uma única espécie com interações a distância*. 2022. Tese de doutorado (Doutorado em física) - PUC-Rio.

4 Trabalhos apresentados em conferências

4.1 Critical patch size reduction by heterogeneous diffusion

Este trabalho foi apresentado em painel no evento científico Conference on Complex Systems ocorrido de 17/10/2022 a 21/10/2022 em Palma de Mallorca, Espanha.

Critical patch size reduction by heterogeneous diffusion

M. A. F. dos Santos[1], Vivian Dornelas[1,2], E. H. Colombo[3,4], and C. Anteneodo[1,5]
[1] Department of Physics, PUC-Rio, Rua Marquês de São Vicente 225, 22451-900, Rio de Janeiro, RJ, Brazil
[2] ICTP-SAIFR & IFT-UNESP, Rua Dr. Bento Teobaldo Ferraz 271, 01140-070, São Paulo, SP, Brazil
[3] Department of Ecology & Evolutionary Biology, Princeton University, Princeton, NJ 08544, USA
[4] Department of Ecology, Evolution, and Natural Resources, Rutgers University, New Brunswick, NJ 08901, USA
[5] Institute of Science and Technology for Complex Systems, Brazil

Population survival depends on a large set of factors and on how they are distributed in space. Due to landscape heterogeneity, species can occupy particular regions that provide the ideal scenario for development, working as a refuge from harmful environmental conditions. Typically, there is a minimum size of the patch, L_c, that separates the extinction and survival regimes, which depends on the details of the environment and population dynamics. Survival occurs if population growth overcomes the losses caused by adventurous individuals that cross the patch edge.

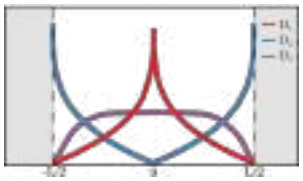

Fig. 1. Different space-dependent diffusion coefficient profiles in a patch of size L. The gray region represents an non-viable region for the population.

In this work, we consider a single species that grows and moves in a bounded domain, with diffusivity that varies in space (see Fig. 1 for an example).

We show analytically, within the Stratonovich framework, that heterogeneous diffusion reduces the minimal patch size for population survival when contrasted with the homogeneous case with the same average diffusivity, favoring the survival. Furthermore, this result is robust regardless of the particular choice of the diffusion coefficient profile.

We also discuss how this picture changes beyond the Stratonovich framework. Particularly, the Itô case, which is nonanticipative, can promote the opposite effect, while Hänggi-Klimontovich interpretation reinforces the reduction effect. That is, the more anticipative is the noise, the stronger is the reduction.

---

[1] M. A. F. dos Santos, V. Dornelas, E. H. Colombo, and C. Anteneodo, PHYSICAL REVIEW E, **v. 102**, p. 042139, (2020).

Critical patch size reduction by heterogeneous diffusion

M. A. F. dos Santos[1], **V. Dornelas**[1,2], E. H. Colombo[3,4] and C. Anteneodo[1,5]

[1] Department of Physics, PUC-Rio, Rio de Janeiro, Brazil [2] ICTP-SAIFR & IFT-UNESP, São Paulo, Brazil [3] Department of Ecology & Evolutionary Biology, Princeton University, Princeton, USA
[4] Department of Ecology, Evolution, and Natural Resources, Rutgers University, New Brunswick, USA [5] Institute of Science and Technology for Complex Systems, Brazil

Population survival depends on a large set of factors and on how they are distributed in space. Due to landscape heterogeneity, species can occupy particular regions that provide the ideal scenario for development, *e.g.* working as a refuge from harmful environmental conditions. In this work, we consider a single species that grows and moves in a bounded domain, with diffusivity that varies in space. We show analytically, within the Stratonovich framework, that heterogeneous diffusion reduces the minimal patch size for population survival when contrasted with the homogeneous case with the same average diffusivity, favoring the survival. Furthermore, this result is robust regardless of the particular choice of the diffusion coefficient profile.

The critical habitat size problem

Survival occurs if population growth overcomes the losses caused by adventurous individuals that cross the patch edge.

Population growth (r) + Homogeneous diffusion (D)

- Spatial distribution of population density in a L size patch:

Survival

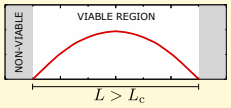

Extinction

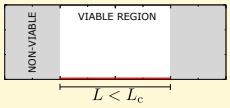

$$L_c = \pi\sqrt{\frac{D}{r}}$$

Model for a space-dependent diffusion

Considering that each individual performs a random walk, in the Stratonovich formalism the individual moviment is described by:

$$\dot{x} = \sqrt{2D(x)}\eta(t)$$

where η is a Gaussian white noise.

In terms of the population density $\rho(x,t)$, and by considering birth/death process:

$$\frac{\partial}{\partial t}\rho(x,t) = r\rho(x,t) + \frac{\partial}{\partial x}\left\{\sqrt{D(x)}\,\frac{\partial}{\partial x}\left[\sqrt{D(x)}\rho(x,t)\right]\right\}$$

Results

To compare these results with the homogeneous diffusion scenario, we are using $\tilde{D}$ as the average value of diffusion coefficient inside the patch, and $\tilde{L}_c$ for its critical habitat size.

- Rectangular profile: $D(x) = D_0\left[1 + d\,H\left(\beta - \frac{2|x|}{L}\right)\right]$

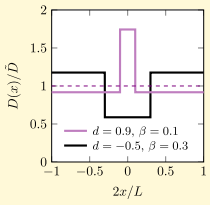

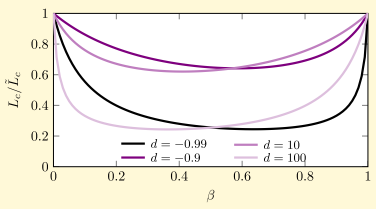

- Sinusoidal profile: $D(x) = D_0\left[1 + a\cos\left(\frac{2k\pi x}{L} + \phi\right)\right]$

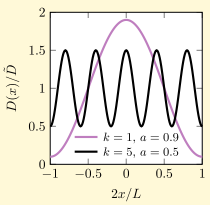

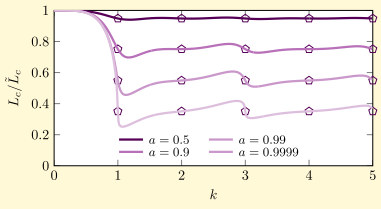

Ongoing Project*: The effect of preferred locations in critical patch size

*Joint work with Ricardo Martínez-García and Pablo de Castro (ICTP-SAIFR & IFT-UNESP)

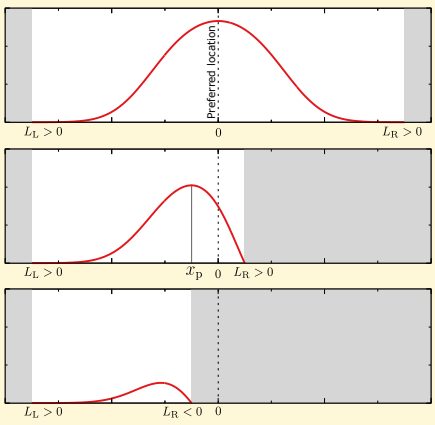

Population growth
+
Competition
+
Homogeneous diffusion
+
Preferred location

- Fraction of total population remaining:

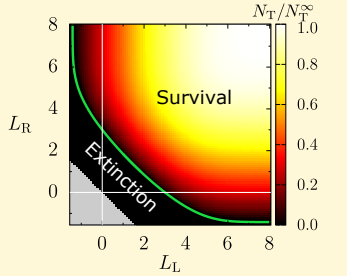

Conclusions

- Space-dependent diffusion, as defined by Stratonovich interpretation, typically favor survival in the population dynamics, by reducing the critical habitat size in comparison to the average level.

- By considering an attraction to a preferred location into individual movement behavior, its possible to understand how biological populations may adjust to habitat destruction depending on how far from the preferred location the habitat is destroyed.

M. A. F. dos Santos, V. Dornelas, E. H. Colombo, and C. Anteneodo, PHYSICAL REVIEW E, **v. 102**, p. 042139, (2020).

4.2 Public good dilemma for a microbial population under the flow

Este trabalho foi apresentado oralmente no evento científico Models in Population Dynamics, Ecology and Evolution ocorrido de 13/06/2022 a 17/06/2022 em Turim, Itália.

V. Dornelas[a,b] CT

Public good dilemma for a microbial population under the flow

joint work with R. Martínez-García[a,b],

[a] ICTP - South American Institute for Fundamental Research
[b] Institute of Theoretical Physics - UNESP

Public goods (PG) are molecules produced by certain microbes that are released into the environment and provide a reproductive benefit for the producers themselves and for other individuals that do not incur in any production cost (free-riders). This poses an interesting evolutionary dilemma: what are the mechanisms that make cooperation evolutionary stable and explain why some individuals invest part of their individual fitness to provide fitness benefits to the collective?

In this work, we analyze whether environmental flows, which are present in many microbial habitats (rivers, lakes, intestines, lungs, nasal cavity...), provide a solution to this dilemma.

For that purpose, we consider a bacterial population made of PG producers and free-riders in a biofilm stage, which we model using a stochastic birth-death process in a lattice. Public goods in our model are released at lattice nodes occupied by producer cells and free to float in the fluid flow. Hence, we couple the birth-death process to a reaction-advection-diffusion for the transport of public goods throughout the system.

We analyze this model for different flows to investigate whether and how the interaction between the environmental flows and the physiological parameters could turn public-good production evolutionarily stable. Our results show that flows may reshape the spatial distribution of public goods and make PG producers and free-riders coexist in condition in which diffusive transport results in the extinction of PG producers.

viviandnunes@gmail.com

Public good dilemma for a microbial population under the flow

Vivian Dornelas
joint work with Ricardo Martínez-García

Institute of Theoretical Physics -UNESP
ICTP South American Institute for Fundamental Research (ICTP-SAIFR)

Public good

Public good: Compounds that provide a benefit to cells in the vicinity of the producer.

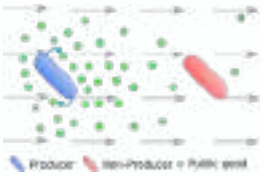

Tragedy of the commons: When non-producers quickly deplete the available resource, increasing their birth rate and therefore dominating the environment and consequently losing the benefit that producer cells could provide.

Public good dilemma

The model

A stochastic birth/death process in which individuals are embedded in the nodes of a regular lattice combined with a transport equation for PG concentration.

Allen, B., Gore, J., & Nowak, M. A. (2013). *Elife*, 2, e01169.

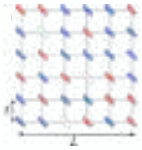

Birth/death stochastic dynamics

Birth rate: NP $\longrightarrow \beta_{NP}(\vec{x}_i) = \beta_0[1 + C(\vec{x}_i, t)]$

P $\longrightarrow \beta_P(\vec{x}_i) = \beta_0[1 + C(\vec{x}_i, t)] - k$

Death rate: $\longrightarrow \gamma$

The model

Public-good concentration dynamics

$$\frac{\partial C}{\partial t} = \alpha\delta(x_i - x_{i,P}) - \lambda C + \vec{v}\cdot\vec{\nabla}C + D\nabla^2 C$$

$$\frac{\partial C}{\partial t} = \frac{\alpha}{\beta_0}\delta(x_i - x_{i,P}) - \frac{\lambda}{\beta_0}C + Da_I^{-1}\hat{v}\cdot\vec{\nabla}C + Da_{II}^{-1}\nabla^2 C$$

$$Da_I = \frac{\text{reaction rate}}{\text{advective mass transport rate}} = \frac{\beta_0 L}{U}$$

$$Da_{II} = \frac{\text{reaction rate}}{\text{diffusive mass transport rate}} = \frac{\beta_0 L^2}{D}$$

$Da \gg 1$ particles go through many generations before being dispersed by the fluid.

$Da \ll 1$ flow time scales is much faster than biological timescales.

Results

$$\frac{\partial C}{\partial t} = \frac{\alpha}{\beta_0}\delta(x_i - x_{i,P}) - \frac{\lambda}{\beta_0}C$$

The simplest case

No flow or diffusion

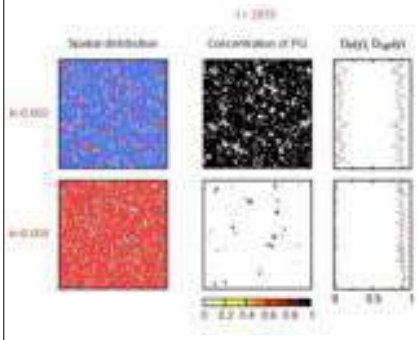

Parameters

Birth:	$\beta_0 = 0.03$
Death:	$\gamma = 0.01$
PG production:	$\alpha = 1$
PG decay:	$\lambda = 1$
Network:	$L = 100$
	$\ell = 1$

- There is no coexistence in the steady state.
- Analytically solving the equation, we can find a critical value for the cost of producing PG, under which only the P-cells survive.
- If $\alpha = \lambda$, $k_c = \frac{\alpha\beta_0}{\lambda}$.

Results

$$\frac{\partial C}{\partial t} = \frac{\alpha}{\beta_0}\delta(x_i - x_{i,P}) - \frac{\lambda}{\beta_0}C + Da_I^{-1}\hat{\mathbf{v}}\cdot\vec{\nabla}C + Da_{II}^{-1}\nabla^2 C$$

Dynamics with diffusion

Without flow

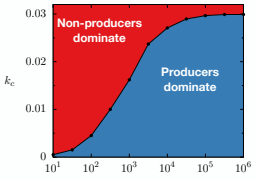

Dynamics with uniform flow

Non-diffusive case

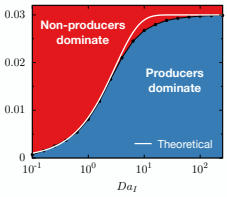

$$k_c = \frac{\alpha\beta_0}{\lambda}\left[1 - e^{-\frac{\lambda Da_I}{\beta_0 L}}\right]$$

Increase diffusion → Decrease k_c → favor NP

Increase velocity flow → Decrease k_c → favor NP

Results

$$\frac{\partial C}{\partial t} = \frac{\alpha}{\beta_0}\delta(x_i - x_{i,P}) - \frac{\lambda}{\beta_0}C + Da_I^{-1}\hat{\mathbf{v}}\cdot\vec{\nabla}C + Da_{II}^{-1}\nabla^2 C$$

Dynamics with parabolic flow

Non-diffusive case

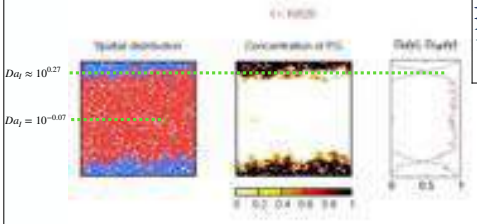

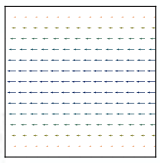

$$Da_I(y) = \frac{Da_I L^2}{6y(L-y)}\hat{x}$$

$$\overline{Da_I}(y) = Da_I$$

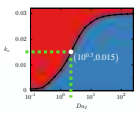

- There is coexistence in the steady state.
- Population divided by niches.

Results

$$\frac{\partial C}{\partial t} = \frac{\alpha}{\beta_0}\delta(x_i - x_{i,P}) - \frac{\lambda}{\beta_0}C + Da_I^{-1}\hat{\mathbf{v}}\cdot\vec{\nabla}C + Da_{II}^{-1}\nabla^2 C$$

Dynamics with parabolic flow

Non-diffusive case

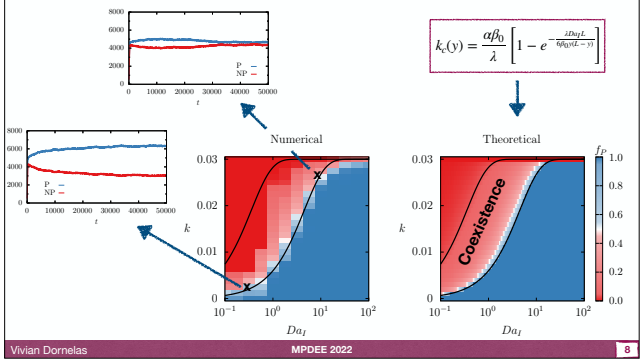

Results

$$\frac{\partial C}{\partial t} = \frac{\alpha}{\beta_0}\delta(x_i - x_{i,P}) - \frac{\lambda}{\beta_0}C + Da_I^{-1}\hat{\gamma}\cdot\vec{\nabla}C + Da_{II}^{-1}\nabla^2 C$$

Dynamics in a time-periodic flow

Non-diffusive case

$$\begin{cases} Da_I^{-1}(x,y) = Da_I^{-1}\cos(2\pi y/L)\,\hat{x}, & \text{for } nT \le t < nT + T/2 \\ Da_I^{-1}(x,y) = Da_I^{-1}\cos(2\pi x/L)\,\hat{y}, & \text{for } nT + T/2 \le t < (n+1)T \end{cases}$$

$$\mu = \frac{T}{Da_I L}$$

Results

$$\frac{\partial C}{\partial t} = \frac{\alpha}{\beta_0}\delta(x_i - x_{i,P}) - \frac{\lambda}{\beta_0}C + Da_I^{-1}\hat{\gamma}\cdot\vec{\nabla}C + Da_{II}^{-1}\nabla^2 C$$

Dynamics in a time-periodic flow

Non-diffusive case

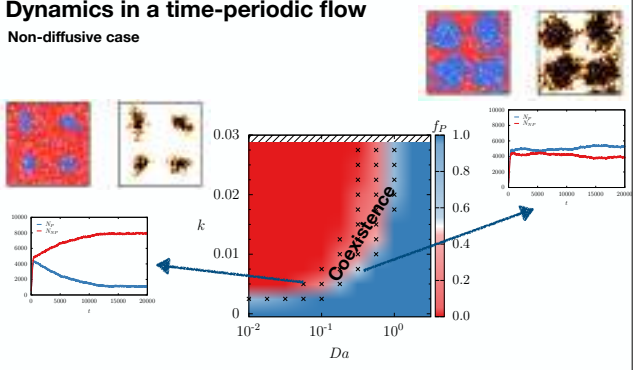

Results

$$\frac{\partial C}{\partial t} = \frac{\alpha}{\beta_0}\delta(x_i - x_{i,P}) - \frac{\lambda}{\beta_0}C + Da_I^{-1}\hat{\gamma}\cdot\vec{\nabla}C + Da_{II}^{-1}\nabla^2 C$$

Dynamics in a Rankine vortex

Non-diffusive case

A vortex with radius R and a rotation rate Γ.

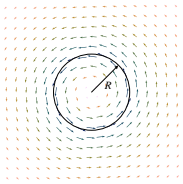

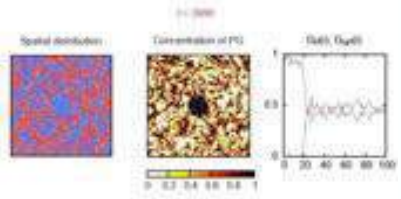

$$Da_I^{-1}(r) = \begin{cases} \dfrac{\Gamma\, r}{2\pi R^2}\hat{\theta}, & r \le R \\ \dfrac{\Gamma}{2\pi r}\hat{\theta}, & r > R \end{cases}$$

Conclusions

- A large amount of microbial populations are subjected to flow effects in a real environment.
- What is the mechanism behind this?
- Low mixing regions favor survival of P cells.
- Flows may enable coexistence of public-good producers and non-producers via spatial niche partitioning.
- The stirring velocity is more important than the way it is mixed for survival of the Producer cells.

Perspectives

- Introducing a cell mutation.
- Introducing PG consumption.
- Exploring another topology:

Allen, B., Gore, J., & Nowak, M. A. (2013). *Elife*, *2*, e01169.

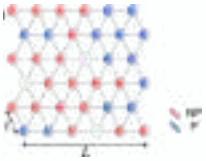

Thank you!

5 Plano de gestão de dados

Nenhum trabalho ou código foi publicado este ano. Os trabalhos que serão submetidos constarão nas seções seguintes.

6 Lista de trabalhos em preparação

O trabalho descrito na Seção 2.1 está em preparação. Aqui segue alguns resultados.

Ecological public good dynamics under environmental flows

Vivian Dornelas[1], Enrico Ser-Giacomi[2], and Ricardo Martinez-Garcia[1]

[1]ICTP South American Institute for Fundamental Research & Instituto de Física Teórica, Universidade Estadual Paulista – UNESP, Rua Dr. Bento Teobaldo Ferraz 271, Bloco 2 – Barra Funda, 01140-070 São Paulo, Brazil

[2]Department of Earth, Atmospheric and Planetary Sciences, Massachusetts Institute of Technology, 54-1514 MIT, Cambridge, MA 02139, USA.

December 15, 2022

Introduction

For several years, microbes were studied as unicellular, solitary organisms that live independently from each other. However, they very often coordinate their behavior collectively to perform several tasks, such as foraging, dispersal, reproduction, or nutrient acquisition West et al. (2007); Tarnita (2017); Crespi (2001). Owing to these varieties of examples, their lab manageability, their fast evolution, and the various possibilities of molecular and genetical manipulations, microbes have become a recurrent model to investigate social behaviors experimentally, and the inspiration of many theoretical models. Microbial social behaviors comprise a wide variety of ecological interactions, all coordinated and executed by the exchange of substances with the extracellular medium termed exoproducts.

From an evolutionary perspective, however, cooperative interactions are particularly interesting because some individuals assume a fitness cost to generate a benefit that is shared with other individuals in the population. A paradigmatic example of cooperation in the microbial world is

the synthesis of public goods (PG), exoproducts that are costly to produce and provide a benefit to cells in the vicinity of the producer, regardless of whether they contribute to its production or not. Examples of PGs are digestive enzymes secreted by certain bacteria in order to break complex polymers into simpler sources of carbon that can be more easily imported and catabolized Drescher et al. (2014).

In a well-mixed population formed by PG producers and non-producers, every cell interacts with each other with the same probability and PGs are equally available for all individuals. In this scenario, non-producers have a growing advantage over producers because they share the benefit of the PG without incurring any production cost. Natural selection thus favors the proliferation of non-producers in the population until they outcompete and eliminate producers. This phenomenon, known as the tragedy of the commons, predicts that cooperation is evolutionary unstable Hardin (1968), in contradiction with the vast number of instances of cooperative behaviors observed in nature Tarnita (2017); Crespi (2001); Nadell et al. (2016), and raises one of the key questions in evolutionary biology: what are the mechanisms that make cooperation evolutionary stable and thus explicate that some individuals invest part of their individual fitness to provide fitness benefits to the collective?

Several mechanisms have been proposed to resolve this question (reviews can be found in West et al. (2007); Tarnita (2017); Nadell et al. (2016); Nowak (2006); Oliveira et al. (2015)): the increase in population size due to PGs makes the system more robust against extinctions induced by demographic fluctuations, the existence of individuals that transiently do not participate in the cooperative behavior but can recover cooperation after it collapses, the partial privatization of the benefits of cooperation by cooperators, or, in contrast with mutualism or antagonism, any form of assortment that makes cooperators more likely to interact with conspecific cooperators. However, investigations on these mechanisms too often focus on a detailed description of the interactions between individuals and simplify the ecological context in which those interactions occur. This approach has resulted in many game-theoretic models that incorporate all the ecological ingredients in the costs and benefits of the cooperative action. In many cases, however, this level of detail is insufficient and an explicit description of the ecological variables is required. For instance, envi-

ronmental processes drive the spatial distribution of cell secretions, including PGs, and determine which individuals in the population can access them. Understanding the feedback between environmental and population dynamics is thus crucial to unmask the processes that deem cooperation evolutionary stable in real microbial ecosystems.

This point has been explicitly addressed by a handful of recent theoretical studies that have extended existing game-theoretic approaches to incorporate the spatiotemporal dynamics of the PG explicitly Nadell et al. (2010); Gerlee and Altrock (2019); Allen et al. (2013); Uppal and Vural (2018); Borenstein et al. (2013). Most of these studies consider that the environment is homogeneous and the spreading of the PG is driven by concentration gradients (Fig 1a). These assumptions lead to the so-called diffusible public goods models, in which the spatial dynamics of the PG are described by a finite diffusion coefficient that concentrates PGs in the near vicinity of producers. Due to this limited spreading, the utilization rates and exploitation benefits at which PG production is evolutionary stable are smaller for diffusible public goods than in the well-mixed limit, represented by an infinite PG diffusion Nadell et al. (2010); Borenstein et al. (2013). Importantly, diffusible public goods frameworks do not allow for the long-term coexistence between PG producers and non-producers predicted by game-theoretic approaches Gerlee and Altrock (2019); Borenstein et al. (2013). Finally, for very high population densities, these results depend on cell morphology and are hence species-specific Allen et al. (2013).

Microbial communities, however, are very often found in aqueous habitats where they can develop either in sessile or planktonic forms. In these environments, external flows propagate both the microorganisms and the substances that they release in forms that are more complex than diffusion (Fig. 1b) Nadell et al. (2017); Thomen et al. (2017); Martínez-García et al. (2018); Wheeler et al. (2019). Despite empirical evidence indicating the importance that they may have for stabilizing PG production Drescher et al. (2014), environmental flows have been barely considered in theoretical models Uppal and Vural (2018); Martínez-García et al. (2018). Thus, we are only starting to understand the feedback between fluid dynamics and the evolutionary trajectory of microbial sociality for a limited range of flows. Uniform flows (Fig. 1b) do not have any effect on the evolutionary stability of PG secretion when compared to the diffusive case, because they can be subsumed in

a mere change in reference frame Uppal and Vural (2018). If gradients of velocity exist, however, they generate shear forces (Fig. 1b) that increase group fragmentation rates thereby limiting the invasion of non-cooperative strains and favoring the evolution of cooperative behaviors Uppal and Vural (2018). Importantly, the effect of the most complex scenarios, represented by the chaotic mixing characteristic of turbulent flows, has been completely ignored by previous studies.

Materials and methods

We study the effect of increasingly complex patterns of stirring, caused by different environmental flows, on the competition between two cell phenotypes for surface colonization. We consider that cells are highly adhesive and thus do not travel with the flow. Both cell phenotypes are identical in any trait except in their ability to produce a non-consumable public good molecule that increases the division rate of those cells that have access to it, regardless of whether they contribute to their production or not. The public good is produced by producer cells and thus released to the external environment at the location of producer cells. Once in the extracellular environment, it is transported both by external flow and molecular diffusion.

Birth-death dynamics. We model the population of cells using a cellular automaton in which cells reside in the nodes of a $N \times N$ regular square lattice of lateral length L and mesh size ℓ. Therefore, the location of each cell is given by a two-dimensional vector $\boldsymbol{r}_{ij} = (x, y)$ where $x = i\,\ell$ and $y = j\,\ell$ with $i,\ j \in (0, \dots N)$ and $N\ell = L$. Square lattices are an accurate representation of the spatial structure of rod-shaped bacteria (Allen et al., 2013).

The surface colonization process is modelled by an on-lattice death-birth stochastic process in which cells die at a constant rate γ regardless of their phenotype and divide at a phenotype-specific rate that depends linearly on public-good local concentration, with birth-rate

$$\beta_{NP}(\boldsymbol{r}_{ij}, t) = \beta_0[1 + C(\boldsymbol{r}_{ij}, t)], \quad (1)$$

$$\beta_{P}(\boldsymbol{r}_{ij}, t) = \beta_0[1 + C(\boldsymbol{r}_{ij}, t)] - k. \quad (2)$$

The subscripts NP and P in Eqs. (1)-(2) account for non-producer and producer respectively, β_0 is the baseline cell division rate, $C(\boldsymbol{r}_{ij})$ is the public-good concentration at lattice node i, j, and k is the metabolic cost associated to public-good production.

Public good dynamics. Because public-good molecules are often orders of magnitude smaller than producer cells, we describe the spatiotemporal distribution of public good in terms of a continuous concentration field C that evolves following a reaction-advection-diffusion equation,

$$\frac{\partial C(\boldsymbol{r},t)}{\partial t} + \boldsymbol{v}\cdot\vec{\nabla}C(\boldsymbol{r},t) = \alpha\sum_{l\in P}\delta(\boldsymbol{r}-\boldsymbol{r}_l) - \lambda\, C(\boldsymbol{r},t) + D\nabla^2 C(\boldsymbol{r},t), \tag{3}$$

where δ is the Dirac delta function, $\boldsymbol{r}_k$ gives the coordinate of every producer cell, α is the public-good production rate, λ is the PG decay rate, D is the diffusion coefficient, and $\boldsymbol{v} = U\hat{\boldsymbol{v}}$ is a two-dimensional velocity field of an incompressible flow. Eq. (3) can be nondimensionalized by the transformations $\tilde{t} = \beta_0\, t$, $\tilde{x} = x/L$. Hence, after removing the tildes from the notation, the nondimensional transport equation is

$$\frac{\partial C(\boldsymbol{r},t)}{\partial t} + \frac{1}{\mathrm{Da}}\,\hat{\boldsymbol{v}}\cdot\vec{\nabla}C(\boldsymbol{r},t) = \frac{\alpha}{\beta_0}\sum_{l\in P}\delta(\boldsymbol{r}-\boldsymbol{r}_l) - \frac{\lambda}{\beta_0}\,C(\boldsymbol{r},t) + (\mathrm{Pe}\,\mathrm{Da})^{-1}\,\nabla^2 C(\boldsymbol{r},t), \tag{4}$$

where $\mathrm{Da} = \beta_0 L/U$ is the Damköhler number, a dimensionless number that characterizes the ratio between the biological and the advective timescales. In the limits, $\mathrm{Da} \gg 1$ and $\mathrm{Da} \ll 1$, the biological dynamics are much faster, respectively slower, than stirring. $\mathrm{Pe} = LU/D$ is the dimensionless Péclet number, that measures the ratio between the strength of the advective and the diffusive transport. The product $(\mathrm{Pe}\,\mathrm{Da})$ is often referred in the literature as the diffusive or second Damköhler number, $\mathrm{Da_{II}}$. We will consider the limit $\mathrm{Pe}\to\infty$ in which advective transport dominates over diffusion and thus neglect the last term in Eq. (4). See the supplementary material for a detailed description of how we implemented the model coupling the individual-based model for cell demography and the transport equation for public-good concentration.

Results

Unidirectional flow

We first consider that producer and non-producer cells are subjected to the effect of a uniform flow of the form $\boldsymbol{v} = U\,\hat{\boldsymbol{e}}_x$. As expected from previous studies considering diffusive public goods, our numerical results show that there is always competitive exclusion and that the identity of the dominant phenotype is determined by PG production cost k and the Damköhler number. The higher Da, the more PG are utilized by producer cells, which allows for producer dominance at higher PG production costs.

To better understand how the different parameters define this transition between producer and non-producer dominance, we solve the PG transport equation, Eq. (4) in a simplified one-dimensional scenario with one producer cell at $x = 0$ and a non-producer one at $x = \ell$. For this configuration, we obtain a stationary PG concentration profile

$$C(x) = \frac{\alpha}{\lambda} \exp\left(-\frac{\lambda\,\mathrm{Da}}{\beta_0} x\right). \tag{5}$$

For this concentration profile, we can approximate the maximum PG production cost that leads to producer dominance k_c as the value of k at which $\beta_{\mathrm{P}}(0) = \beta_{\mathrm{NP}}(\ell)$. From Eqs. (1) and (2), we obtain

$$k_c = \frac{\alpha\,\beta_0}{\lambda}\left[1 - \exp\left(-\frac{\lambda\,\ell\,\mathrm{Da}}{\beta_0}\right)\right], \tag{6}$$

which deviates slightly from numerical results only for a narrow range of intermediate values of the Damköhler number (see the white line in Fig. 1).

By observing Fig. 1, we can conclude that the increase in flow velocity favours NP-cells for the same intrinsic characteristics of the population since they can access the good without paying the cost. Therefore, we can infer that if the population are immersed in a unidirectional flow in which velocity is varying with the "height", it can lead to a spatial distribution of cells separated by niches, where velocity defines which type of phenotype will dominate each region. Examples of this kind of flow are often observed in nature, such as the parabolic flow, the Couette flow, and the

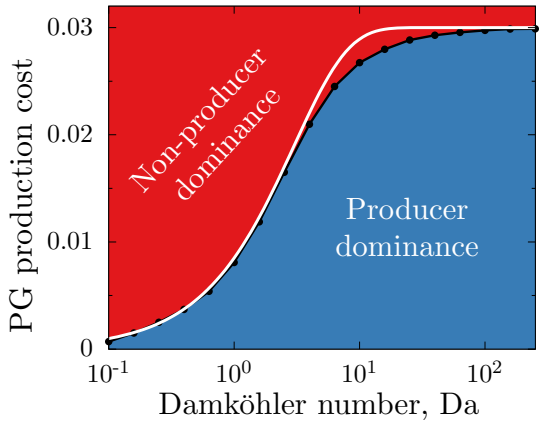

Figure 1: **Dominant population under constant velocity flow:** there is no coexistence between different phenotypes in the steady state. The white curve represents the theoretical prediction given by Eq. 6. Data: $\alpha = \lambda = 1$, $\beta_0 = 0.03$, and $\gamma = 0.01$.

Hagen-Poiseuille flow, in which velocity is given by $\boldsymbol{v} = v(y)\,\hat{\boldsymbol{e}}_x$, or even the Rankine vortex, where $\boldsymbol{v} = v(r)\,\hat{\boldsymbol{e}}_\theta$.

In Fig. 2 we are showing the spatial distribution of the population for two paradigmatic examples, the parabolic given by $v(y) = 6\,Uy(L-y)/L^2$, which mean velocity is U for $y \in [0, L]$, and the Rankine vortex with radius R and a rotation rate Γ, given by $v(r) = \Gamma r/(2\pi R^2)$ inside the radius, and $v(r) = \Gamma/(2\pi r)$ outside.

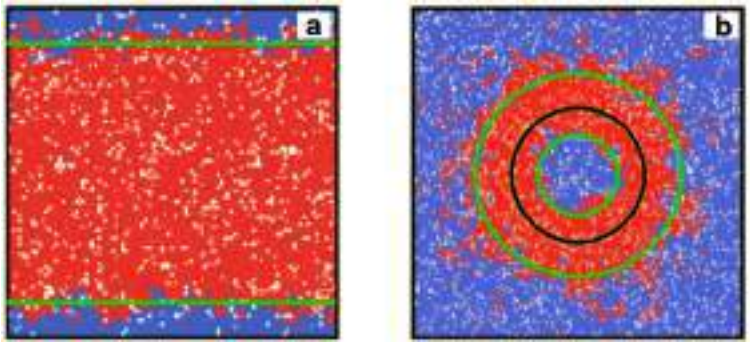

Figure 2: **Spatial distribution of population divided by niches:** (a) Parabolic flow and (b) Rankine vortex. Green lines represent the critical velocity for change in dominance. The black line in (b) shows the radius R.

Following these observations, we can predict the fraction of the environment that will be populated by P-cells by a direct relation to the fraction of the population under flow whose velocity is

below the critical one. Then, in Fig. 3, we can compare both theoretical prediction, by Eq. 6, and numerical simulation for the population living under a parabolic flow. The white lines are delimiting the coexistence zone from a theoretical perspective.

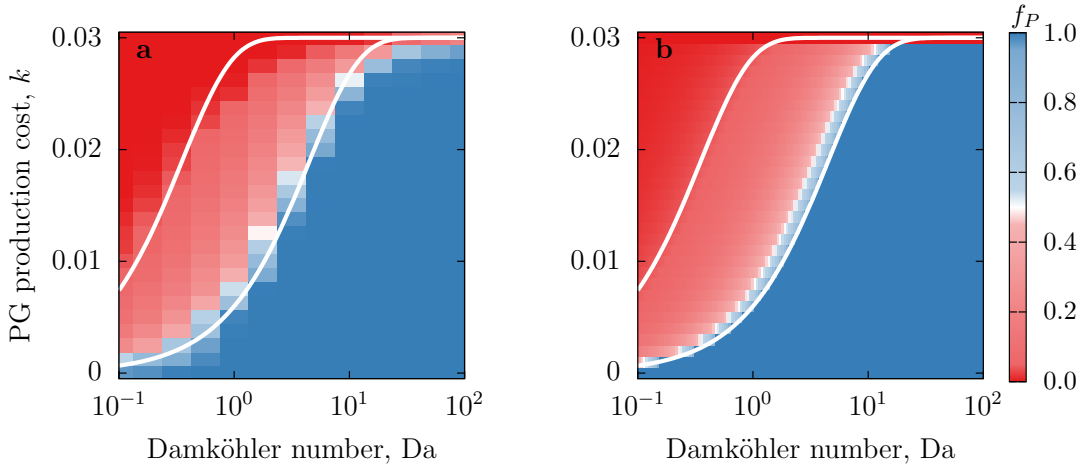

Figure 3: **Parabolic flow:** (a) Numerical simulation. (b) Theoretical predictions.

Discussion

Conclusion

Supporting information

Acknowledgments

V.D and R.M.G. were supported by FAPESP through grant ICTP-SAIFR 2016/01343-7 (V.D. and R.M.G.), postdoctoral fellowship 2020/04751-4 (V.D.) and Programa Jovens Pesquisadores em Centros Emergentes grant 2019/05523-8; and by Instituto Serrapilheira through grant Serra-1911-31200. RMG was partially supported by the Simons Foundation. The authors would like to thank Cristóbal López for useful discussions. This research was supported by resources supplied by the Center for Scientific Computing (NCC/GridUNESP) of the São Paulo State University (UNESP).

References

Allen, B., J. Gore, and M. A. Nowak, 2013: Spatial dilemmas of diffusible public goods. *Elife*, **2**, e01 169.

Borenstein, D. B., Y. Meir, J. W. Shaevitz, and N. S. Wingreen, 2013: Non-local interaction via diffusible resource prevents coexistence of cooperators and cheaters in a lattice model. *PloS one*, **8 (5)**, e63 304.

Crespi, B. J., 2001: The evolution of social behavior in microorganisms. *Trends in ecology & evolution*, **16 (4)**, 178–183.

Drescher, K., C. D. Nadell, H. A. Stone, N. S. Wingreen, and B. L. Bassler, 2014: Solutions to the public goods dilemma in bacterial biofilms. *Current Biology*, **24 (1)**, 50–55.

Gerlee, P., and P. M. Altrock, 2019: Persistence of cooperation in diffusive public goods games. *Physical Review E*, **99 (6)**, 062 412.

Hardin, G., 1968: The tragedy of the commons: the population problem has no technical solution; it requires a fundamental extension in morality. *science*, **162 (3859)**, 1243–1248.

Martínez-García, R., C. D. Nadell, R. Hartmann, K. Drescher, and J. A. Bonachela, 2018: Cell adhesion and fluid flow jointly initiate genotype spatial distribution in biofilms. *PLoS computational biology*, **14 (4)**, e1006 094.

Nadell, C. D., K. Drescher, and K. R. Foster, 2016: Spatial structure, cooperation and competition in biofilms. *Nature Reviews Microbiology*, **14 (9)**, 589–600.

Nadell, C. D., K. R. Foster, and J. B. Xavier, 2010: Emergence of spatial structure in cell groups and the evolution of cooperation. *PLoS computational biology*, **6 (3)**, e1000 716.

Nadell, C. D., D. Ricaurte, J. Yan, K. Drescher, and B. L. Bassler, 2017: Flow environment and matrix structure interact to determine spatial competition in pseudomonas aeruginosa biofilms. *Elife*, **6**, e21 855.

Nowak, M. A., 2006: Five rules for the evolution of cooperation. *science*, **314 (5805)**, 1560–1563.

Oliveira, N. M., E. Martinez-Garcia, J. Xavier, W. M. Durham, R. Kolter, W. Kim, and K. R. Foster, 2015: Biofilm formation as a response to ecological competition. *PLoS biology*, **13 (7)**, e1002 191.

Tarnita, C. E., 2017: The ecology and evolution of social behavior in microbes. *The Journal of Experimental Biology*, **220 (1)**, 18–24, doi:10.1242/jeb.145631, URL http://jeb.biologists.org/lookup/doi/10.1242/jeb.145631.

Thomen, P., J. Robert, A. Monmeyran, A.-F. Bitbol, C. Douarche, and N. Henry, 2017: Bacterial biofilm under flow: first a physical struggle to stay, then a matter of breathing. *PloS one*, **12 (4)**, e0175 197.

Uppal, G., and D. C. Vural, 2018: Shearing in flow environment promotes evolution of social behavior in microbial populations. *Elife*, **7**, e34 862.

West, S. A., S. P. Diggle, A. Buckling, A. Gardner, and A. S. Griffin, 2007: The social lives of microbes. *Annual Review of Ecology, Evolution, and Systematics*, **38 (1)**, 53–77, doi:10.1146/annurev.ecolsys.38.091206.095740, URL https://doi.org/10.1146/annurev.ecolsys.38.091206.095740, https://doi.org/10.1146/annurev.ecolsys.38.091206.095740.

Wheeler, J. D., E. Secchi, R. Rusconi, and R. Stocker, 2019: Not just going with the flow: the effects of fluid flow on bacteria and plankton. *Annual review of cell and developmental biology*, **35**, 213–237.

7 Lista de trabalhos preparados

O trabalho a seguir é referente ao descrito na Seção 2.2.

The effect of preferred location on population persistence and spread

Vivian Dornelas,[1,*] Pablo de Castro,[1,*] William F. Fagan,[2]
Justin M. Calabrese,[3] and Ricardo Martinez-Garcia[1,†]

[1] *ICTP South American Institute for Fundamental Research & Instituto de Física Teórica, Universidade Estadual Paulista - UNESP, São Paulo, Brazil*

[2] *Department of Biology, University of Maryland, College Park, MD, USA*

[3] *Center for Advanced Systems Understanding (CASUS), Görlitz, Germany*

(Dated: October 14, 2022)

A central question in ecology is how the demographic and movement parameters of a population determine its spatial spread and the critical habitat size that can sustain it. Yet, most studies make oversimplifying assumptions about individual movement behavior, which may result in inaccurate predictions. Here, we study the persistence and spread of a population of individuals which experience an effective attraction towards a preferred location in space. Using explicit growth-dispersal models with advective terms, we show how biological populations may adjust to habitat destruction depending on how far from the preferred location the habitat is destroyed. We also incorporate a matrix escape response by turning on attraction towards habitat edges for individuals located in the harsh environmental matrix surrounding the habitat. In particular, our results show that increasing attraction strengths may not always be beneficial. When the attraction center is located near habitat edges, animals may spend too much time exposed to higher death rates, which decreases the total population. Also, for intermediate matrix escape response strengths, death by competition inside the habitat may win over the individual benefit of escaping away sooner from the matrix, leading to overall smaller populations. Our results constitute an important first step towards a more realistic understanding of preferred-location effects at the population level.

I. INTRODUCTION

The critical size of a patch or habitat that makes a population go extinct is a central problem in ecology. Habitat sizes are closely connected with population persistence, species interactions, and habitat fragmentation [1]. For habitat sizes larger than the critical habitat size, a related problem is how a biological population spreads in space. Assuming simple Brownian diffusion models of spatial dispersal for the individuals, as well as a completely non-viable deadly environmental matrix surrounding the habitat, population spread and persistence are well understood at the theoretical level [2].

* These two authors contributed equally.
† ricardom@ictp-saifr.org

However, advances in tracking devices and statistical methods enable us to better understand how animals move. In particular, the above model overlooks the fact that many species do not spread in space in a purely diffusive manner; rather, they are subject to range residency or somewhat similar preferred-location effects [3]. It has been shown using GPS-tracking data that these animals use space non-uniformly, occupying ranges substantially smaller than the population range [4]. The reason why animals may exhibit this kind of behavior has to do with the existence of attractive centers located at places with special properties or resources (including ponds, nests, and shelter), which usually assume a fixed position in time.

A successful way to model preferred-location effects is by introducing an "advection" or "attraction" contribution into a growth-dispersal diffusion-like model. This new term originates from an attractive spring-like force towards a preferred location [3, 5]. This generates a kind of motion equation called Ornstein-Uhlenbeck (OU) model, where the animal velocity is a combination of random noise and a restoration contribution that increases linearly with the distance to a preferred location. The OU model has been shown to be more accurate for animal movement at long time scales than pure Brownian motion [3]. Yet, theoretical development incorporating the long-term consequences of preferred location at the population and community level are rare [4, 5].

In this paper, we provide the first study quantifying how preferred-location attraction may impact critical habitat size as well as how the different individual-level movement parameters and different spatial patterns of habitat destruction may affect population persistence in heterogeneous landscapes. Importantly, such comparison is possible because, in the infinite habitat size case, OU movement leads to a stationary spatial distributions of population density with finite variance around a well-defined mean. In essence, we extend the definition of critical habitat size to account for the spatial location of the habitat edges relative to key resources in the environment that determine the area of occurrence of a given species. In our model, besides assuming that individual movement can be described with an OU movement term towards a preferred location (a point in space), we consider that individuals change their movement behavior once located in the harsh matrix by turning on an additional OU movement term that corresponds to a matrix escape response towards habitat edges. Also, we assume a logistic population growth and a harsh matrix in which individuals die after a characteristic time rather than instantaneously. We incorporate all these ingredients in a partial differential equation for the population density, which we analyze in a one-dimensional finite domain. These ingredient allows us to incorporate two additional layers of complexity and study how the total size and spatial pattern of a population respond to habitat destruction depending on how far from the preferred location the habitat is destroyed. Such questions have not been explored before and are the main focus of our analysis.

This paper is organized as follows. Section II defines our mathematical model and approach. Section

III brings our analytical and numerical results. In Section IV we present our conclusions.

II. MODEL

We consider a population where each individual moves following a one-dimensional Ornstein-Uhlenbeck (OU) model [5] equipped with, in principle, two attractive terms: (i) towards a preferred location and (ii), if the animal is outside the patch, towards the closer edge of the patch. That is, the habitat itself is a preferred *region*, existing besides the preferred point-like location. The corresponding equation of motion for the position x at time t is

$$\dot{x}(t) = -\tau^{-1}\left[x(t) - \lambda\right] - g_{\mathrm{M}}(x)\left[x(t) - \lambda_{\mathrm{E}}(x)\right] + \sqrt{2D}\xi(t), \tag{1}$$

where $\xi(t)$ is a zero-mean white noise with variance unity, D is the diffusion coefficient, τ^{-1} is the preferred-location attraction rate, with dimensions of inverse time, $g_{\mathrm{M}}(x)$ is the matrix escape response strength, or edge attraction rate, which is turned on only for x in the matrix, and $\lambda_{\mathrm{E}}(x)$ is the location of the corresponding habitat edge (left or right, depending on x). For simplicity, and without loss of generality, in the following we set the origin of coordinates at the preferred location, i.e., the position of the attraction center is $x = \lambda = 0$. We also define $x = -L_{\mathrm{L}}$ and $x = +L_{\mathrm{R}}$ for the locations of the left and right habitat edges, respectively. Thus, $\lambda_{\mathrm{E}}(x) = -L_{\mathrm{L}}$ for $x < -L_{\mathrm{L}}$ and $\lambda_{\mathrm{E}}(x) = L_{\mathrm{R}}$ for $x > L_{\mathrm{R}}$. Also, $g_{\mathrm{M}}(x) = \tau_{\mathrm{M}}^{-1}$ for $x < -L_{\mathrm{L}}$ or $x > L_{\mathrm{R}}$, and zero otherwise, with τ_{M}^{-1} constant. The total habitat size is $L = L_{\mathrm{L}} + L_{\mathrm{R}}$.

We further assume that all individuals within the population have the same preferred location, which is a good assumption for non-territorial species and/or scenarios in which the preferred location is determined by the presence of key resources.

For the population dynamics, we assume that the population follows a logistic growth model with net reproduction rate $r(x)$ and constant competition parameter γ (see below). To mimic the effects of a harsh matrix, we use that $r(x) = r_{\mathrm{in}}$ inside the habitat and $r(x) = -d_{\mathrm{out}}$ outside, with r_{in} and d_{out} positive constants. Logisitic growth coupled to OU movement leads to the following partial differential equation for the spatiotemporal dynamics of the population density $u(x,t)$:

$$\frac{\partial u(x,t)}{\partial t} = r(x)u(x,t) - \gamma u(x,t)^2 + D\frac{\partial^2 u(x,t)}{\partial x^2} + \tau^{-1}\frac{\partial}{\partial x}\left[(x-\lambda)u(x,t)\right] + g_{\mathrm{M}}(x)\frac{\partial}{\partial x}\left[(x-\lambda_{\mathrm{E}}(x))u(x,t)\right]. \tag{2}$$

Mathematically, Eq. (2) is an extension of the well-known Fisher-Kolmogorov equation (diffusion and logistic population growth) that includes two advection terms to account for the attractions to the preferred location and to the habitat.

III. RESULTS

To build intuition progressively, we start by presenting our results for the critical habitat size, spatial distribution, and total population in the case where the animal cannot survive in the matrix, i.e., $d_{\text{out}}^{-1} = 0$, considering preferred-location attraction. Then, we turn on d_{out}^{-1}, first without matrix escape response, i.e, $\tau_{\text{M}}^{-1} = 0$, and finally with matrix escape response, i.e., $\tau_{\text{M}}^{-1} \neq 0$.

A. Extremely harsh matrix: $d_{\text{out}}^{-1} = 0$

For an extremely harsh matrix, i.e., $d_{\text{out}} \to \infty$, since the individuals do not change their movement inside the habitat close to the habitat edges, the boundary conditions are absorbing and read $u(-L_{\text{L}}, t) = u(L_{\text{R}}, t) = 0$. In this case, it does not make a difference to have or not a matrix escape rate since individuals die there instantaneously. Because we are interested in determining the habitat configurations $(L_{\text{L}}, L_{\text{R}})$ that lead to the long-term extinction of the population, we perform a linear stability analysis of the solution $u(x, t \to \infty) \equiv u_{\text{s}}(x) = 0$. By doing so, we can calculate the critical *total* habitat size L_c of the population. In what follows, we prefer to choose L_{L} and obtain the critical *right-hand side* habitat size $L_{\text{R,c}}$, without loss of generality. To that end, we neglect the quadratic term in the logistic growth and take the $t \to \infty$ limit in Eq. (2), which means setting $\partial_t u(x, t) = 0$. In this limit, Eq. (2) becomes an ordinary differential equation with solution $u_{\text{s}}(x)$ of the following form (shown here for completeness only):

$$u_{\text{s}}(x) = \exp\left(-\frac{x^2}{2\tau D}\right)\left[aH_{r\tau}\left(\frac{x}{\sqrt{2D\tau}}\right) + b\ {}_1F_1\left(-\frac{r\tau}{2}; \frac{1}{2}; \frac{x^2}{2D\tau}\right)\right], \tag{3}$$

where a and b are constants to be determined by boundary conditions, H_n is the Hermite polynomial of order n, such that $H_0(x) = 1, H_1(x) = 2x, \ldots$, and ${}_1F_1$ is the confluent hypergeometric function of the first kind [6]. Imposing the boundary conditions to Eq. (3), one obtains a system of two equations for a and b. Because we do not know the value of $u_s(x)$ elsewhere other than at the edges, the equations for a and b can only be used to find out the shape of $u_s(x)$ and therefore the stability of the $u_s(x) = 0$ solution. This is done by noticing that, in order for this system of equations to have non-trivial solutions different than $a = b = 0$, its determinant has to be zero, with a and b being the variables. With this condition for the determinant and assuming that L_{L} is fixed, we obtain a transcendental equation in L_{R} that can be solved numerically to obtain the critical right-hand side habitat size $L_{\text{R,c}}$. We compare the results from this semi-analytical method with those obtained from the numerical integration of the full nonlinear Eq. (2). We use a central Euler method to solve Eq. (2) starting from a random positive initial condition for u that obeys the absorbing boundary conditions. This allows $L_{\text{R,c}}$ to be easily calculated:

by varying $L_{\rm R}$, the critical value is reached once the steady-state total population size transitions from non-zero to zero.

Before showing our results for the critical habitat sizes and total population, we start understanding the the impact of habitat destruction on the spatial spread of our population by looking into the stationary profiles of population density $u_{\rm s}(x)$. This is done via numerical integration of the full nonlinear Eq. (2) for three different combinations of $L_{\rm L}$ and $L_{\rm R}$ that result in population persistence (Fig. 1). That is, we consider three habitat spatial configurations such that $L_{\rm L} + L_{\rm R} > L_c$. We observe that when habitat destruction is not symmetric around the preferred location, i.e., $L_{\rm L} \neq L_{\rm R}$, the location of the maximum population density $x_{\rm p}$ deviates from the preferred location, resulting in a skewed or asymmetric population density distribution. Interestingly, we observe that survival is possible even if the preferred location is situated in the matrix (see Fig. 1c), a scenario that could arise if an important resource ended up being located in the matrix, e.g., a lake in a deforested region.

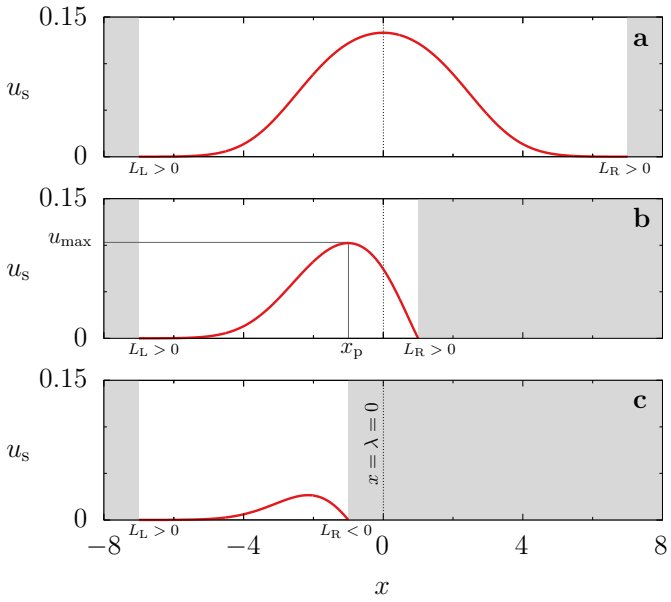

FIG. 1. Stationary population density distribution $u_{\rm s}(x)$ for (a) $L_{\rm R} = 7$ and $L_{\rm L} = 7$, (b) $L_{\rm R} = 1$ and $L_{\rm L} = 7$, and (c) $L_{\rm R} = -1$ and $L_{\rm L} = 7$, as calculated by numerically integrating Eq. (2). Other parameters: $r_{\rm in} = 0.1$, $d_{\rm out}^{-1} = 0$, $\gamma = 1$, $D = 0.1$, $\lambda = 0$, and $\tau^{-1} = 0.05$. $u_{\rm max}$ is the maximum population density and $x_{\rm p}$ its location. Gray regions represent the matrix.

We now explore the $L_{\rm R}$-$L_{\rm L}$ parameter space for different values of τ^{-1} (Fig. 2a-c). We can use numerical simulations of Eq. (2) to measure the total population fraction lost to deforestation (from $L \to \infty$ to finite $L_{\rm L}$ and $L_{\rm R}$). We actually plot the remaining total population fraction $\eta \equiv N_{\rm T}/N_{\rm T}^{\infty}$, where $N_{\rm T} \equiv \int u_{\rm s}(x)dx$ integrating over the entire range, and similarly for $N_{\rm T}^{\infty}$, for each parameter combination. The critical habitat size obtained via stability analysis from Eq. (3) as described above (solid line in Fig. 2a-c) shows an excellent agreement with the full numerical simulations. As expected, the behavior of

η is symmetric about the $L_R = L_L$ diagonal. Moreover, for sufficiently large L_R or L_L, further increasing habitat size does not change the population size because the flux of individuals through the habitat edges becomes negligible when these are very far from the population preferred location. This explains why the green solid lines in Fig. 2a-c are horizontal and vertical in the limits $L_L \to \infty$ and $L_R \to \infty$, respectively, and why they tend to this asymptotic behavior faster for higher τ^{-1}. Finally, Fig. 2a shows that the population can survive even when the preferred location lies within the matrix, as already observed in Fig. 1c. That is, the population can survive even when L_R and L_L have opposite signs (see Fig. 1a).

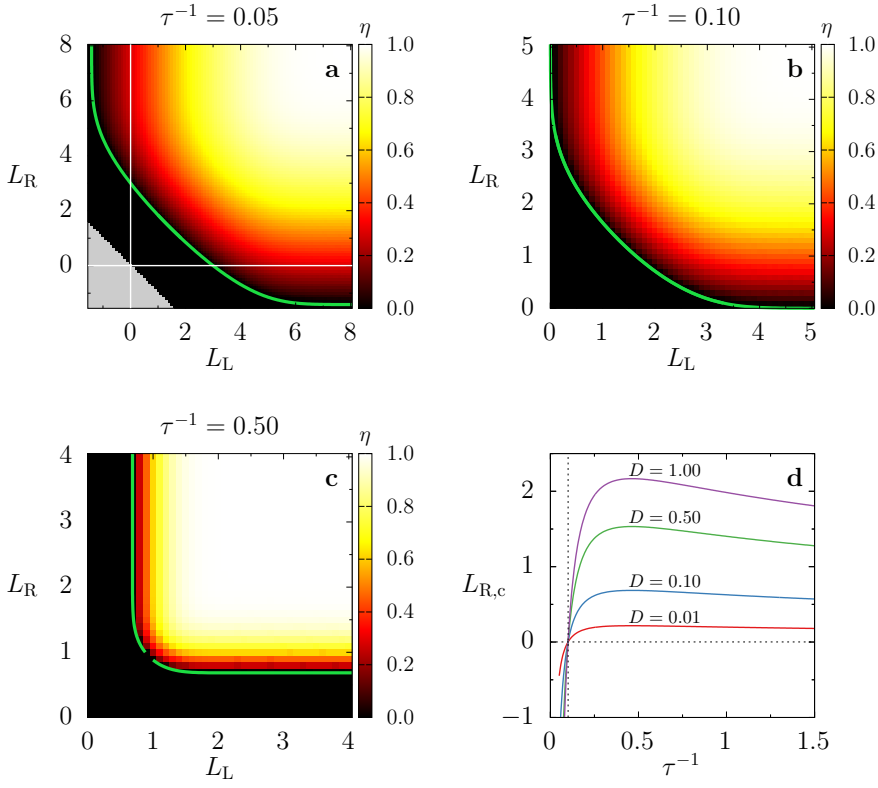

FIG. 2. (a)-(c): "Heat" map of total population (divided by the infinite-habitat population) η in the habitat sizes plane L_R versus L_L for (a) $\tau^{-1} = 0.05$, (b) $\tau^{-1} = 0.1$, and (c) $\tau^{-1} = 0.5$. Other parameters: $r_{in} = 0.1$, $d_{out}^{-1} = 0$, $D = 0.1$, and $\gamma = 1$. The solid line (green) shows the numerical solution from stability analysis for the critical habitat sizes line. In (a), the origin is marked to highlight the existence of survivability in a negative L_R and L_L region. The gray area is undefined as it would correspond to the "right" border being on the left and vice-versa. (d) Critical right habitat size $L_{R,c}$ as a function of τ^{-1} for distinct values of D, as indicated, $r_{in} = 0.1$, $d_{out}^{-1} = 0$, and $L_L = 100$.

The total population fraction lost to deforestation η can be plotted against the remaining fraction of habitat above the critical habitat size $\epsilon \equiv L/L_c$, as shown in Fig. 3 for $\lambda = 0$. For $\tau^{-1} = 0$, one would have $N_T^{\infty} \to \infty$ and thus $\eta \to 0$ since the population spreads homogeneously everywhere without borders and increases to a finite population size set by γ. By increasing τ^{-1}, the curve $\eta(\epsilon)$ moves up, indicating that a sharper decrease occurs towards extinction as one moves towards the critical habitat size. In other

words, close to the critical habitat size, lower-τ^{-1} centralized populations are more sensitive to the same relative habitat loss. In particular, Fig. 3 provides the percentage losses depending on such sensibility controlled by τ^{-1}. For instance, for $\tau^{-1} = 0.05$, even when the habitat size is still twice the critical habitat size ($\epsilon = 2$), the population goes down to about 50% of what it could be without deforestation or habitat limitations.

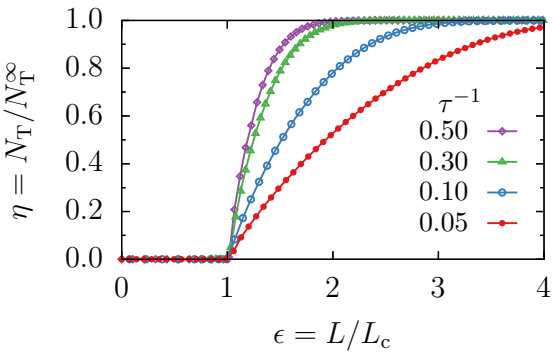

FIG. 3. Ratio between the total population for L and for $L \to \infty$, η, versus $\epsilon \equiv L/L_c$ for various τ^{-1} as indicated. Other parameters: $D = 0.1$, $\gamma = 1$, $r_{in} = 0.1$, $d_{out}^{-1} = 0$, and $\lambda = 0$.

To further investigate the behavior of the critical habitat size, we calculated the critical location of the right habitat edge $L_{R,c}$ in the case where death at the left one is negligible, obtained with $L_L \to \infty$. We conducted this analysis for several values of τ^{-1} and D. We identify three different regimes in the relationship between $L_{R,c}$ and τ^{-1} (see Fig. 2d). First, at intermediate values of τ^{-1}, $L_{R,c}$ is positive and increases with increasing τ^{-1} until it peaks at a value of τ^{-1} that depends on the intensity of the random component of movement, D. In this regime, individuals need a larger area to ensure population survival even if they would exhibit smaller home ranges in infinite habitats (higher values of τ^{-1} result in narrower distributions). This is due to the fact that the preferred location is located close to the habitat edges and, therefore, individuals need to spend more time away from it to minimize death risk and ensure population persistence. Then, for large values of τ^{-1}, $L_{R,c}$ decreases with increasing τ^{-1} because preferred-location attraction dominates individual movement; in this case, individual area requirements are small and the population is confined within a "safe", small region around the preferred location. Finally, at low values of τ^{-1} such that $\tau^{-1} < r_{in}$, one has that $L_{R,c}$ is negative, which means that the population can persist even if its preferred location is in the matrix. In this low-τ^{-1} regime, decreasing τ^{-1} (or increasing diffusion) leads to $L_{R,c}$ becoming more negative (i.e., the preferred location can be located further inside the matrix) because individuals are more spread around the preferred location, including towards the infinite side, and thus less individuals die crossing the edge attracted to the preferred location.

Next, we characterize the impact of different patterns of habitat destruction, represented by the locations of the habitat edges, on the spatial pattern of population density. As discussed in previous sections,

the distance between the spatial coordinate with maximum population density and the preferred location is a measure of the asymmetry of $u_s(x)$ (and also indicates skewness in this case). This distance quantifies how much the location of the maximum population density deviates from the expected valued in an infinite habitat and, because the preferred location is located at the origin of coordinates, this distance is equal to the location of the peak, x_p. Fig. 4a shows x_p as a function of the total habitat size $L = L_L + L_R$ for different levels of symmetry in habitat destruction. To implement asymmetry in habitat destruction systematically, we use L_L as a control parameter and define $L_R = \alpha L_L$. In the limit $\alpha = 1$, $L_R = L_L$ and habitat destruction is symmetric about the preferred location. As α decreases, habitat destruction becomes more asymmetric. We consider $\alpha = 0.25$, 0.5, 0.75, and 1.0. In the highest asymmetry case, $\alpha = 0.25$, x_p increases up to a certain value of L and then it has to decrease since, in the infinite habitat size limit, the maximum population density coincides with the OU home-range center [5]. For higher α, we see a similar behavior but with a progressively lower peak for $x_p(L)$. To validate our results, we check that, for symmetric habitat destruction, $x_p = 0$ for all values of the habitat size. The spread of $u_s(x)$, i.e., the standard deviation of x, is shown in Fig. 4b, confirming that the closer to a border the narrower the spatial distribution becomes.

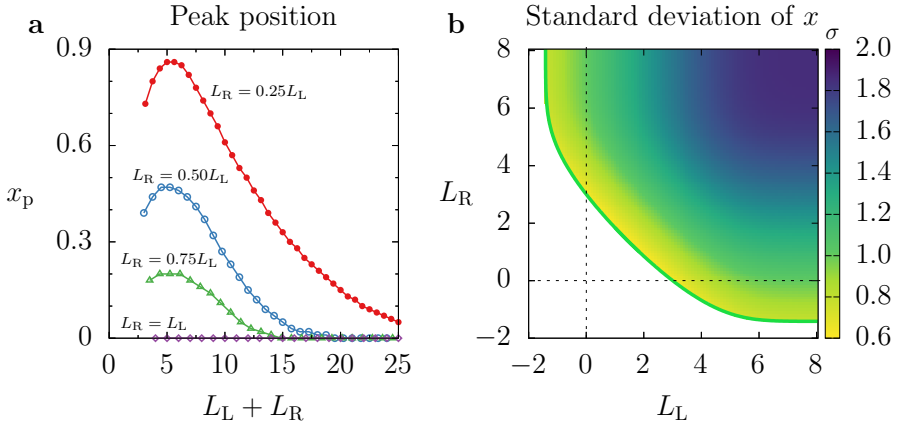

FIG. 4. (a) Peak position as a function of the total habitat size $L = L_L + L_R$ for $L_R = 0.25L_L$ (filled red disks), $L_R = 0.5L_L$ (empty blue circles), $L_R = 0.75L_L$ (empty green triangles), and $L_R = L_L$ (empty purple diamonds). (b) "Heat" map of the standard deviation of x. Other parameters: $r_{in} = 0.1$, $d_{out}^{-1} = 0$, $D = 0.1$, and $\tau^{-1} = 0.05$.

B. Partially harsh matrix with and without matrix escape response: $d_{out}^{-1} \neq 0$

Fig. 5 shows the stationary spatial distribution considering that the animal can now still survive for a time of the order $1/d_{out}$ outside the habitat, where $d_{out} > 0$ is thus the finite death rate in the matrix, and without matrix escape response ($\tau_M^{-1} = 0$). Our previous scenario corresponds to $d_{out} \to \infty$. The population now persists outside the matrix, which is best observed using a log scale for the u_s axis, as

shown on the right-hand side of Fig. 5. Notice the exponential tail indicated by a straight line when the u_s axis is in log scale. More importantly, the general qualitative behavior of the habitat size problem remains unaltered and therefore one can rely on our previous observations for the case with instantaneous death in the matrix.

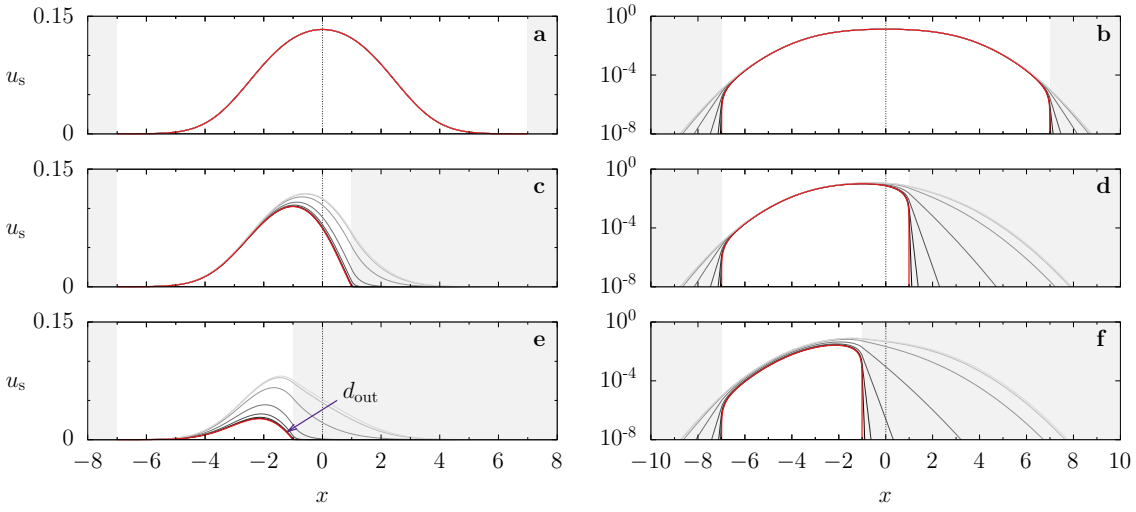

FIG. 5. Left: Stationary population density distribution $u_s(x)$ for the same parameters as in Fig. 1, with (a) corresponding to Fig. 1a, (c) to Fig. 1b, and (e) to Fig. 1c, but now with a finite negative net reproduction rate outside the habitat of magnitudes $d_{out} = 10^{-3}$, 10^{-2}, 10^{-1}, 10^0, 10^1, 10^2, and 10^3 increasing as indicated in (e). Right: Same as left side but with the u_s axis in log scale.

By turning on matrix escape response ($\tau_M^{-1} \neq 0$), the spatial distribution enters into the habitat, as shown in Fig. 6. In the symmetric case (Fig. 6a), as the individuals accumulate equally on both sides. For large enough τ_M^{-1}, the edges act as almost hard walls. Fig. 6 shows an asymmetric case where the preferred location is situated in the matrix. Even though the individuals are attracted to the matrix due to the preferred location attraction, for large enough matrix escape response, individuals will mostly accumulate at the habitat edge, in a highly asymmetric way.

Fig. 6 suggests a competition between two effects: the individual (and therefore populational) benefit of escaping from the matrix versus death by resource competition inside the habitat as more individuals dwell in it due to the matrix escape response. To understand that, we plot the total population (divided by the infinite habitat population) η versus τ_M^{-1}. For simplicity, we consider only the symmetric case. For sufficiently low d_{out}, a minimum in η versus τ_M^{-1} is observed. This is related to the balance between the spatial distribution mass outside versus inside as τ_M^{-1} is changed. In simple terms, by increasing τ_M^{-1}, resource competition inside the habitat increases more than the population gain obtained by individual escape since d_{out} is low. By further increasing τ_M^{-1}, the matrix escape response is so high that only a small amount of individuals enter (and potentially die in) the matrix and thus this effect now wins over the population loss that arises from additional resource competition inside the habitat.

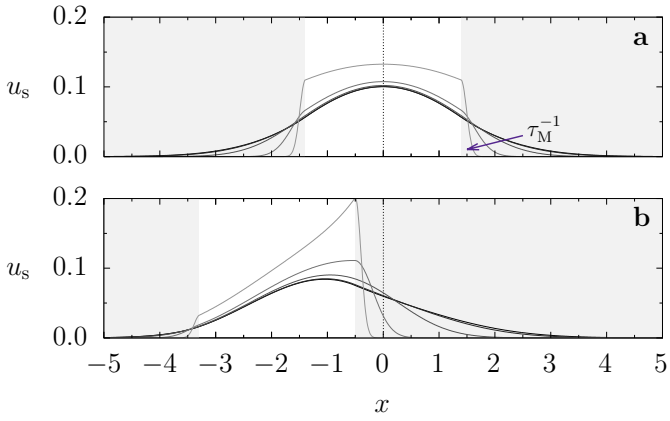

FIG. 6. Stationary population density distribution $u_s(x)$ for $L = 2.8$, smaller than the L_c of the extremely harsh matrix symmetric case, $\tau^{-1} = 0.05$, $d_{out} = 10^{-3}$, and $\tau_M^{-1} = 10^{-3}$, 10^{-2}, 10^{-1}, 10^0, and 10^1 increasing as indicated in the figure. (a) $L_R = L_L = 1.4$ and (b) $L_R = -0.5$ and $L_L = 3.3$. Other parameters as in Fig. 1.

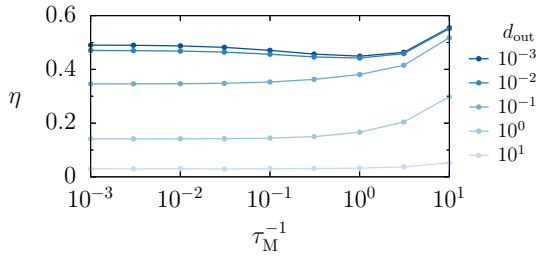

FIG. 7. Ratio between the total population for L and for $L \to \infty$, η, versus τ_M^{-1}. $L_R = L_L = 1.4$ and $d_{out} = 10^{-3}$, 10^{-2}, 10^{-1}, 10^0, and 10^1, with lighter colors corresponding to larger d_{out}.

IV. CONCLUSIONS

Here we addressed the movement ecology question of how preferred-location effects alter spatial spread at the population level. A growth-dispersal model with advective currents is introduced and solved to show how the populations adjust to habitat destruction depending on the position of the preferred location with respect to habitat edges. A matrix escape response has been incorporated (also as an advective/attraction term) and is turned on only for individuals located in the matrix. We have shown that the population size depends non-monotonically on attraction strengths. For an attraction center located near habitat edges, animals live around higher death rates and thus the total population decreases. For intermediate matrix escape response, death by competition inside the habitat is more important than the individual benefit of escaping from the matrix. This also leads to a decrease in total population.

Our findings highlight the importance of considering preferred location effects into individual movement behavior and its consequences to the populations. In particular, our calculation shows that, for the same habitat size, different levels of preferred-location (and/or matrix escape response) strengths lead to significantly different population fractions of the corresponding infinite-habitat population. This is

expected to motivate new observational and theoretical work to further understand the role of several kinds of non-Brownian movement aspects in the persistence and spread of biological populations, including applications to conservation biology.

ACKNOWLEDGMENTS

V.D. and P.d.C were supported by São Paulo Research Foundation (FAPESP, Brazil) postdoctoral fellowships #2020/04751-4 and #2021/10139-2, respectively. R.M.-G was supported by the FAPESP program Jovens Pesquisadores through grant no. 2019/05523-8, the ICTP through the Associates Programme, and the Simons Foundation through grant no. 284558FY19. V.D, P.C., and R.M.-G. were supported by FAPESP through ICTP-SAIFR grant no. 2016/01343-7. This research was supported by resources supplied by the Center for Scientific Computing (NCC/GridUNESP) of the São Paulo State University (UNESP).

[1] D. M. Debinski and R. D. Holt, A survey and overview of habitat fragmentation experiments, Conservation biology **14**, 342 (2000).

[2] H. Kierstead and L. B. Slobodkin, The size of water masses containing plankton blooms, J. mar. Res **12**, 141 (1953).

[3] C. H. Fleming, J. M. Calabrese, T. Mueller, K. A. Olson, P. Leimgruber, and W. F. Fagan, From fine-scale foraging to home ranges: a semivariance approach to identifying movement modes across spatiotemporal scales, The American Naturalist **183**, E154 (2014).

[4] M. J. Noonan, R. Martinez-Garcia, G. H. Davis, M. C. Crofoot, R. Kays, B. T. Hirsch, D. Caillaud, E. Payne, A. Sih, D. L. Sinn, *et al.*, Estimating encounter location distributions from animal tracking data, Methods in Ecology and Evolution **12**, 1158 (2021).

[5] R. Martinez-Garcia, C. H. Fleming, R. Seppelt, W. F. Fagan, and J. M. Calabrese, How range residency and long-range perception change encounter rates, Journal of theoretical biology **498**, 110267 (2020).

[6] G. B. Arfken and H. J. Weber, Mathematical methods for physicists (1999).

ICTP | International Centre for Theoretical Physics
SAIFR | South American Institute for Fundamental Research

Final Scientific Report

Movement strategies and population dynamics in heterogeneous environments

---

Postdoctoral Fellow: Gabriel Andreguetto Maciel

Supervisor: Nathan Jacob Berkovits

Fapesp process: 2019/21227-0

Project duration: 01/Jan/2020 - 31/Jul/2022

Reporting period: 01/Dez/2021 - 31/Jul/2022

August, 2022

Abstract

This project was initially intended to investigate the interplay between movement strategies and the consequent dynamics of population spreading and growth. Two main projects were developed during the period of the fellowship. In the first project we studied the dynamics of populations that interact non-locally. We explored how long range interactions can potentially generate spatial patterns of distribution and change competition dynamics. This study was published in the Journal of Theoretical Biology (Maciel and Martinez-Garcia, 2021). The second project explores the phenomenon of antagonistic facilitation in plants. We build and analyse evolutionary game models for species that can modify the environment and improve survival and growth conditions, the so called ecosystem engineers. The effect of engineering for a single and two interacting species are studied. We show that there are conditions where opportunist (not engineer) plants are facilitated by engineer plants. This means that the net fitness gain of the opportunist plant is higher in the presence of an engineer than when solo and we have a situation termed antagonistic facilitation. We are in the stage of writing a scientific article about this project.

1 Enhanced species coexistence in Lotka-Volterra competition models due to nonlocal interactions

1.1 Overview

In order to understand how competition systems, that are apparently highly unstable systems, are so ubiquitous in nature, in the past few decades a vast wealth of studies have looked for mechanisms present in real populations that could facilitate the coexistence of two competing species. Differences of space use in heterogeneous space, seasonal fluctuations of resource availability and diet differentiation are some of the basic mechanisms that have been shown to promote coexistence of competitors (Amarasekare, 2003; Chesson, 2000; Cantrell et al., 2007). There are systems with coexisting competitors, however, in which none of these mechanisms is present. In these cases, from which plant communities are a particular important example, how species manage to coexist thus remain an unresolved puzzle (Silvertown, 2004). In this work we explored in detail a much less studied mechanism based on the spatial self-organization of organisms.

In ecological models, spatial patterns of species distributions can be formed in the presence of short-range positive and long-range negative feedbacks (Rietkerk and van de Koppel, 2008; Meron, 2018). The effects of nonlocal interactions on two-species competition has been investigated in previous studies (Britton, 1989; Segal et al., 2013; Bayliss and Volpert, 2015). Their analysis, however, was limited to regimes where the species coexist in the classical model.

In this work, we study through kernel-based models the dynamics of non-local competition between two species and explicitly show that competitors coexist in situations where competitive exclusion occurs in the absence of long-range interactions.

1.2 Models

We study a spatial version of the two-species competitive Lotka-Volterra equations in a one-dimensional domain. In addition to exponential growth and local competition, our model also includes individual dispersal and nonlocal interactions, two inherently spatial processes. The density of individuals of each species thus changes according to

$$\frac{\partial \rho_1(x,t)}{\partial t} = D_1 \frac{\partial^2 \rho_1}{\partial x^2} + b_1\, \rho_1 \left(1 - \frac{a_{11}\rho_1 + a_{12}\rho_2}{K_1} - h_{11}\widetilde{\rho}_{11} - h_{12}\widetilde{\rho}_{12}\right) \tag{1}$$

$$\frac{\partial \rho_2(x,t)}{\partial t} = D_2 \frac{\partial^2 \rho_2}{\partial x^2} + b_2\, \rho_2 \left(1 - \frac{a_{21}\rho_1 + a_{22}\rho_2}{K_2} - h_{21}\widetilde{\rho}_{21} - h_{22}\widetilde{\rho}_{22}\right). \tag{2}$$

The first term in each equation accounts for dispersal with species-specific diffusion D_i $(i = 1, 2)$. The second term corresponds to species intrinsic growth at rate b_i and pairwise local and nonlocal competition. Local competition is modeled as in the classical Lotka-Volterra model with competition coefficients a_{ij} $(i, j = 1, 2)$. The local interactions represent, for example, competition for space or for any other resource that is gathered locally by the individuals. K_i is the carrying capacity of species i. The coefficients h_{ij} give the intensity of nonlocal competition interactions of species i with itself and with the other competitor. $\widetilde{\rho}_{ij}$ is the average density of j-individuals in a neighborhood centered at x, which is a proxy for the mean number of i-j interactions within that neighborhood. In general, we can weigh the average by the effect that the i-j inter-individual distance has on the intensity of the interaction between them. If we assume spatial isotropy, $\widetilde{\rho}_{ij}$ is:

$$\widetilde{\rho}_{ij}(x,t) = \int dx'\, G_{ij}(|x - x'|)\rho_j(x',t) \tag{3}$$

where G_{ij} is a kernel function that weighs the influence that individuals from species j exert on the growth rate of species i when they are at a distance $|x - x'|$. These nonlocal terms represent, for example, competition for resources that are acquired by individuals within a finite neighborhood or direct interference mediated by forces that have a non-zero range of action. For example, in plant communities, the nonlocal terms could account for root-mediated competition for resources. Local competition could represent competition for space during plant establishment or competition for light, assuming that the size of the canopy is negligible compared to the range

of the root system.

We consider normalized top-hat kernel functions for the sake of mathematical simplicity. For two species, i and j, with interaction range R_{ij}, the kernel function is given by:

$$G_{ij}(r) = \Pi_{2R_{ij}}(r) = \begin{cases} \frac{1}{2R_{ij}} & \text{if} \quad r \leq R_{ij} \\ 0 & \text{if} \quad r > R_{ij}. \end{cases} \tag{4}$$

To reduce the number of free parameters we first derive the nondimensional version of Eqs. (1)-(2). We use b_1^{-1} as the reference time scale and R_1 as the reference length scale. Therefore, the nondimensional influence range of species 1 is the unity and the nondimensional influence range of species 2 is given by the ratio $q = R_2/R_1$. A similar argument follows for the rescaled time, and we write the new space and time variables as $\xi = x/R_1$ and $\tau = b_1 t$, respectively. Using the nondimensional quantities $u_1 = \rho_1/K_1$, $u_2 = \rho_2/K_2$, $d_1 = D_1/(d_1 R_1^2)$, $d_2 = D_2/(d_1 R_1^2)$, $c_{12} = a_{12}K_2/K_1$, $c_{21} = a_{21}K_1/K_2$, $\beta = b_2/b_1$, $\phi_{11} = K_1 h_{11}$, $\phi_{22} = K_2 h_{22}$, $\phi_{12} = K_2 h_{12}$, $\phi_{21} = K_1 h_{21}$ in Eqs. (1)-(2), the model equations become:

$$\begin{aligned} \frac{\partial u_1}{\partial \tau} &= d_1 \frac{\partial^2 u_1}{\partial \xi^2} + u_1 \Bigg[1 - u_1 - c_{12} u_2 \\ &\quad - \phi_{11} \int \Pi_2(|\xi - \xi'|) u_1(\xi', \tau) d\xi' - \phi_{12} \int \Pi_{2q}(|\xi - \xi'|) u_2(\xi', \tau) d\xi' \Bigg] \end{aligned} \tag{5}$$

$$\begin{aligned} \frac{\partial u_2}{\partial \tau} &= d_2 \frac{\partial^2 u_2}{\partial \xi^2} + \beta u_2 \Bigg[1 - u_2 - c_{21} u_1 \\ &\quad - \phi_{22} \int \Pi_{2q}(|\xi - \xi'|) u_2(\xi', \tau) d\xi' - \phi_{21} \int \Pi_2(|\xi - \xi'|) u_1(\xi', \tau) d\xi' \Bigg]. \end{aligned} \tag{6}$$

The long-term behavior of the model is studied combining numerical and analytical methods and we focus on understanding how nonlocal competition and the emergent spatial patterns of population densities stabilize species coexistence.

1.3 Results

The main results of our analysis are summarized in Figure 1. In this figure parameter regimes for species exclusion and coexistence are shown. The light blue and gray regions indicate the conditions in which the local model predicts species coexistence and exclusion respectively. The diagonal stripes highlight where a derived approximated invasion condition (not shown in this report) for species 2 is satisfied and hence the nonlocal model predicts species coexistence. The dots indicate the pairs c_{21}, ϕ_{21} used to obtain the spatial patterns shown in panels (c)-(k). In panel b) we have the average density of species 2 as a function of c_{21}, ϕ_{21}, $\tilde{u}_2 \neq 0$ indicates species coexistence and $\tilde{u}_2 = 0$ competitive exclusion of species 2. The black dashed

lines indicate the end of the striped and light blue region in panel a.

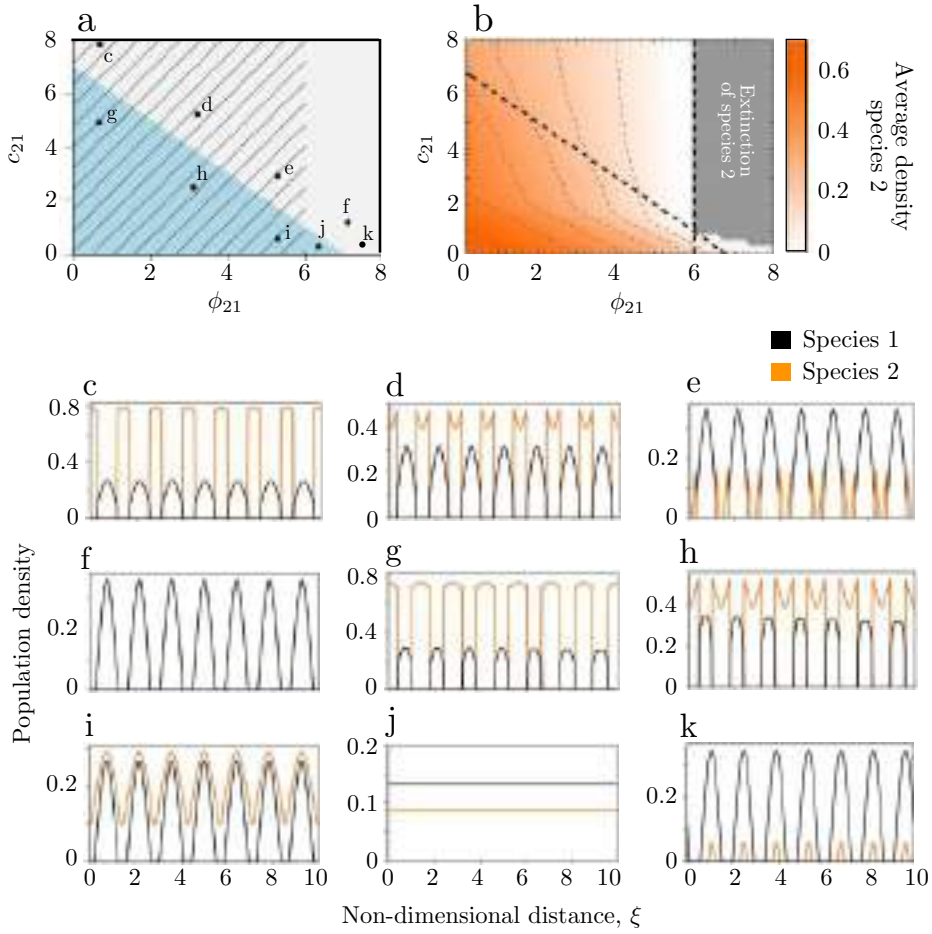

Figure 1

Note that the dots c, d and e in panel a are in the parameters region where Species 2 is competitively excluded in the local model. However, when interaction is non-local the species coexist as can be seen in the patterns distribution in in panel b.

We have shown that coexistence through the invasion of the weaker competitor of sparsely populated areas can occur in the absence of facilitation mechanisms. We have also provided a thoroughly exploration of coexistence conditions and of the distribution patterns that can be formed.

2 The evolutionary dilemma of antagonistic facilitation in plants

2.1 Overview

Plants have developed a rich variety of strategies to cope with different soil conditions and interactions with competitors. Cabal et al. (2020) used experiments and an evolutionary game theory framework to study the spatial distribution of roots when two competing plants are close to each other. They show that plants overgrow roots at points further from the other competing plant and undergrow roots at points with higher densities of the other plant roots. In that study no consideration on soil amelioration strategies by the plants is made.

Many plants species are able to modify their environment and improve conditions for growth. These species are then called ecosystem engineers. Improved soil conditions increase engineers growth but it can also benefit potential competing plants, a phenomenon that has been termed antagonistic facilitation. Although some empirical studies have suggested that antagonistic facilitation may be ubiquitous in nature, it is still not clear if it can be evolutionarily stable and under what conditions.

In this work we build and analyse game theoretical model for the growth and evolution of plants with facilitation mechanisms. We initially study the effect of engineering for a single plant. Then we investigate the interaction of two plant species, one of them is an ecosystem engineer and the other is a similar species that does not employ engineering mechanisms, which we refer as opportunists. We show that there are conditions under which antagonistic facilitation occurs.

2.2 Single plant model

We initially consider a single plant engineer that feeds on a given resource. Root and resource biomass densities are denoted, respectively, by $R(x,t)$ and $W(x,t)$, where x and t are the spatial location and time. We assume resource grows via the net result of an input rate in the system, natural decaying rate and plant consumption. As the engineer potentially modifies the resource availability in the system we write the input rate as $I(R(x,t))$. Accordingly, we model resource dynamics by the equation:

$$\frac{\partial W(x,t)}{\partial t} = I(R(x,t)) - \delta W(x,t) - \alpha R(x,t) W(x,t), \tag{7}$$

where δ is the resource natural decaying rate and α is the consumption rate of resources per unit of root biomass.

We further assume that the environment provides resources at a constant rate ω

but only a fraction $f(R(x,t))$ of these resources become available for the plant. We thus write the input rate function $I(R(x,t))$ as:

$$I(R(x,t)) = \omega f(R(x,t)), \tag{8}$$

where $f(R(x,t))$ is given by the following rational function:

$$f(R(x,t)) = \frac{b + \phi\ R(x,t)}{1 + \phi\ R(x,t)}. \tag{9}$$

The constant b gives the fraction of ω that becomes available resource when there is no engineering ($\phi = 0$ or $R = 0$). The function f above has the basic desirable properties for our system. The input fraction increases with the root density as a result of engineering and saturates at $f = 1$ for large R, where the plant can access the full intake ω. Parameter ϕ determines how fast the input increases and therefore controls the engineering level.

We build the fitness-generating function for the plant as the difference between the gain from resource consumption and the costs of growing roots:

$$G(x,t) = [Q\alpha W(x,t) - C(x)]\, R(x,t), \tag{10}$$

where Q is the conversion factor and $C(x)$ accounts for the costs. We consider the cost function is a sum of three independent sources of fitness reduction. We have a spatially independent cost C_b which accounts for the cost of growing and maintaining fine roots responsible for absorbing nutrients. We also have the cost of growing and maintaining coarse roots, responsible for the transport of nutrients, which is dependent on spatial location. More specifically, the cost here increases with the distance from the insertion point and we hypothesize that it grows with the squared distance. Finally, engineering induces an extra cost that we assume to be proportional to the engineering parameter ϕ. Hence, taking $x = 0$ as the insertion point, we write:

$$C(x) = C_b + C_t x^2 + C_e \phi, \tag{11}$$

where C_t and C_e are parameters that control coarse roots and engineering costs, respectively.

Combining equations (7)-(11) we can write the resource growth and fitness-generating function equations as:

$$\frac{\partial W(x,t)}{\partial t} = \omega \left(\frac{b + \phi\ R(x,t)}{1 + \phi\ R(x,t)} \right) - \delta W(x,t) - \alpha W(x,t) R(x,t) \tag{12}$$

$$G(x,t) = [Q\alpha W(x,t) - (C_b + C_t x^2 + C_e \phi)] R(x,t). \tag{13}$$

If we further assume that resource dynamics occurs on a much faster time scale than evolution, than the resource can be assumed to be at the equilibrium during the evolution process. Finding the equilibrium resource density from Equation (12) and substituting it into (13) we have:

$$G(x) = \left[\bar{\omega} \frac{\left(\frac{b+\phi\ R(x)}{1+\phi\ R(x)} \right)}{\bar{\delta} + R(x)} - (C_b + C_t x^2 + C_e \phi) \right] R(x). \tag{14}$$

where we have also used the rescaling $\bar{\omega} = Q\omega$ and $\bar{\delta} = \delta/\alpha$.

The evolutionarily stable strategies (ESS) are found by maximizing the fitness generating function with respect to the strategies. The total biomass at the ESS as a function of b and ϕ is shown in Figure (2). The black region indicates that the biomass is zero. We notice that for low or no engineering roots can only grow if b is larger than a given threshold. For intermediate values of ϕ roots grow for any value of b because engineering provides enough resources for the plant. We also observe that roots can not grow for very large ϕ. This occurs because the cost of engineering becomes too high.

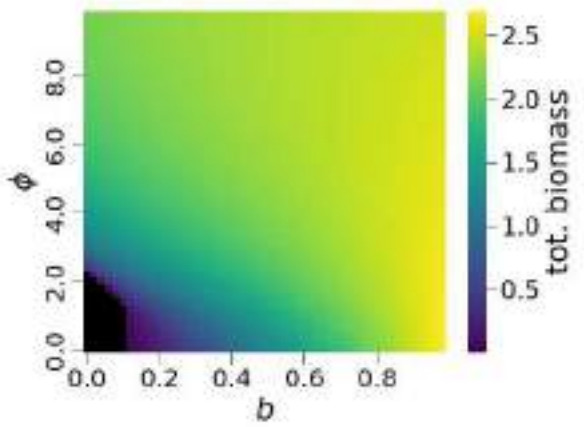

Figure 2: Total biomass at the ESS of a single plant species as a function of the basal income b and the engineering parameter ϕ. In panel (B) we zoom in the lower part of panel (A).

3 Two plants model

We also studied the evolutionary dynamics of two plant species that feed on a shared resource. One plant is an ecosystem engineer and the other is an opportunistic plant. The insertion points of the two plants are assumed to be at a distance d apart. We extend the single species modelling equations to include the opportunist. Denoting the root densities of engineer and opportunist by $R_1(x)$ and $R_2(x)$, respectively, the two plants model equations are written as:

$$\frac{\partial W(x,t)}{\partial t} = \omega\left(\frac{b+\phi\ R_1(x,t)}{1+\phi\ R_1(x,t)}\right) - \delta W(x,t) - \alpha_1 W(x,t)R_1(x,t) - \alpha_2 W(x,t)R_2(x,t) \tag{15}$$

$$G_1(x,t) = [Q_1\alpha_1 W(x,t) - (C_{b1} + C_{t1}x^2 + C_e\phi)]R_1(x,t) \tag{16}$$

$$G_2(x,t) = [Q_2\alpha_2 W(x,t) - (C_{b2} + C_{t2}(x-d)^2)]R_2(x,t), \tag{17}$$

where $G_i(x,t)$ is the fitness-generating function of species $i = \{1,2\}$. Parameters have the same interpretation as in equations (12)-(13) and some have become species specific. Note that as species 2 is not an engineer there is no cost associated with engineering in its fitness equation.

Throughout the evolutionary history engineers and opportunists interact at different distances and in different numbers of plants. In our analysis we set $C_{t2} = 0$, so that the opportunist fully occupies the environment and it could be a representation of a mean effect of opportunists through evolutionary time.

At equilibrium resource density is given by:

$$W^*(x) = \frac{\omega\left(\frac{b+\phi\ R_1(x)}{1+\phi\ R_1(x)}\right)}{\delta + \alpha_1 R_1(x) + \alpha_2 R_2(x)} \tag{18}$$

and, using the rescaling $\bar{\omega} = \omega Q_1$, $q = Q_2/Q_1$, $\bar{\delta} = \delta/\alpha_1$, $a = \alpha_2/\alpha_1$, we have:

$$G_1^*(x) = \left[\bar{\omega}\frac{\left(\frac{b+\phi\ R_1(x)}{1+\phi\ R_1(x)}\right)}{\bar{\delta} + R_1(x) + aR_2(x)} - (C_{b1} + C_{t1}x^2 + C_e\phi)\right] R_1(x,t). \tag{19}$$

$$G_2^*(x) = \left[\bar{\omega}qa\frac{\left(\frac{b+\phi\ R_1(x)}{1+\phi\ R_1(x)}\right)}{\bar{\delta} + R_1(x) + aR_2(x)} - C_{b2}\right] R_2(x,t), \tag{20}$$

Figure 3 summarizes the main findings of the two species model. Dashed blue and orange lines give, respectively, the total fitness of the engineer and opportunist at the ESS when solo. We observe that only the engineer survives at low b. The

solid lines give the total fitness at the ESS when the two species interact. Then the opportunist persists at low b because it its facilitated by the engineer.

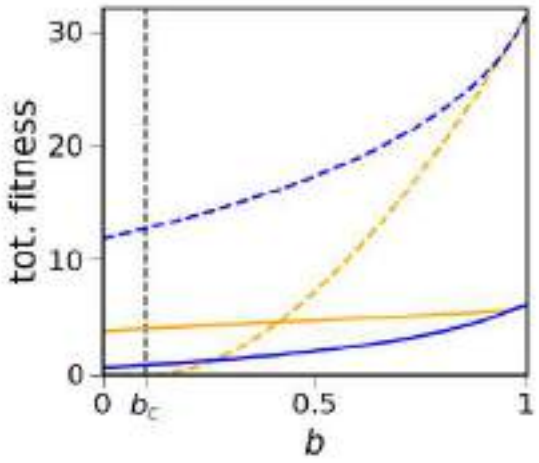

Figure 3: Total fitness at the ESS for single plants (dashed lines) and interacting species (solid lines).

4 Participation in scientific events

The fellow did not attend scientific events in this reporting period.

5 Publications

We published the work entitled "Enhanced species coexistence in Lotka-Volterra competition models due to nonlocal interactions" on the Journal of Theoretical Biology (Maciel and Martinez-Garcia, 2021).

References

Amarasekare, P. (2003). Competitive coexistence in spatially structured environments: a synthesis. *Ecology Letters*, 6:1109–1122.

Bayliss, A. and Volpert, V. A. (2015). Patterns for competing populations with species specific nonlocal coupling. *Mathematical Modelling of Natural Phenomena*, 10(6):30–47.

Britton, N. F. (1989). Aggregation and the competitive exclusion principle. *Journal of Theoretical Biology*, 136:57–66.

Cabal, C., Martínez-García, R., de Castro Aguilar, A., Valladares, F., and Pacala, S. W. (2020). The exploitative segregation of plant roots. *Science*, 370(6521):1197–1199.

Cantrell, R. S., Cosner, C., and Lou, Y. (2007). Advection-mediated coexistence of competing species. *Proceedings of the Royal Society of Edinburgh Section A: Mathematics*, 137(3):497–518.

Chesson, P. (2000). Mechanisms of maintenance of species diversity. *Annual Review of Ecology and Systematics*, 31:343–366.

Dohn, J., adn Moussa Karembé, F. D., Moustakas, A., Amévor, K. A., and Hanan, N. P. (2013). Tree effects on grass growth in savannas: competition, facilitation and the stress-gradient hypothesis. *Journal of Ecology*, 101:202–209.

Hastings, A., , Byers, J. E., Crooks, J. A., Cuddington, K., Jones, C. G., Lambrinos, J. G., Talley, T. S., and Wilson, W. G. (2007). Ecosystem engineering in space and time. *Ecology Letters*, 10:153–164.

Hauggaard-Nielsen, H. and Jensen, E. S. (2005). Facilitative root interactions in intercrops. *Plant and Soil*, 274:237–250.

Ludwig, F., Dawson, T. E., Prins, H. H. T., Berendse, F., and de Kroon, H. (2004). Below-ground competition between trees and grasses may overwhelm the facilitative effects of hydraulic lift. *Ecology Letters*, 7:623–631.

Maciel, G. A. and Martinez-Garcia, R. (2021). Enhanced species coexistence in lotka-volterra competition models due to nonlocal interactions. *Journal of Theoretical Biology*, 530:110872.

Meron, E. (2018). From patterns to function in living systems: Dryland ecosystems as a case study. *Annual Review of Condensed Matter Physics*, 9:79–103.

Rietkerk, M. and van de Koppel, J. (2008). Regular pattern formation in real ecosystems. *Trends in Ecology and Evolution*, 23(3):169–175.

Segal, B. L., Volpert, V. A., and Bayliss, A. (2013). Pattern formation in a model of competing populations with nonlocal interactions. *Physica D*, 253:12–22.

Silvertown, J. (2004). Plant coexistence and the niche. *Trends in Ecology and Evolution*, 19(11):605–611.

RELATORIO CIENTÍFICO

Título do projeto Um estudo das perturbações não lineares em modelos cosmológicos alternativos

Número do Processo FAPESP 2021/10290-2

Período de vigência 01/01/2022 a 30/11/2022

Período coberto pelo Relatório Científico em questão 01/01/2022 a 30/11/2022

Bolsista: Wilmar Alberto Cardona Castro

Supervisor: Nathan Jacob Berkovits

Resumo

Neste projeto estudamos um conjunto de teorias que compreendem vários modelos cosmológicos alternativos [e.g., f (R), KGB, Scalar-Vector-Tensor (SVT)]. As pesquisas teóricas que têm sido desenvolvidas fizeram énfasis nas perturbações lineares. Embora existam trabalhos que estudaram perturbações não lineares, esses se focalizaram no modelo padrão da cosmologia. Aqui nós queremos desenvolver ferramentas para a pesquisa de modelos cosmológicos alternativos além da ordem linear.

Nas últimas décadas os pesquisadores fizeram grandes avanços no estudo das perturbações não lineares teoricamente e numericamente. As simulações a grande escala do universo agora são uma ferramenta de grande utilidade para os pesquisadores. Embora as simulações N-body são muito importantes para entender a formação de estruturas não lineares, poucos códigos incluem efeitos relativistas. Além disso, esses códigos se enfocam no modelo padrão.

A presente proposta de pesquisa terá em consideração as seguintes linhas de orientação: modelado cuidadoso, análises estatísticas versáteis, e modelos fisicamente sólidos. Nosso alvo é pesquisar aquilo que poderia estar causando a expansão acelerada do universo. Estudaremos modelos cosmológicos que são plausíveis, mas receberam pouca atenção nos últimos anos. A proposta se enfoca em desenvolver ferramentas para o cômputo de propriedades estatísticas dos observáveis em este tipo de modelos até segunda ordem nas perturbações, incluindo efeitos relevantes em análises de experimentos futuros. O meu plano e a implementação dos modelos cosmológicos em solucionadores Boltzmann. Finalmente faremos análises estatísticos Bayesianos (p.ex., likelihood-base e likelihood-free) com os dados disponíveis e também predições do funcionamento de experimentos futuros. Meus objetivos são:

1. Estudar escenarios cosmológicos alternativos onde a matéria escura interage com a energia escura principalmente em escalas pequenas, teorias Hordeski, e teorias SVT. O objetivo principal é determinar se esses modelos podem explicar a expansão acelerada do universo levando em conta os dados disponíveis e os experimentos futuros;

2. Profundizar meu conhecimento sobre as ondas gravitacionais, análise de dados, estatística, desenvolvimento de software, teoria de perturbações cosmológicas da segunda ordem, modelos cosmológicos alternativos, solucionadores Boltzmann, simulações N-body, e observáveis em cosmologia. Além disso espero melhorar minhas capacidades de liderar projetos e orientar estudantes (p. ex., estudantes de doutorado)

Realizacoes no período

SVT theories involve scalar and vector fields which may be coupled to gravity. Although they may have an interesting phenomenology (e.g., they are more general than Horndeski theories), SVT theories have been poorly studied over the past years. I led a research project published in JCAP (see "*An effective fluid description of scalar-vector-tensor theories under the sub-horizon and quasi-static approximations*" below) where linear perturbations for SVT theories were carefully investigated. We worked out background evolution equations as well as equations governing the linear order perturbations. For the latter we took advantage of both quasi-static and sub-horizon approximations. We managed to find a fluid description of general SVT theories compatible with current constraints of gravitational waves. Analytical expressions for the equation of state, sound speed, and anisotropic stress were derived. We showed our results can be used to find cosmological models satisfying certain conditions. For instance, we were able to find a SVT model matching the behaviour of LCDM at the background level while having non-vanishing dark energy perturbations. Finally, we implemented our design SVT model in a Boltzmann solver (made publicly available), solved the perturbation equations, and computed observables such as the CMB angular power spectrum. In summary, our project allows testing SVT theories against data.

Dark Matter and Dark Energy, the two most abundant ingredients in the LCDM model, are collectively known as the dark sector. In the standard cosmological model they only interact gravitationally. There is however the possibility that the dark sector exchanges energy or/and momentum. Thus the detection of a momentum transfer in the dark sector may challenge the LCDM model while also clarifying current tensions in cosmological parameters such as the strength of matter clustering. I led a research project published in JCAP (see "*Momentum transfer in the dark sector and lensing convergence in upcoming galaxy surveys*" below) where we investigated a well-motivated Dark Energy model also taking into account momentum transfer in the dark sector. We computed cosmological constraints using available data sets and carried out forecasts for EUCLID, an upcoming galaxy survey. We found current data favour a vanishing momentum transfer in the dark sector. Our investigation showed lensing convergence, a relevant relativistic effect, must be included in analyses of galaxy surveys going deep in redshift and covering large regions in the sky. Otherwise, several cosmological parameters would be misestimated being heavily biased. Moreover, neglecting lensing convergence in future analyses of galaxy surveys (as currently done) might exacerbate current discrepancies in the Hubble constant and the strength of matter clustering.

Discrepancies in cosmological parameters are challenging the success of the standard cosmological model. I led a research project submitted to JCAP (see "*Holographic energy density, dark energy sound speed, and tensions in cosmological parameters: H_0 and S_8*" below) where we investigated a dark energy model with an evolving equation of state, vanishing dark energy anisotropic stress, and constant dark energy sound speed. We focused on a class of dark energy models whose energy density comes from the Holographic Principle applied to the whole Universe. We carefully studied the phenomenology of both background and linear order perturbations. Furthermore, we implemented the model in a Boltzmann solver and computed observables using the PPF formalism for the first time in the literature. Our code allowed us to compute cosmological constraints. We found values for the Hubble constant and the strength of matter clustering in good agreement with low redshift probes when using all data sets considered in our work. However, our result for the baryon density is in 3σ with the BBN constraint.

Machine learning based techniques are positively impacting many areas and cosmology is not an exception. My Phd student Bayron Orjuela, our collaborator Savvas Nesseris, and I performed a research project submitted to PRD (see "*Using machine learning to compress the matter transfer function T(k)*" below). Our work used Genetic Algorithms to carry out symbolic regression. In particular, we were able to find a simple, accurate analytical expression for the matter transfer function which outperforms the popular Eisenstein-Hu formula.

I also carried out other activities during this year. Firstly, I am acting as co-supervisor for Bayron Orjuela (Phd student) and Jose Palacios (MSc student). Bayron Orjuela and I co-authored two research papers (one already published in JCAP and another under review in PRD). He presented our published work in two international conferences (i.e., COSMO'22 in Rio de Janeiro and Texas Symposium on Relativistic Astrophysics in Prague) and a couple of seminars in Madrid (i.e., Institute for Theoretical Physics IFT-UAM/CSIC and Universidad Complutense de Madrid). Jose Palacios is working on a model considering dark energy is sourced by a vector field coupled with dark matter. We implemented the model in a Boltzmann solver (available in my GitHub account) and we plan to study the phenomenology of the model at the level of linear order perturbations. Secondly, I prepared and sent grant applications (e.g., Marie Curie, La Caixa, USAL for Excellence) to carry out my future research. Thirdly, I had an active participation in the journal clubs organised by the cosmology group at ICTP-SAIFR.

Gestao de dados

Preprint versions of all the publications are publicly available on the repository Arxiv

https://arxiv.org/search/?searchtype=author&query=Cardona%2C+W

Software developed during the project is publicly available in my GitHub and Docker repositories

https://github.com/wilmarcardonac

https://hub.docker.com/u/wilmarcardonac

Lista de publicações

1. **Wilmar Cardona**, J. Bayron Orjuela-Quintana, and Cesar A. Valenzuela-Toledo, "*An effective fluid description of scalar-vector-tensor theories under the sub-horizon and quasi-static approximations*", JCAP 08 (2022) 08, 059 [arXiv:2206.02895]
2. **Wilmar Cardona** and David Figueruelo, "*Momentum transfer in the dark sector and lensing convergence in upcoming galaxy surveys*", JCAP 12 (2022) 010 [arXiv:2209.12583]

Lista de trabalhos submetidos

1. **Wilmar Cardona** and M. A. Sabogal, "*Holographic energy density, dark energy sound speed, and tensions in cosmological parameters: H_0 and S_8* " under review in Journal of Cosmology and Astroparticle Physics [arXiv:2210.13335]
2. J. Bayron Orjuela-Quintana, Savvas Nesseris, and **Wilmar Cardona**, "*Using machine learning to compress the matter transfer function T(k)*" under review in Physical Review D [arXiv:2211.06393]

Visita Universidade de Pisa (Itália)

I spent a few weeks (from September the 12th to October the 31st, 2022) at University of Pisa visiting Prof. Giovanni Marozzi. We discussed the results in my recent paper concerning SVT theories ("*An effective fluid description of scalar-vector-tensor theories under the sub-horizon and quasi-static approximations*") and its possible extension to non-linear scales. In particular, we discussed details of the Light Cone Gauge approach where Prof. Marozzi is a worldwide expert. During my visit I also gave an informal talk (October the 14th, 2022) to Prof. Marozzi and his students about my paper "*Holographic energy density, dark energy sound speed, and tensions in cosmological parameters:* H_0 *and* S_8 " and received interesting suggestions, comments, criticisms.

Journal of Cosmology and Astroparticle Physics
An IOP and SISSA journal

An effective fluid description of scalar-vector-tensor theories under the sub-horizon and quasi-static approximations

Wilmar Cardona,[a] **J. Bayron Orjuela-Quintana**[b] **and César A. Valenzuela-Toledo**[b]

[a]ICTP South American Institute for Fundamental Research & Instituto de Física Teórica, Universidade Estadual Paulista, 01140-070, São Paulo, Brazil
[b]Departamento de Física, Universidad del Valle, Ciudad Universitaria Meléndez, 760032, Cali, Colombia

E-mail: wilmar.cardona@unesp.br, john.orjuela@correounivalle.edu.co, cesar.valenzuela@correounivalle.edu.co

Received June 10, 2022
Accepted July 29, 2022
Published August 26, 2022

Abstract. We consider scalar-vector-tensor (SVT) theories with second-order equations of motion and tensor propagation speed equivalent to the speed of light. Under the sub-horizon and the quasi-static approximations we find analytical formulae for an effective dark energy fluid, i.e., sound speed, anisotropic stress as well as energy density and pressure. We took advantage of our general, analytical fluid description and showed that it is possible to design SVT cosmological models which are degenerate with ΛCDM at the background level while having gravity strength $G_{\rm eff} < G_{\rm N}$ at late-times as well as non-vanishing dark energy perturbations. We implemented SVT designer models in the widely used Boltzmann solver `CLASS` thus making it possible to test SVT models against astrophysical observations. Our effective fluid approach to SVT models reveals non trivial behaviour in the sound speed and the anisotropic stress well worth an investigation in light of current discrepancies in cosmological parameters such as H_0 and σ_8.

Keywords: Cosmological perturbation theory in GR and beyond, dark energy theory, Gauss-Bonnet-Lovelock-Horndeski-Palatini etc gravity theories, modified gravity

ArXiv ePrint: 2206.02895

https://doi.org/10.1088/1475-7516/2022/08/059

JCAP08(2022)059

Contents

JCAP08(2022)059

Journal of Cosmology and Astroparticle Physics
An IOP and SISSA journal

Momentum transfer in the dark sector and lensing convergence in upcoming galaxy surveys

Wilmar Cardona[a] **and David Figueruelo**[b]

[a]ICTP South American Institute for Fundamental Research
& Instituto de Física Teórica, Universidade Estadual Paulista,
01140-070, São Paulo, Brazil
[b]Departamento de Física Fundamental and IUFFyM, Universidad de Salamanca,
E-37008 Salamanca, Spain

E-mail: wilmar.cardona@unesp.br, davidfiguer@usal.es

Received October 5, 2022
Accepted November 25, 2022
Published December 7, 2022

Abstract. We investigated a cosmological model that allows a momentum transfer between dark matter and dark energy. The interaction in the dark sector mainly affects the behaviour of perturbations on small scales while the background evolution matches the wCDM solution. As a result of the momentum transfer, these kinds of models help alleviating the σ_8 discrepancy in the standard model, but do not resolve the so-called H_0 tension. We confirm that this is indeed the case by computing cosmological constraints. While our analysis tends to favour σ_8 values lower than in ΛCDM, we do not find evidence for a non-vanishing momentum transfer in the dark sector. Since upcoming galaxy surveys will deliver information on scales and red-shift relevant for testing models allowing momentum transfer in the dark sector, we also carried out forecasts using different survey configurations. We assessed the relevance of neglecting lensing convergence κ when modelling the angular power spectrum of number counts fluctuations $C_\ell^{\rm ij}(z,z')$. We found that not including κ in analyses leads to biased constraints ($\approx 1-5\,\sigma$) of cosmological parameters even when including information from other experiments. Incorrectly modelling $C_\ell^{\rm ij}(z,z')$ might lead to spurious detection of neutrino masses and exacerbate discrepancies in H_0 and σ_8.

Keywords: cosmological parameters from LSS, dark energy theory, dark matter theory

ArXiv ePrint: 2209.12583

 https://doi.org/10.1088/1475-7516/2022/12/010

JCAP12(2022)010

Contents

1 Introduction

Finding the reason why the expansion of the Universe is speeding up remains one the biggest challenges in cosmology. Although there is compelling observational evidence from different probes such as supernovae type Ia [1–4], Baryon Acoustic Oscillations (BAO) [5], large-scale structure [6, 7], weak lensing [8], and Cosmic Microwave Background (CMB) radiation [9], our theoretical description of the phenomenon lacks in fundamental grounds. While the standard cosmological model Λ-Cold-Dark-Matter (ΛCDM) fits very well most astrophysical observations, we must bear in mind that ΛCDM is just a pretty good phenomenological description of observations with two big drawbacks. Firstly, effective Quantum Field Theory prediction for Λ hugely disagrees from observations, giving rise to the so-called Cosmological Constant Problem [10, 11]. Secondly, we are still pretty uncertain of the nature of Cold Dark Matter (CDM) since its detection remains elusive in laboratories [12–14], only having evidence for CDM through its gravitational effects.

The concordance model ΛCDM is successful at describing observations but lacks a fundamental theory supporting it. Therefore alternative models having a more sound theoretical ground have emerged in the literature. Matter fields in theories beyond the Standard Model of Particle Physics could fill the gap in the energy budget and provide a plausible explanation for the late-time accelerating expansion without a cosmological constant. This appealing approach is generally dubbed Dark Energy (DE) [15], but thus far no new fields have been detected neither in the laboratory nor in astrophysical measurements. Another popular

JCAP12(2022)010

Holographic energy density, dark energy sound speed, and tensions in cosmological parameters: H_0 and S_8

Wilmar Cardona,[a,1] **M. A. Sabogal,**[b]

[a]ICTP South American Institute for Fundamental Research & Instituto de Física Teórica, Universidade Estadual Paulista, 01140-070, São Paulo, Brazil

[b]Programa de Física, Universidad del Atlántico, Carrera 30 Número 8-49, Puerto Colombia-Atlántico, Colombia

E-mail: wilmar.cardona@unesp.br, msabogal@est.uniatlantico.edu.co

Abstract. Interesting discrepancies in cosmological parameters are challenging the success of the ΛCDM model. Direct measurements of the Hubble constant H_0 using Cepheid variables and supernovae turn out to be higher than inferred from the Cosmic Microwave Background (CMB). Weak galaxy lensing surveys consistently report values of the strength of matter clustering σ_8 lower than values derived from the CMB in the context of ΛCDM. In this paper we address these discrepancies in cosmological parameters by considering Dark Energy (DE) as a fluid with evolving equation of state $w_{\rm de}(z)$, constant sound speed squared $\hat{c}_{\rm s}^2$, and vanishing anisotropic stress σ. Our $w_{\rm de}(z)$ is derived from the Holographic Principle and can consecutively exhibit radiation-like, matter-like, and DE-like behaviour, thus affecting the sound horizon and the comoving angular diameter distance, hence H_0. Here we show DE sound speed plays a part in the matter clustering behaviour through its effect on the evolution of the gravitational potential. We compute cosmological constraints using several data set combinations including primary CMB, CMB lensing, redshift-space-distortions, local distance-ladder, supernovae, and baryon acoustic oscillations. In our analysis we marginalise over $\hat{c}_{\rm s}^2$ and find $\hat{c}_{\rm s}^2 = 1$ is excluded at $\gtrsim 3\sigma$. For our baseline result including the whole data set we found H_0 and σ_8 in good agreement (within $\approx 2\sigma$) with low redshift probes. Our constraint for the baryon energy density $\omega_{\rm b}$ is however in $\approx 3\sigma$ tension with BBN constraints. We conclude evolving DE also having non-standard clustering properties [e.g., $\hat{c}_{\rm s}^2(z,k)$] might be relevant for the solution of current discrepancies in cosmological parameters.

[1]Corresponding author.

Contents

1 Introduction

While the concordance model provides a reasonable, good phenomenological description of most astrophysical measurements [1–4], it also becomes clear that our ignorance about the nature of Dark Matter as well as the so-called cosmological constant problem represent major drawbacks in the model. In addition, over the past years we have seen the emergence of pretty interesting discrepancies (e.g., the Hubble constant H_0, the strenght of matter clustering σ_8) in cosmological parameters whose understanding could reveal new physics disregarded in the standard cosmological model [5–25].

Although Bayesian analyses show that the standard cosmological model ΛCDM performs better than its simplest alternatives [26], there exists the possibility that more elaborate models could explain the shortcomings ΛCDM is facing. Dynamical Dark Energy and Modified Gravity (MG) have become the two leading approaches when trying to explain the late-time accelerating universe [27–30]. There is however no conclusive evidence for new Dark Energy (DE) fields or deviations from General Relativity [31–33].

Within the wide spectrum of proposals to address the DE problem, there is a hypothesis known as the Holographic Principle (HP). Roughly speaking, the HP asserts that everything inside a region of space can be described by bits of information confined to the boundary [34–39]. This non-extensive scaling would suggest that quantum field theory ceases to be valid in a large volume. Nevertheless, it is also true that the performance of local quantum field theory at describing particle phenomenology is quite remarkable. It turns out that a relationship between ultraviolet (UV) and infrared (IR) cut-offs of an effective quantum field theory could make these regimes compatible with each other [40]. If ρ is the quantum zero-point energy density associated to a UV cut-off, the total energy in a region of size L should not exceed the mass of a black hole of the same size, namely,

$$L^3\rho \leq LM_{\rm p}^2, \tag{1.1}$$

where $M_{\rm p}$ is the reduced Planck mass. The largest, allowed IR cut-off $L_{\rm IR}$ saturates the inequality (1.1) so that the maximum energy density in the effective theory is given by

$$\rho = 3\gamma^2 M_{\rm p}^2 L_{\rm IR}^{-2}, \tag{1.2}$$

where γ is an arbitrary parameter. The UV/IR relationship (1.2) is a consequence of recognising that quantum field theory overestimates states. Moreover, it offers a possible way of understanding the cosmological constant problem [41, 42], one of the main shortcomings of the standard cosmological model ΛCDM.

Interestingly, the UV/IR relation (1.2) has been widely applied in cosmology as an alternative to the cosmological constant causing the late-time accelerating expansion in the concordance model. These kinds of cosmological models are now known as Holographic Dark Energy (HDE) models (see [43] for a review). In this context, the IR cut-off $L_{\rm IR}$ has a cosmological origin and various choices are found in the literature [44–50]. Despite being appealing as an alternative to ΛCDM, the HDE models investigated here are not derived from a Lagrangian which is a disadvantage when studying the evolution of cosmological perturbations: since HDE models do not have a Lagrangian, we cannot derive equations of motion for linear order perturbations.[1] Nevertheless, fairly general theories relying on scalar and vector fields (e.g., scalar-vector-tensor theories [52]) could provide background phenomenology matching HDE models while allowing the investigation of cosmological perturbations. Here we will adopt a phenomenological approach and assume the existence of a DE fluid having an evolving equation of state $w_{\rm de}(a)$ derived from the UV/IR relation (1.2). As for the description of DE perturbations, we opt for a constant sound speed in the fluid rest-frame $\hat{c}_{\rm s}^2$ and vanishing anisotropic stress $\pi = 0$.

In this work we want to determine whether or not HDE is viable given current astrophysical measurements. Although cosmological constraints have been computed for HDE models (see, for instance, [53–67]), a few details have been overlooked. Firstly, while HDE models usually feature an evolving $w_{\rm de}(a)$ which might cross the phantom divide $w_{\rm de} = -1$, this behaviour is not properly addressed in the literature when also considering the evolution of perturbations. Here we will take it into consideration by using the Parameterized Post-Friedmann (PPF) formalism [68]. Secondly, when modelling DE perturbations, studies exist which a priori set $\hat{c}_{\rm s}^2$ to a constant value. However, this choice could bias cosmological constraints as it directly affects the clustering properties of DE. In our investigation we marginalise over $\hat{c}_{\rm s}^2$ and inquire about its phenomenological signatures in the context of HDE. Thirdly, with regard to cosmological constraints of HDE models, most studies focus on the background evolution and use only low red-shift data to constrain the parameter space fully disregarding the impact on earlier stages of the Universe. Here we fill this gap in the literature by also studying the impact of HDE on linear order perturbations.

The manuscript is organised as follows. In Section 2 we set our notation, discuss the particular HDE model and explain its background phenomenology as well as the behaviour of linear order perturbations. In Sections 3-4 we present and discuss results for cosmological constraints. Finally, in Section 5 we give our conclusions.

2 Theoretical framework and holographic dark energy model

The Einstein-Hilbert action reads

$$S = \int d^4x\sqrt{-g}\left(\frac{R}{2\kappa} + \mathcal{L}_{\rm m}\right), \tag{2.1}$$

where $\mathcal{L}_{\rm m}$ denotes the Lagrangian for any matter fields appearing in the theory, g is the determinant of the metric $g_{\mu\nu}$, R is the Ricci scalar and $\kappa \equiv 8\pi G$ is a constant with G being

[1] However, see Ref. [51] for a relation between HDE and massive gravity theory that could provide a framework for investigating perturbations.

the bare Newtons constant. By applying the Principle of Least Action we can derive the well known Einstein field equations

$$R_{\mu\nu} - \frac{1}{2}Rg_{\mu\nu} = \kappa T_{\mu\nu}, \tag{2.2}$$

where $R_{\mu\nu}$ is the Ricci tensor and $T_{\mu\nu}$ is the energy-momentum tensor of matter fields.[2] Since observations and simulations indicate that on large enough scales the Universe is statistically homogeneous and isotropic also having vanishing curvature [1, 69–71], here we will assume a flat, linearly perturbed Friedmann-Lemaître-Robertson-Walker metric (FLRW). In the conformal Newtonian gauge [72]

$$ds^2 = a(\tau)^2\left[-(1+2\psi(\vec{x},\tau))d\tau^2 + (1-2\phi(\vec{x},\tau))d\vec{x}^2\right], \tag{2.3}$$

where $a(\tau)$ is the scale factor, and ψ, ϕ denote the gravitational potentials. As usual we will consider the material content as described by a perfect fluid with energy-momentum tensor

$$T^{\mu}_{\nu} = P_{\rm fld}\delta^{\mu}_{\nu} + (\rho_{\rm fld} + P_{\rm fld})U^{\mu}, \tag{2.4}$$

where $\rho_{\rm fld}$, $P_{\rm fld}$, and U^{μ} respectively denote the energy density, pressure, and four-velocity vector of the fluid. At first order the four-velocity vector is given by $U^{\mu} = a(\tau)^{-1}(1-\psi,\vec{u})$, which satisfies $U^{\mu}U_{\mu} = -1$, with $\vec{u} = \dot{\vec{x}}$. Taking into account linear perturbations, the elements of the energy-momentum tensor are given by

$$T^0_0 = -(\bar{\rho}_{\rm fld} + \delta\rho_{\rm fld}), \tag{2.5}$$
$$T^0_i = (\bar{\rho}_{\rm fld} + \bar{P}_{\rm fld})u_i, \tag{2.6}$$
$$T^i_j = (\bar{P}_{\rm fld} + \delta P_{\rm fld})\delta^i_j + \Sigma^i_j, \tag{2.7}$$

where $\bar{\rho}_{\rm fld}$, $\bar{P}_{\rm fld}$ are background quantities and only depend on time. The perturbations $\delta\rho_{\rm fld}$, $\delta P_{\rm fld}$, Σ^i_j depend on $(\vec{x},\tau)$. The anisotropic stress tensor of the fluid is defined as $\Sigma^i_j \equiv T^i_j - \delta^i_j T^k_k/3$.

2.1 Background

From the time-time component of Eq. (2.2) and using the unperturbed (i.e., $\psi = \phi = 0$) FLRW metric (2.3), we obtain

$$H^2 = \frac{\kappa}{3}(\rho_{\rm r} + \rho_{\rm m} + \rho_{\rm de}), \tag{2.8}$$

where the Hubble parameter $H \equiv \dfrac{1}{a(t)}\dfrac{da}{dt}$, and $\rho_{\rm de}$, $\rho_{\rm r}$, $\rho_{\rm m}$ respectively denote DE, radiation, and matter energy densities. While radiation and matter will be taken into account as in the standard cosmological model ΛCDM, we will consider DE as a fluid with energy density given by (1.2). We choose the so-called GO cut-off [46]

$$L_{\rm IR}^{-2} \equiv \alpha H^2 + \beta\frac{dH}{dt} \tag{2.9}$$

[2] Unless stated otherwise, throughout this paper we adopt the following conventions: speed of light $c = 1$, τ is the conformal time, $\vec{x}$ denotes conformal comoving coordinates, and the metric signature is $(-+++)$. For a generic function f, $\dfrac{df}{d\tau} \equiv \dot{f}$ and $\dfrac{df}{da} \equiv f'$. Cosmic time t and conformal time τ are related via $d\tau = dt/a(\tau)$.

where α and β are dimensionless constants. Eqs. (1.2) and (2.9) allow us to define a HDE density

$$\rho_{\rm de} = \frac{3}{\kappa}\left(\alpha H^2 + \beta\frac{dH}{dt}\right), \tag{2.10}$$

where the constant γ was absorbed by α and β. Taking into account Eq. (2.10), we can rewrite the Friedmann equation (2.8) as[3]

$$H^2 = \Omega_{\rm r,0}H_0^2a^{-4} + \Omega_{\rm m,0}H_0^2a^{-3} + \left(\alpha H^2 + \beta\frac{a}{2}\frac{dH^2}{da}\right). \tag{2.11}$$

We define $E^2 \equiv \frac{H^2}{H_0^2}$ and find an analytical solution for the differential equation (2.11) given by

$$E^2(a) = \Omega_{\rm r,0}^{\rm eff}a^{-4} + \Omega_{\rm m,0}^{\rm eff}a^{-3} + \Omega_{\rm de,0}^{\rm eff}a^{\frac{-2(\alpha-1)}{\beta}}, \tag{2.12}$$

where

$$\Omega_{\rm r,0}^{\rm eff} \equiv \left(1 + \frac{(\alpha-2\beta)}{(1-\alpha+2\beta)}\right)\Omega_{\rm r,0}, \tag{2.13}$$

$$\Omega_{\rm m,0}^{\rm eff} \equiv \left(1 + \frac{(2\alpha-3\beta)}{(2-2\alpha+3\beta)}\right)\Omega_{\rm m,0}, \tag{2.14}$$

$$\Omega_{\rm de,0}^{\rm eff} \equiv \left(1 - \frac{2\Omega_{\rm m,0}}{(2-2\alpha+3\beta)} - \frac{\Omega_{\rm r,0}}{(1-\alpha+2\beta)}\right), \tag{2.15}$$

and the effective parameter densities satisfy $\Omega_{\rm m,0}^{\rm eff} + \Omega_{\rm r,0}^{\rm eff} + \Omega_{\rm de,0}^{\rm eff} = 1$. Note that the HDE parameter density reads

$$\Omega_{\rm de} = \left(\frac{\alpha-2\beta}{1-\alpha+2\beta}\right)\Omega_{\rm r,0}a^{-4} + \left(\frac{2\alpha-3\beta}{2-2\alpha+3\beta}\right)\Omega_{\rm m,0}a^{-3} + \Omega_{\rm de,0}^{\rm eff}a^{\frac{-2(\alpha-1)}{\beta}}. \tag{2.16}$$

Assuming a barotropic fluid with $P_{\rm de} = w_{\rm de}\rho_{\rm de}$, from the condition for energy conservation

$$\frac{d\rho_{\rm de}}{dt} + 3H\rho_{\rm de}\left(1 + w_{\rm de}\right) = 0 \tag{2.17}$$

and Eqs. (2.10) and (2.12), we can derive the equation of state for our DE fluid

$$w_{\rm de}(a) = \frac{\left(\frac{2\alpha-3\beta-2}{3\beta}\right)\Omega_{\rm de,0}^{\rm eff}a^{\frac{-2(\alpha-1)}{\beta}} + \left(\frac{2\beta-\alpha}{3\alpha-6\beta-3}\right)\Omega_{\rm r,0}a^{-4}}{\left(\frac{2\alpha-3\beta}{2-2\alpha+3\beta}\right)\Omega_{\rm m,0}a^{-3} + \left(\frac{\alpha-2\beta}{1-\alpha+2\beta}\right)\Omega_{\rm r,0}a^{-4} + \Omega_{\rm de,0}^{\rm eff}a^{\frac{-2(\alpha-1)}{\beta}}}. \tag{2.18}$$

Figure 1 shows the evolution of parameter densities as well as the HDE equation of state $w_{\rm de}(a)$ in Eq. (2.18). It becomes clear that when $\alpha > 2\beta$ the HDE equation of state evolves from radiation-like $[w_{\rm de}(a) \approx 1/3]$ to pressure-less matter-like $[w_{\rm de}(a) \approx 0]$ until reaching a DE-like $[w_{\rm de}(a) < -1/3]$ behaviour at late times. Consequently, a non-vanishing HDE (2.10) can effectively add both pressure-less matter and radiation to the cosmological model [see Eqs. (2.13)-(2.14)]. While for the case where $\alpha = 2\beta$ there is no radiation-like behaviour of HDE in the early universe, HDE contributes to the effective matter parameter density in the matter dominated epoch. Since in this work we focus on a possible explanation

[3] As it is usual, we define the density parameters $\Omega_{i,0} \equiv \frac{\kappa}{3H_0^2}\rho_{i,0}$ and use $\frac{d}{dt} = aH\frac{d}{da}$.

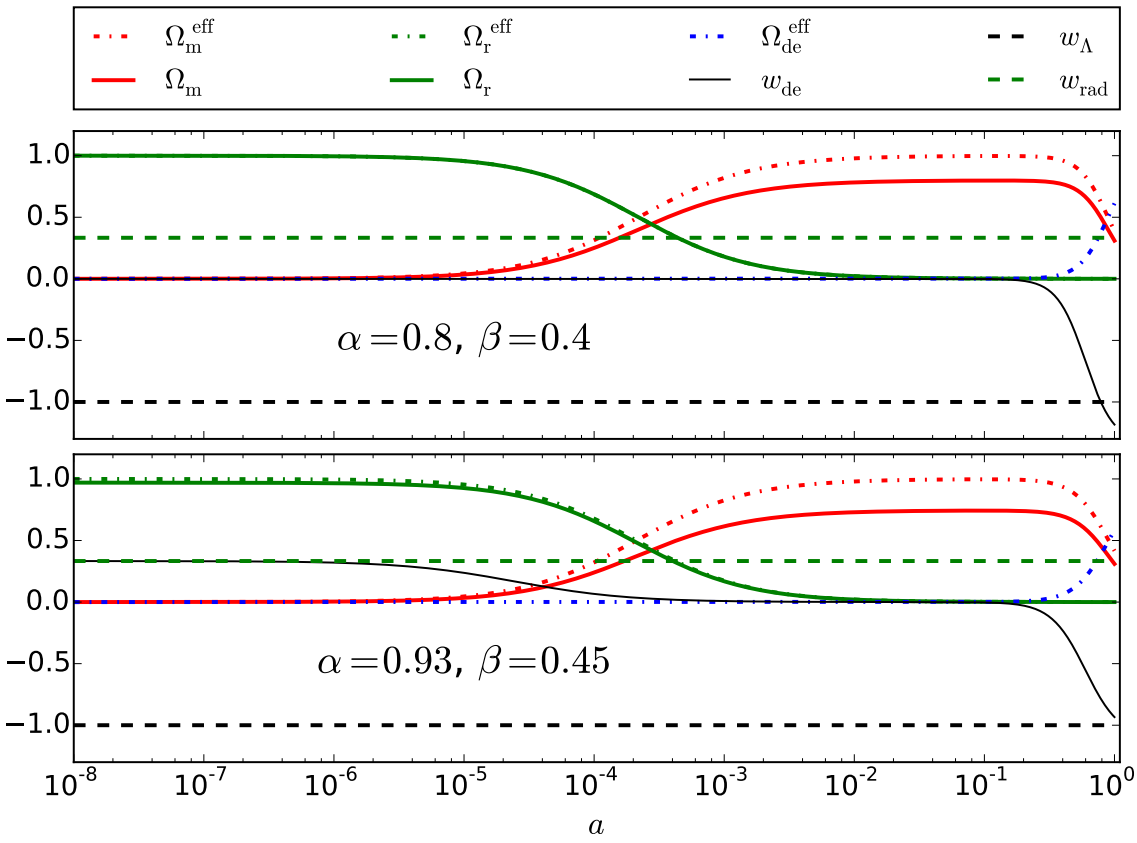

Figure 1. Evolution of parameter densities and HDE equation of state $w_{\rm de}$ for the HDE model. Note that $w_{\rm de}$ can cross the phantom divide. Here we use $\Omega_{m,0} = 0.31$ and $\Omega_{r,0} = 8.5 \times 10^{-5}$. While in the lower panel ($\alpha > 2\beta$) the HDE equation of state has a radiation-like behaviour at early times, in the upper panel ($\alpha = 2\beta$) $w_{\rm de}$ is matter-like when the universe is under radiation dominance.

for the late time accelerating expansion of the Universe and its relation with the formation of structures, we constrain the HDE model to satisfy $\Omega_{\rm r,0}^{\rm eff} = \Omega_{\rm r,0}$ later when computing cosmological constraints. From Eq. (2.13), the latter is fulfilled for $\alpha = 2\beta$. In this way we make sure that the early universe is described as in the ΛCDM model. Later in Section 4 we will expand on this constraint in relation with previous works.

With the constraint $\alpha = 2\beta$, the HDE density in Eq. (2.10) becomes the well known Ricci Dark Energy (RDE) which only has a single free parameter. Then, the normalised Hubble parameter (2.12) and the HDE equation of state (2.18) are simplified

$$E^2(a) = \Omega_{\rm r,0} a^{-4} + \left(1 + \frac{\alpha}{4-\alpha}\right) \Omega_{\rm m,0} a^{-3} + \left(1 - \frac{\Omega_{\rm m,0}}{1-\frac{\alpha}{4}} - \Omega_{\rm r,0}\right) a^{\frac{4-4\alpha}{\alpha}}, \tag{2.19}$$

$$w_{\rm de}(a) = \frac{\alpha - 4}{3\alpha \left(1 - \frac{\alpha \Omega_{\rm m,0}}{(\alpha-4)(1-\Omega_{\rm r,0})+4\Omega_{\rm m,0}} a^{\frac{\alpha-4}{\alpha}}\right)}. \tag{2.20}$$

From Eq. (2.19) we can easily extract the HDE density

$$\tilde{\rho}_{\rm de}(a) = \frac{\alpha}{(4-\alpha)}\Omega_{\rm m,0}a^{-3} + \left(1 - \frac{4}{(4-\alpha)}\Omega_{\rm m,0} - \Omega_{\rm r,0}\right) a^{\frac{4-4\alpha}{\alpha}}, \tag{2.21}$$

where $\tilde{\rho}_{\rm de} \equiv \frac{\rho_{\rm de}}{H_0^2}$. Moreover, from the conservation equation (2.17) we can derive an expression for the HDE pressure $\tilde{P}_{\rm de} \equiv \frac{P_{\rm de}}{H_0^2}$

$$\tilde{P}_{\rm de}(a) = -\frac{4-\alpha}{3\alpha}\left(1 - \frac{4}{(4-\alpha)}\Omega_{\rm m,0}\right) a^{\frac{4-4\alpha}{\alpha}}, \tag{2.22}$$

which in turn allows us to compute the adiabatic sound speed squared for the DE fluid

$$\begin{aligned} c_a^2 \equiv \frac{dP_{\rm de}}{d\rho_{\rm de}} &= w_{\rm de} - \frac{\dot{w_{\rm de}}}{3H(1+w_{\rm de})} = w_{\rm de} - \frac{w'_{\rm de}a}{3(1+w_{\rm de})} \\ &= \frac{4(\alpha-4)}{3\alpha\left(4 - \frac{3\alpha^2\Omega_{\rm m,0}}{(\alpha-1)((\alpha-4)(1-\Omega_{\rm r,0})+4\Omega_{\rm m,0})}a^{\frac{\alpha-4}{\alpha}}\right)}. \end{aligned} \tag{2.23}$$

We will use the previous expressions to derive simplified, approximate solutions for the DE perturbations during matter dominance in the next section.

2.2 First order perturbations

In this work we are interested in computing statistical properties of observables such as the CMB angular power spectra and the matter power spectrum as predicted by the HDE model. Here we limit ourselves to first order scalar perturbations and therefore we need to solve the differential equations governing the linearised Einstein field equations (2.2). Using the conformal Newtonian gauge (2.3) and taking into account a general fluid (2.5)-(2.7), we obtain

$$k^2\phi + 3\frac{\dot{a}}{a}\left(\dot{\phi} + \frac{\dot{a}}{a}\psi\right) = 4\pi G a^2 \delta T^0_0, \tag{2.24}$$

$$k^2\left(\dot{\phi} + \frac{\dot{a}}{a}\psi\right) = 4\pi G a^2(\bar{\rho}_{\rm fld} + \bar{P}_{\rm fld})\theta_{\rm fld}, \tag{2.25}$$

$$\ddot{\phi} + \frac{\dot{a}}{a}(\dot{\psi} + 2\dot{\phi}) + \left(2\frac{\ddot{a}}{a} - \frac{\dot{a}^2}{a^2}\right)\psi + \frac{k^2}{3}(\phi - \psi) = \frac{4\pi}{3}G a^2 \delta T^i_i, \tag{2.26}$$

$$k^2(\phi - \psi) = 12\pi G a^2(\bar{\rho}_{\rm fld} + \bar{P}_{\rm fld})\sigma_{\rm fld}, \tag{2.27}$$

where k is the wavenumber, the divergence of the velocity field is defined as $\theta_{\rm fld} \equiv ik^j u_j$, and $\sigma_{\rm fld}$ is the anisotropic stress. In the cases where the universe is regarded as composed by several fluids, the right-hand side in Eqs. (2.24)-(2.27) is intended to be a sum over all species (e.g., radiation, matter, dark energy). From the conservation of energy-momentum ($\nabla_\mu T^{\mu\nu} = 0$) for a single fluid we obtain

$$\dot{\delta}_{\rm fld} = -V_{\rm fld} + 3(1+w_{\rm fld})\dot{\phi} - 3\frac{\dot{a}}{a}\left(\frac{\delta P_{\rm fld}}{\bar{\rho}_{\rm fld}} - w_{\rm fld}\delta_{\rm fld}\right), \tag{2.28}$$

$$\dot{V}_{\rm fld} = -\frac{\dot{a}}{a}(1-3w_{\rm fld})V_{\rm fld} + \frac{\delta P_{\rm fld}}{\bar{\rho}_{\rm fld}}k^2 + k^2(1+w_{\rm fld})\phi, \tag{2.29}$$

where we have used the scalar velocity perturbation $V_{\rm fld} \equiv ik_j T_0^j/\bar{\rho} = (1+w_{\rm fld})\theta_{\rm fld}$ and disregarded anisotropic stress.

Since we are interested in the observational signatures of the HDE cosmological model at late-times, in the remainder of this section we will discuss the behaviour of matter and DE perturbations starting our analysis in the matter dominated epoch. We consider pressure-less matter with $w_{\rm m}=0$, $\delta P_{\rm m}=0$, $\sigma_{\rm m}=0$ and assume HDE as a fluid having DE equation of state (2.18), pressure perturbation $\delta P_{\rm de}$, and vanishing anisotropic stress $\sigma_{\rm de}=0$. The latter and Eq. (2.27) imply that at late-times the gravitational potentials $\phi=\psi$.

We parameterise the DE pressure perturbation as

$$\frac{\delta P_{\rm de}}{\bar{\rho}_{\rm de}} = \hat{c}_{\rm s}^2\delta + \frac{3aH\left(\hat{c}_{\rm s}^2 - c_a^2\right)}{k^2}V \tag{2.30}$$

where $\hat{c}_{\rm s}^2$ is the DE sound speed squared in the rest-frame, δ is the DE density perturbation, and V is the DE velocity perturbation. Using (2.30), we rewrite Eqs. (2.28)-(2.29) for the DE perturbations

$$\delta' = -\frac{V}{Ha^2}\left(1+\frac{9a^2H^2\left(\hat{c}_{\rm s}^2-w_{\rm de}\right)}{k^2}+\frac{3a^3H^2w'_{\rm de}}{k^2(1+w_{\rm de})}\right)-\frac{3}{a}\left(\hat{c}_{\rm s}^2-w_{\rm de}\right)\delta+3(1+w_{\rm de})\phi', \tag{2.31}$$

$$V' = -\left(1-3\hat{c}_{\rm s}^2-\frac{aw'_{\rm de}}{(1+w_{\rm de})}\right)\frac{V}{a}+\frac{k^2\hat{c}_{\rm s}^2}{Ha^2}\delta+(1+w_{\rm de})\frac{k^2}{Ha^2}\phi, \tag{2.32}$$

whereas for matter the perturbation equations (2.28)-(2.29) become

$$\delta'_{\rm m} = -\frac{V_{\rm m}}{Ha^2}+3\phi', \tag{2.33}$$

$$V'_{\rm m} = -\frac{V_{\rm m}}{a}+\frac{k^2}{Ha^2}\phi. \tag{2.34}$$

Note we can combine Eqs. (2.24)-(2.25) and obtain

$$k^2\phi = -4\pi Ga^2\sum_j \rho_j\left(\delta_j+\frac{3aH}{k^2}V_j\right). \tag{2.35}$$

2.2.1 Matter dominance

Here we will work out the solution for the system of differential equations (2.31)-(2.34) governing the evolution of matter and DE perturbations. We focus on late times starting from the epoch when matter becomes dominant so that we can safely neglect radiation in the model. Since we are interested in analytical, approximate solutions, to simplify our problem we assume that during Matter Dominance (MD) the Hubble parameter is

$$H^2 = H_0^2\Omega_{\rm m,0}^{\rm eff}a^{-3}. \tag{2.36}$$

For the standard cosmological model ΛCDM only matter contributes to the pressure perturbation in the right-hand side of Eq. (2.26), hence the solution for the gravitational potential ϕ takes on a constant value under MD. The situation is different for the HDE we investigate here because the DE fluid might have not negligible contributions to the pressure perturbation. The latter is parameterised by Eq. (2.30) and therefore we identify two situations

where ϕ is constant as in ΛCDM : i) $\alpha = 2\beta$ ($c_{\rm a}^2 = 0$) and $\hat{c}_{\rm s}^2 = 0$ so that $\delta P_{\rm de} = 0$; ii) the more general scenario where α, β are independent parameters ($c_{\rm a}^2 \approx 0$) and $\hat{c}_{\rm s}^2 = 0$ implying $\delta P_{\rm de} \approx 0$.

We could only find analytical solutions for the perturbations when the gravitational potential takes on a constant value ϕ_0. Therefore, using Eq. (2.36) in Eqs. (2.31)-(2.34), we find the solutions for both matter and DE perturbations in MD

$$\delta_{\rm m} = \delta_0 \left(a + 3\frac{H_0^2 \Omega_{\rm m,0}^{\rm eff}}{k^2} \right), \tag{2.37}$$

$$V_{\rm m} = -\delta_0 H_0 \sqrt{\Omega_{\rm m,0}^{\rm eff}}\, a^{1/2}, \tag{2.38}$$

$$\delta = \delta_{\rm m}, \tag{2.39}$$

$$V = V_{\rm m}, \tag{2.40}$$

where

$$\delta_0 \equiv -\frac{2k^2\phi_0}{3H_0^2\Omega_{\rm m,0}^{\rm eff}}. \tag{2.41}$$

Note that the potential ϕ in Eq. (2.35) also receives contributions from the DE fluid in MD: DE perturbations behave as matter perturbations [see Eqs. (2.39)-(2.40)] and the background DE density is not negligible [see Eq. (2.16)] under MD.

We numerically solved the system of differential equations (2.31)-(2.34) also taking into account the expression (2.35) for the gravitational potential. The latter is depicted in Figure 2 for the standard cosmological model ΛCDM along with solutions for HDE and RDE models. It becomes clear that while models having $\hat{c}_{\rm s}^2 = 1$ exhibit a varying gravitational potential during MD, models with a vanishing sound speed present a behaviour similar to ΛCDM, namely, a constant ϕ. Note that for the given set of cosmological parameters, HDE ($\hat{c}_{\rm s}^2 = 0$) enters later than RDE ($\hat{c}_{\rm s}^2 = 0$) the regime of MD; the small variation of ϕ in this case is due to a non-vanishing adiabatic sound speed affecting the DE pressure perturbation, hence the gravitational potential.

In Figure 3 we show the numerical solutions for the matter perturbations. We display solutions for the concordance model ΛCDM and for the RDE ($\hat{c}_{\rm s}^2 = 0$) model. In the case of ΛCDM we also show the well-known analytical solutions in the MD epoch. Differences in the solutions of density perturbations arise mainly before horizon crossing and when DE becomes dominant. This is indeed due to the modifications introduced by the RDE via $\Omega_{\rm m,0}^{\rm eff}$. With regard to the velocity perturbations, we can see that even though the dependence with the scale factor is the same in the two models, the RDE ($\hat{c}_{\rm s}^2 = 0$) solution fully disagrees with the standard model due to $\Omega_{\rm m,0}^{\rm eff}$.

In Figure 4 we compare the numerical solutions for DE perturbations against the analytical, approximate solutions (2.39)-(2.40) valid in the MD regime. We carry out the comparison for HDE ($\hat{c}_{\rm s}^2 = 0$) in the left panel and RDE ($\hat{c}_{\rm s}^2 = 0$) in the right panel. While analytical solutions describe pretty well the behaviour of δ and V in the RDE ($\hat{c}_{\rm s}^2 = 0$) model during MD, we find disagreement for the HDE ($\hat{c}_{\rm s}^2 = 0$) model. This is mainly due to the fact that in the latter full MD starts later than in RDE ($\hat{c}_{\rm s}^2 = 0$) for the given set of cosmological parameters.

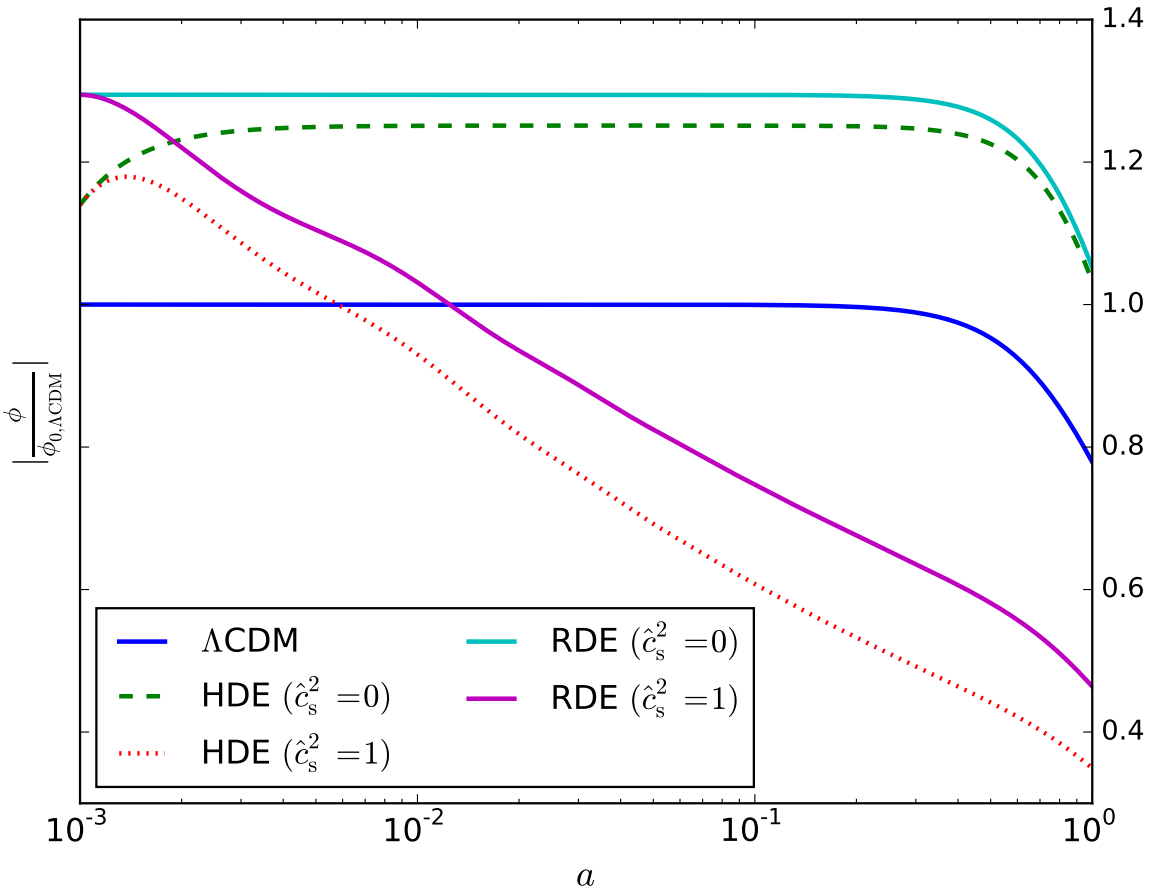

Figure 2. Evolution of the gravitational potential in ΛCDM, HDE, and RDE cosmological models. All the plots are normalised by the initial value in ΛCDM. Common cosmological parameters used to numerically solve the system of differential equations are: $\Omega_{\mathrm{r},0} = 0$, $\Omega_{\mathrm{m},0} = 0.3$, $H_0 = 70\,\mathrm{km\,s^{-1}\,Mpc^{-1}}$, $k = 25H_0$, $\delta_0 = 1$; for RDE $\alpha = 0.91$; for HDE $\alpha = 0.88$ and $\beta = 0.39$.

2.2.2 Implementation in Boltzmann solver

Thus far in our treatment of perturbations, we regarded DE perturbations as governed by fluid equations. We used a prescription for the pressure perturbation given by (2.30). However, this approach has problems (e.g., divergences, instabilities) when the DE equation of state crosses the phantom divide which turns out to be the case in the HDE model we investigate here (see Fig. 1). Not allowing cosmological models to cross $w_\mathrm{de} = -1$ could introduce unwanted bias in our modelling since the phantom divide is currently a crucial point [73]. By requiring strict energy and momentum conservation, the PPF formalism (also implemented in the Boltzmann solver `CLASS`) can deal with smooth DE crossing the phantom divide [68].

The PPF description of DE replaces the density and momentum components with a single joint dynamical variable

$$\Gamma \equiv -\frac{4\pi G a^2}{k^2 c_K}\delta\hat{\rho}_\mathrm{de}, \tag{2.42}$$

thus reducing closure conditions, but requiring strict conservation of energy and momentum in its equation of motion. Here $c_K = 1 - 3K/k^2$, where K is the space-time curvature that

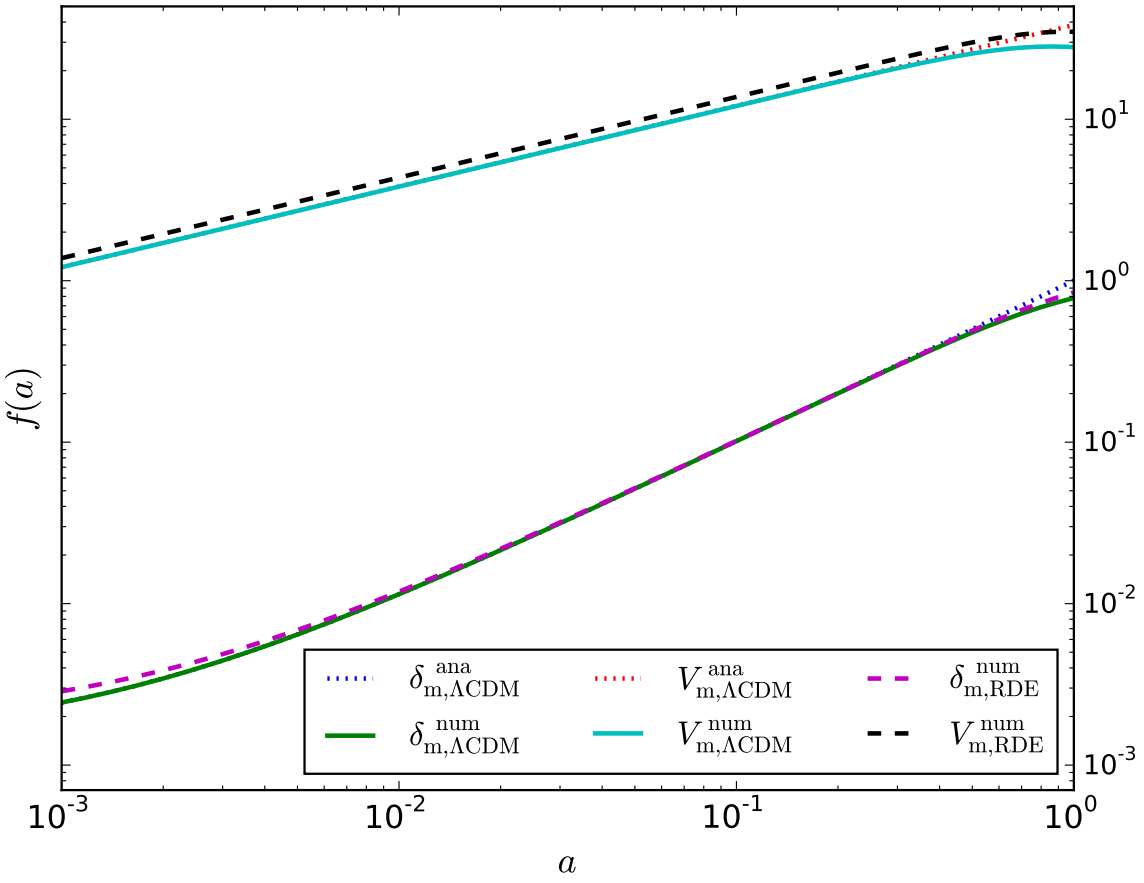

Figure 3. Evolution of density and velocity matter perturbations in the ΛCDM and RDE ($\hat{c}_{\rm s}^2 = 0$) model. We show the numerical solutions (solid and dashed curves) as well as the analytical solutions (dotted curves) in MD for the standard cosmological model. Cosmological parameters are as specified in Fig. 2.

we set to $K = 0$. The evolution equation for Γ is given by

$$\left(1 + c_\Gamma^2 k_H^2\right)\left[\frac{\dot{\Gamma}}{H} + \Gamma + c_\Gamma^2 k_H^2 \Gamma\right] = S, \tag{2.43}$$

where $c_\Gamma \equiv 0.4\,\hat{c}_{\rm s}$ calibrates the scale of the transition, $k_H = k^2/aH$ and

$$S = \frac{\dot{a}}{a}\frac{4\pi G}{H^2}\rho_{\rm de}\left(1 + w_{\rm de}\right)\frac{\theta_T}{k^2} \tag{2.44}$$

where the subscript T denotes all species except dark energy.

Figure 5 shows the output of our implementation in `CLASS` for a RDE model crossing the phantom divide. We use the best fit cosmological parameters in Ref. [55] and depict ΛCDM along with RDE model for different values of the DE sound speed $\hat{c}_{\rm s}^2$. The latter has a relevant effect in both CMB angular power spectrum and matter power spectrum (not shown in Ref. [55]).

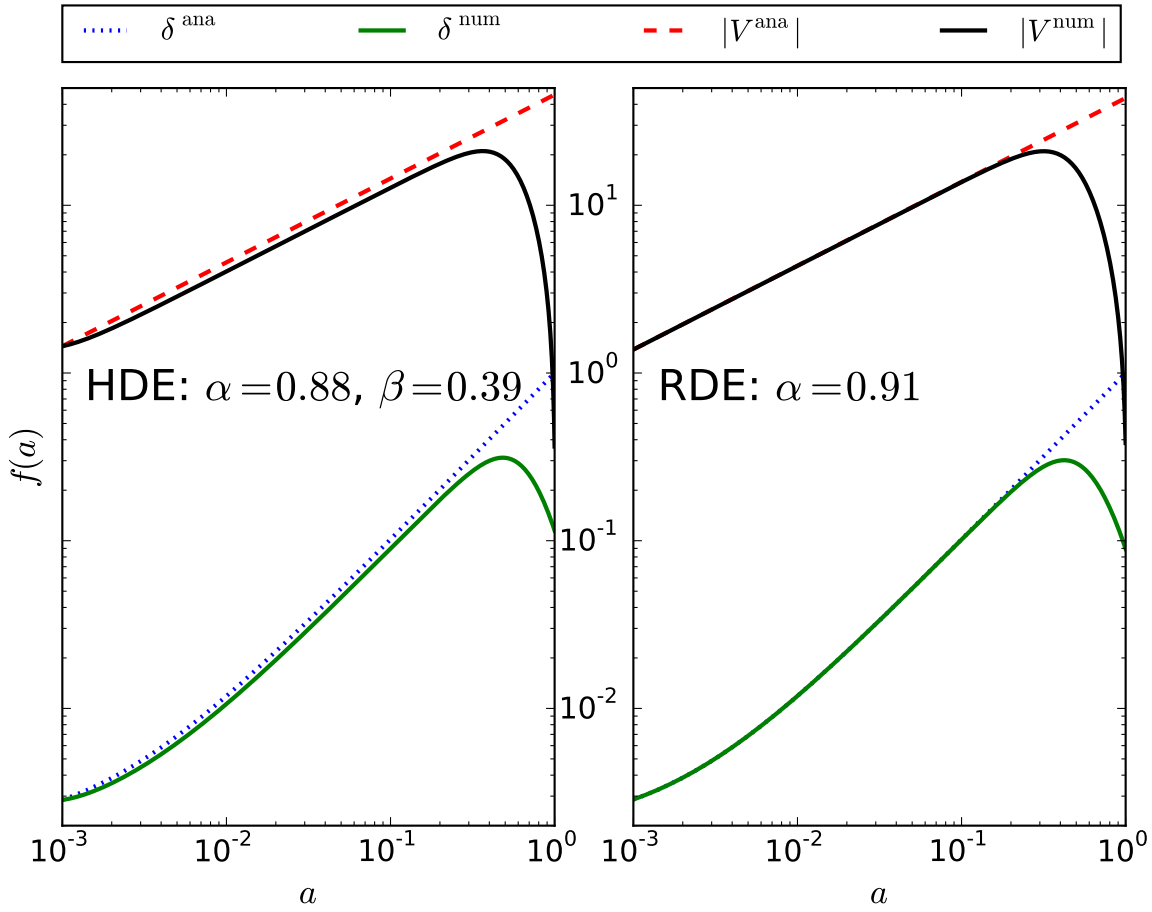

Figure 4. The evolution of DE perturbations in HDE (left panel) and RDE (right panel). We compare analytical (dashed and dotted curves) and numerical (solid curves) solutions for the system of differential equations (2.31)-(2.34). Cosmological parameters are as specified in Fig. 2.

3 Data and Methodology

In order to compute cosmological constraints for the cosmological model including DE as given by the DE energy density (2.10), we carried out the analysis in two parts. Firstly, we performed an analysis only taking into consideration background data. Secondly, we add data from the CMB anisotropies and Redshift-Space-Distortions (`RSD`) that constrain the model further.

Data constraining the background evolution of the model include: Baryon Acoustic Oscillations (`BAO`) from Refs. [74–76], Pantheon supernovae (`SNe`) data set from Ref. [77], and the SH0ES local measurement of the Hubble constant (`H0`) from Ref. [8] that we introduce as a Gaussian prior. As for data constraining linear order perturbations we take in information from CMB lensing (`lensing`) as well as temperature and polarisation anisotropies of the CMB (`TTTEEE`) measured by the Planck Collaboration [1], and a compilation of `RSD` as explained in Ref. [78].

As discussed previously, we implemented the HDE cosmological model by considering a DE fluid with DE equation of state (2.18), constant sound speed $\hat{c}_{\rm s}^2$, and vanishing anisotropic

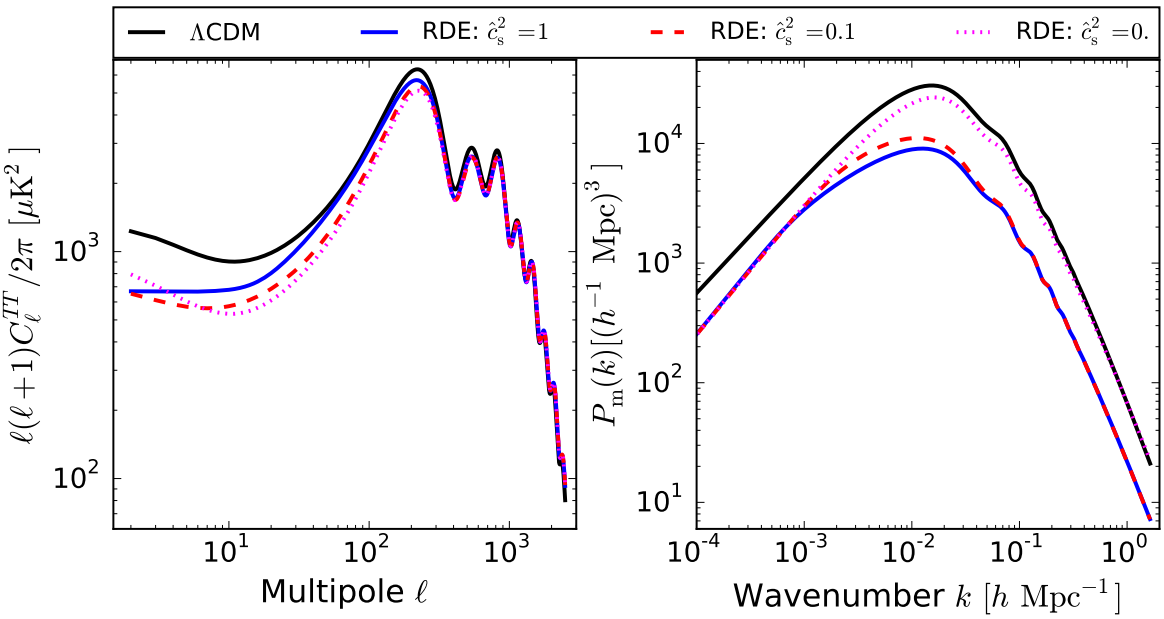

Figure 5. CMB temperature angular power spectrum C_l^{TT} and matter power spectrum $P(k, z = 0)$ for different values of $\hat{c}_s^2$. We fix other cosmological parameters to the best fit values reported in Table 1 [WMAP+BAO+SNIa] of Ref. [55], namely: for RDE $\omega_b = 0.0241$, $\omega_{cdm} = 0.1086$, $H_0 = 72.26\,\mathrm{km\,s^{-1}\,Mpc^{-1}}$, $n_s = 1.0871$, $\ln 10^{10} A_s = 3.122$, $\tau = 0.1382$ and $\alpha = 0.6904$ (note that authors in Ref. [55] actually report $\beta = 0.3452$); for ΛCDM $\omega_b = 0.0226$, $\omega_{cdm} = 0.1123$, $H_0 = 70.38\,\mathrm{km\,s^{-1}\,Mpc^{-1}}$, $n_s = 0.9691$, $\ln 10^{10} A_s = 3.180$, $\tau = 0.0877$.

stress. We carried out the implementation in the widely used Boltzmann solver `CLASS`. For a given set of cosmological parameters, the code computes all the relevant quantities (e.g., luminosity distances, CMB angular power spectrum) so that theoretical predictions can be compared with astrophysical measurements. We performed a Markov Chain Monte Carlo (MCMC) statistical analysis by sampling the parameter space with the code `Monte Python` [79, 80]. The latter is linked to `CLASS` and samples the parameter space with the default Metropolis-Hastings algorithm. In a first stage, a covariance matrix is adjusted so that the acceptance rate is ≈ 0.25. Then, in a second stage of the analysis, the covariance matrix is fixed and the code performs $\sim 10^6$ iterations until reaching convergence which we estimate with the Gelman-Rubin statistic R satisfying the condition $R - 1 \lesssim 0.01$ for all the varying parameters. We marginalise over the following cosmological parameters: baryon density today $\omega_b \equiv \Omega_b h^2$; cold dark matter density today $\omega_{cdm} \equiv \Omega_{cdm} h^2$; $100\times$ angular size of sound horizon at redshift $z_\star$ (redshift for which the optical depth equals unity) $100\theta_\star$; Log power of the primordial curvature perturbations $\ln 10^{10} A_s$; scalar spectrum power-law index n_s; Thomson scattering optical depth due to reionisation τ; sound speed squared on the rest-frame of the fluid $\log \hat{c}_s^2$; parameters determining the holographic DE density α and β. In our MCMC analyses we also marginalise over a few nuisance parameters whose number depends on the specific probe combination. For common cosmological parameters we use the same prior range as specified in Table 1 of Ref. [81].

When performing the first part of our statistical analysis (only background data), we vary the parameters ω_b, ω_{cdm}, α, and β (and H_0 when introduced as a Gaussian prior); the HDE parameters α and β were introduced with an unbounded flat prior. In the second part

of our analysis (taking into consideration background data as well as CMB anisotropies and Redshift-Space-Distortions), we set $\beta = \alpha/2$ as argued earlier in Section 2. Therefore, we vary the parameters $\omega_{\rm b}$, $\omega_{\rm cdm}$, $100\theta_\star$, $\ln 10^{10} A_{\rm s}$, $n_{\rm s}$, τ, $\log \hat{c}_{\rm s}^2$, and α. In this case for the parameters describing the DE fluid we use the prior range specified in Table 1.

While the analysis carried out in Ref. [55] seems to have fixed the DE sound speed $\hat{c}_{\rm s}^2 = 1$, here we marginalise over $\hat{c}_{\rm s}^2$. In Figure 5 we show CMB angular power spectra along with matter power spectra for different values of $\hat{c}_{\rm s}^2$. It becomes clear that $\hat{c}_{\rm s}^2$ plays a part in the analysis, hence fixing the DE sound speed might lead to biased constraints.

Parameter	Prior range
α	$[0.01,\ 1.35]$
$\log \hat{c}_{\rm s}^2$	$[-10,\ 0]$

Table 1. Flat prior bounds used in the full analysis including background and linear perturbations.

4 Results and discussion

MCMC results for the first part of our analysis constraining the background evolution are summarised in Fig. 6 and Table 2. Mean values for the HDE parameters α and β are in good agreement with previous works using different data sets [56, 66, 82]. Although we do not put any hard bound for α and β in our MCMC analysis, in Fig. 6 we can clearly see that there are no samples in the region satisfying $\alpha < 2\beta$. This is due to the fact that in this region the HDE density becomes negative and we have required the condition $\rho_{\rm de} \geq 0$ to hold. Figure 7 shows the behaviour of parameter densities and $w_{\rm de}$ for a model having $\alpha < 2\beta$ (upper panel) as well as the best fit for the case `HDE:BAO+SNe+H0` in Table 2 (lower panel). While in the upper panel we clearly see that $w_{\rm de}$ has a singularity when $\Omega_{\rm de}$ changes sign, the lower panel shows a non-negligible amount of HDE during both radiation dominated epoch and DM domination. This behaviour can be understood if we note that, whatever probe combination in Table 2, samples for α and β satisfy $\alpha > 2\beta$ and therefore HDE effectively contributes to matter and radiation [see Eqs. (2.13)-(2.14)]. Consequently, we observe in Fig. 6 a degeneracy between the matter parameter density $\Omega_{\rm m,0}$ and the HDE parameter α. The degeneracy is even more evident for the green contours showing results for the RDE model.

Parameter	`HDE:BAO`	`HDE:BAO+SNe`	`HDE:BAO+SNe+H0`	`RDE:BAO+SNe+H0`
$\omega_{\rm b}$	$0.0195^{-0.0144}_{+0.0051}$	$0.0151^{-0.0097}_{+0.0025}$	$0.0176^{-0.0108}_{+0.0039}$	$0.0228^{-0.0106}_{+0.0048}$
$\omega_{\rm cdm}$	$0.0688^{-0.0585}_{+0.0334}$	$0.0821^{-0.0261}_{+0.0363}$	$0.1010^{-0.0319}_{+0.0384}$	$0.1202^{-0.0292}_{+0.0408}$
β	$0.49^{-0.13}_{+0.08}$	$0.43^{-0.08}_{+0.04}$	$0.40^{-0.08}_{+0.06}$	–
α	$1.14^{-0.18}_{+0.22}$	$0.98^{-0.13}_{+0.10}$	$0.95^{-0.11}_{+0.10}$	$0.92^{-0.13}_{+0.10}$
$\Omega_{\rm m,0}$	$0.195^{-0.091}_{+0.077}$	$0.214^{-0.054}_{+0.063}$	$0.222^{-0.054}_{+0.062}$	$0.268^{-0.045}_{+0.056}$

Table 2. Mean values and 68% confidence limits on cosmological parameters. Here we only use data constraining the background.

Next we explain the second part of our analysis where data constraining linear order perturbations are also considered and we set $\beta = \alpha/2$. Statistical information derived from our MCMC results is presented in Table 3, while Fig. 8 contains confidence contours and

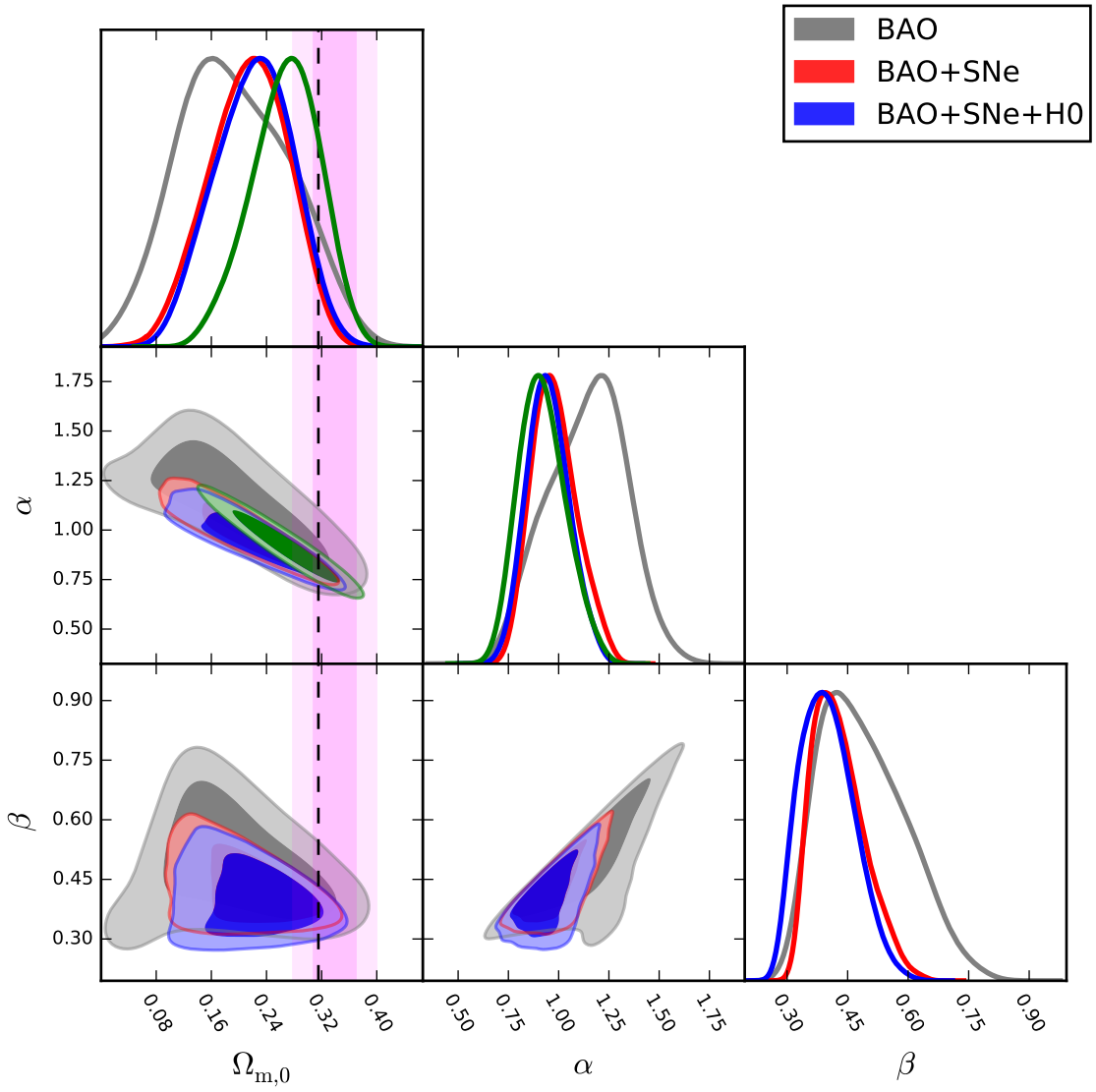

Figure 6. 1D marginalised likelihoods as well as confidence contours (i.e., 68% and 95%) for the HDE (i.e., gray, red, and blue) cosmological model. Green contours and curves show results for the RDE model with `BAO+SNe+H0`. Note that here we plot the matter density parameter $\Omega_{\rm m,0} \equiv (\omega_{\rm b} + \omega_{\rm cdm})/h^2$ which is a derived parameter in our analysis. Dashed, vertical line indicates the result obtained by the Planck Collaboration using the standard cosmological model (see Table 2, column `TTTEEE+lowE+lensing` in Ref. [1]). Vertical bands indicate DES results (68% and 95% confidence intervals) for ΛCDM reported in Ref. [13].

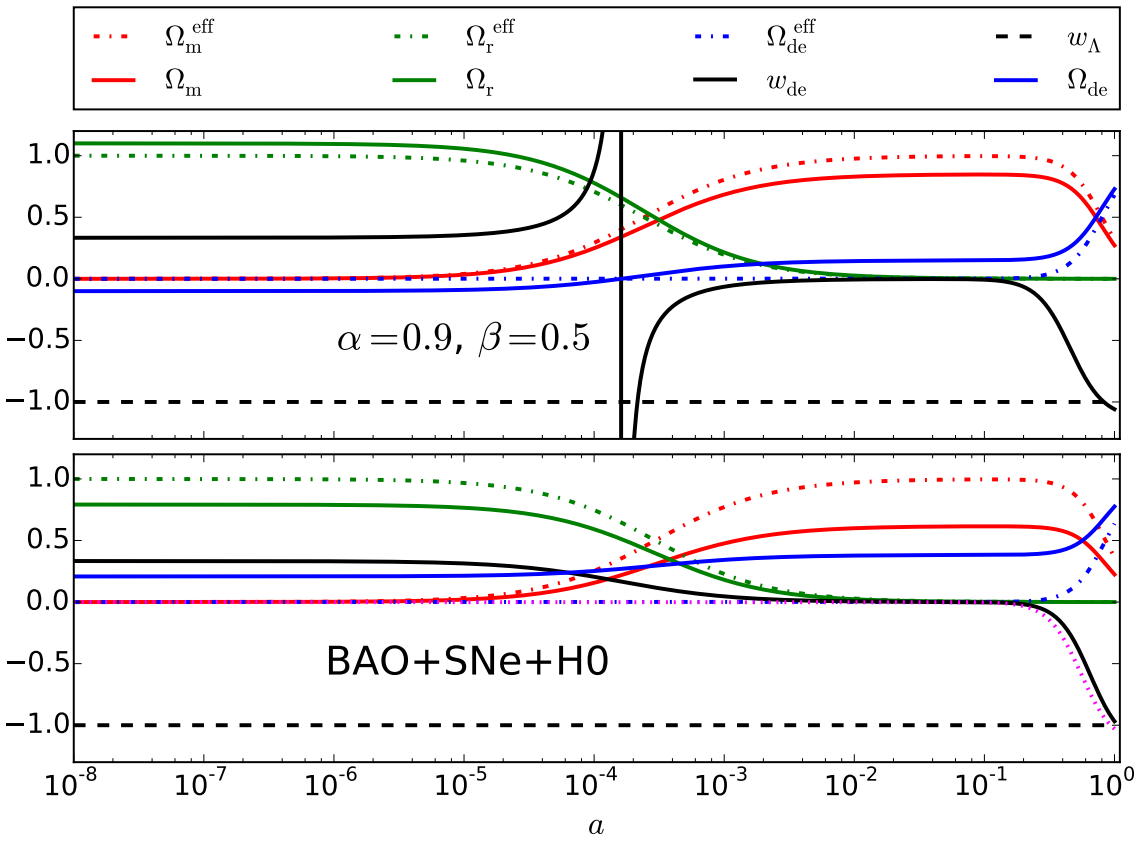

Figure 7. Evolution of parameter densities and HDE equation of state $w_{\rm de}$ for the HDE model. In the lower panel we use the best fit values for `HDE:BAO+SNe+H0` ($\alpha = 0.906$, $\beta = 0.349$, $H_0 = 72.90\,{\rm km\,s^{-1}\,Mpc^{-1}}$, $\Omega_{\rm m,0} = 0.224$). The magenta, dotted curve shows $w_{\rm de}$ for the best fit of `RDE:BAO+SNe+H0` ($\alpha = 0.893$, $H_0 = 73.12\,{\rm km\,s^{-1}\,Mpc^{-1}}$, $\Omega_{\rm m,0} = 0.281$). We set $\Omega_{\rm r,0} = 8.5 \times 10^{-5}$, and for the upper panel we use $\Omega_{\rm m,0} = 0.2713$.

marginalised 1D posteriors. Several comments can be made. Firstly, by comparing Figs. 6 and 8 we note that while background data sets seem compatible with each other, also taking Planck data into consideration introduces a discordance in the determination of some cosmological parameters (see dark, blue and light, green contours in Fig. 8), namely, H_0, $\omega_{\rm cdm}$, σ_8, $n_{\rm s}$, and α. Secondly, with regard to the RDE parameter α, we can see that in this case it is well constrained and its mean value is significantly shifted towards lower values than reported in Table 2. Although we use different data sets, constraints for α agree at the 2σ level with results in Ref. [55]; there are however noticeable differences in other cosmological parameters such as $\omega_{\rm b}$, $\omega_{\rm cdm}$, $n_{\rm s}$, τ, and $\Omega_{\rm m,0}$. Thirdly, even though the sound speed squared $\log \hat{c}_{\rm s}^2$ hits the lower bound in the prior and we can only set an upper limit, it becomes clear from our results that $\hat{c}_{\rm s}^2 = 1$ is excluded by more than 3σ. This result calls in question the assumption of fixing $\hat{c}_{\rm s}^2$ in Ref. [55] (presumably to $\hat{c}_{\rm s}^2 = 1$). A comparison between Figs. 5 and 9 clearly confirms that the DE sound speed plays a role in the analysis of RDE. A lower DE sound speed along with changes in $\omega_{\rm b}$, $\omega_{\rm cdm}$, $n_{\rm s}$, and τ show a much better fit than previous results fixing $\hat{c}_{\rm s}^2 = 1$. Fourthly, regardless of the probe combination, the only parameter which shows relatively good agreement with the baseline result reported by the Planck Collaboration for

the ΛCDM model is the Thomson scattering optical depth due to reionisation τ. All other parameters in common with the standard cosmological model appear relatively discrepant. Fifthly, our analysis discloses a slight degeneracy between α and the parameters H_0, $\omega_{\rm b}$, $\omega_{\rm cdm}$, and σ_8 (see Fig. 8). Sixthly, while for the analysis in Table 2 only including background data the DE equation of state $w_{\rm de}(a=1) \approx -1$ (see lower panel in Fig. 7), the analysis in Table 3 also including CMB and RSD data yields $w_{\rm de}(a=1) < -1$ (see Fig. 10). Then, despite having a present DE budget similar to the ΛCDM ($\Omega_{\rm de}(a=1) \approx 0.7$), we conclude the RDE model struggles to simultaneously fit low and high redshift data.

Parameter	TTTEEE+lensing+SNe	{...}+BAO	{...}+H0	{...}+RSD	TTTEEE+lensing+BAO+H0
$\omega_{\rm b}$	$0.02288^{-0.00015}_{+0.00016}$	0.02347 ± 0.00015	0.02349 ± 0.00015	0.02357 ± 0.00015	0.02317 ± 0.00015
$\omega_{\rm cdm}$	0.1301 ± 0.0011	0.1219 ± 0.0010	0.1218 ± 0.0010	0.1209 ± 0.0010	$0.1232^{-0.0010}_{+0.0009}$
H_0	$64.95^{-0.83}_{+0.84}$	$71.65^{-0.73}_{+0.75}$	$72.12^{-0.62}_{+0.60}$	$71.91^{-0.61}_{+0.59}$	$77.55^{-0.85}_{+0.82}$
σ_8	$0.748^{-0.010}_{+0.013}$	0.765 ± 0.010	0.769 ± 0.009	$0.752^{-0.008}_{+0.014}$	0.825 ± 0.012
$n_{\rm s}$	0.9226 ± 0.0038	0.9425 ± 0.0038	0.9431 ± 0.0037	$0.9445^{-0.0037}_{+0.0038}$	0.9412 ± 0.0037
τ	$0.0411^{-0.0061}_{+0.0071}$	$0.0605^{-0.0085}_{+0.0072}$	$0.0612^{-0.0090}_{+0.0070}$	$0.0596^{-0.0086}_{+0.0070}$	$0.0547^{-0.0073}_{+0.0065}$
$\log \hat{c}_{\rm s}^2$	-7^{-2}_{+1}	< -8	< -7	< -6	-8^{-2}_{+1}
α	0.642 ± 0.013	0.643 ± 0.011	0.640 ± 0.010	0.650 ± 0.010	0.571 ± 0.011
$\Omega_{\rm m,0}$	0.363 ± 0.011	$0.283^{-0.007}_{+0.006}$	$0.279^{-0.006}_{+0.005}$	0.279 ± 0.005	$0.243^{-0.005}_{+0.006}$
$100\theta_\star$	1.03999 ± 0.00028	1.04084 ± 0.00028	1.04088 ± 0.00028	1.04092 ± 0.00028	1.04076 ± 0.00028
S_8	$0.822^{-0.012}_{+0.014}$	0.744 ± 0.010	0.742 ± 0.010	$0.726^{-0.010}_{+0.014}$	0.743 ± 0.010

Table 3. Mean values and 68% confidence limits on cosmological parameters for the RDE model. Here {...} stands for the inclusion of data from column on the left.

In Fig. 9 we show the CMB TT angular power spectrum and the matter power spectrum corresponding to the best fits of analyses in Table 3 and Fig. 8. For the sake of comparison we also depicted the Plack baseline result for the ΛCDM model. Main differences in the CMB angular power spectrum appear on very large angular scales where cosmic variance dominates the error budget and the Sachs-Wolfe effect becomes important: the enhancement of power at small ℓ is due to lower values for the spectral index than in ΛCDM as well as the evolution of gravitational potentials (affected by α and $\hat{c}_{\rm s}^2$) when DE dominates the energy budget (see also left panel of Fig. 11). Concerning the matter power spectrum, we can see that it is heavily modified with respect to the ΛCDM solution depending on the data set used in the analysis. Except for the combination TTTEEE+lensing+SNe, data favour more power on large scales than in the ΛCDM model. Except for the combination TTTEEE+lensing+BAO+H0, data favour less power on small scales than in the standard model. Our baseline result TTTEEE+lensing+BAO+RSD+SNe+H0 keeps the angular acoustic scale in good agreement with the Planck Collaboration baseline result. Right panel of Fig. 11 shows the effect of changing α and $\hat{c}_{\rm s}^2$ that we explain below.

In what follows we focus on our baseline result TTTEEE+lensing+BAO+RSD+SNe+H0 which seems to bring in relative good agreement CMB and Large Scale Structure data. First, note that although we do not use data from the Dark Energy Survey (DES), our derived constraints for S_8 and $\Omega_{\rm m,0}$ (see Table 3) are compatible with DES measurements are $S_8 = 0.776 \pm 0.017$ and $\Omega_{\rm m,0} = 0.339^{+0.032}_{-0.031}$ within $\approx 2\sigma$. Second, we can see in the right panel of Fig. 9 than on large scales (wavenumber $k \lesssim 10^{-2}\,{\rm h\,Mpc^{-1}}$) beyond the reach of current galaxy surveys, the RDE model predicts more power than the standard model. This difference is due to a few changes with respect to the concordance model: i) a smaller spectral index ($n_{\rm s} = 0.9649$ in ΛCDM); ii) a slight shift in the pivot scale; iii) differences in the evolution of matter perturbations in the RDE model (see Fig. 3). Third, we constrain the redshift dependence in the linear matter power spectrum by using the parameter $f\sigma_8$ through the likelihood

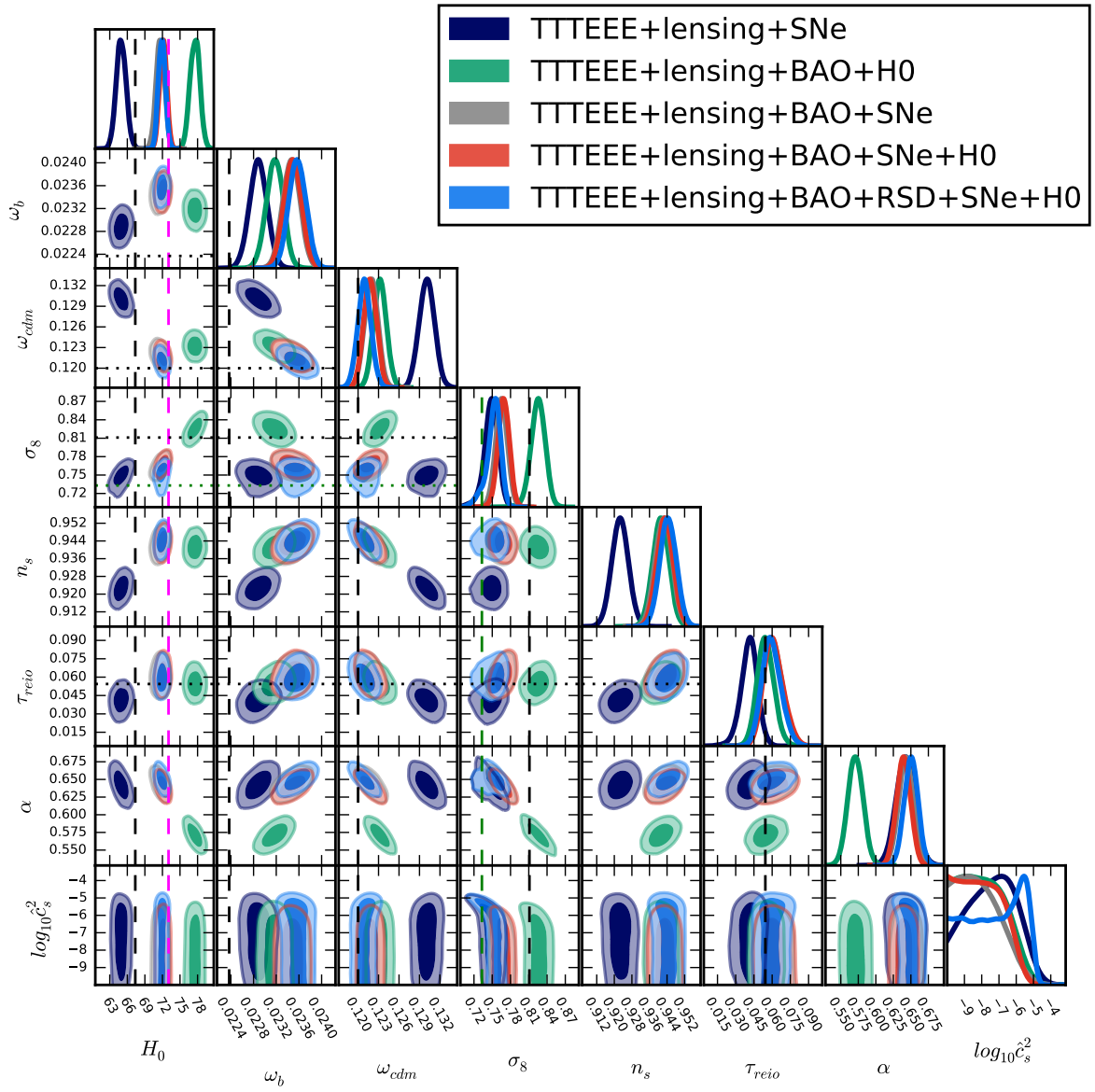

Figure 8. 1D marginalised likelihoods as well as confidence contours (i.e., 68% and 95%) for the RDE cosmological model. Dashed, vertical and dotted, horizontal black lines indicate the results obtained by the Planck Collaboration using the standard cosmological model (see Table 2, column `TTTEEE+lowE+lensing` in Ref. [1]). Note that here we plot the Hubble constant H_0 and the strength of matter clustering σ_8 which are derived parameters in our analysis. Vertical, dashed, magenta line indicates SH0ES value $73.04\,\mathrm{km\,s^{-1}\,Mpc^{-1}}$ [8]. Dashed, vertical and dotted, horizontal green lines indicate DES value $\sigma_8 = 0.733$ for the analysis of large scale structure combining three two-point correlation functions [13].

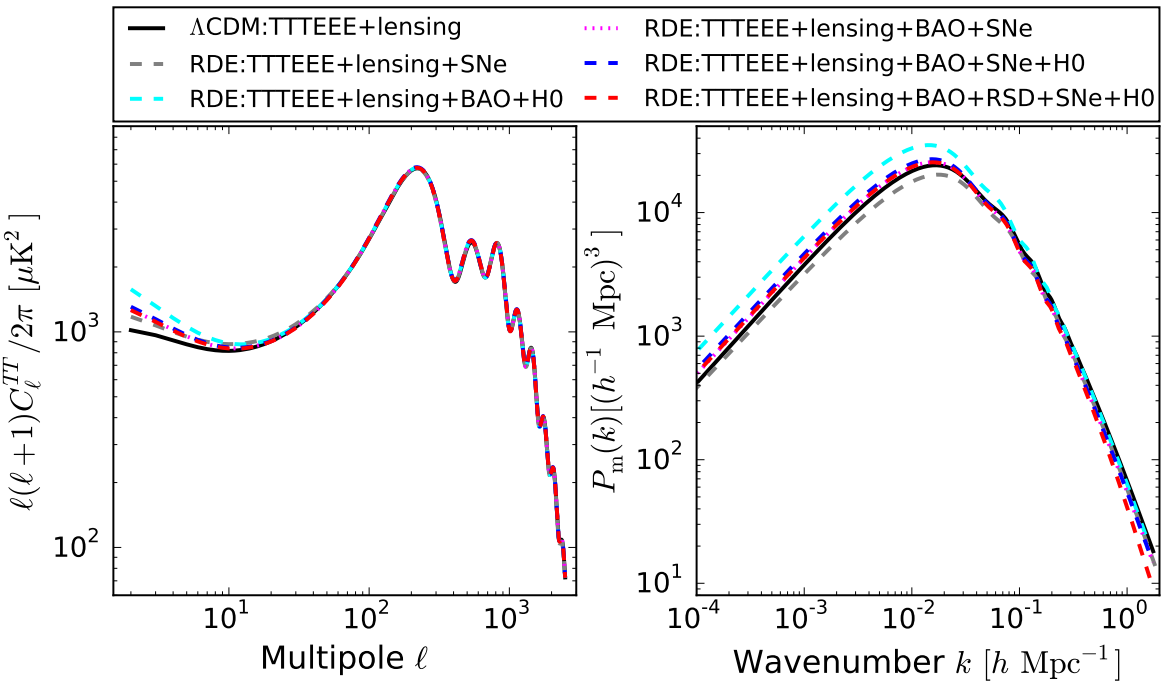

Figure 9. Left: CMB temperature angular power spectrum C_l^{TT}. Right: linear theory matter power spectrum $P_{\rm m}(k, z = 0)$. We plot the baseline result reported by the Planck Collaboration (ΛCDM) along with best fits of analyses in Fig. 8 for the RDE model. Our baseline result (`TTTEEE+lensing+BAO+RSD+SNe+H0`) has the following best fit values for cosmological parameters: $\omega_{\rm b} = 0.02351$, $\omega_{\rm cdm} = 0.1214$, $100\theta_{\rm s} = 1.04087$, $\ln 10^{10} A_{\rm s} = 3.014$, $n_{\rm s} = 0.9440$, $\tau = 0.0551$, $\alpha = 0.651$, $\log \hat{c}_{\rm s}^2 = -6$, $\sigma_8 = 0.736$, $H_0 = 71.44\,{\rm km\,s^{-1}\,Mpc^{-1}}$.

`RSD` which relies on linear perturbation theory.[4] Our constraint for the strength of matter clustering σ_8 turns out to be lower than in the ΛCDM model Planck baseline. Since matter velocity perturbations might be greater in RDE than in ΛCDM (see Fig. 3), we expect less matter clustering in RDE. Moreover, since the rms linear theory mass fluctuation in a sphere of radius $R = 8\,{\rm Mpc\,h^{-1}}$ at $z = 0$

$$(\sigma_8)^2 \equiv \frac{1}{2\pi^2} \int d\log k\, W^2(kR)\, k^3\, P_{\rm m}(k), \tag{4.1}$$

where $W(kR)$ is a spherical top-hat filter, is predominantly determined by contributions on small scales and the matter power spectrum $P_{\rm m}$ predicts less power in RDE than in ΛCDM, we can expect $\sigma_8^{\rm RDE} < \sigma_8^{\Lambda{\rm CDM}}$ as we indeed found.

Another interesting aspect of our analysis concerns the constraint for the Hubble constant H_0. Fig. 8 indicates that the RDE model can simultaneously relax the current tension in H_0 and σ_8 (see case `TTTEEE+lensing+BAO+SNe`). The angular acoustic scale

$$\theta_{\rm s} = \frac{r_{\rm s}(z_\star)}{D_{\rm A}(z_\star)}, \tag{4.2}$$

[4] We also computed non-linear corrections for the RDE using HALOFIT [83]. However, since HALOFIT is optimised for the standard model, we do not use it in this work. Even when including these non-linear corrections we observe less power on small scales in the RDE model than predicted by the ΛCDM model. Non-linear evolution of DE perturbations could also be investigated along the lines explained in Refs. [84, 85].

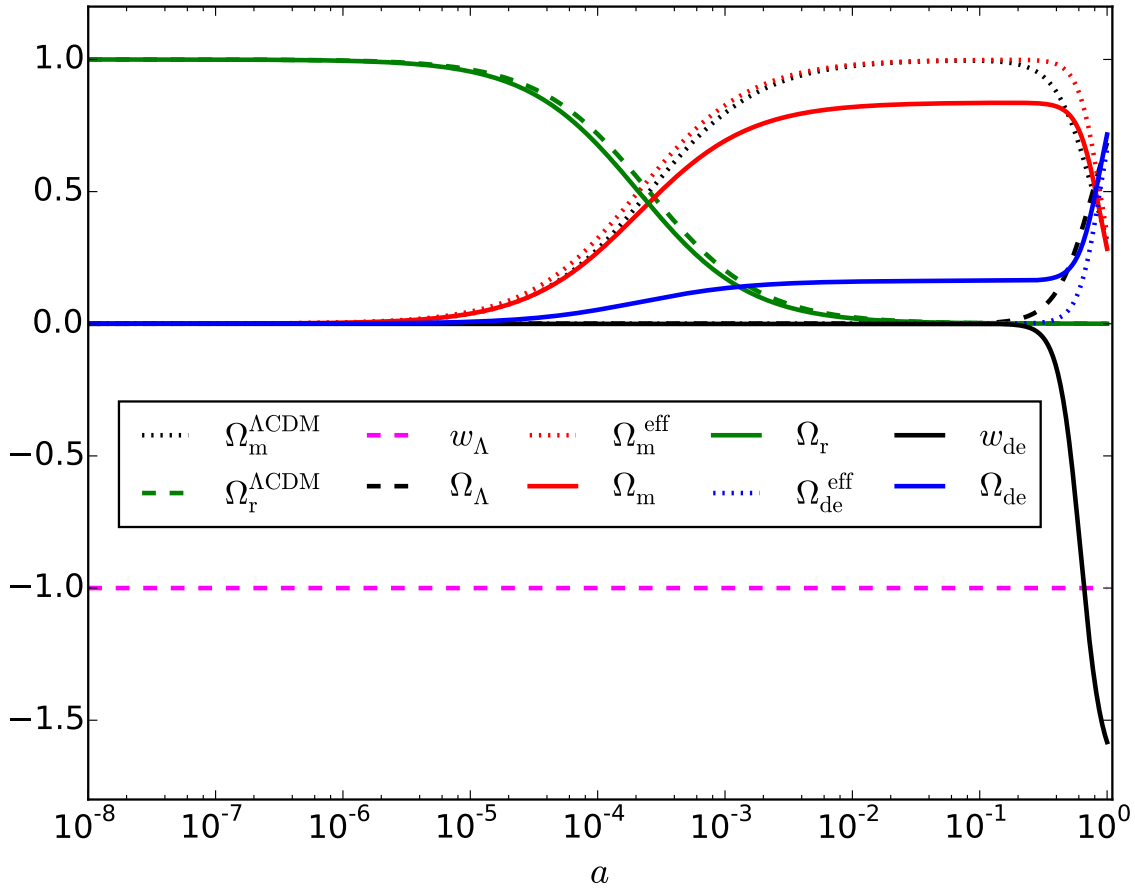

Figure 10. Evolution of parameter densities and DE equation of state $w_{\rm de}$ for the RDE model. Here we use the best fit values for our baseline result (`TTTEEE+lensing+BAO+RSD+SNe+H0`) analysis in Fig. 8. For sake of comparison we also plot the ΛCDM baseline result by the Planck Collaboration.

is pretty well constrained by CMB observations. In Eq. (4.2), $r_{\rm s}$ and $D_{\rm A}$ respectively denote the sound horizon

$$r_{\rm s} = \int_{z_\star}^{\infty} \frac{c_{\rm s}(z)}{H(z)} dz, \tag{4.3}$$

and the comoving angular diameter distance

$$D_{\rm A} = \int_{0}^{z_\star} \frac{dz}{H(z)}. \tag{4.4}$$

While for the ΛCDM Planck baseline

$$100\theta_{\rm s} = 1.04110, \quad r_{\rm s}(z_\star) = 144.531055\,{\rm Mpc}, \quad {\rm d_A(z_\star)} = 12.738778\,{\rm Mpc}, \tag{4.5}$$

our baseline result (the best fit)

$$100\theta_{\rm s} = 1.04087, \quad r_{\rm s}(z_\star) = 136.800000\,{\rm Mpc}, \quad {\rm d_A(z_\star)} = 12.053113\,{\rm Mpc}, \tag{4.6}$$

where the comoving angular diameter distance is related to the angular diameter distance $d_{\rm A}$ via $D_{\rm A}(z) = (1+z)d_{\rm A}$. The RDE model decreases both the sound horizon and the comoving

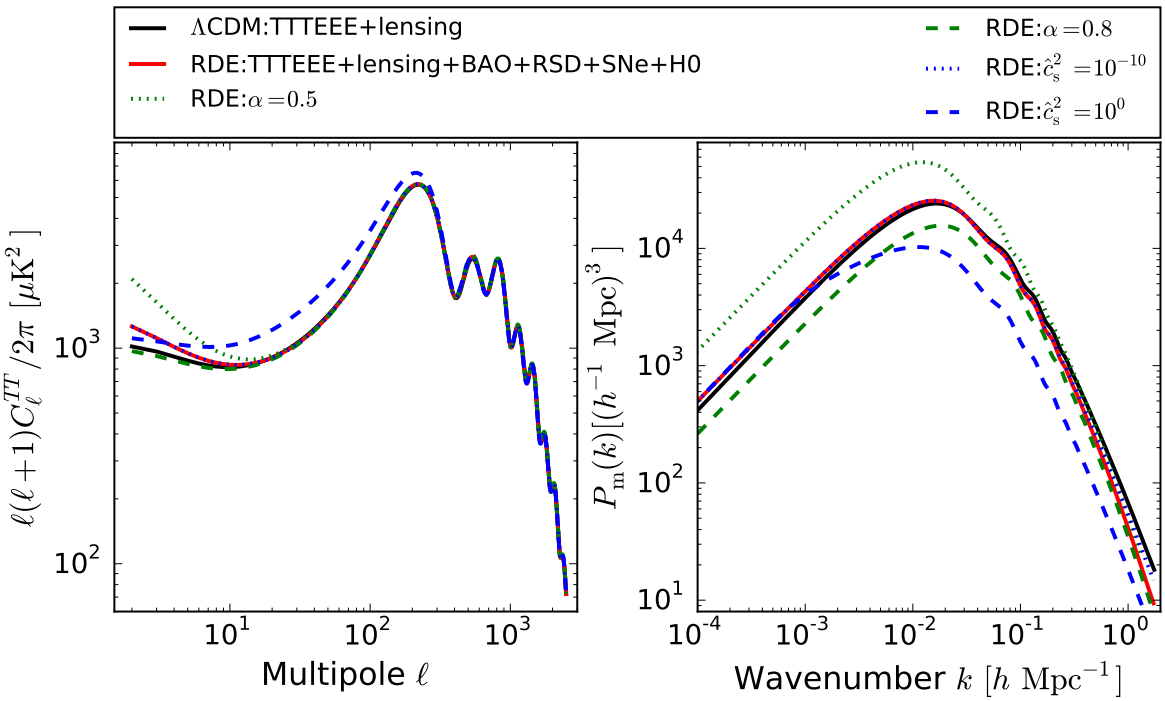

Figure 11. Left: CMB angular power spectrum. Right: linear theory matter power spectrum. Solid, black lines show the Planck Collaboration baseline result for the standard model. Solid, red lines show our baseline result for the RDE model. Green, dotted (dashed) line shows the effect of decreasing (increasing) α with respect to the best fit value. Blue, dotted (dashed) line shows the effect of decreasing (increasing) $\hat{c}_s^2$ with respect to the best fit value.

angular diameter distance while keeping the angular acoustic scale in good agreement with the ΛCDM solution. These changes can be understood from Figure 12. On the one hand, in the RDE model the expansion rate is enhanced with respect to the standard model in two stages ($10^0 \lesssim z \lesssim 10^5$ and at late times $z \lesssim 10^{-1}$). On the other hand, for a relatively short period of time the universe expands faster in ΛCDM than in RDE for $10^{-1} \lesssim z \lesssim 10^0$. While the Early Dark Energy model of Ref. [86] mainly changes the sound horizon through the enhancement of $H(z)$ prior to recombination, the RDE model introduces changes in the expansion rate prior and post recombination.

Although our RDE baseline result brings into $\approx 2\sigma$ agreement H_0 and σ_8, other parameters get shifted in order to maintain the fit to primary CMB and RSD data.[5] Besides the shift of n_s towards lower values than allowed in the ΛCDM analysis of Planck, we also obtain a value of baryon matter density ω_b higher than in the Planck ΛCDM baseline result. This value actually exacerbates the existing $\approx 2\sigma$ discrepancy in the ΛCDM model with values inferred from Big Bang Nucleosynthesis (BBN) [88].[6]

We finalize our discussion by comparing our findings with previous results. First, whereas in Ref. [55] authors do not seem to have properly included radiation in their analysis

[5] In the EDE scenario alleviating the H_0 tension, a similar situation occurs. However, the EDE exacerbates the σ_8 tension while including large scale structure data in the analysis [87].

[6] Recent analyses using an improved rate of deuterium burning estimate a $\omega_b = 0.02233 \pm 0.00036$ in excellent agreement with the Planck baseline result [4]. This value is discrepant with our baseline RDE result at the 3σ level.

when solving for the background evolution (see their Eq. 5 for the Hubble parameter), here we have derived the full expression in Eq. (2.19) [or the more general Eq. (2.12)]. Second, since the RDE model can cross the phantom divide $w_{\rm de} = -1$ we have used the PPF formalism so that perturbations behave properly. Authors in Ref. [55] split the whole region of $w_{\rm de}$ into three regions ending up with a much more involved implementation. Third, while in Ref. [55] values $n_{\rm s} > 1$ are preferred, our analysis favours values $n_{\rm s} < 1$. This is due to the much better constraining power added by Planck data on small scales in comparison to WMAP data.

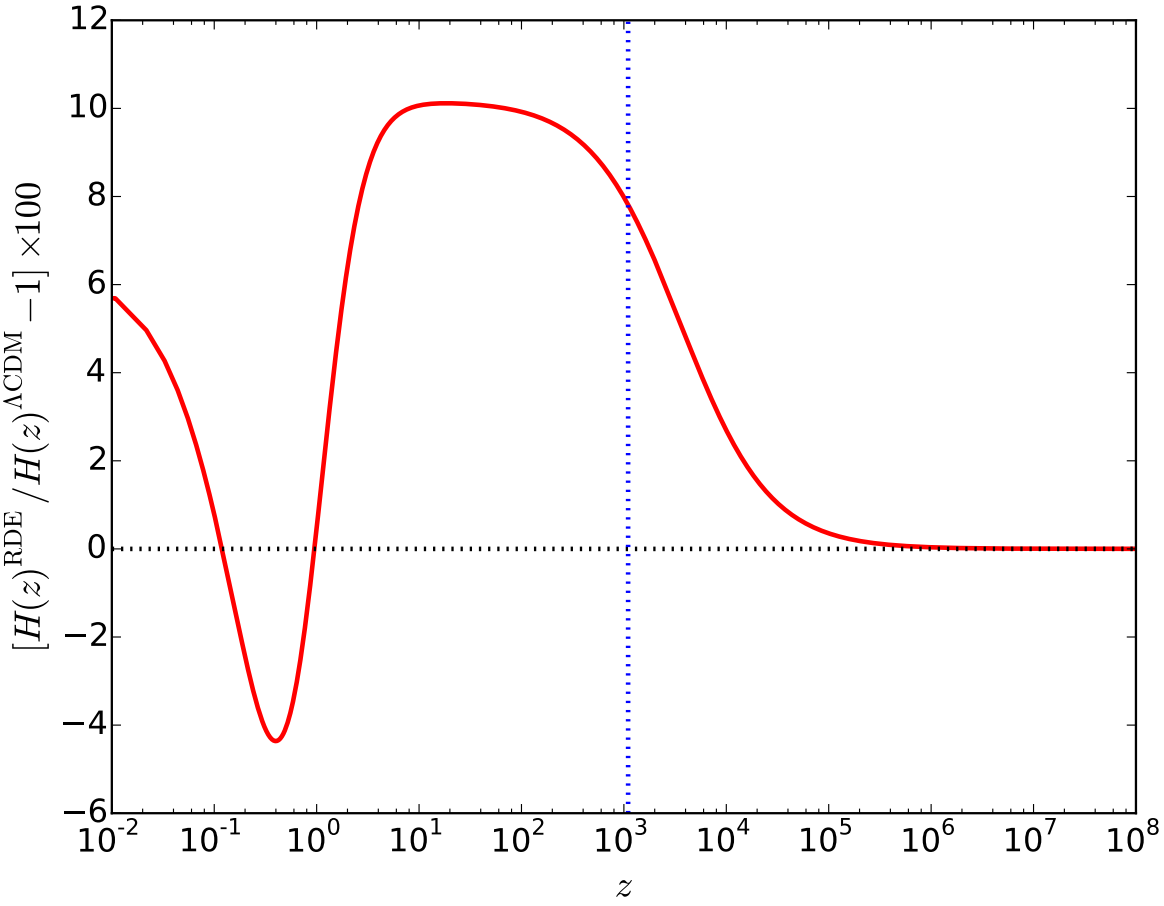

Figure 12. Percentage difference in the Hubble parameter for the RDE model (best fit of our baseline result) with respect to the Planck ΛCDM baseline result. Blue, vertical dotted line indicates $z_\star$.

5 Conclusions

Holographic Dark Energy (HDE) seems to offer a plausible alternative to the simple, but troublesome cosmological constant. While the holographic approach does not require modifications to General Relativity, neither does it require new dynamical Dark Energy (DE) fields, it does need an arbitrary choice. In these kinds of DE models the length scale fixing the maximum energy density in the effective field theory becomes important. In the literature there exist a few ultraviolet/infrared relationships that avoid the problem of causality

as well as the coincidence issue. In this work we studied two infrared (IR) cut-offs: the Ricci scalar curvature (also dubbed RDE) and its more general version the Granda-Oliveros (GO) IR cut-off.

Thus far most works studying phenomenological aspects of HDE models have focused on the background. Here we scrutinised HDE models derived from both GO and RDE cut-offs also considering linear order perturbations. Our investigation refined upon previous works as we summarise below.

Concerning the background evolution. We noted that in previous works radiation is not properly taken into account when solving for the Hubble parameter. We showed this might not be a good approximation: depending on the cut-off choice, new terms might appear playing a part in early stages of the universe expansion. As a result, the holographic energy density using the GO cut-off can be radiation-like, matter-like, or DE-like depending on the component that dominates the energy budget. For the RDE IR cut-off the holographic energy density can only be matter-like or DE-like, since the constraint $\alpha = 2\beta$ excludes a radiation-like behaviour (see Fig. 1). Interestingly, the peculiar behaviour in the holographic energy density changes the expansion rate prior and post-recombination (see Fig. 12). Consequently, the RDE cosmological model can decrease both sound horizon and comoving angular diameter distance while keeping good agreement with CMB measurements of the angular acoustic scale. This feature might help to relax the current discrepancy in the Hubble constant between low and high redshift probes.

Considering a DE fluid having a background evolution matching the RDE model, we proceeded to the investigation of linear order perturbations and assumed our DE as having a constant sound speed $\hat{c}_{\rm s}^2$ as well as vanishing anisotropic stress. We managed to find analytical, approximate solutions for matter and DE perturbations in the regime of matter dominance and when the gravitational potential can be regarded as constant. Our findings show that matter perturbations behave slightly different with respect to the standard cosmological model ΛCDM (see Fig. 3). Due to the matter-like behaviour of the holographic density in the RDE model, DE clusters in the same way as matter perturbations when its sound speed vanishes.

Differences in the matter clustering properties of the RDE model with respect to ΛCDM become apparent in the matter power spectrum. We implemented the RDE model in the popular Boltzmann solver `CLASS` so that predictions for the statistical properties of CMB and matter fluctuations could be computed. Whereas previous works artificially considered the possibility of $w_{\rm de}$ crossing the phantom divide, here we used the PPF formalism fully granting energy-momentum conservation. Another important difference with respect to previous works concerns the treatment we gave to $\hat{c}_{\rm s}^2$. In the literature, a RDE model with fixed $\hat{c}_{\rm s}^2 = 1$ has been investigated. Nevertheless, we showed this choice might not be appropriate as it heavily affects matter clustering through changes in the gravitational potential during matter dominance (see Fig. 2).

We computed cosmological constraints for the RDE model marginalising over $\hat{c}_{\rm s}^2$. In our investigation we regarded CMB data (i.e., temperature, polarisation, lensing), baryon acoustic oscillations, supernovae, redshift space distortions, and the local measurement of the Hubble constant. For our baseline result using all data sets we found that $\hat{c}_{\rm s}^2 = 1$ is excluded at $\gtrsim 3\sigma$. We also obtained a value of the strength of matter clustering σ_8 lower than in the ΛCDM model and in good agreement ($\approx 2\sigma$) with recent DES results. Our constraint on the Hubble constant H_0 value is also in good concordance ($\approx 2\sigma$) with local, model independent measurements using Cepheid variables. This can be explained by the

presence of a turning point in the Hubble parameter $H(z)$ for $z < 0.1$ which is still consistent with SNe observations [89]. While the scalar spectral index n_s takes on lower values in the RDE model than in the ΛCDM analysis, the constraint on the baryon density ω_b in our RDE baseline result appears to be in $\approx 3\sigma$ tension with BBN measurements (see Fig. 8 and Table 3).

The RDE model has an evolving DE equation of state which according to our baseline result $w_{de}(z = 0) < -1$ (see Fig. 10). However, when only considering background data we found $w_{de}(z = 0) \approx -1$ (see Fig. 7), thus showing RDE model struggles to simultaneously fit background and perturbations data. It remains to be seen whether or not a more general IR cut-off such as GO having $\alpha > 2\beta$ (RDE has $\alpha = 2\beta$) might be able to provide a better fit to the background data than RDE while also relaxing tensions in cosmological parameters (e.g., H_0, σ_8, ω_b). Our work shows that dynamical DE also having non standard clustering properties may play a part in the solution of discrepancies in cosmological parameters (other possibilities relying on new physics discussed, for instance, in Refs. [18–22, 25, 90]). Scalar-Vector-Tensor theories provide a fairly general framework where $w_{de}(z)$, $\hat{c}_s^2(z, k)$, and $\sigma(z, k)$ worthwhile an investigation in light of current and upcoming experiments [91, 92].

Acknowledgements

We are grateful to Giovanni Marozzi and Alexander Oliveros for helpful discussions. WC thanks University of Pisa for hospitality. WC acknowledges financial support from the São Paulo Research Foundation (FAPESP) through grant #2021/10290-2. This research was supported by resources supplied by the Center for Scientific Computing (NCC/GridUNESP) of the São Paulo State University (UNESP) and the Datacenter CIBioFi (Universidad del Valle). The statistical analyses as well as the plots were made with the Python package GetDist https://github.com/cmbant/getdist.

Numerical codes

Modified CLASS code reproducing results in this work can be found in the GitHub branch HDE of the repository EFCLASS.

References

[1] Planck collaboration, *Planck 2018 results. VI. Cosmological parameters*, *Astron. Astrophys.* **641** (2020) A6 [1807.06209].

[2] DES collaboration, *Cosmological Constraints from Multiple Probes in the Dark Energy Survey*, *Phys. Rev. Lett.* **122** (2019) 171301 [1811.02375].

[3] DES collaboration, *Dark Energy Survey Year 1 Results: Cosmological Constraints from Cluster Abundances, Weak Lensing, and Galaxy Correlations*, *Phys. Rev. Lett.* **126** (2021) 141301 [2010.01138].

[4] V. Mossa et al., *The baryon density of the Universe from an improved rate of deuterium burning*, *Nature* **587** (2020) 210.

[5] E. Abdalla et al., *Cosmology Intertwined: A Review of the Particle Physics, Astrophysics, and Cosmology Associated with the Cosmological Tensions and Anomalies*, in *2022 Snowmass Summer Study*, 3, 2022, 2203.06142.

[6] A. G. Riess, S. Casertano, W. Yuan, L. M. Macri and D. Scolnic, *Large Magellanic Cloud Cepheid Standards Provide a 1% Foundation for the Determination of the Hubble Constant and Stronger Evidence for Physics beyond ΛCDM*, *Astrophys. J.* **876** (2019) 85 [1903.07603].

[7] W. L. Freedman, *Measurements of the Hubble Constant: Tensions in Perspective*, *Astrophys. J.* **919** (2021) 16 [2106.15656].

[8] A. G. Riess et al., *A Comprehensive Measurement of the Local Value of the Hubble Constant with 1 km s^1 Mpc^1 Uncertainty from the Hubble Space Telescope and the SH0ES Team*, *Astrophys. J. Lett.* **934** (2022) L7 [2112.04510].

[9] S. Joudaki et al., *CFHTLenS revisited: assessing concordance with Planck including astrophysical systematics*, *Mon. Not. Roy. Astron. Soc.* **465** (2017) 2033 [1601.05786].

[10] C. Heymans et al., *KiDS-1000 Cosmology: Multi-probe weak gravitational lensing and spectroscopic galaxy clustering constraints*, *Astron. Astrophys.* **646** (2021) A140 [2007.15632].

[11] O. H. E. Philcox and M. M. Ivanov, *BOSS DR12 full-shape cosmology: ΛCDM constraints from the large-scale galaxy power spectrum and bispectrum monopole*, *Phys. Rev. D* **105** (2022) 043517 [2112.04515].

[12] A. Blanchard and S. Ilić, *Closing up the cluster tension?*, *Astron. Astrophys.* **656** (2021) A75 [2104.00756].

[13] DES collaboration, *Dark Energy Survey Year 3 results: Cosmological constraints from galaxy clustering and weak lensing*, *Phys. Rev. D* **105** (2022) 023520 [2105.13549].

[14] R. A. Battye, T. Charnock and A. Moss, *Tension between the power spectrum of density perturbations measured on large and small scales*, *Phys. Rev. D* **91** (2015) 103508.

[15] E. Macaulay, I. K. Wehus and H. K. Eriksen, *Lower growth rate from recent redshift space distortion measurements than expected from planck*, *Phys. Rev. Lett.* **111** (2013) 161301.

[16] S. Vagnozzi, *Consistency tests of ΛCDM from the early integrated Sachs-Wolfe effect: Implications for early-time new physics and the Hubble tension*, *Phys. Rev. D* **104** (2021) 063524 [2105.10425].

[17] N. Schöneberg, G. Franco Abellán, A. Pérez Sánchez, S. J. Witte, V. Poulin and J. Lesgourgues, *The H0 Olympics: A fair ranking of proposed models*, *Phys. Rept.* **984** (2022) 1 [2107.10291].

[18] A. Gómez-Valent, Z. Zheng, L. Amendola, V. Pettorino and C. Wetterich, *Early dark energy in the pre- and postrecombination epochs*, *Phys. Rev. D* **104** (2021) 083536 [2107.11065].

[19] L. A. Anchordoqui, E. Di Valentino, S. Pan and W. Yang, *Dissecting the H0 and S8 tensions with Planck + BAO + supernova type Ia in multi-parameter cosmologies*, *JHEAp* **32** (2021) 28 [2107.13932].

[20] M. Rashkovetskyi, J. B. Muñoz, D. J. Eisenstein and C. Dvorkin, *Small-scale clumping at recombination and the Hubble tension*, *Phys. Rev. D* **104** (2021) 103517 [2108.02747].

[21] S. Bansal, J. H. Kim, C. Kolda, M. Low and Y. Tsai, *Mirror twin Higgs cosmology: constraints and a possible resolution to the H_0 and S_8 tensions*, *JHEP* **05** (2022) 050 [2110.04317].

[22] L. Heisenberg, H. Villarrubia-Rojo and J. Zosso, *Can late-time extensions solve the H0 and σ8 tensions?*, *Phys. Rev. D* **106** (2022) 043503 [2202.01202].

[23] M. G. Dainotti, B. De Simone, T. Schiavone, G. Montani, E. Rinaldi and G. Lambiase, *On the Hubble constant tension in the SNe Ia Pantheon sample*, *Astrophys. J.* **912** (2021) 150 [2103.02117].

[24] M. G. Dainotti, B. De Simone, T. Schiavone, G. Montani, E. Rinaldi, G. Lambiase et al., *On the Evolution of the Hubble Constant with the SNe Ia Pantheon Sample and Baryon Acoustic*

Oscillations: A Feasibility Study for GRB-Cosmology in 2030, *Galaxies* **10** (2022) 24 [2201.09848].

[25] R. Murgia, S. Gariazzo and N. Fornengo, *Constraints on the Coupling between Dark Energy and Dark Matter from CMB data*, *JCAP* **04** (2016) 014 [1602.01765].

[26] A. Heavens, Y. Fantaye, E. Sellentin, H. Eggers, Z. Hosenie, S. Kroon et al., *No evidence for extensions to the standard cosmological model*, *Phys. Rev. Lett.* **119** (2017) 101301 [1704.03467].

[27] E. J. Copeland, M. Sami and S. Tsujikawa, *Dynamics of dark energy*, *Int. J. Mod. Phys. D* **15** (2006) 1753 [hep-th/0603057].

[28] T. Clifton, P. G. Ferreira, A. Padilla and C. Skordis, *Modified Gravity and Cosmology*, *Phys. Rept.* **513** (2012) 1 [1106.2476].

[29] M. Li, X.-D. Li, S. Wang and Y. Wang, *Dark Energy*, *Commun. Theor. Phys.* **56** (2011) 525 [1103.5870].

[30] K. Bamba, S. Capozziello, S. Nojiri and S. D. Odintsov, *Dark energy cosmology: the equivalent description via different theoretical models and cosmography tests*, *Astrophys. Space Sci.* **342** (2012) 155 [1205.3421].

[31] LIGO Scientific and Virgo Collaborations collaboration, *Tests of general relativity with gw150914*, *Phys. Rev. Lett.* **116** (2016) 221101.

[32] T. E. Collett, L. J. Oldham, R. J. Smith, M. W. Auger, K. B. Westfall, D. Bacon et al., *A precise extragalactic test of General Relativity*, *Science* **360** (2018) 1342 [1806.08300].

[33] Planck collaboration, *Planck 2015 results. XIV. Dark energy and modified gravity*, *Astron. Astrophys.* **594** (2016) A14 [1502.01590].

[34] G. 't Hooft, *Dimensional reduction in quantum gravity*, *Conf. Proc. C* **930308** (1993) 284 [gr-qc/9310026].

[35] L. Susskind, *The World as a hologram*, *J. Math. Phys.* **36** (1995) 6377 [hep-th/9409089].

[36] S. W. Hawking, *Particle Creation by Black Holes*, *Commun. Math. Phys.* **43** (1975) 199.

[37] J. D. Bekenstein, *Black holes and entropy*, *Phys. Rev. D* **7** (1973) 2333.

[38] R. Bousso, *The Holographic principle*, *Rev. Mod. Phys.* **74** (2002) 825 [hep-th/0203101].

[39] R. Bousso, *A Covariant entropy conjecture*, *JHEP* **07** (1999) 004 [hep-th/9905177].

[40] A. G. Cohen, D. B. Kaplan and A. E. Nelson, *Effective field theory, black holes, and the cosmological constant*, *Phys. Rev. Lett.* **82** (1999) 4971 [hep-th/9803132].

[41] S. Weinberg, *The Cosmological Constant Problem*, *Rev. Mod. Phys.* **61** (1989) 1.

[42] S. M. Carroll, *The Cosmological constant*, *Living Rev. Rel.* **4** (2001) 1 [astro-ph/0004075].

[43] S. Wang, Y. Wang and M. Li, *Holographic Dark Energy*, *Phys. Rept.* **696** (2017) 1 [1612.00345].

[44] S. Nojiri and S. D. Odintsov, *Unifying phantom inflation with late-time acceleration: Scalar phantom-non-phantom transition model and generalized holographic dark energy*, *Gen. Rel. Grav.* **38** (2006) 1285 [hep-th/0506212].

[45] S. Nojiri and S. D. Odintsov, *Covariant Generalized Holographic Dark Energy and Accelerating Universe*, *Eur. Phys. J. C* **77** (2017) 528 [1703.06372].

[46] L. N. Granda and A. Oliveros, *Infrared cut-off proposal for the Holographic density*, *Phys. Lett. B* **669** (2008) 275 [0810.3149].

[47] C. Gao, F. Wu, X. Chen and Y.-G. Shen, *A Holographic Dark Energy Model from Ricci Scalar Curvature*, *Phys. Rev. D* **79** (2009) 043511 [0712.1394].

[48] S. Nojiri, S. D. Odintsov and T. Paul, *Different Faces of Generalized Holographic Dark Energy*, *Symmetry* **13** (2021) 928 [2105.08438].

[49] S. Nojiri, S. D. Odintsov and T. Paul, *Barrow entropic dark energy: A member of generalized holographic dark energy family*, *Phys. Lett. B* **825** (2022) 136844 [2112.10159].

[50] S. Nojiri, S. D. Odintsov and T. Paul, *Early and late universe holographic cosmology from a new generalized entropy*, *Phys. Lett. B* **831** (2022) 137189 [2205.08876].

[51] C. Lin, *An effective field theory of holographic dark energy*, *Journal of Cosmology and Astroparticle Physics* **2021** (2021) 003.

[52] L. Heisenberg, *Scalar-Vector-Tensor Gravity Theories*, *JCAP* **10** (2018) 054 [1801.01523].

[53] X. Zhang, *Holographic Ricci dark energy: Current observational constraints, quintom feature, and the reconstruction of scalar-field dark energy*, *Phys. Rev. D* **79** (2009) 103509 [0901.2262].

[54] L. Xu and Y. Wang, *Observational Constraints to Ricci Dark Energy Model by Using: SN, BAO, OHD, fgas Data Sets*, *JCAP* **06** (2010) 002 [1006.0296].

[55] Y. Wang, L. Xu and Y. Gui, *Probing Ricci dark energy model with perturbations by using WMAP seven-year cosmic microwave background measurements, BAO and Type Ia supernovae*, *Phys. Rev. D* **84** (2011) 063513 [1110.4401].

[56] I. A. Akhlaghi, M. Malekjani, S. Basilakos and H. Haghi, *Model selection and constraints from Holographic dark energy scenarios*, *Mon. Not. Roy. Astron. Soc.* **477** (2018) 3659 [1804.02989].

[57] H. Hossienkhani, N. Azimi and H. Yousefi, *Constraints on the Ricci dark energy cosmologies in Bianchi type I model*, *Int. J. Geom. Meth. Mod. Phys.* **18** (2021) 2150095.

[58] A. Najafi and H. Hossienkhani, *Using Pantheon and Hubble parameter data to constrain the Ricci dark energy in a Bianchi I Universe*, *Commun. Theor. Phys.* **74** (2022) 065401.

[59] A. Cid, C. Rodriguez-Benites, M. Cataldo and G. Casanova, *Bayesian Comparison of Interacting Modified Holographic Ricci Dark Energy Scenarios*, *Eur. Phys. J. C* **81** (2021) 31 [2005.07664].

[60] M. Malekjani, M. Rezaei and I. A. Akhlaghi, *Can Holographic dark energy models fit the observational data?*, *Phys. Rev. D* **98** (2018) 063533 [1809.08792].

[61] V. H. Cardenas, A. Bonilla, V. Motta and S. del Campo, *Constraints on Holographic cosmologies from strong lensing systems*, *JCAP* **11** (2013) 053 [1310.8251].

[62] L. Xu, *Constraints on the holographic dark energy model from type ia supernovae, wmap7, baryon acoustic oscillation, and redshift-space distortion*, *Phys. Rev. D* **87** (2013) 043525.

[63] Z.-P. Huang and Y.-L. Wu, *Cosmological Constraint and Analysis on Holographic Dark Energy Model Characterized by the Conformal-age-like Length*, *Int. J. Mod. Phys. A* **27** (2012) 1250130 [1202.3517].

[64] Z. Zhang, M. Li, X.-D. Li, S. Wang and W.-S. Zhang, *Generalized Holographic Dark Energy and its Observational Constraints*, *Mod. Phys. Lett. A* **27** (2012) 1250115 [1202.5163].

[65] T.-F. Fu, J.-F. Zhang, J.-Q. Chen and X. Zhang, *Holographic Ricci dark energy: Interacting model and cosmological constraints*, *Eur. Phys. J. C* **72** (2012) 1932 [1112.2350].

[66] Y. Wang and L. Xu, *Current observational constraints to the holographic dark energy model with a new infrared cutoff via the markov chain monte carlo method*, *Phys. Rev. D* **81** (2010) 083523.

[67] M. Li, X.-D. Li, S. Wang and X. Zhang, *Holographic dark energy models: A comparison from the latest observational data*, *JCAP* **06** (2009) 036 [0904.0928].

[68] W. Fang, W. Hu and A. Lewis, *Crossing the Phantom Divide with Parameterized Post-Friedmann Dark Energy*, *Phys. Rev. D* **78** (2008) 087303 [0808.3125].

[69] D. W. Hogg, D. J. Eisenstein, M. R. Blanton, N. A. Bahcall, J. Brinkmann, J. E. Gunn et al., *Cosmic homogeneity demonstrated with luminous red galaxies*, *Astrophys. J.* **624** (2005) 54 [astro-ph/0411197].

[70] C. Marinoni, J. Bel and A. Buzzi, *The Scale of Cosmic Isotropy*, *JCAP* **10** (2012) 036 [1205.3309].

[71] Planck collaboration, *Planck 2015 results. XVI. Isotropy and statistics of the CMB*, *Astron. Astrophys.* **594** (2016) A16 [1506.07135].

[72] C.-P. Ma and E. Bertschinger, *Cosmological perturbation theory in the synchronous and conformal newtonian gauges*, *The Astrophysical Journal* **455** (1995) 7.

[73] M. Kunz and D. Sapone, *Crossing the phantom divide*, *Physical Review D* **74** (2006) 123503.

[74] BOSS collaboration, *The clustering of galaxies in the completed SDSS-III Baryon Oscillation Spectroscopic Survey: cosmological analysis of the DR12 galaxy sample*, *Mon. Not. Roy. Astron. Soc.* **470** (2017) 2617 [1607.03155].

[75] F. Beutler, C. Blake, M. Colless, D. H. Jones, L. Staveley-Smith, L. Campbell et al., *The 6df galaxy survey: baryon acoustic oscillations and the local hubble constant*, *Monthly Notices of the Royal Astronomical Society* **416** (2011) 30173032.

[76] A. J. Ross, L. Samushia, C. Howlett, W. J. Percival, A. Burden and M. Manera, *The clustering of the SDSS DR7 main Galaxy sample – I. A 4 per cent distance measure at* $z = 0.15$, *Mon. Not. Roy. Astron. Soc.* **449** (2015) 835 [1409.3242].

[77] Pan-STARRS1 collaboration, *The Complete Light-curve Sample of Spectroscopically Confirmed SNe Ia from Pan-STARRS1 and Cosmological Constraints from the Combined Pantheon Sample*, *Astrophys. J.* **859** (2018) 101 [1710.00845].

[78] R. Arjona, J. García-Bellido and S. Nesseris, *Cosmological constraints on nonadiabatic dark energy perturbations*, *Phys. Rev. D* **102** (2020) 103526 [2006.01762].

[79] B. Audren, J. Lesgourgues, K. Benabed and S. Prunet, *Conservative Constraints on Early Cosmology: an illustration of the Monte Python cosmological parameter inference code*, *JCAP* **1302** (2013) 001 [1210.7183].

[80] T. Brinckmann and J. Lesgourgues, *MontePython 3: boosted MCMC sampler and other features*, *Phys. Dark Univ.* **24** (2019) 100260 [1804.07261].

[81] Planck collaboration, *Planck 2013 results. XVI. Cosmological parameters*, *Astron. Astrophys.* **571** (2014) A16 [1303.5076].

[82] A. Oliveros, M. A. Sabogal and M. A. Acero, *Barrow holographic dark energy with Granda-Oliveros cut-off*, *The European Physical Journal Plus* **137** (2022) [2203.14464].

[83] VIRGO Consortium collaboration, *Stable clustering, the halo model and nonlinear cosmological power spectra*, *Mon. Not. Roy. Astron. Soc.* **341** (2003) 1311 [astro-ph/0207664].

[84] L. R. Abramo, R. C. Batista, L. Liberato and R. Rosenfeld, *Structure formation in the presence of dark energy perturbations*, *JCAP* **11** (2007) 012 [0707.2882].

[85] L. R. Abramo, R. C. Batista, L. Liberato and R. Rosenfeld, *Physical approximations for the nonlinear evolution of perturbations in inhomogeneous dark energy scenarios*, *Phys. Rev. D* **79** (2009) 023516 [0806.3461].

[86] V. Poulin, T. L. Smith, T. Karwal and M. Kamionkowski, *Early dark energy can resolve the hubble tension*, *Phys. Rev. Lett.* **122** (2019) 221301.

[87] J. C. Hill, E. McDonough, M. W. Toomey and S. Alexander, *Early dark energy does not restore cosmological concordance*, *Phys. Rev. D* **102** (2020) 043507.

[88] R. J. Cooke, M. Pettini and C. C. Steidel, *One Percent Determination of the Primordial Deuterium Abundance*, *Astrophys. J.* **855** (2018) 102 [1710.11129].

[89] E. O. Colgáin and M. M. Sheikh-Jabbari, *A critique of holographic dark energy*, *Class. Quant. Grav.* **38** (2021) 177001 [2102.09816].

[90] S. J. Clark, K. Vattis, J. Fan and S. M. Koushiappas, *The H_0 and S_8 tensions necessitate early and late time changes to ΛCDM*, 2110.09562.

[91] V. I. Sabla and R. R. Caldwell, *Microphysics of early dark energy*, *Phys. Rev. D* **106** (2022) 063526 [2202.08291].

[92] W. Cardona, J. B. Orjuela-Quintana and C. A. Valenzuela-Toledo, *An effective fluid description of scalar-vector-tensor theories under the sub-horizon and quasi-static approximations*, *JCAP* **08** (2022) 059 [2206.02895].

IFT-UAM/CSIC-22-127

Using machine learning to compress the matter transfer function $T(k)$

J. Bayron Orjuela-Quintana,[1,2,*] Savvas Nesseris,[2,†] and Wilmar Cardona[3,‡]

[1] *Departamento de Física, Universidad del Valle, Ciudad Universitaria Meléndez, Santiago de Cali 760032, Colombia*

[2] *Instituto de Física Teórica UAM-CSIC, Universidad Autonóma de Madrid, Cantoblanco, 28049 Madrid, Spain*

[3] *ICTP South American Institute for Fundamental Research & Instituto de Física Teórica, Universidade Estadual Paulista, 01140-070, São Paulo, Brazil*

The linear matter power spectrum $P(k,z)$ connects theory with large scale structure observations in cosmology. Its scale dependence is entirely encoded in the matter transfer function $T(k)$, which can be computed numerically by Boltzmann solvers, and can also be computed semi-analytically by using fitting functions such as the well-known Bardeen-Bond-Kaiser-Szalay (BBKS) and Eisenstein-Hu (EH) formulae. However, both the BBKS and EH formulae have some significant drawbacks. On the one hand, although BBKS is a simple expression, it is only accurate up to 10%, which is well above the 1% precision goal of forthcoming surveys. On the other hand, while EH is as accurate as required by upcoming experiments, it is a rather long and complicated expression. Here, we use the Genetic Algorithms (GAs), a particular machine learning technique, to derive simple and accurate fitting formulae for the transfer function $T(k)$. When the effects of massive neutrinos are also considered, our expression slightly improves over the EH formula, while being notably shorter in comparison.

I. INTRODUCTION

Almost two decades ago, the ΛCDM model was designated as the standard model of cosmology [1]. The concordance model is supported by several observations including the angular power spectrum of the cosmic microwave background [2], the distribution of galaxies at large scales [3–5], the late-time accelerated expansion of the Universe [6–8], the acoustic peaks as a fingerprint of the baryon acoustic oscillations in the early Universe [9–11]. These are just some of the many observational tests the ΛCDM model has overcome [12–16].

However, it is fair to mention that there exist some discrepancies in ΛCDM, such as the H_0 and σ_8 tensions [17, 18]. In general, alleviation of any of these tensions and others (see Refs. [18–23]) requires either the introduction of non-standard matter fields [24–26], or modifications to gravity [27–29]. Nonetheless, these theoretical alternatives, although physically viable in light of observations, usually introduce additional parameters, and hence they are not preferred over ΛCDM which is described by only six-parameters and provides an excellent fit to most of available data. In summary, ΛCDM is the simplest and most accurate model we currently have, given that no extensions to this paradigm have been detected so far [30–34].

One of the most important cosmological probes we have in favor of the concordance model is the distribution of galaxies at large scales [35, 36]. In order to contrast our theoretical predictions against these observational data, it is necessary to extract the statistical information in the distribution of the large scale structure by computing the matter power spectrum, $P(k,z)$, which depends on the scale k and the redshift z. It can be shown that at first order in cosmological perturbations, and neglecting neutrinos, the dependence of $P(k,z)$ on k is encoded in the so-called matter transfer function $T(k)$, while the dependence on z is encoded in the growth factor $D_+(z)$ [37]. Therefore, for a fixed redshift, the matter power spectrum is a function only of the scale and its form is mostly described by the matter transfer function (see Sec. II).

The calculation of $P(k,z)$ generally requires to solve the multi-species Boltzmann equations, which can be done numerically in a matter of seconds using Boltzmann solvers, like the codes `CLASS` [38] and `CAMB` [39]. However, to have an accurate analytical description for specific quantities is always desirable. Following this line of thought, Bardeen, Bond, Kaiser, and Szalay found a fitting function for the transfer function considering radiation, baryons, and cold dark matter [40]. This BBKS formula is accurate up to 10% which is well-below the precision of current data [41]. A better alternative is the fitting formula given by Eisenstein and Hu (EH) in Ref. [42]. The EH formula achieves a precision of around 1-2%, however it is given in terms of around 30 different, complicated expressions. These fitting formulae have been extensively used in the literature [43–45].

Machine learning has long been exploited in physics (see Ref. [46] for a review). In particular, machine learning has been used to address symbolic regression problems, i.e., finding an analytical expression that accurately describe a given data set [47–52]. In this work,

* john.orjuela@correounivalle.edu.co
† savvas.nesseris@csic.es
‡ wilmar.cardona@unesp.br

we use a specific machine learning technique known as Genetic Algorithms (GAs). GAs are loosely based on biological evolution concepts. In a nutshell, they attempt to improve the goodness of fit of the candidate expressions by randomly combining them and/or modifying some parts of them [53]. This approach seems to be suitable for finding analytical formulae for quantities of interest in cosmology [54–60]. Here, we use GAs to find analytical functions for the matter transfer function with accuracy of around 1% while being significantly shorter and thus easier to handle than other available formulae.

The organization of this paper is as follows. In Sec. III, we discuss existing fitting functions for the matter transfer function, while some generalities on the GA are given in Sec. IV. Then, we present our results in Sec. V, and in Sec. VI we summarize our conclusions.

II. THE MATTER TRANSFER FUNCTION

As mentioned in Sec. I, on large scales where nonlinearities are negligible, the linear matter power spectrum can be compared against observations of galaxy clustering, and gravitational lensing, among others [61–63]. In the concordance model, the primordial curvature perturbations generated during inflation are related to the gravitational potential at late times by means of two functions: *i*) the matter transfer function $T(k)$ which encodes its scale dependence and describes the evolution of perturbations during horizon crossing and transition from radiation to matter domination, *ii*) the growth factor $D_+(a)$ which describes the time-dependent growth of matter density perturbations at late times. Thus, the gravitational potential can be written as

$$\Phi(k,a) \propto \mathcal{R}(k) T(k) D_+(a), \tag{1}$$

where $\mathcal{R}$ is the primordial curvature perturbation, and a is the scale factor. At late times, for sub-horizon modes, and neglecting massive neutrinos, this gravitational potential can be related to the matter contrast δ_m by means of the Poisson equation:

$$k^2 \Phi(k,a) \propto \rho_m a^2 \delta_m(k,a), \tag{2}$$

where ρ_m is the background density of pressure-less matter. Taking into account that the primordial perturbations are nearly Gaussian with zero mean [14], the linear matter power spectrum can be written as [37]

$$P(k,a) \propto \frac{k^{n_s}}{\Omega_m^2} D_+^2(a) T^2(k), \tag{3}$$

where n_s is the scalar spectral index of primordial fluctuations, and Ω_m is the density parameter of pressure-less matter. Therefore, for a fixed redshift, the power spectrum is given by

$$P(k) \propto k^{n_s} T^2(k), \tag{4}$$

namely, it is fully determined by the transfer function. In this work, we present a very accurate fitting formula for $T(k)$ as a function of the density of baryons and matter, such that it is straightforward to compute the linear matter power spectrum.

As it is well-known from experiments, neutrinos are massive [64, 65]. At sufficiently small scales, free streaming massive neutrinos imprint their effects on the cosmological evolution, which translates to a further suppression of the matter power spectrum. In this case, the growth factor acquires a scale dependency, making nontrivial a similar separation as in Eq. (3). However, for a fixed redshift, it is possible to absorb all the scale dependent effects in an effective matter transfer function, as shown in Ref. [66].

III. PREVIOUS FITTING FORMULAE

Before the advent of fast and accurate Boltzmann solvers, several attempts were made to describe analytically the matter transfer function. One of the most remarkable results of this pursuit is the BBKS formula which is based on previous fitting formulae by Bardeen, Bond, Efstathiou, and Szalay [67–69]. In the case that $\Omega_b \ll \Omega_m$, that is, the main contribution to the matter content is in the form of Cold Dark Matter (CDM), the BBKS formula reads

$$T_{c,\mathrm{BBKS}}(k) \equiv \frac{\ln(1+2.34q)}{2.34q}\Big[1+3.89q + (16.1q)^2 + (5.46q)^3 + (6.71q)^4\Big]^{-1/4}, \tag{5}$$

where

$$q(k) \equiv \frac{k\theta^{1/2}}{(\omega_m - \omega_b)\mathrm{Mpc}^{-1}}, \qquad \theta \equiv \frac{\rho_r}{1.68\rho_\gamma}, \tag{6}$$

and $\omega_X \equiv \Omega_X h^2$ the reduced density parameter (Ω_X being the density parameter of species X), h the reduced Hubble constant, ρ_X the background density, and $X = b,\, c,\, m,\, r,\, \nu,\, \gamma$ denotes baryons, CDM, pressure-less matter, radiation, neutrinos, photons, respectively. When ω_b is not negligible, the transfer function is modified as

$$T_{\mathrm{BBKS}}(k;\omega_b,\omega_m) \equiv T_{c,\mathrm{BBKS}}(k)\left[1+\frac{(kR_{\mathrm{Jr}})^2}{2}\right]^{-1}, \tag{7}$$

where $R_{\mathrm{Jr}} \equiv 1.6(\omega_m - \omega_b)^{-1/2}\,\mathrm{kpc}$.

A more accurate formula was presented by Eisenstein and Hu in Ref. [42]. This formula is constructed from several physically motivated terms, such as acoustic oscillations, Compton drag, velocity overshoot, baryon infall, adiabatic damping, Silk damping, CDM suppression. These terms accurately describe, for instance, the suppression in the transfer function on small scales due to the presence of baryons, and the amplitude and location of baryonic oscillations [42]. All the mentioned effects are taken into account in the EH formula by around 30 expressions, which we present in Appendix A.

The free-streaming scale of massive neutrinos is imprinted in the transfer function, which translates to a further suppression on the smallest scales. In Ref. [66], Eisenstein and Hu provided a fitting formula when baryons, CDM and massive neutrinos are considered. The latter formulation also requires around 30 expressions, which we write in Appendix B.

Although accurate and based on known physics, the EH expressions are, at the end, fitting formulae and not a fundamental result. As we will show, our GA fitting formulae are notably shorter, as accurate as the EH expression when only baryons and CDM are considered, and slightly more accurate when the effects of massive neutrinos are non-negligible. Therefore, our GA provides compelling alternatives to other available fitting formulae.

IV. GENETIC ALGORITHMS

Here we briefly review the GA, which is a stochastic symbolic regression approach. Basically, the symbolic regression problem consists in finding a fitting function for a given dataset, and thus defining a non-parametric approach to describe data. There are several free and commercial codes to perform symbolic regression [47–52]. The GAs have been widely used in several branches of physics, like particle physics [70–72], astrophysics [73, 74], and cosmology [75–80].

In the GA, which is a machine learning technique inspired by concepts in evolutionary biology [53], a population composed by several individuals (mathematical expressions in this case) evolves expecting to optimize the goodness of fit of next generations to a given dataset, which can be measured by a goodness of fit function, usually taken to be a χ^2. Each individual is in turn composed by a selected set of basic operations, i.e., the grammar, which are randomly selected depending on the "nucleotides". These nucleotides are random numbers which in group form the genes setting the mathematical expression of an individual. Once the initial population is created, i.e., the progenitors, the goodness of fit of each individual is measured and, using a tournament scheme, a set containing the best prospects is selected for reproduction and survival to contribute to the next generation.

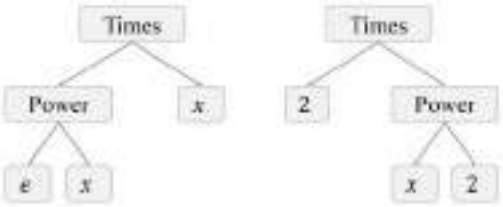

FIG. 1. Two exemplifying grammatical expressions corresponding to the individuals xe^x and $2x^2$.

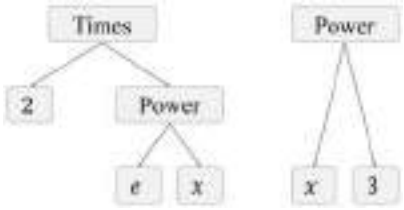

FIG. 2. The two selected individuals have been combined to produce two new individuals: $2e^x$ and x^3.

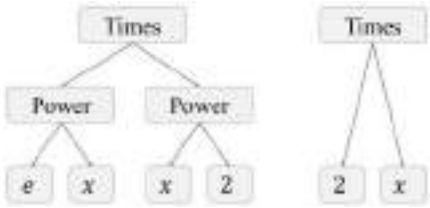

FIG. 3. The two selected individuals have suffered a mutation to become two new individuals: x^2e^x and $2x$.

The reproduction is carried out by the so-called genetic operators, namely, crossover and mutation. In the crossover stage, two individuals are randomly combined to produce new individuals sharing characteristics of both parents. In the mutation stage, one nucleotide of an individual is randomly selected and modified. This process is repeated for a given number of generations.

Now, we describe the way reproduction works in GA with an example. In Fig. 1, there are two expressions in tree representation, i.e., two individuals xe^x and $2x^2$. Let us assume that these individuals were selected for reproduction. Figure 2 shows possible combinations of the two individuals, while Fig. 3 shows their possible mutations. For instance, the new individual in the left-hand side of Fig. 2 is born from the combination of the expressions e^x and 2 from its parents, while the other individual is made from the remaining parts, x and x^2, using the proper basic operation "Times" or product. During the mutation stage, a selected individual is altered randomly. As shown in Fig. 3, for instance, the

	Expression	% Accuracy
BBKS	Eq. (7)	8.70957
EH	Appendix A	0.777504
GA	Eq. (11)	0.815012

TABLE I. Expression and accuracy of the fitting formulae for the matter transfer function as a function of k, ω_b, and ω_m. Although the GA does not provide a more accurate formula than the EH formula, the simplicity of the former [Eq. (11)] is a major improvement over the EH formula (Appendix A).

individual xe^x mutated to x^2e^x, and the individual $2x^2$ mutated to $2x$.

V. RESULTS

In this section, we present our fitting formulae for the matter transfer function. We firstly consider the case when $T(k)$ depends only on the amount of baryons and matter, and then we add the effects of massive neutrinos. For both cases, we start describing how the data for the fitting process was gathered using `CLASS`, and later we proceed to introduce the simple fitting function we found using the GA.

A. Baryons and Matter

1. *Data*

We use the Boltzmann solver `CLASS` to compute the linear matter transfer function[1] $T(k)$. In this code, each pair of parameters $\{\omega_b, \omega_m\}$ defines a cosmology for which we can compute the gravitational potential Φ as a function of the scale k at a fixed redshift. Hence, to see the dependence of the transfer function on these parameters, we make a grid of 4×4 pairs of $\{\omega_b, \omega_m\}$ and compute the gravitational potential for each pair. We consider that $\omega_b \in [0.0214, 0.0234]$, and $\omega_m \in [0.13, 0.15]$, which are around 10σ from the best-fit values found by the Planck Collaboration [2]. For each considered cosmology (16 in total), `CLASS` retrieves 114 points $\{k, \Phi\}$. Therefore, our preliminary dataset is composed by 1824 points whose rows are given as $\{k, \omega_b, \omega_m, \Phi\}$. Now, since the transfer function is basically the normalized potential, we normalize each of the 16 sub-datasets to get $T(k; \omega_b, \omega_m)$. At the end, our final dataset is a table of dimensions 1824×4 with data points given as $\{k, \omega_b, \omega_m, T\}$.

We quantify the goodness of fit of a given analytical expression by the following function

$$\%\text{Acc} = \frac{100}{N}\sum_{i=1}^{N}\left|\frac{T_{i,\text{CLASS}} - T_{i,\text{analytical}}}{T_{i,\text{CLASS}}}\right|, \qquad (8)$$

where $N = 1824$ is the number of data points in our dataset, and T_i is a simplified notation for the transfer function evaluated at k_i, ω_{b_i}, and ω_{m_i}.

2. *Fitting Formula from the GA*

Here, we give a few details concerning the specific GA configuration we used and present our fitting formula.

As explained in Sec. IV, the GA looks for a fitting formula to a dataset by evolving the population, which is composed by expressions combining specific operations (grammar) and coefficients. Schematically, our GA is searching for a function of the form

$$T_{\text{GA}}(x) \equiv [1 + f_{\text{GA}}(x)]^{-1/4}, \qquad (9)$$

where

$$x \equiv \frac{k\,\text{Mpc}}{\omega_m - \omega_b}, \quad f_{\text{GA}} \equiv \sum_{i=1}^{4} a_i g_i\left((b_i x)^{c_i}\right). \qquad (10)$$

We see that x is a dimensionless quantity since k is given in units $[h\,\text{Mpc}^{-1}]$, h the reduced Hubble parameter. The constants a_i, b_i, c_i are non-negative random numbers, and g_i is an operation in the grammar set, which we consider to be simply of the form $\{x\}$. The quantities a_i, g_i, b_i, and c_i are the 4 nucleotides. The sum goes from 1 to 4 because we are considering that the genome of the individuals is formed by 4 genes, each one composed by the 4 nucleotides, such that the chromosomes are 4×4 matrices. This configuration, although restrictive, fixes the length of the expressions, thus avoiding over-fitting problems. A couple of reasons motivate the specific forms of Eqs. (9) and (10): *i*) the transfer function has specific limits: $T \to 0$ when $k \to \infty$, and $T \to 1$ when $k \to 0$, *ii*) the transfer function only takes on non-negative values, and *iii*) $T(k)$ is smooth.

Now, we present our fitting formula when only baryons and matter are considered. Using the configuration of the GA as explained, the stochastic search ended up with the function

[1] Note that `CLASS` can take into account non-linear effects via fitting functions such as HALOFIT [81]. Here however we focus on the linear regime and neglect non-linear contributions when generating the data.

$$T_{\rm GA}(k;\omega_b,\omega_m) = \left[1 + 59.0998\,x^{1.49177} + 4658.01\,x^{4.02755} + 3170.79\,x^{6.06} + 150.089\,x^{7.28478}\right]^{-1/4}, \qquad (11)$$

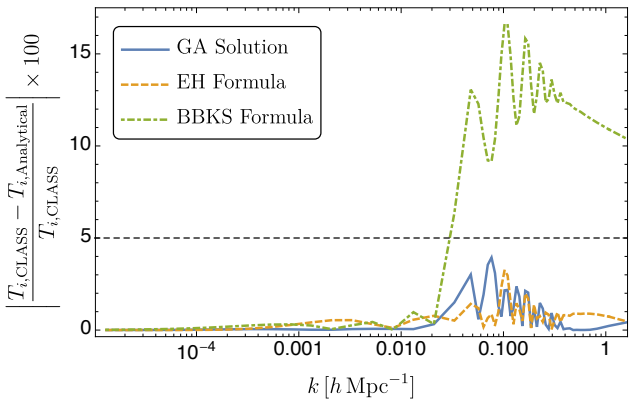

FIG. 4. Accuracy of the BBKS (green dot-dashed line), EH (mustard dashed line), and the GA (blue solid line) fitting formulae as a function of the scale k. The parameters for these plots are: $\omega_b = 0.02273$, and $\omega_m = 0.1366$. Note that the accuracy of the three formulae notably decrease on the scales where the effects of baryons are most prominent on the cosmological evolution. However, the accuracy of the EH and GA formulae are below 5% in this scale.

whose goodness of fit, as measured by Eq. (8), is $\%\mathrm{Acc}_{\rm GA} = 0.815012$. The accuracy of the BBKS formula in Eq. (7) is $\%\mathrm{Acc}_{\rm BBKS} = 8.70957$, and for the EH formula is $\%\mathrm{Acc}_{\rm EH} = 0.777504$. We compile these results in Table I. In Fig. 4, we compare the performance of the fitting formulae. As it can be seen, the three formulae are very accurate on the large scales ($k < 0.01h\,\mathrm{Mpc}^{-1}$), while for smaller scales ($k > 0.01h\,\mathrm{Mpc}^{-1}$), where the effects of baryons are most prominent on the cosmological evolution, the accuracy of the three formulae decrease. However, we note that our GA formula and the EH formula can be accurate up to 5%, while the BBKS formula is accurate up to 18% in these scales. We would like to emphasize that our GA formula in Eq. (11) is remarkably simpler than the EH formula which is described by around 30 expressions which occupy the whole Appendix A, while their difference in accumulative accuracy is just about 0.04. We also want to stress that, in principle, the GA could get even better results if some modifications are introduced. For instance, a larger grammar set and a more complex $f_{\rm GA}$ function [instead of Eq. (10)]. Nonetheless, our choices avoid over-fitting while yielding a smooth transfer function with the correct limits in k.

B. Baryons, Matter and Massive Neutrinos

1. *Data*

Apart of baryons and cold dark matter, massive neutrinos can contribute to the matter content once they are freely streaming. We can take into account the effects of massive neutrinos in the matter transfer function using `CLASS`. We compute $T(k)$ at redshift zero as a function of ω_b, ω_m in the same ranges as in Sec. V A, and $\omega_\nu \equiv 0.0107(\sum_\nu m_\nu/1.0\,\mathrm{eV})$, assuming just one massive neutrino, and that the total mass of massive neutrinos is in the range $0.06\,\mathrm{eV} \leq \sum m_\nu \leq 0.12\,\mathrm{eV}$. The lower bound of the later constraint corresponds to the minimum mass allowed from neutrino flavour oscillation experiments [64], and the upper bound is the maximum mass value allowed by Planck [2]. In this case, we get a grid of $4 \times 4 \times 4$ data points for $\{\omega_b, \omega_m, \omega_\nu\}$ and compute the gravitational potential for each triad. Again, for each considered cosmology (64 in total), `CLASS` retrieves 114 points $\{k, \Phi\}$. Normalizing the potential to get the transfer function, our final data set is a table of dimensions 7296×5 with data points given as $\{k, \omega_b, \omega_m, \omega_\nu, T\}$. We use Eq. (8) to quantify the goodness of fit of the analytical expressions, but now $N = 7296$ is the number of data points in our dataset, and T_i is the transfer function evaluated at k_i, ω_{b_i}, ω_{m_i}, and ω_{ν_i}.

2. *Fitting Formula from the GA*

Based on the success of the GA in finding an accurate formula for $T(k)$ when neutrinos are massless, this time our GA is looking for a function of the form

$$T_{\rm GA}(y) \equiv \left[1 + f_{\rm GA}(y)\right]^{-1/4}, \qquad (12)$$

where

$$y \equiv \frac{k\,\mathrm{Mpc}}{\omega_m - \omega_b + \omega_\nu}, \quad f_{\rm GA} \equiv \sum_{i=1}^{4} a_i g_i\left((b_i y)^{c_i}\right). \qquad (13)$$

Now, we present our fitting formula which considers baryons, matter, and one massive neutrino:

$$T_{\rm GA}(k;\omega_b,\omega_m) = \left[1 + 56.4933\, y^{1.48261} + 3559.23\, y^{3.76407} + 4982.44\, y^{5.68246} + 374.167\, y^{7.14558}\right]^{-1/4}, \qquad (14)$$

	Expression	% Accuracy
EH	Appendix B	1.23449
GA	Eq. (14)	0.993916

TABLE II. Expression and accuracy of the fitting formulae for the matter transfer function as a function of k, ω_b, ω_m, and ω_ν. Although the accuracy of both formulations are similar, the simplicity of the GA function in Eq. (14) is a major improvement over the EH formula, which is fully displayed in Appendix B.

whose goodness of fit, as measured by Eq. (8), is $\%\mathrm{Acc}_{\rm GA} = 0.993916$. The accuracy of the extended EH formula considering massive neutrinos is $\%\mathrm{Acc}_{\rm EH} = 1.23449$. We compile these results in Table II. In Fig. 5, we compare the performance of the fitting formulae. Similar to the last section, the formulae are more accurate on large scales ($k < 0.01h\,\mathrm{Mpc}^{-1}$) than on the smaller scales ($k > 0.01h\,\mathrm{Mpc}^{-1}$). Note that the accuracy of the GA formula is below the 5% in the whole range of k. Furthermore, the GA formula (14) is significantly simpler than the EH formula, whose description requires around 30 expression which we give in full in Appendix B. Our result is a compelling analytical alternative to compute the matter transfer function.

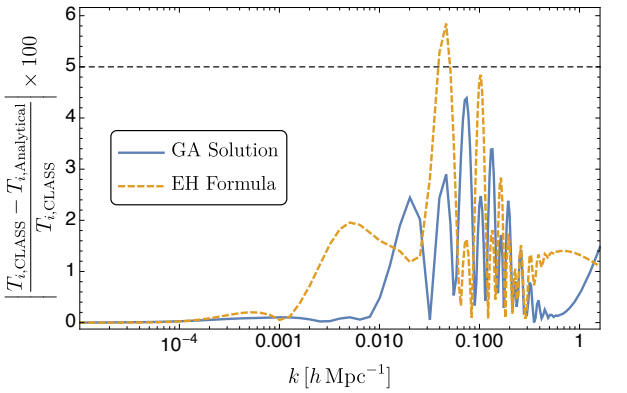

FIG. 5. Accuracy of the EH (mustard dashed line), and the GA (blue solid line) fitting formulae as a function of the scale k. The parameters for these plots are: $\omega_b = 0.02206$, $\omega_m = 0.1499$, and $\omega_\nu = 0.0008599$ which corresponds to a mass of $\sum_\nu m_\nu = 0.08\,\mathrm{eV}$. As can be seen, the accuracy of the GA formula is below 5% on the whole range of k considered here.

VI. CONCLUSIONS

Genetic Algorithms (GAs), a machine learning technique, have been previously used to obtain improved formulation of cosmological quantities of interest such as the redshift at recombination and the sound horizon at drag epoch [58], and also to perform consistency tests to probe for deviations from ΛCDM [32, 55, 56, 59, 60, 82, 83]. Here we used the GA to find analytical alternatives to existing fitting functions for the matter transfer function, such as the BBKS and the EH formulae.

When the transfer function depends only on ω_b and ω_m, the GA finds a very simple fitting formula for $T(k)$ [see Eq. (11)], which is as accurate as the EH formula, while being significantly shorter (see Appendix A). In a more realistic scenario, at least one neutrino should be massive. In this case, our GA finds a fitting function which is both more accurate and notably simpler [see Eq. (14)] than the EH formula in Appendix B. The simplicity of the GA fitting formulae and their accuracy represent a major improvement over other existing analytical formulations of the matter transfer function which are extensively used in the literature [43–45]. Therefore, the GA formulae in Eqs. (11) and (14) are compelling semi-analytic alternatives to easily and accurately compute the matter power spectrum.

ACKNOWLEDGEMENTS

The authors would like to thank R. Arjona for useful discussions at a very early stage of this project, and also to Jose Palacios for carefully reading the manuscript and providing useful comments. BOQ would like to express his gratitude to the Instituto de Física Téorica UAM-CSIC, in Universidad Autonóma de Madrid, for the hospitality and kind support during all the stages of this work. BOQ is also supported by Patrimonio Autónomo - Fondo Nacional de Financiamiento para la Ciencia, la Tecnología y la Innovación Francisco José de Caldas (MINCIENCIAS - COLOMBIA) Grant No. 110685269447 RC-80740-465-2020, projects 69723 and 69553. WC acknowledges financial support from the São Paulo Research Foundation (FAPESP) through grant #2021/10290-2. This research was supported by resources supplied by the Center for Scientific Computing (NCC/GridUNESP) of the São Paulo State University (UNESP). SN acknowl-

edges support from the research projects PGC2018-094773-B-C32 and PID2021-123012NB-C43, and by the Spanish Research Agency (Agencia Estatal de Investigación) through the Grant IFT Centro de Excelencia Severo Ochoa No CEX2020-001007-S, funded by MCIN/AEI/10.13039/501100011033.

NUMERICAL CODES

The genetic algorithm code used here can be found in the GitHub repository https://github.com/BayronO/Transfer-Function-GA of BOQ. This code is based on the GA code by SN which can be found at https://github.com/snesseris/Genetic-Algorithms.

Appendix A: EH Formula

The transfer function given by Eisenstein and Hu [42] has the following form:

$$T(k) = \frac{\Omega_b}{\Omega_0} T_b(k) + \frac{\Omega_c}{\Omega_0} T_c(k), \tag{A1}$$

where $\Omega_0 = \Omega_b + \Omega_c$. The terms involved in this formula are the following:

$$T_b = \left[\frac{\tilde{T}_0(k;1,1)}{1+(ks/5.2)^2} + \frac{\alpha_b}{1+(\beta_b/ks)^3} e^{-\left(\frac{k}{k_{\rm Silk}}\right)^{1.4}} \right] j_0(k\tilde{s}), \tag{A2}$$

$$T_c = f\tilde{T}_0(k,1,\beta_c) + (1-f)\tilde{T}_0(k,\alpha_c,\beta_c), \tag{A3}$$

$$\tilde{T}_0(k,\alpha_c,\beta_c) = \frac{\ln(e+1.8\beta_c q)}{\ln(e+1.8\beta_c q) + Cq^2}, \tag{A4}$$

$$f = \frac{1}{1+(ks/5.4)^4}, \tag{A5}$$

$$C = \frac{14.2}{\alpha_c} + \frac{386}{1+69.9q^{1.08}}, \tag{A6}$$

$$q = \frac{k}{13.41 k_{\rm eq}}, \tag{A7}$$

$$R \equiv 3\rho_b/4\rho_\gamma = 31.5\omega_b \Theta_{2.7}^{-4}(z/10^3)^{-1}, \tag{A8}$$

$$k_{\rm Silk} = 1.6\omega_b^{0.52}\omega_0^{0.73}\left[1+(10.4\,\omega_0)^{-0.95}\right]\ {\rm Mpc}^{-1}, \tag{A9}$$

$$k_{\rm eq} = 7.46\times10^{-2}\omega_0\Theta_{2.7}^{-2}\,{\rm Mpc}^{-1}, \tag{A10}$$

$$\alpha_b = 2.07 k_{\rm eq} s (1+R_d)^{-3/4} G\left(\frac{1+z_{\rm eq}}{1+z_d}\right), \tag{A11}$$

$$\beta_b = 0.5 + \frac{\Omega_b}{\Omega_0} + \left(3 - 2\frac{\Omega_b}{\Omega_0}\right)\sqrt{(17.2\,\omega_0)^2+1}, \tag{A12}$$

$$\beta_{\rm node} = 8.41\omega_0^{0.435}, \tag{A13}$$

$$s = \frac{2}{3k_{\rm eq}}\sqrt{\frac{6}{R_{\rm eq}}}\ln\frac{\sqrt{1+R_d}+\sqrt{R_d+R_{\rm eq}}}{1+\sqrt{R_{\rm eq}}}, \tag{A14}$$

$$\tilde{s} = s\left[1+\left(\frac{\beta_{\rm node}}{ks}\right)^3\right]^{-1/3}, \tag{A15}$$

$$G(y) = -6y\sqrt{1+y} + y(2+3y)\ln\left(\frac{\sqrt{1+y}+1}{\sqrt{1+y}-1}\right), \tag{A16}$$

$$y \equiv \frac{1+z_{\rm eq}}{1+z}, \tag{A17}$$

$$\alpha_c = a_1^{-\Omega_b/\Omega_0} a_2^{-(\Omega_b/\Omega_0)^3}, \tag{A18}$$

$$a_1 = (46.9\omega_0)^{0.670}[1+(32.1\omega_0)^{-0.532}], \tag{A19}$$

$$a_2 = (12.0\omega_0)^{0.424}[1+(45.0\omega_0)^{-0.582}], \tag{A20}$$

$$\beta_c^{-1} = 1 + b_1[(\Omega_c/\Omega_0)^{b_2}-1], \tag{A21}$$

$$b_1 = 0.944[1+(458\omega_0)^{-0.708}]^{-1}, \tag{A22}$$

$$b_2 = (0.395\omega_0)^{-0.0266}. \tag{A23}$$

$$z_{\rm eq} = 2.50\times10^4\omega_0\Theta_{2.7}^{-4}, \tag{A24}$$

$$z_d = 1291\frac{\omega_0^{0.251}}{1+0.659\omega_0^{0.828}}\left[1+b_{1,z}\omega_b^{b_{2,z}}\right], \tag{A25}$$

$$b_{1,z} = 0.313\omega_0^{-0.419}\left[1+0.607\omega_0^{0.674}\right], \tag{A26}$$

$$b_{2,z} = 0.238\omega_0^{0.223}, \tag{A27}$$

where we have defined $\omega_0 = (\Omega_c+\Omega_b)h^2$, and $T_{\rm CMB} \equiv 2.7\Theta_{2.7}\,{\rm K}$, $R_d \equiv R(z_d)$ and $R_{\rm eq} \equiv R(z_{\rm eq})$

Appendix B: EH Formula with Massive Neutrinos

The transfer function given by Eisenstein and Hu considering massive neutrinos has the following form [66]:

$$T_{cb\nu}(k,z) = T_{\rm master}(k)\frac{D_{cb\nu}(k,z)}{D_1(z)}, \tag{B1}$$

The terms involved in this formula are the following:

$$T_{\rm master}(k) = T_{\rm sup}(k)B(k), \tag{B2}$$

$$D_{cb\nu}(z,q) = \left[f_{cb}^{0.7/p_{cb}} + \left(\frac{D_1(z)}{1+y_{\rm fs}(q;f_\nu)}\right)^{0.7}\right]^{p_{cb}/0.7} \times D_1(z)^{1-p_{cb}}, \tag{B3}$$

$$D_1(z) = \left(\frac{1+z_{eq}}{1+z}\right)\frac{5\Omega(z)}{2}\left\{\Omega(z)^{4/7} - \Omega_\Lambda(z) + \left[1+\frac{\Omega(z)}{2}\right]\left[1+\frac{\Omega_\Lambda(z)}{70}\right]\right\}^{-1}, \tag{B4}$$

$$\Omega(z) = \Omega_0(1+z)^3 g^{-2}(z), \tag{B5}$$

$$\Omega_\Lambda(z) = \Omega_\Lambda g^{-2}(z), \tag{B6}$$

$$g^2(z) = (1-\Omega_0-\Omega_\Lambda)(1+z)^2 + \Omega_0(1+z)^3 + \Omega_\Lambda, \tag{B7}$$

$$T_{\rm sup}(k) = \frac{L}{L+Cq_{\rm eff}^2}, \tag{B8}$$

$$L = \ln(e+1.84\beta_c\sqrt{\alpha_\nu}q_{\rm eff}), \tag{B9}$$

$$C = 14.4 + \frac{325}{1+60.5q_{\rm eff}^{1.08}}, \tag{B10}$$

$$\beta_c = (1-0.949f_{\nu b})^{-1}, \tag{B11}$$

$$y_{\rm fs}(q) = 17.2f_\nu(1+0.488f_\nu^{-7/6})(qN_\nu/f_\nu)^2, \tag{B12}$$

$$q = \frac{k}{\rm Mpc^{-1}}\Theta_{2.7}^2\omega_0^{-1}, \tag{B13}$$

$$B(k) = 1 + \frac{1.24f_\nu^{0.64}N_\nu^{0.3+0.6f_\nu}}{q_\nu^{-1.6}+q_\nu^{0.8}}, \tag{B14}$$

$$q_\nu = 3.92q\sqrt{\frac{N_\nu}{f_\nu}} \tag{B15}$$

$$f_c = \frac{\Omega_b}{\Omega_m+\Omega_\nu}, \quad f_\nu = \frac{\Omega_\nu}{\Omega_m+\Omega_\nu}, \quad f_{cb} = \frac{\Omega_m}{\Omega_m+\Omega_\nu}, \quad f_{\nu b} = \frac{\Omega_b+\Omega_\nu}{\Omega_m+\Omega_\nu}, \tag{B16}$$

$$q_{\rm eff} = \frac{k\Theta_{2.7}^2}{\Gamma_{\rm eff}\,\rm Mpc^{-1}}, \tag{B17}$$

$$\Gamma_{\rm eff} = \omega_0\left[\sqrt{\alpha_\nu} + \frac{1-\sqrt{\alpha_\nu}}{1+(0.43ks)^4}\right], \tag{B18}$$

$$\alpha_\nu = \frac{f_c}{f_{cb}}\frac{5-2(p_c+p_{cb})}{5-4p_{cb}} \times \frac{1-0.553f_{\nu b}+0.126f_{\nu b}^3}{1-0.193\sqrt{f_\nu N_\nu}+0.169f_\nu N_\nu^{0.2}}(1+y_d)^{p_{cb}-p_c} \times \left[1+\frac{p_c-p_{cb}}{2}\left(1+\frac{1}{(3-4p_c)(7-4p_{cb})}\right)\times(1+y_d)^{-1}\right], \tag{B19, B20}$$

$$p_c \equiv \frac{1}{4}\left[5-\sqrt{1+24f_c}\right], \tag{B21}$$

$$p_{cb} \equiv \frac{1}{4}\left[5-\sqrt{1+24f_{cb}}\right], \tag{B22}$$

$$z_{\rm eq} = 2.50\times10^4\omega_0\Theta_{2.7}^{-4}, \tag{B23}$$

$$z_d = 1291\frac{\omega_0^{0.251}}{1+0.659\omega_0^{0.828}}\left[1+b_{1,z}\omega_b^{b_{2,z}}\right], \tag{B24}$$

$$b_1 = 0.313\omega_0^{-0.419}\left[1+0.607\omega_0^{0.674}\right], \tag{B25}$$

$$b_2 = 0.238\omega_0^{0.223}, \tag{B26}$$

$$y \equiv \frac{1+z_{\rm eq}}{1+z}, \tag{B27}$$

$$s = \frac{44.5\ln(9.83\omega_0)}{\sqrt{1+10\omega_b^{3/4}}}\,\rm Mpc, \tag{B28}$$

where N_ν is the number of massive neutrinos, Ω_Λ is the density parameter of cosmological constant, and we have redefine some terms like $\Omega_0 = \Omega_c + \Omega_b + \Omega_\nu$, and $\omega_0 = \Omega_0 h^2$.

[1] P. J. E. Peebles, *Cosmology's Century: An Inside History of Our Modern Understanding of the Universe*. Princeton University Press, 2020.

[2] **Planck** Collaboration, N. Aghanim *et al.*, "Planck 2018 results. VI. Cosmological parameters," *Astron. Astrophys.* **641** (2020) A6, arXiv:1807.06209 [astro-ph.CO]. [Erratum: Astron.Astrophys. 652, C4 (2021)].

[3] **DES** Collaboration, M. A. Troxel *et al.*, "Dark Energy Survey Year 1 results: Cosmological constraints from cosmic shear," *Phys. Rev. D* **98** no. 4, (2018) 043528, arXiv:1708.01538 [astro-ph.CO].

[4] **DES** Collaboration, T. M. C. Abbott *et al.*, "Dark Energy Survey Year 1 Results: Constraints on Extended Cosmological Models from Galaxy Clustering and Weak Lensing," *Phys. Rev. D* **99** no. 12, (2019) 123505, arXiv:1810.02499 [astro-ph.CO].

[5] **DES** Collaboration, T. M. C. Abbott *et al.*, "Dark Energy Survey Year 3 results: Cosmological

constraints from galaxy clustering and weak lensing," *Phys. Rev. D* **105** no. 2, (2022) 023520, arXiv:2105.13549 [astro-ph.CO].

[6] **Supernova Search Team** Collaboration, A. G. Riess *et al.*, "Observational evidence from supernovae for an accelerating universe and a cosmological constant," *Astron. J.* **116** (1998) 1009–1038, arXiv:astro-ph/9805201.

[7] **Supernova Cosmology Project** Collaboration, S. Perlmutter *et al.*, "Measurements of Ω and Λ from 42 high redshift supernovae," *Astrophys. J.* **517** (1999) 565–586, arXiv:astro-ph/9812133.

[8] **Supernova Search Team** Collaboration, A. G. Riess *et al.*, "Type Ia supernova discoveries at z > 1 from the Hubble Space Telescope: Evidence for past deceleration and constraints on dark energy evolution," *Astrophys. J.* **607** (2004) 665–687, arXiv:astro-ph/0402512.

[9] W. percival *et al.*, "Baryon acoustic oscillations in the Sloan Digital Sky Survey Data Release 7 galaxy sample," *Monthly Notices of the Royal Astronomical Society* **401** no. 4, (2010) 2148–2168.

[10] C. Blake *et al.*, "The WiggleZ Dark Energy Survey: mapping the distance-redshift relation with baryon acoustic oscillations," *Monthly Notices of the Royal Astronomical Society* **418** no. 3, (2011) 1707–1724.

[11] E. Aubourg *et al.*, "Cosmological implications of baryon acoustic oscillation measurements," *Phys. Rev. D* **92** no. 12, (2015) 123516, arXiv:1411.1074 [astro-ph.CO].

[12] **Boomerang** Collaboration, P. de Bernardis *et al.*, "A Flat universe from high resolution maps of the cosmic microwave background radiation," *Nature* **404** (2000) 955–959, arXiv:astro-ph/0004404.

[13] A. H. Jaffe *et al.*, "Recent results from the maxima experiment," *New Astron. Rev.* **47** (2003) 727–732, arXiv:astro-ph/0306504.

[14] **Planck** Collaboration, Y. Akrami *et al.*, "Planck 2018 results. X. Constraints on inflation," *Astron. Astrophys.* **641** (2020) A10, arXiv:1807.06211 [astro-ph.CO].

[15] **Planck** Collaboration, Y. Akrami *et al.*, "Planck 2018 results. VII. Isotropy and Statistics of the CMB," *Astron. Astrophys.* **641** (2020) A7, arXiv:1906.02552 [astro-ph.CO].

[16] **DES** Collaboration, T. M. C. Abbott *et al.*, "Cosmological Constraints from Multiple Probes in the Dark Energy Survey," *Phys. Rev. Lett.* **122** no. 17, (2019) 171301, arXiv:1811.02375 [astro-ph.CO].

[17] A. G. Riess *et al.*, "Large Magellanic Cloud Cepheid Standards Provide a 1% Foundation for the Determination of the Hubble Constant and Stronger Evidence for Physics beyond ΛCDM," *Astrophys. J.* **876** no. 1, (2019) 85, arXiv:1903.07603 [astro-ph.CO].

[18] E. Abdalla *et al.*, "Cosmology intertwined: A review of the particle physics, astrophysics, and cosmology associated with the cosmological tensions and anomalies," *JHEAp* **34** (2022) 49–211, arXiv:2203.06142 [astro-ph.CO].

[19] A. Joyce, L. Lombriser, and F. Schmidt, "Dark Energy Versus Modified Gravity," *Ann. Rev. Nucl. Part. Sci.* **66** (2016) 95–122, arXiv:1601.06133 [astro-ph.CO].

[20] E. Di Valentino *et al.*, "In the realm of the Hubble tension — a review of solutions," *Class. Quant. Grav.* **38** no. 15, (2021) 153001, arXiv:2103.01183 [astro-ph.CO].

[21] L. Heisenberg, H. Villarrubia-Rojo, and J. Zosso, "Simultaneously solving the H_0 and σ_8 tensions with late dark energy," arXiv:2201.11623 [astro-ph.CO].

[22] L. Perivolaropoulos and F. Skara, "Challenges for ΛCDM: An update," *New Astron. Rev.* **95** (2022) 101659, arXiv:2105.05208 [astro-ph.CO].

[23] W. Cardona and M. A. Sabogal, "Holographic energy density, dark energy sound speed, and tensions in cosmological parameters: H_0 and S_8," arXiv:2210.13335 [astro-ph.CO].

[24] R.-Y. Guo, J.-F. Zhang, and X. Zhang, "Can the H_0 tension be resolved in extensions to ΛCDM cosmology?," *JCAP* **02** (2019) 054, arXiv:1809.02340 [astro-ph.CO].

[25] P. Agrawal, F.-Y. Cyr-Racine, D. Pinner, and L. Randall, "Rock 'n' Roll Solutions to the Hubble Tension," arXiv:1904.01016 [astro-ph.CO].

[26] L. Heisenberg and H. Villarrubia-Rojo, "Proca in the sky," *JCAP* **03** (2021) 032, arXiv:2010.00513 [astro-ph.CO].

[27] T. Clifton, P. G. Ferreira, A. Padilla, and C. Skordis, "Modified Gravity and Cosmology," *Phys. Rept.* **513** (2012) 1–189, arXiv:1106.2476 [astro-ph.CO].

[28] L. Heisenberg, R. Kase, and S. Tsujikawa, "Cosmology in scalar-vector-tensor theories," *Phys. Rev. D* **98** no. 2, (2018) 024038, arXiv:1805.01066 [gr-qc].

[29] W. Cardona, J. B. Orjuela-Quintana, and C. A. Valenzuela-Toledo, "An effective fluid description of scalar-vector-tensor theories under the sub-horizon and quasi-static approximations," *JCAP* **08** no. 08, (2022) 059, arXiv:2206.02895 [astro-ph.CO].

[30] A. Heavens *et al.*, "No evidence for extensions to the standard cosmological model," *Phys. Rev. Lett.* **119** no. 10, (2017) 101301, arXiv:1704.03467 [astro-ph.CO].

[31] S. Singh *et al.*, "On the detection of a cosmic dawn signal in the radio background," arXiv:2112.06778 [astro-ph.CO].

[32] R. Arjona, A. Melchiorri, and S. Nesseris, "Testing the ΛCDM paradigm with growth rate data and machine learning," *JCAP* **05** no. 05, (2022) 047, arXiv:2107.04343 [astro-ph.CO].

[33] **Euclid** Collaboration, D. Camarena *et al.*, "Euclid: Testing the Copernican principle with next-generation surveys," arXiv:2207.09995 [astro-ph.CO].

[34] W. Cardona, R. Arjona, A. Estrada, and S. Nesseris, "Cosmological constraints with the Effective Fluid approach for Modified Gravity," *JCAP* **05** (2021) 064, arXiv:2012.05282 [astro-ph.CO].

[35] **SDSS** Collaboration, M. Tegmark *et al.*, "The 3-D power spectrum of galaxies from the SDSS," *Astrophys. J.* **606** (2004) 702–740, arXiv:astro-ph/0310725.

[36] **BOSS** Collaboration, S. Alam *et al.*, "The clustering of galaxies in the completed SDSS-III Baryon Oscillation Spectroscopic Survey: cosmological analysis of the DR12 galaxy sample," *Mon. Not. Roy. Astron. Soc.* **470** no. 3, (2017) 2617–2652, arXiv:1607.03155 [astro-ph.CO].

[37] S. Dodelson and F. Schmidt, *Modern Cosmology*. Elsevier Science, 2020.

[38] D. Blas, J. Lesgourgues, and T. Tram, "The Cosmic Linear Anisotropy Solving System (CLASS). Part II: Approximation schemes," *Journal of Cosmology and Astroparticle Physics* **2011** no. 07, 034–034.

[39] A. Lewis, A. Challinor, and A. Lasenby, "Efficient computation of CMB anisotropies in closed FRW models," *Astrophys. J.* **538** (2000) 473–476, arXiv:astro-ph/9911177.

[40] J. M. Bardeen, J. R. Bond, N. Kaiser, and A. S. Szalay, "The Statistics of Peaks of Gaussian Random Fields," *Astrophys. J.* **304** (1986) 15–61.

[41] M. S. Turner, "The Road to Precision Cosmology," arXiv:2201.04741 [astro-ph.CO].

[42] D. J. Eisenstein and W. Hu, "Baryonic features in the matter transfer function," *Astrophys. J.* **496** (1998) 605, arXiv:astro-ph/9709112.

[43] D. Boyanovsky, H. J. de Vega, and N. G. Sanchez, "The dark matter transfer function: free streaming, particle statistics and memory of gravitational clustering," *Phys. Rev. D* **78** (2008) 063546, arXiv:0807.0622 [astro-ph].

[44] A. Dvornik *et al.*, "KiDS-1000: Combined halo-model cosmology constraints from galaxy abundance, galaxy clustering and galaxy-galaxy lensing," arXiv:2210.03110 [astro-ph.CO].

[45] N. Schöneberg, L. Verde, H. Gil-Marín, and S. Brieden, "BAO+BBN revisited – Growing the Hubble tension with a 0.7km/s/Mpc constraint," arXiv:2209.14330 [astro-ph.CO].

[46] G. Carleo *et al.*, "Machine learning and the physical sciences," *Rev. Mod. Phys.* **91** no. 4, (2019) 045002, arXiv:1903.10563 [physics.comp-ph].

[47] M. Schmidt and H. Lipson, "Distilling Free-Form Natural Laws from Experimental Data," *Science* **324** (2009) 81–85.

[48] S. L. Brunton, J. L. Proctor, and J. N. Kutz, "Discovering governing equations from data by sparse identification of nonlinear dynamical systems," *Proceedings of the National Academy of Sciences* **113** no. 15, (2016) 3932–3937, arXiv:1509.03580 [math.DS].

[49] D. Izzo, F. Biscani, and A. Mereta, "Differentiable Genetic Programming," *arXiv e-prints* (2016) , arXiv:1611.04766 [cs.NE].

[50] S.-M. Udrescu and M. Tegmark, "AI Feynman: a Physics-Inspired Method for Symbolic Regression," *Sci. Adv.* **6** no. 16, (2020) eaay2631, arXiv:1905.11481 [physics.comp-ph].

[51] M. Cranmer *et al.*, "Discovering Symbolic Models from Deep Learning with Inductive Biases," arXiv:2006.11287 [cs.LG].

[52] Z. Liu and M. Tegmark, "Machine Learning Hidden Symmetries," *Phys. Rev. Lett.* **128** no. 18, (2022) 180201, arXiv:2109.09721 [cs.LG].

[53] J. Koza and J. Koza, *Genetic Programming: On the Programming of Computers by Means of Natural Selection*. Bradford, 1992.

[54] R. Arjona and S. Nesseris, "Hints of dark energy anisotropic stress using Machine Learning," *JCAP* **11** (2020) 042, arXiv:2001.11420 [astro-ph.CO].

[55] **EUCLID** Collaboration, M. Martinelli *et al.*, "Euclid: Forecast constraints on the cosmic distance duality relation with complementary external probes," *Astron. Astrophys.* **644** (2020) A80, arXiv:2007.16153 [astro-ph.CO].

[56] R. Arjona and S. Nesseris, "Novel null tests for the spatial curvature and homogeneity of the Universe and their machine learning reconstructions," *Phys. Rev. D* **103** no. 10, (2021) 103539, arXiv:2103.06789 [astro-ph.CO].

[57] **Euclid** Collaboration, M. Martinelli *et al.*, "Euclid: Constraining dark energy coupled to electromagnetism using astrophysical and laboratory data," *Astron. Astrophys.* **654** (2021) A148, arXiv:2105.09746 [astro-ph.CO].

[58] A. Aizpuru, R. Arjona, and S. Nesseris, "Machine learning improved fits of the sound horizon at the baryon drag epoch," *Phys. Rev. D* **104** no. 4, (2021) 043521, arXiv:2106.00428 [astro-ph.CO].

[59] **Euclid** Collaboration, S. Nesseris *et al.*, "Euclid: Forecast constraints on consistency tests of the ΛCDM model," *Astron. Astrophys.* **660** (2022) A67, arXiv:2110.11421 [astro-ph.CO].

[60] G. Alestas, L. Kazantzidis, and S. Nesseris, "Machine learning constraints on deviations from general relativity from the large scale structure of the Universe," arXiv:2209.12799 [astro-ph.CO].

[61] B. A. Reid. *et al.*, "Cosmological constraints from the clustering of the Sloan Digital Sky Survey DR7 luminous red galaxies," *Mon. Not. Roy. Astron. Soc.* **404** no. 1, (2010) 60–85, arXiv:0907.1659 [astro-ph.CO].

[62] A. Díaz Rivero, C. Dvorkin, F.-Y. Cyr-Racine, J. Zavala, and M. Vogelsberger, "Gravitational Lensing and the Power Spectrum of Dark Matter Substructure: Insights from the ETHOS N-body Simulations," *Phys. Rev. D* **98** no. 10, (2018) 103517, arXiv:1809.00004 [astro-ph.CO].

[63] S. Chabanier, M. Millea, and N. Palanque-Delabrouille, "Matter power spectrum: from Lyα forest to CMB scales," *Mon. Not. Roy. Astron. Soc.* **489** no. 2, (2019) 2247–2253, arXiv:1905.08103 [astro-ph.CO].

[64] J. Lesgourgues, G. Mangano, G. Miele, and S. Pastor, *Neutrino Cosmology*. Cambridge University Press, 2, 2013.

[65] **KATRIN** Collaboration, M. Aker *et al.*, "Direct neutrino-mass measurement with sub-electronvolt sensitivity," *Nature Phys.* **18** no. 2, (2022) 160–166, arXiv:2105.08533 [hep-ex].

[66] D. J. Eisenstein and W. Hu, "Power spectra for cold dark matter and its variants," *Astrophys. J.* **511**

(1997) 5, arXiv:astro-ph/9710252.

[67] J. R. Bond and A. S. Szalay, "The collisionless damping of density fluctuations in an expanding universe," *Astrophys. J., Lett. Ed.* **274** (1983) 443–468.

[68] J. R. Bond and G. Efstathiou, "Cosmic background radiation anisotropies in universes dominated by nonbaryonic dark matter," *Astrophys. J., Lett. Ed.* **285** (1984) L45–L48.

[69] E. W. Kolb and M. S. Turner, *The Early Universe*, vol. 69. Front. Phys., 1990.

[70] B. C. Allanach, D. Grellscheid, and F. Quevedo, "Genetic algorithms and experimental discrimination of SUSY models," *JHEP* **07** (2004) 069, arXiv:hep-ph/0406277.

[71] Y. Akrami, P. Scott, J. Edsjo, J. Conrad, and L. Bergstrom, "A Profile Likelihood Analysis of the Constrained MSSM with Genetic Algorithms," *JHEP* **04** (2010) 057, arXiv:0910.3950 [hep-ph].

[72] S. Abel, D. G. Cerdeño, and S. Robles, "The Power of Genetic Algorithms: what remains of the pMSSM?," arXiv:1805.03615 [hep-ph].

[73] X.-L. Luo, J. Feng, and H.-H. Zhang, "A genetic algorithm for astroparticle physics studies," *Comput. Phys. Commun.* **250** (2020) 106818, arXiv:1907.01090 [astro-ph.HE].

[74] M. Ho *et al.*, "A Robust and Efficient Deep Learning Method for Dynamical Mass Measurements of Galaxy Clusters," *Astrophys. J.* **887** (2019) 25, arXiv:1902.05950 [astro-ph.CO].

[75] C. Bogdanos and S. Nesseris, "Genetic Algorithms and Supernovae Type Ia Analysis," *JCAP* **05** (2009) 006, arXiv:0903.2805 [astro-ph.CO].

[76] S. Nesseris and A. Shafieloo, "A model independent null test on the cosmological constant," *Mon. Not. Roy. Astron. Soc.* **408** (2010) 1879–1885, arXiv:1004.0960 [astro-ph.CO].

[77] S. Nesseris and J. Garcia-Bellido, "A new perspective on Dark Energy modeling via Genetic Algorithms," *JCAP* **11** (2012) 033, arXiv:1205.0364 [astro-ph.CO].

[78] S. Nesseris and J. García-Bellido, "Comparative analysis of model-independent methods for exploring the nature of dark energy," *Phys. Rev. D* **88** no. 6, (2013) 063521, arXiv:1306.4885 [astro-ph.CO].

[79] D. Sapone, E. Majerotto, and S. Nesseris, "Curvature versus distances: Testing the FLRW cosmology," *Phys. Rev. D* **90** no. 2, (2014) 023012, arXiv:1402.2236 [astro-ph.CO].

[80] R. Arjona and S. Nesseris, "What can Machine Learning tell us about the background expansion of the Universe?," *Phys. Rev. D* **101** no. 12, (2020) 123525, arXiv:1910.01529 [astro-ph.CO].

[81] **VIRGO Consortium** Collaboration, R. E. Smith, J. A. Peacock, A. Jenkins, S. D. M. White, C. S. Frenk, F. R. Pearce, P. A. Thomas, G. Efstathiou, and H. M. P. Couchmann, "Stable clustering, the halo model and nonlinear cosmological power spectra," *Mon. Not. Roy. Astron. Soc.* **341** (2003) 1311, arXiv:astro-ph/0207664.

[82] F. Renzi, N. B. Hogg, M. Martinelli, and S. Nesseris, "Strongly lensed supernovae as a self-sufficient probe of the distance duality relation," *Phys. Dark Univ.* **32** (2021) 100824, arXiv:2010.04155 [astro-ph.CO].

[83] R. Arjona, H.-N. Lin, S. Nesseris, and L. Tang, "Machine learning forecasts of the cosmic distance duality relation with strongly lensed gravitational wave events," *Phys. Rev. D* **103** no. 10, (2021) 103513, arXiv:2011.02718 [astro-ph.CO].

Scientific Report
FAPESP
Post-doctoral Fellowship

Process: 2021/10139-2

Title: Pattern formation in active matter and biology: bacterial mixtures and vegetation

Beneficiary: Pablo Souza de Castro Melo

Advisor: Nathan Jacob Berkovits

Host institution: Instituto de Física Teórica/IFT/UNESP

Duration: 01/01/2022 to 30/11/2022

Report period: 01/01/2022 to 30/11/2022

Contents

1 Project summary

The emergence of complex biological functions depends on the spontaneous formation of spatiotemporal patterns between agents such as cells, plants, and animals. In the first part of this project, we will investigate the collective behavior of binary mixtures of bacterial cells and how they undergo cooperative or competitive pattern formation. We will focus on phenomena similar to so-called "motility-induced phase separation" found in collections of active (i.e., motile) particles like bacterial fluids, where persistent motion takes the role of "attractive forces" in generating agglomeration. It is known that, compared with systems of identical particles, the phenomenology of passive (i.e., nonmotile) mixtures is much richer. The study of bacterial mixtures is therefore of great relevance as different bacterial species and strains frequently coexist in Nature. This project aims to discover new features that appear only for mixtures, e.g., the slow approach to stationary segregation in crowded environments, for which there are no results. Our research questions will be answered via a combination of theoretical methods, simulations, and collaboration with experimentalists.

Initially, we will consider reciprocal mixtures where both types of bacteria have the same motility properties, i.e., the same self-propulsion speeds and reorientation rates. As found in Biology, we will consider the scenario where the motility properties of each type are affected reciprocally by the presence of the other type. These "quorum-sensing" interactions can be achieved and tuned in the lab by genetically modifying each type's biochemical signalling; in doing so, their motility properties will depend on the concentration of highly-diffusive molecules produced exclusively by the other type. With this mechanism, it was shown that co-localization (or anti-localization) of the bacterial types emerges. Nonetheless, several questions remain open. One example is the environmental coupling that arises for bacterial mixtures compartmentalized in spatial niches. Another question is whether bacterial types, say, A and B, can regulate their motilities such that A moves at higher self-propulsion speed in the presence of B while B moves at lower self-propulsion speed in the presence of A, effectively leading to a phenomenon preliminarily dubbed "type chasing". Finally, we will consider mixtures of bacteria with different motilities. Answering these questions will provide important steps towards avoiding the pathogenic formation of bacterial agglomerates found in medical contamination.

Secondly, we will investigate the minimal ecological requirements for the formation of vegetation patterns. Particularly, we will study the structural effects of rainfall spatial gradients (as at the border of deserts) and their seasonal temporal variability. These features are expected to generate the coexistence of distinct patterns. A similar behavior occurs during the phase separation of thermodynamic fluids, where abrupt environmental changes are known to generate secondary domains on a matrix of evolving primary structures. Later in the dynamics, all domains merge together as the system approaches thermodynamic equilibrium. For vegetation patterns, however, thermodynamic equilibrium is absent, meaning that primary and secondary "domains" coexist indefinitely. The implications of such primary-secondary domain coupling will be analyzed. Our results will be compared with image analysis from available satellite data.

This project is designed to bring outstanding advances to the lively fields of active matter and theoretical ecology. It involves a synergy of interests as well as theoretical and

experimental expertises. The proposal is physically relevant, viable, and presents great potential for applications.

2 Achievements

During the course of the project, collaboration opportunities have made our focus shift slightly. Still, our research questions remained well within the original plan. This can be seen from the five manuscripts already submitted or to be submitted (see other sections below). As initially planned, we unravelled multiple *effects of heterogeneity* (mostly mixtures of particles with different motilities) on the motion-shaped patterns of biologically inspired systems of particles.

These effects have been studied using simulations, PDEs and other kinds of kinetic theory modelling. They can be summarized as follows. (i) We identified a two-stage pattern formation dynamics for the persistent-motion-induced wall accumulation of fast and slow self-propelled particles (like bacteria), where segregation concentrations are adjusted over long timescales due to particle crowding. (ii) We studied the interaction of fast-slow bacterial mixtures with asymmetric obstacles, which, as we found out, generates vortices at corners, wall accumulation, fast-slow spatial segregation, and motion rectification (nonzero transport due to a coupling between obstacle asymmetry and motion persistence). (iii) We have studied critical habitat sizes (the minimal size for the habitat of a biological population below which they go extinct, a topic relevant for discussing deforestation effects). In particular, we considered long timescales where reproduction and death play important roles, coupled to a scenario where spatial heterogeneity is introduced such that there is a preferred location toward which individuals advect, on top of their diffusion/dispersal movement. Counter-intuitively, we have found that/how advection may be detrimental to survival if the preferred location is located close to the edges to harsh environments. (iv) We have calculated how motility-induced clustering properties, such as number of clusters, distance between clusters, sizes of clusters, etc., change the final outcome of the spreading of diseases in systems of susceptible, infected, and recovered active particles. Among other things, this is important in the context of phage therapy, where viruses are deliberately employed to spread in and kill bacterial colonies. (v) Finally, we have studied single-particle systems of individuals undergoing random searches guided by smell cues emitted by a pattern of targets (vegetation patches, food, mates, etc.) and calculated the corresponding optimal random motion parameters toward which some species may have evolved, as hinted by experiments with bees and deer.

Also, I participated and/or presented in a number of conferences and events. Moreover, there has been another publication (not totally related to the project but still connected) published during the fellowship period under the fellowship affiliation. Finally, other points are to be highlighted below, namely the conclusion of the supervision of a MSc student where I was the main advisor, the participation as main supervisor in a one-week full-time project within the Quantitative Biology program as well as invited talks, and work as reviewer for a couple of journals.

Invited talks

1. "Partículas autopropelidas: acumulação, diversidade, epidemias e buscas aleatórias", Physics Department, Universidade de Pernambuco, Recife, Brazil.

2. "Self-Propelled Particles: Accumulation, Diversity, Epidemics and Random Searches", Coloquinho, IFT-UNESP, São Paulo, Brazil

3. "Reduced mixing generates oscillations and chaos in the oceanic deep chlorophyll maximum", Journal club paper presentation and discussion at Quantitative Biology program, ICTP-SAIFR, São Paulo, Brazil

Journal reviewer

1. *Physical Review Letters*, American Physical Society.

2. *Physical Review E*, American Physical Society.

Thesis committee & Supervision

1. **Committee**: Pablo de Castro Melo; Rodrigo Soto Bertrán; María Luisa Cordero Garayar; Gustavo Düring Hidalgo; Cynthia J. Olson Reichhardt.
   Role: Advisor of Maurício Rojas Vega.
   Thesis title: "Active mixtures interacting with walls and asymmetric obstacles".
   Degree, institution and year: MSc in Physics, Universidad de Chile, 2022.
   Repository link: https://repositorio.uchile.cl/handle/2250/184694.

2. **Activity**: Supervision of Hands-on project within Quantitative Biology program at ICTP-SAIFR, August 2022.
   Role: Advisor of students group.
   Project title: "Movement Ecology and Active Matter: Optimal survival strategies under chemotaxis".
   Final presentation link: www.pdf.weebly.com/uploads/3/7/9/8/37986405/group3.pdf.
   Program link: www.ictp-saifr.org/qbioprogram/.

3 Data management plan

The relevant data was published together with the works mentioned in Section 5 below and/or can be found in the graphs and text of the manuscripts in the sections below. On top of that, there is a link for the codes: www.bit.ly/3BJZ0J1.

4 Participation in scientific events

Presentations in conferences

Only the Chile conference below used "Reserva Técnica" funds. The slides of the corresponding oral presentation can be found in Section 5.

1. **Event**: Encontro de Outono da SBF, São Paulo, Brazil, 10-14 April 2022.
   Oral presentation: *"Fast and slow self-propelled particles: Wetting, segregation, rectification, and vorticity"*
   Event webpage: www1.fisica.org.br/ eosbf/2022/index.php/pt/

2. **Event**: ACTIVE & INTELLIGENT LIVING MATTER CONFERENCE ERICE, SICILY June 26 - July 1, 2022
   Poster presentation: *"Contagion dynamics of agglomerating self-propelled particles in narrow environments"*
   Event webpage: www.doostmohammadilab.com/erice2022

3. **Event**: Conference Physics of Active Matter, Coyhaique, Chile, October 24-28, 2022
   Oral presentation: *"Contagion dynamics of agglomerating self-propelled particles in narrow environments"*
   Official note: "This work was presented by Pablo de Castro as an oral presentation at the scientific event Conference Physics of Active Matter held from October 24 to October 28, 2022, in Coyhaique, Chile" using "**Reserva Técnica**" funds. In Portuguese for official completeness, this reads "Este trabalho foi apresentado por Pablo de Castro oralmente no evento científico Conference Physics of Active Matter ocorrido de 24 a 28 de Outubro de 2022 em Coyhaique, Chile" usando fundos da **Reserva Técnica**.
   Event webpage: www.activematter.dfi.uchile.cl/conference2022/

Attendance of school

1. **Event**: Two-week event entitled *School on Disordered Elastic Systems* at ICTP-SAIFR where elastic systems such as those in active matter were discussed.
   Event webpage: www.ictp-saifr.org/des2022/

5 List of publications

Publication 1 below is related to the fellowship only indirectly in two contexts: (i) chiral microswimmers and (ii) double-arm centrifugation for segregation of bio-mixtures. Since it has been published during the relevant period, it has been included for completeness. Publication 2 is a poster presented at a conference, where I worked out the motility-induced clustering dynamics of evolving mixtures of susceptible, infected, and recovered active particles. Publication 3 is an oral presentation related to Publication 2.

Following this section, the first pages of these works can be found.

1. **Authors**: Pablo de Castro, Tiago Araújo, and Fernando Parisio
   Title: "Spinning rigid bodies driven by orbital forcing: The role of dry friction"
   Publication journal details: *Nonlinear Dynamics* 107, 3473–3484.
   Journal link: www.link.springer.com/article/10.1007/s11071-021-07175-8
   Repository link: www.repositorio.unesp.br/handle/11449/230192

2. **Authors**: Pablo de Castro, Felipe Urbina, Ariel Norambuena, Francisca Guzman-Lastra, and Ricardo Martinez-Garcia
   Title: "Contagion dynamics of agglomerating self-propelled particles in narrow environments"
   Details: Presented at "ACTIVE & INTELLIGENT LIVING MATTER CONFERENCE ERICE, SICILY June 26 - July 1, 2022"
   Open-access link: www.pdc.weebly.com/uploads/3/7/9/8/37986405/erice.pdf

3. **Authors**: Pablo de Castro, Felipe Urbina, Ariel Norambuena, Francisca Guzman-Lastra, and Ricardo Martinez-Garcia
   Title: "Contagion dynamics of agglomerating self-propelled particles in narrow environments"
   Details: Presented at "Conference Physics of Active Matter, Coyhaique, Chile, October 24-28, 2022"
   Open-access link: https://bit.ly/3WnXnIM

Nonlinear Dyn (2022) 107:3473–3484
https://doi.org/10.1007/s11071-021-07175-8

ORIGINAL PAPER

Spinning rigid bodies driven by orbital forcing: the role of dry friction

Pablo de Castro · **Tiago Araújo Lima** · **Fernando Parisio**

Received: 30 March 2021 / Accepted: 24 December 2021 / Published online: 7 January 2022

Abstract A "circular orbital forcing" makes a chosen point on a rigid body follow a circular motion while the body spins freely around that point. We investigate this problem for the planar motion of a body subject to dry friction. We focus on the effect called *reverse rotation* (RR), where spinning and orbital rotations are antiparallel. Similar reverse dynamics include the rotations of Venus and Uranus, journal machinery bearings, tissue production reactors, and chiral active particles. Due to dissipation, RRs are possible only as a transient. Here, the transient or *flip* time t_f depends on the circular driving frequency ω, unlike the viscous case previously studied. We find $t_f \sim \omega^{\gamma-1}\mu^{-\gamma/2}$, where μ is the friction coefficient and $\gamma = 0$ ($\gamma = 2$) for low (high) ω. Whether RRs really occur depends on the initial conditions as well as on μ and H, a geometrical parameter. The critical $H_c(\mu)$ where RRs become possible follows a q-exponential with $q \simeq 1.9$, a more restrictive RR scenario than in the wet case. We use animations to visualize the different dynamical regimes that emerge from the highly nonlinear dissipation mechanism of dry friction. Our results are valid across multiple investigated rigid body shapes.

Keywords Reverse rotations · Rigid-body dynamics · Dry friction · Circular orbital forcing

1 Introduction

Venus rotates around itself in the opposite direction to its rotation around the Sun [1,2]. The same occurs with Uranus [3]. The magnitude and the *sign* of the ratio between the spinning and orbital angular velocities of a planet (or a star) [4] can remarkably alter the tidal instabilities that take place inside its liquid core [5]. Dynamical behaviors where the spinning and orbital rotations of a body are antiparallel are dubbed *reverse rotations* (RRs). Examples include bodies inside rotating chambers filled with viscous fluids [6–8], the parametrically excited damped pendulum [9], the dynamics of bearings of journal machinery [10], chiral active particles [11], and the problem of biological tissue production. In the latter, a common method to generate tissue is the rotating vessel bioreactor, which consists of a container filled with a nutrient-rich medium rotating about

Pablo de Castro: Performed at Departamento de Física, FCFM, Universidad de Chile.

Supplementary Information The online version contains supplementary material available at https://doi.org/10.1007/s11071-021-07175-8.

P. de Castro ( )
ICTP South American Institute for Fundamental Research & Instituto de Física Teórica - UNESP, São Paulo, Brazil
e-mail: pablo.castro@unesp.br

T. A. Lima
Ser Educacional S.A., Recife, Pernambuco, Brazil
e-mail: tiago.arj@gmail.com

T. A. Lima · F. Parisio
Departamento de Física, Universidade Federal de Pernambuco, Recife, Pernambuco 50670-901, Brazil
e-mail: fernando.parisio@ufpe.br

Contagion dynamics of agglomerating self-propelled particles in narrow environments

Pablo de Castro[1], **Felipe Urbina**[2], **Ariel Norambuena**[2], **Francisca Guzmán-Lastra**[3] **& Ricardo Martínez-García**[1]

[1]ICTP South American Institute for Fundamental Research & IFT - UNESP, São Paulo, Brazil
[2] Vicerrectoría de Investigación, Universidad Mayor, Santiago, Chile
[3] Department of Physics, Faculty of Sciences, Universidad de Chile, Santiago, Chile

1: Introduction and Overview

- **How does an epidemics spread between persistence-induced clusters of active matter?**

- Self-propelled swimmers spontaneously agglomerate into clusters;
- In 1D, the clusters do not coalesce macroscopically;
- Using theory and simulations, we study how epidemics spread in such environments;
- We consider run-and-tumble (RT) particles under a susceptible-infected-recovered (SIR) dynamics
- **Also relevant to bacterial biochemical signaling, social consensus and light-controlled colloids.**

2: Run-and-tumble clustering in 1D

- Consider a periodic 1D lattice with $N = 2000$ sites and M particles;
- The maximal occupancy per site is one particle;
- Each particle has a director (self-propulsion direction): towards right or left;
- $\phi \equiv M/N$ is the dimensionless concentration;
- At each time step, particles are chosen sequentially at random;
- New director is randomly chosen with probability ν;
- If the director points to empty neighboring site, the particle moves into it;
- Initial state: random mutually-excluding positions and directors;
- Continue until M particles are random selected within same time step;
- There is no alignment interaction
- Free-particle speed fluctuates around $v = 1$;

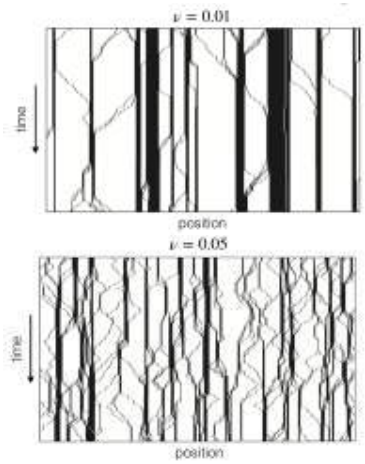

Stationary clusters for $\phi = 0.2$; shows 300 time steps.

- Distributions of cluster and gas region (i.e., empty region) sizes [1]:

$$F_c(l) \sim \exp(-l/L_c), \quad F_g(l) \sim \exp(-l/L_g) \qquad (1)$$

- Average cluster and gas region sizes:

$$L_c = \sqrt{\frac{2v\phi}{\nu(1-\phi)}}, \quad L_g = \sqrt{\frac{2v(1-\phi)}{\nu\phi}} \qquad (2)$$

3: SIR dynamics

- After stationary clustering, infect randomly selected particle;
- Within same time step, select another particle. If it is infected, infect its susceptible neighbors;
- With probability r_{rec}, selected particle recovers;
- If it is susceptible and any of its neighbors is infected, make it infected;
- As before, draw new direction and move;
- Continue until M particles are random selected within same time step;
- Repeat for other time steps until epidemics ends;

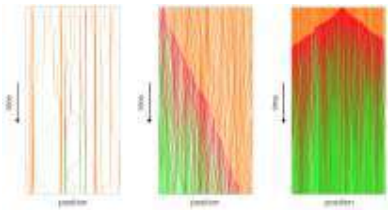

From left to right: $\phi = 0.1$, 0.5, 0.9, $\nu = 0.005$, 0.5, 0.5 and $r_{\text{rec}} = 0.001$ for all. Color scheme in the next figure.

- Single experiment evolution shows peaks due to clusters

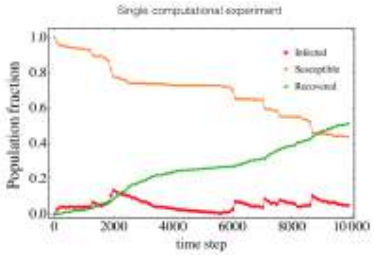

Parameter choice is irrelevant: 1D nature leads to same general qualitative population fraction evolution for all parameter sets.

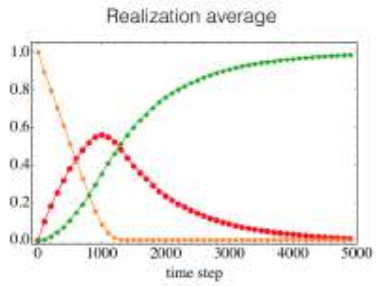

Realization average of population fractions. As in the above figure, parameters choice is irrelevant.

- Denote the realization averages of the global SIR variables as S, I, and R
- $S+I+R = M$ and $X_\infty \equiv X(t \to \infty)$ for $X = S, I, R$.
- A phenomenological theory holds (fitting β and a):

$$\frac{dS}{dt} = -\beta \tanh[a(S - S_\infty)], \qquad (3)$$

$$\frac{dI}{dt} = \beta \tanh[a(S - S_\infty)] - r_{\text{rec}} I \qquad (4)$$

$$\frac{dR}{dt} = r_{\text{rec}} I, \text{ where } S + I + R = M \qquad (5)$$

4: Microscopic Theory

- Microscopic theory for (realization average) total amount of infected particles at the end:

$$R_\infty = L_c + 2L_c(1-r_{\text{rec}})^{\tau_b} + 2L_c(1-r_{\text{rec}})^{2\tau_b} + \cdots \qquad (6)$$

- There are $\frac{N_c-1}{2}$ terms after the first one, N_c being the amount of clusters (known analytically);
- Time to tumble and travel btw clusters: $\tau_b \equiv \frac{2}{v} + \frac{L_g}{v}$

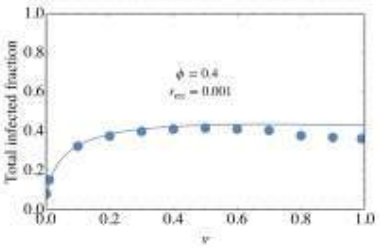

Total fraction of infected versus ν.

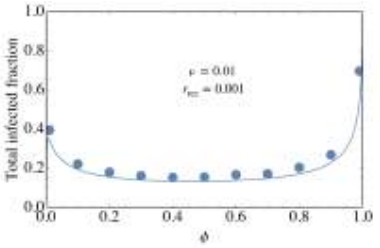

Total final fraction of infected versus ϕ.

- Upcoming important corrections:
- Considering superdiffusive rather than completely ballistic travels between clusters;
- Particles may get blocked in a gas region by a particle *travelling* in the opposite direction.

5: Conclusions

- We studied the contagion of agglomerating self-propelled particles in narrow environments;
- Generally, by decreasing motion persistence, the total final fraction of infected particles increases;
- That's because particles leave clusters sooner and infect other clusters;
- However, by further decreasing persistence, the total final fraction of infected particles decreases;
- That's because particles return to their "original" clusters before infecting other clusters;
- Model provides insights into how active clustering plays distinct roles into the efficiency of epidemics.

Further info

- **Contact**
  pabloodecastro@gmail.com
  pablodecastro.weebly.com

- **References**

[1] Soto & Golestanian, ***Phys. Rev. E***, 2014, **89**, 012706

- **Acknowledgements**

PdC: FAPESP grant 2021/10139-2;
AN: Fondecyt Iniciación No 11220266.
RMG: Serrapilheira grant Serra 1911-31200.

Contagion dynamics of self-propelled agents in narrow environments: Role of spontaneous agglomeration

Pablo de Castro*
Ricardo Martinez-Garcia
ICTP-SAIFR
IFT-UNESP

Ariel Norambuena
Felipe J. Valencia
DAiTA Lab
Universidad Mayor

Francisca Guzmán-Lastra
Departamento de Fisica
Facultad de Ciencias
Universidad de Chile

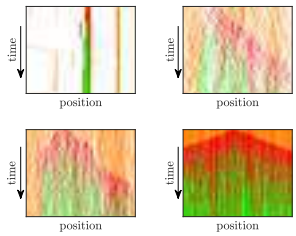

Contagion dynamics
SIR

of self-propelled agents
of run-and-tumble particles

in narrow environments
in 1D

Role of spontaneous agglomeration
Role of clustering induced by persistent-direction motion

Role of *motion-driven* spatial heterogeneity in *motion-driven* epidemics

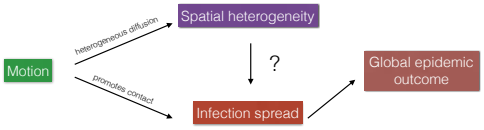

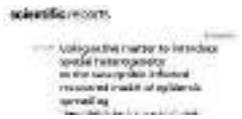

low transmissibility

high transmissibility
+ obstacles

susceptible
infected
recovered

Present work

persistent motion

excluded volume

motility-induced clustering

cluster-cluster effects

analytical theory

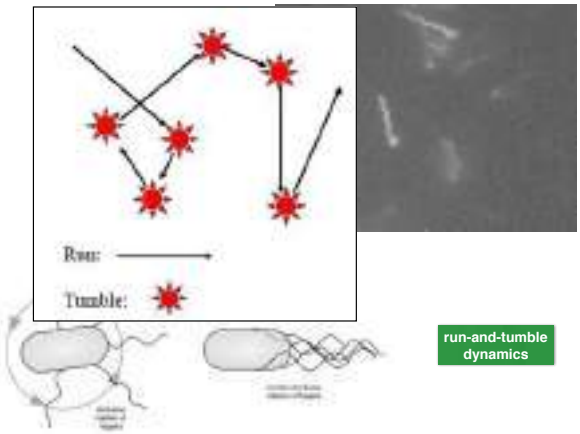

run-and-tumble dynamics

Run-and-tumble lattice gas

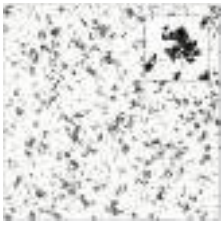

Model

- Maximal occupancy of **one particle per site**
- Dimensionless concentration: ϕ
- Total number of particles: M
- Each particles has 4 possible directions (2D)
- At each time step, particles are chosen sequentially at random
- A new director is chosen at random with tumbling probability ν
- If particle points to empty site, move into it
- Periodic boundary conditions
- Random initial state
- No alignment interaction
- Continue until you have M particle selections within same time step
- Free-particle speed fluctuates around $v = 1$

RT lattice gas clustering
Rodrigo Soto and Ramin Golestanian, PRE 2014

Run-and-tumble lattice gas: clustering in 1D

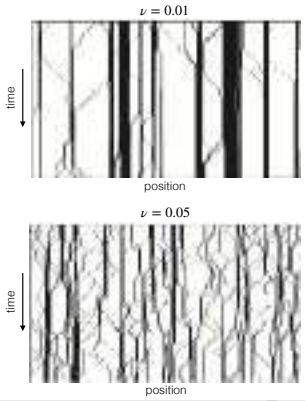

$\phi = 0.2 \implies M = 400$

300 time steps in the steady-state

section of 500 sites of a lattice with $N = 2000$

Minimalistic model

R. Soto and R. Golestanian, PRE 2014

Distribution of cluster sizes

$$F_c(l) = A_c \exp(-l/L_c)$$

Distribution of sizes for "gas" regions (empty sites)

$$F_g(l) = A_g \exp(-l/L_g)$$

L_c (on average) L_g (on average)

R. Soto and R. Golestanian, PRE 2014

R. Soto and R. Golestanian, PRE 2014

Distribution of cluster sizes

$$F_c(l) = A_c \exp(-l/L_c)$$

Distribution of sizes for "gas" regions (empty sites)

$$F_g(l) = A_g \exp(-l/L_g)$$

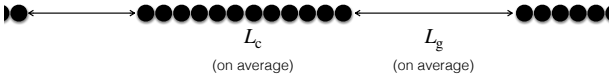

L_c (on average) L_g (on average)

$$L_c = \sqrt{\frac{2v\phi}{\nu(1-\phi)}} \qquad L_g = \sqrt{\frac{2v(1-\phi)}{\nu\phi}}$$

Clustering-contagion dynamics

Susceptible-Infected-Recovered (SIR) algorithm

1. After stationary clustering, let 1 random particle become infected
2. Within same time step, select another particle randomly. If it is an I, infect its S neighbors. If it is an S next to an I, infect it.
3. The selected particle recovers with fixed probability r_{rec}
4. Draw new direction and move
5. Repeat randomly until you have M particle selections within same time step
6. Repeat randomly for other time steps until epidemics ends

Contagion dynamics: SIR model

When a border particle gets infected, two scenarios are possible:

1. Particle will flip and infect other cluster/particle
2. Particle recovers before that

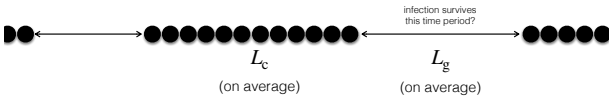

Goal: calculate fraction of infected people at the end, averaged over many epidemic realizations

Temporal evolution

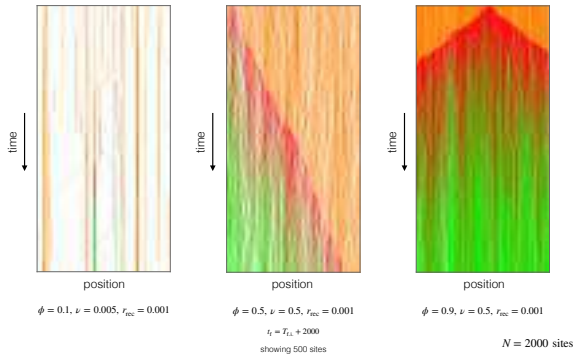

Temporal evolution

Single realization

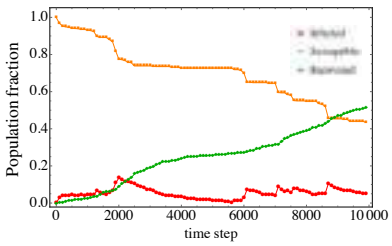

$\phi = 0.4,\ \nu = 0.001,\ r_{rec} = 0.001$

Final fraction of recovered individuals

Final fraction of ever-infected individuals

$$f_R^{\infty} \equiv \frac{R(t \to \infty)}{N\phi}$$

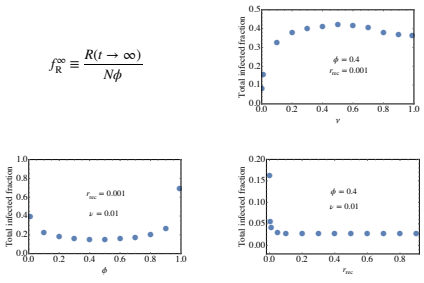

Mean-cluster theory

Final number of recovered individuals

$$R_\infty = L_c + 2L_c(1 - r_{rec})^{\tau_b} + 2L_c(1 - r_{rec})^{\tau_b} \times (1 - r_{rec})^{\tau_b} + \cdots$$

Flip-travel time τ_b

Mean-cluster theory

$$R_\infty = L_c + 2L_c(1 - r_{rec})^{\tau_b} + 2L_c(1 - r_{rec})^{\tau_b} \times (1 - r_{rec})^{\tau_b} + \cdots$$

$\frac{N_c - 1}{2}$ terms

$$R_\infty = L_c \left[1 + 2 \sum_{k=1}^{(N_c-1)/2} (1 - r_{rec})^{k\tau_b} \right]$$

Flip-travel time τ_b

Mean-cluster theory

$$R_\infty = L_c + 2L_c(1-r_{rec})^{\tau_b} + 2L_c(1-r_{rec})^{\tau_b} \times (1-r_{rec})^{\tau_b} + \cdots$$

$\frac{N_c - 1}{2}$ terms

$$R_\infty = \frac{L_c\left[1 + (1-r_{rec})^{\tau_b} - 2(1-r_{rec})^{\frac{1}{2}\tau_b(N_c+1)}\right]}{1-(1-r_{rec})^{\tau_b}}$$

Flip-travel time τ_b

Flip-travel time τ_b

$$\tau_b = 2/\nu + \mathrm{MSD}^{-1}(L_g^2)$$

flip time | diffusion time

$$f_R^\infty \equiv \frac{R(t\to\infty)}{N\phi}$$

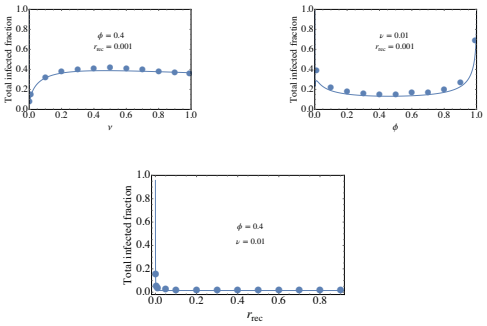

$$f_R^\infty \equiv \frac{R(t\to\infty)}{N\phi}$$

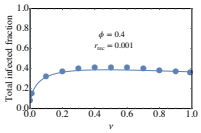

τ_b decreases with $\nu \Longrightarrow$ total infected **increases**

N_c increases with $\nu \Longrightarrow$ total infected **increases**

L_c decreases with $\nu \Longrightarrow$ total infected **decreases**

$$f_R^\infty \equiv \frac{R(t\to\infty)}{N\phi}$$

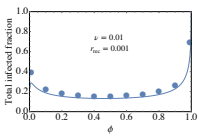

τ_b decreases with $\phi \Longrightarrow$ total infected **increases**

N_c increases with $\phi < 0.5 \Longrightarrow$ total infected **increases**

L_c increases with $\phi \Longrightarrow$ total infected **increases**

However, f_R^∞ is number of total infected *divided by* ϕ

In each realization, peaks occur at different times and are averaged out in the realization average

Temporal evolution

Realization average

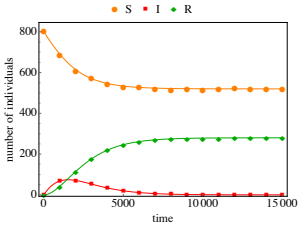

$\phi = 0.4$, $\nu = 0.1$, $r_{rec} = 0.001$, $N = 2000$, $v = 1$

Temporal evolution

In each realization, peaks occur at different times and are averaged out in the realization average

Realization average

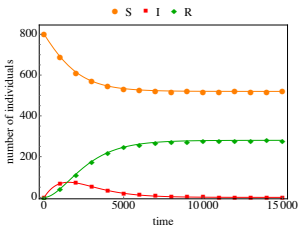

$S \gg S_\infty$

$$\frac{dS}{dt} = -\beta$$

$$\frac{dI}{dt} = \beta - r_{rec} I$$

$$\frac{dR}{dt} = r_{rec} I$$

$\phi = 0.4,\ \nu = 0.1,\ r_{rec} = 0.001,\ N = 2000,\ v = 1$

fit β

Temporal evolution

In each realization, peaks occur at different times and are averaged out in the realization average

Realization average

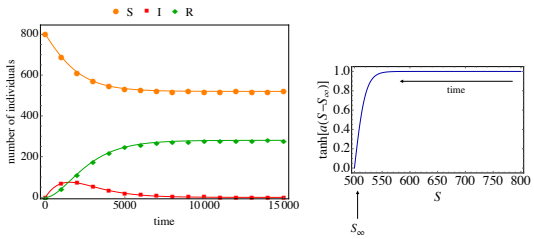

$\phi = 0.4,\ \nu = 0.1,\ r_{rec} = 0.001,\ N = 2000,\ v = 1$

Temporal evolution

In each realization, peaks occur at different times and are averaged out in the realization average

Realization average

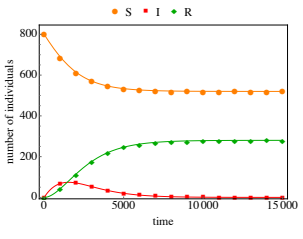

$S \approx S_\infty$

$$\frac{dS}{dt} = -\beta \tanh\left[a\,(S - S_\infty)\right]$$

$$\frac{dI}{dt} = \beta \tanh\left[a\,(S - S_\infty)\right] - r_{rec} I$$

$$\frac{dR}{dt} = r_{rec} I$$

$\phi = 0.4,\ \nu = 0.1,\ r_{rec} = 0.001,\ N = 2000,\ v = 1$

fit β and a
find or fit S_∞

Temporal evolution

Realization average

Phenomenological theory

$$S(t) \simeq S_\infty + \cosh^{-1}\left[e^{\beta a t}\cosh\left[a\,(M - S_\infty)\right]\right]/a,$$

$$I(t) = \frac{\beta}{r_{rec}}\left[{}_2f_1\left(\frac{r_{rec}}{2a\beta}, e^{2\beta a t}\cosh^2\left[a\,(M - S_\infty)\right]\right)\right.$$

$$\left. - e^{-r_{rec} t}\,{}_2f_1\left(\frac{r_{rec}}{2a\beta}, \cosh^2\left[a\,(M - S_\infty)\right]\right)\right],$$

$$R(t) = M - S(t) - I(t),$$

${}_2f_1\left(\frac{r_{rec}}{2a\beta}; x\right) \equiv {}_2F_1\left(\frac{1}{2}, \frac{r_{rec}}{2a\beta}; \frac{r_{rec}}{2a\beta} + 1; x\right)$

fit β and a
find or fit S_∞

Concluding remarks

1. We developed theory and simulations for the contagion of self-agglomerating active particles in narrow environments
2. The aftermath impact of an epidemics can be measured by the final fraction of total infected individuals, which our theory can calculate using clustering and microscopic parameters.
3. Insights were obtained for the the total final fraction of infected particles versus other microscopic parameters
4. A dynamical phenomenological theory has been developed, with excellent agreement
5. We hope our work paves the way to more complicated SIR*D* and two-dimensional theories

Collaborators and funding

Peter Sollich
King's College London
Universität Göttingen

Rodrigo Soto
Universidad de Chile

Francisco Rocha
Aix-Marseille Université

Daniel Goldman
Georgia Tech

Saulo Diles
Univ. Federal do Pará

Mauricio Rojas
IST Austria

Andrea Villa-Torrealba
Universidad de Chile

Tiago Araújo
Univ. Federal de Pernambuco

Francisca Guzmán-Lastra
Universidad Mayor

Fernando Parisio
Univ. Federal de Pernambuco

Ricardo Martínez-García
ICTP Brazil

Vivian Dornelas
ICTP Brazil

6 List of submitted or written papers

Copies of the following manuscripts can be found after this section.

1. **Authors**: Mauricio Rojas-Vega, Pablo de Castro, and Rodrigo Soto
   Title: "Wetting dynamics by mixtures of fast and slow self-propelled particles"
   Status: **submitted** to *Physical Review Letters*.

2. **Authors**: Mauricio Rojas-Vega, Pablo de Castro, and Rodrigo Soto
   Title: "Fast and slow self-propelled particles interacting with asymmetric obstacles"
   Status: **submitted** to *Physical Review E*.

3. **Authors**: Vivian Dornelas, Pablo de Castro, and Ricardo Martinez-Garcia
   Title: 'The effect of preferred location on population persistence and spread"
   Status: to be submitted to *Journal of Theoretical Biology* within 3-4 weeks.

4. **Authors**: Pablo de Castro, Francisca Guzman-Lastra, and Ricardo Martinez-Garcia
   Title: "Contagion dynamics of self-propelled agents in narrow environments"
   Status: to be submitted to *Physical Review E* within 2-3 weeks.

5. **Authors**: Pablo de Castro and Ricardo Martinez-Garcia
   Title: "Optimal random searches with chemotaxis"
   Status: to be submitted to *PLOS Computational Biology* within 5-6 weeks.

Wetting dynamics by mixtures of fast and slow self-propelled particles

Mauricio Rojas-Vega,[1,2] Pablo de Castro,[3] and Rodrigo Soto[1]

[1] *Departamento de Física, FCFM, Universidad de Chile, Santiago, Chile*
[2] *Institute of Science and Technology Austria, Klosterneuburg, Austria*
[3] *ICTP South American Institute for Fundamental Research & Instituto de Física Teórica, Universidade Estadual Paulista - UNESP, São Paulo, Brazil*

(Dated: November 2, 2022)

We study active surface wetting using a minimal model of bacteria that takes into account the intrinsic motility diversity of living matter. A mixture of "fast" and "slow" self-propelled Brownian particles is considered in the presence of a wall. The evolution of the wetting layer thickness shows an overshoot before stationarity and its composition evolves in two stages, equilibrating after a slow elimination of excess particles. Non-monotonic evolutions are shown to arise from delayed avalanches towards the dilute phase combined with the emergence of a transient particle front.

Introduction.—Natural active matter, such as collections of organisms, is *not* composed of identical self-propelling agents [1]. Instead, a wide distribution of motility properties exists due to different ages, reproduction stages, shapes, and sizes [2–4]. Moreover, active particles typically interact with "surfaces", e.g., bacteria swimming near boundaries of their host body or of contaminated medical instruments [5, 6]. For simplicity, models usually ignore at least one of these two ingredients, i.e., diversity and surface effects.

A persistent particle has a self-propulsion direction that fluctuates stochastically and, typically, slowly [7]. Consequently, active matter accumulates on surfaces to an extent dependent on persistence and density [8]. For bacteria, this mechanism initiates biofilm formation [9]. Thick biofilms are hard to kill with antibiotics since bacteria in the aggregate are protected by others. Surface accumulation by persistence is called active wetting [10–13]. Three phases are possible [8]: complete wetting, where the wetting layer covers the wall completely; incomplete wetting, where only a fraction of the wall becomes covered; and "unwetting" or "drying", where no dense phase exists. Active wetting was studied mostly for identical particles. However, passive and active phase behaviors can depend strongly on "diversity" in some particle attribute [14–29].

In this Letter, we study a mixture of "fast" and "slow" active Brownian disks moving in 2D, in the presence of a flat impenetrable wall. Each type has its own self-propulsion speed, defining a degree of *speed diversity*. Besides simulations, a dynamical kinetic theory is developed by extending the approach of Redner *et al.* [30] in three fronts: to mixtures, to include walls, and to incorporate time-dependence. This approach calculates the absorption and emission rates for the agglomerate directly from microscopic considerations and is therefore different than free-energy-like approximations [31] or phenomenological theories [32] that can be harder to connect with microscopic properties. Our theory relies on one fitting parameter only (similarly to Redner's original theory [30]), which assumes a single value across all parameters, somewhat like a "universal constant". To isolate surface effects, we choose a range of densities that allows for significant complete wetting while bulk motility-induced phase separation (MIPS) remains absent. Instead of focusing on "equilibrium" wetting-drying transitions [8], we study the wetting dynamics, i.e., the mechanisms involved in setting the composition and thickness of the wetting layer versus time and how motility diversity affects those. A two-stage evolution is found. Moreover, we identify a transient overshoot of the layer thickness, which occurs even without diversity but whose intensity depends non-monotonically on it.

Model and simulation method.—We consider a binary mixture in 2D composed of N active Brownian disks (labeled by i) where $N/2$ of them are "fast" particles, with self-propulsion speed $v_i = v_\mathrm{f} \equiv v_0(1+\delta)$, and the other $N/2$ are "slow" particles, with $v_i = v_\mathrm{s} \equiv v_0(1-\delta)$. Thus $\delta \in [0,1]$ is the degree of speed diversity [33]. Hereafter "f" and "s" denote "fast" and "slow" particles, respectively. Their dynamics obeys

$$\partial_t \boldsymbol{r}_i = v_i\,\hat{\boldsymbol{\nu}}_i + \mu \boldsymbol{F}_i + \boldsymbol{\xi}_i, \quad \partial_t \theta_i = \eta_i(t), \qquad (1)$$

where $\hat{\boldsymbol{\nu}}_i = (\cos\theta_i, \sin\theta_i)$ is the self-propulsion direction, μ is the mobility and $\boldsymbol{F}_i = \sum_j \boldsymbol{F}_{ij} + \boldsymbol{F}_i^{\mathrm{wall}}$ is the net force on particle i due to interactions with other particles and with the wall. The noise terms $\boldsymbol{\xi}_i(t)$ and $\eta_i(t)$ are Gaussian and white, with zero mean and correlations $\langle \xi_{i\lambda}(t)\xi_{j\beta}(t')\rangle = 2\xi\delta_{ij}\delta_{\lambda\beta}\delta(t-t')$ (the Greek letters denote coordinates) and $\langle \eta_i(t)\eta_j(t')\rangle = 2\eta\delta_{ij}\delta(t-t')$, where ξ and η are the

translational [34] and rotational diffusion coefficients, respectively.

We model particle interactions by a soft repulsive WCA-like potential [35], $U = 2^{3/2}(\sigma_{ij}/r_{ij})^3 - 3(\sigma_{ij}/r_{ij})^6 + (\sigma_{ij}/r_{ij})^{12} - 3/4$ for $r_{ij} \leq 2^{\frac{1}{6}}\sigma_{ij}$ and $U = 0$ otherwise [36], with r_{ij} the interparticle distance and $\sigma_{ij} \equiv \frac{1}{2}(d_i + d_j)$, where d_i is the diameter of particle i. To avoid crystallization [37], each particle is randomly assigned one of two diameters, $d_{\rm small} = d_0$ or $d_{\rm large} = 1.4d_0$, uncorrelated with self-propulsion speeds. We focus on speed diversity effects and thus the system is said to be just binary (the observed size segregation is weak). We choose $v_0 = 1$, $d_0 = 1$, $\mu = 1$, $\xi = 5 \times 10^{-4}$, $\eta = 5 \times 10^{-3}$ and the forward Euler method with time step $\Delta t = 10^{-4}$. Initially, positions and velocity directions are randomly distributed independent of types.

Figure 1(a) shows the system in the steady state (SS). The simulation box—which has total dimensions $L_x = 400$ and $L_y = 100$ and periodic boundary conditions—is shown only partially. An impenetrable flat wall (with sides at $x = 195$ and $x = 205$) is placed at the center. For particle-wall interactions, the same potential is used with $d_j = 0$. The occupied area fraction ϕ is the total area occupied by particles divided by the area of the simulation box minus the wall. In all simulations, $\phi = 0.18$, i.e., 6000 particles, leading to complete wetting during the whole dynamics without bulk MIPS, and we focus on varying δ. The average free-particle persistence length is $\ell \equiv v_0/\eta = 200$, which is comparable to the system size but sufficiently small to avoid ballistic motion between wall sides. Thus, each wall is treated independently and we average data from both sides. For complete wetting, increasing ϕ or ℓ trivially increases the layer thickness. For SS averages, only configurations after $t = 100\tau$ were used, where $\tau \equiv \eta^{-1} = 200$ is the rotational diffusion time.

Wetting.—To characterize accumulation, two particles were considered "connected" if $r_{ij} < 1.1\sigma_{ij}$, allowing us to identify the cluster of connected particles in contact with each wall. The mean wetting layer thickness $\langle h \rangle$ is obtained by averaging the position of the outermost particle in each of the 128 bins in which L_y is divided. Figure 1(b) shows $\langle h \rangle(t)$. The initial growth rate is constant and independent of δ. However, at long times, the higher the δ, the thinner the SS layer. For $\delta = 1$ (active-passive mixture), the thickness is approximately half the value for $\delta = 0$ as passive disks cannot wet. The layer thickness exhibits a transient overshoot before reaching stationarity. The gap between the peak of $\langle h \rangle(t)$ and

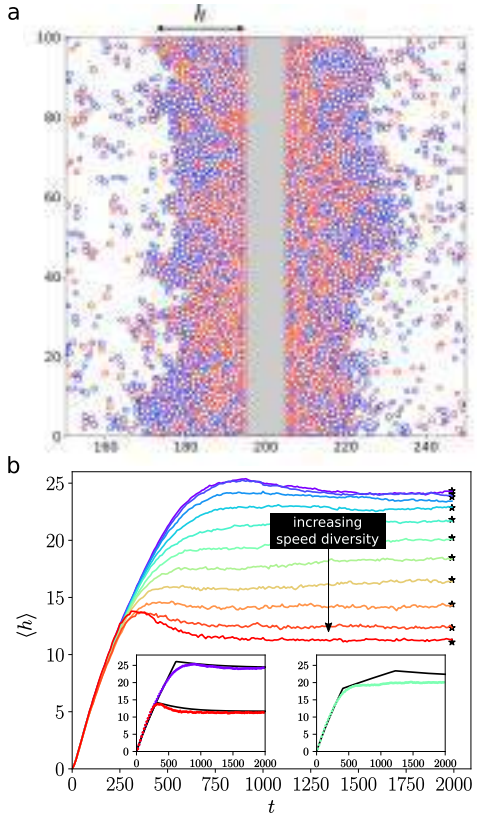

FIG. 1. (a) Snapshot for speed diversity $\delta = 0.5$ and $\phi = 0.18$ in the SS. Fast (slow) particles are in red (blue). (b) Temporal evolution of the mean wetting layer thickness for $\phi = 0.18$ and δ from 0 to 1 every 0.1. Stars indicate SS averages ($t > 100\tau$). Insets: $\delta = 0$ and $\delta = 1$ on the left and $\delta = 0.5$ on the right. Solid lines are the theory.

$\langle h \rangle(t \to \infty)$ depends on δ. Such overshoot will be elucidated below.

The evolution of the layer composition is shown in Figure 2 (see the Supplemental Material for a movie). The layer is always richer in fast particles than the overall system. In phase-separation problems, this is known as "fractionation" [16, 18]. The fractionation degree, however, is not constant. There is a first stage where the ratio of fast and slow particles remains constant, depending on δ. A second slower stage then starts, in which the composition is finely adjusted towards the SS. For $\delta > 0.7$, excess slow particles are eliminated, while for $\delta < 0.7$, additional slow particles are incorporated. This slow dynamics occurs simultaneously with changes in $\langle h \rangle$, with both processes being non-monotonic.

To model the accumulation dynamics, we first analyze the spatial distribution of orientations by

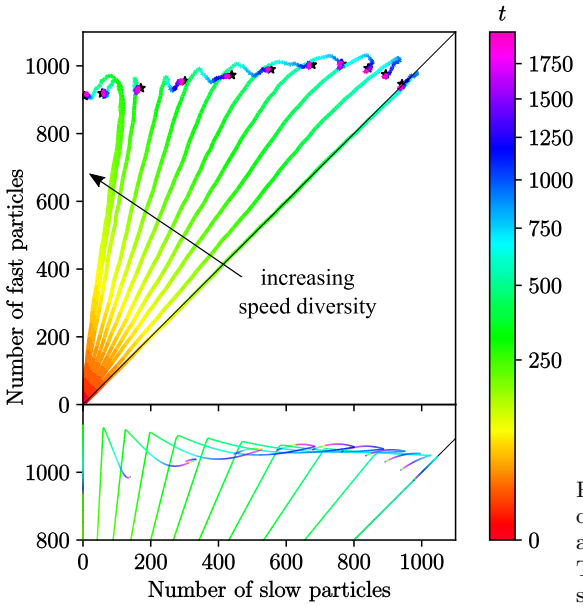

FIG. 2. Top: Wetting layer composition evolution for δ from 0 to 1 every 0.1 and $\phi = 0.18$ (6000 particles in total), measured by the amount of fast and slow particles in it. The diagonal corresponds to the same amount of fast and slow particles. Star symbols show results for the SS. The colorbar shows time (in a nonlinear scale, to focus on the final stage). Bottom: Theory.

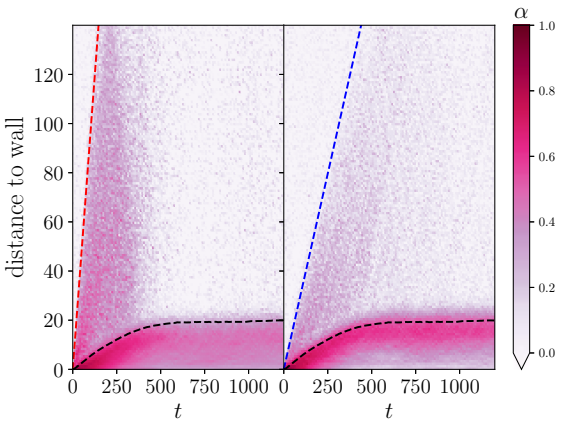

FIG. 3. Spatiotemporal diagram of the self-propulsion orientation parameter $\alpha(x) = \langle \hat{n} \cdot \hat{\nu} \rangle$, for fast (left) and slow (right) particles, with $\delta = 0.5$ and $\phi = 0.18$. The black dashed lines show the mean thickness data shown in Fig. 1(b). The dashed red and blue lines are the "cleaning signals" with velocities $\langle v_x^{(\mathrm{f/s})} \rangle$ (see main text).

computing $\alpha(x) \equiv \langle \hat{n} \cdot \hat{\nu} \rangle$, shown in Fig. 3, where $\hat{n}$ is the inwards normal to the walls and the average is performed over all particles within a y-axis stripe of width d_0, centered at position x. Initially, all particles are randomly oriented, implying $\alpha(x) = 0$ everywhere. Later, particles pointing away from the walls abandon them, leaving regions close to the walls with particles mostly moving towards them. This manifests as regions of $\alpha(x) > 0$ which grow linearly in time; see red and blue lines. This "cleaning signal" has the mean velocity in the x direction at which a randomly oriented particle joins a wall, $\langle v_x^{(\mathrm{f/s})} \rangle = \int_{-\pi/2}^{\pi/2} v_{\mathrm{f/s}} \cos\theta d\theta/\pi = \frac{2v_{\mathrm{f/s}}}{\pi}$, considering only particles moving towards the wall.

At the interface, particles must point towards the wall as otherwise they escape. Consequently, the maximum of $\alpha(x)$ independently locates the interface [see Fig. 3 and compare with the thickness from Fig. 1(b)].

Kinetic theory.—To understand the above results, we develop a simple kinetic theory that estimates the emission and absorption rates of fast and slow particles, $k_{\mathrm{out}}^{(\mathrm{f/s})}$ and $k_{\mathrm{in}}^{(\mathrm{f/s})}$, and thus the layer thickness and composition versus time. For that, we generalize a previous theory originally developed for systems without walls [30] to include mixtures (beyond the simpler approximation for mixtures in Ref. [19]).

Since the global density is low, we use an ideal gas approximation in the gas (see Supplemental Material for density profiles), i.e., particles there do not interact. The rate of absorption of particles by the layer, i.e., the incoming flux per unit length, is written as $k_{\mathrm{in}}^{(\mathrm{f/s})} = \frac{\rho_{\mathrm{g}}^{(\mathrm{f/s})}}{2\pi} \int_{-\pi/2}^{\pi/2} v^{(\mathrm{f/s})} \cos\theta d\theta = \frac{\rho_{\mathrm{g}}^{(\mathrm{f/s})} v^{(\mathrm{f/s})}}{\pi}$, where we integrate v_x over random orientations leading to the particle entering the layer (on the right without loss of generality) weighted by the distribution $\rho_g^{(\mathrm{f/s})}/2\pi$ where $\rho_g^{(\mathrm{f/s})}$ are the gas number densities in contact with the layer. For a time $t^*_{(\mathrm{f/s})}$, $\rho_g^{(\mathrm{f/s})}$ is approximately constant and equal to the initial density as the front of non-interacting gas particles arrives at the layer. Only later, once the "cleaning signal" mentioned before has overcome the entire system, $\rho_g^{(\mathrm{f/s})}$ evolves into the current bulk gas density obtained from the absorption-evaporation balance. We estimate $t^*_{(\mathrm{f/s})} = L_x/\langle v_x^{(\mathrm{f/s})} \rangle$. Finally, $\rho_g^{(\mathrm{f/s})}$ are assumed to change abruptly at $t^*_{(\mathrm{f/s})}$ between their two values. This approximation is more accurate for fast particles (see Fig. 3-left), as the crossover time is smaller and the rotational diffusion has not significantly acted yet; for slow particles, the transition is smoother (see Fig. 3-right).

The SS $k_{\rm out}$ is calculated by solving the diffusion equation in angular space for P, the distribution of orientations at the interface, i.e., $\partial_t P(\theta,t) = \eta\partial_\theta^2 P(\theta,t)$ with absorbing boundaries at $\pm\pi/2$ and initial condition given by the distribution of incident particles, i.e., $P(\pm\pi/2,t)=0$ and $P(\theta,0) = \cos\theta/2$ (as particles with $|\theta| \geq \pi/2$ cannot reach the wall and those with adequate θ will hit it with probability proportional to the x-axis velocity, normalized by integrating between $\pm\pi/2$). The solution is $P(\theta,t) = e^{-\eta t}\cos\theta/2$. For average diameter σ and identical speeds, one can write $k_{\rm out} \equiv -\frac{\dot{N}_{\rm interface}}{\sigma N_{\rm interface}} = \frac{\eta}{\sigma} \to \frac{\kappa\eta}{\sigma}$ where $N_{\rm interface} = \int_{-\pi/2}^{\pi/2} P(\theta,t)$ is the number of particles at the interface and the dot is the time derivative. The result is corrected by a factor κ: when a particle escapes, some inner particles pointing towards the gas follow it in an avalanche-like effect (see Supplemental Material). In the SS, the average number of particles leaving the layer per escape event is denoted $\kappa = 1+\kappa_{\rm excess}$. The value of $\kappa_{\rm excess}$ is treated as a fitting parameter (Ref. [30] found that $\kappa_{\rm excess}\approx 3.5$ works well for all studied v and ϕ in one-component systems without walls; in 1D, $\kappa_{\rm excess}=1$ [38]). However, since at early stages particles in the layer are highly oriented towards the wall (see Fig. 3), avalanche effects become strong only after τ. Before that, once a particle escapes, other particles are likely to be still pointing towards the wall and therefore will not escape. This is incorporated by considering that κ is time-dependent: $\kappa(t) = 1+\kappa_{\rm excess}(1-e^{-\eta t})$, meaning that avalanche events occur with probability $(1-e^{-\eta t})$ as particles start to rotate away from the wall. Finally, with speed diversity, one has

$$k_{\rm out}^{\rm (f/s)} = \frac{N_\ell^{\rm (f/s)}}{N_\ell^{\rm (f)}+N_\ell^{\rm (s)}}\frac{\kappa(t)\eta}{\sigma}, \qquad (2)$$

where $N_\ell^{\rm (f/s)}$ is the number of particles of each type in the layer. Crucially, the factor $N_\ell^{\rm (f/s)}/\left(N_\ell^{\rm (f)}+N_\ell^{\rm (s)}\right)$, which states that particle emission is taken as proportional to the fraction of particles of each type in the layer, nonlinearly couples the occupations of both types.

The evolution of the parameters involved in the absorption and emission rates provides the layer thickness and composition at any time via $dN_\ell^{\rm (f/s)}/dt = \left(k_{\rm in}^{\rm (f/s)} - k_{\rm out}^{\rm (f/s)}\right)L_y$. Assuming particle conservation and that the layer is rectangular and close-packed with the hard-disk occupied area fraction $\phi_{\rm cp} = \pi/(2\sqrt{3})$ (as observed in simulations; see Supplemental Material), we obtained a theory for $\langle h(t)\rangle$. A good agreement occurs for δ near 0 and near 1—see left side of inset of Fig. 1(b). For intermediate δ, the value of $t_{\rm s}^*$ grows larger than the diffusion time and the theory becomes less good for intermediate times—see right side of inset of Fig. 1(b). Also, the theory predicts that the initial deposition rate is independent of δ, $dN_\ell/dt = L_y(\rho_0 v_0/\pi - \eta/\sigma)$, in agreement with the simulations [Fig. 1(b)]. Notably, the overshoot in $\langle h(t)\rangle$ is well captured, which is not the case if either the effect of t^* or the relaxation of κ are not included in the model. The layer composition evolution is also well captured (Fig. 2-bottom), showing also the two stages found in the simulations. For $\delta = 1$, the theory predicts no slow particles are in the layer as they are nonmotile; however, in simulations the transient concentration of slow particles is finite, with an ulterior elimination of them. This difference, also present for $\delta = 0.9$, is due to an induced accumulation of slow particles pushed by fast ones, an effect that is neglected by the ideal gas assumption in the gas. Figure 4 compares theory and simulation for the fraction of slow particles in the layer. In the inset, this comparison is shown for the SS layer thickness, with very good agreement.

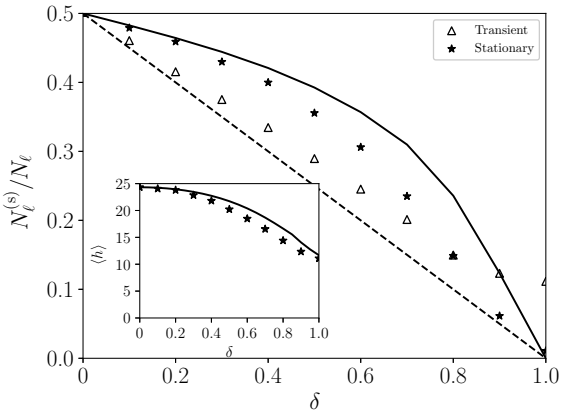

FIG. 4. Ratio between the number of slow particles and the total number of particles in the layer for $\phi = 0.18$ as a function of δ. Dashed and solid lines show the theory for the transient and for the SS, respectively. Triangles and stars show simulation results for the transient and for the SS, respectively. Inset: Stationary mean layer thickness. Stars are simulation and the solid line is the theory.

Conclusions.—Self-propelled Brownian particles under repulsive interactions spontaneously exhibit complete wetting layer formation in the presence of a flat wall due to persistent motion. With simulations and a theory with speed diversity, we cal-

culate and explain the wetting layer composition and thickness. We reveal a two-stage evolution for the layer composition and a transient overshoot for the layer thickness, explained only when the theory considers delayed avalanche-like emissions outwards and a transient front of particles moving towards the walls.

An implicit assumption of the theory is that no segregation develops inside the layers [mean-field approximation in Eq. (2)]. However, Fig. 1(a) indicates that spatial segregation does exist, with fast particles closer to the wall. Concentration profiles confirm this [39]; a more detailed analysis is beyond our scope here. Note that in Ref. [19], for a much denser case showing bulk MIPS ($\phi = 0.6$), the opposite is seen: faster particles accumulate at cluster boundaries.

Since thicker biofilms can protect bacteria, our work shows how biological variability of motility properties can play a central role in determining the survivability of microorganisms. More broadly, our results provide important insights into the behavior of active matter such as the origin of swim pressure overshoots previously seen in confined systems [40]. Furthermore, our framework can be adapted to study bacterial types competing to colonize niches in confined systems [41] as well as the puzzling formation of multi-cellular aggregates such as ameboid slime mold, where slower cells hijack the motion of faster cells to move further and spread their spores at low energy cost [42].

ACKNOWLEDGMENTS

MR-V and RS are supported by Fondecyt Grant No. 1180791 and ANID – Millennium Science Initiative Program – NCN19_170D, Chile. PdC is supported by grant #2021/10139-2, São Paulo Research Foundation (FAPESP), Brazil.

[1] Fernando Peruani, Jörn Starruß, Vladimir Jakovljevic, Lotte Søgaard-Andersen, Andreas Deutsch, and Markus Bär. Collective motion and nonequilibrium cluster formation in colonies of gliding bacteria. *Physical review letters*, 108(9):098102, 2012.

[2] Iván Berdakin, Alejandro V Silhanek, Hernán N Moyano Cortéz, Verónica I Marconi, and Carlos A Condat. Quantifying the sorting efficiency of self-propelled run-and-tumble swimmers by geometrical ratchets. *Central European Journal of Physics*, 11(12):1653–1661, 2013.

[3] Emiliano Perez Ipiña, Stefan Otte, Rodolphe Pontier-Bres, Dorota Czerucka, and Fernando Peruani. Bacteria display optimal transport near surfaces. *Nature Physics*, 15(6):610–615, 2019.

[4] Howard C Berg. *E. coli in Motion*. Springer Science & Business Media, 2008.

[5] Diego Lopez and Eric Lauga. Dynamics of swimming bacteria at complex interfaces. *Physics of Fluids*, 26(7):400–412, 2014.

[6] Soumya Satpathy, Sudip Kumar Sen, Smaranika Pattanaik, and Sangeeta Raut. Review on bacterial biofilm: An universal cause of contamination. *Biocatalysis and agricultural biotechnology*, 7:56–66, 2016.

[7] Andrea Villa-Torrealba, Cristóbal Chávez-Raby, Pablo de Castro, and Rodrigo Soto. Run-and-tumble bacteria slowly approaching the diffusive regime. *Physical Review E*, 101:062607, Jun 2020.

[8] Néstor Sepúlveda and Rodrigo Soto. Wetting transitions displayed by persistent active particles. *Physical Review Letters*, 119(7):078001, 2017.

[9] Iago Grobas, Marco Polin, and Munehiro Asally. Swarming bacteria undergo localized dynamic phase transition to form stress-induced biofilms. *Elife*, 10:e62632, 2021.

[10] René Wittmann and Joseph M Brader. Active brownian particles at interfaces: An effective equilibrium approach. *Europhysics Letters*, 114(6):68004, 2016.

[11] Francesco Turci and Nigel B Wilding. Wetting transition of active brownian particles on a thin membrane. *Physical Review Letters*, 127(23):238002, 2021.

[12] PD Neta, Mykola Tasinkevych, MM Telo da Gama, and CS Dias. Wetting of a solid surface by active matter. *Soft Matter*, 17(9):2468–2478, 2021.

[13] Néstor Sepúlveda and Rodrigo Soto. Universality of active wetting transitions. *Physical Review E*, 98(5):052141, 2018.

[14] Pablo de Castro, Saulo Diles, Rodrigo Soto, and Peter Sollich. Active mixtures in a narrow channel: Motility diversity changes cluster sizes. *Soft Matter*, 17(8):2050–2061, 2021.

[15] Sameer Kumar, Jay Prakash Singh, Debaprasad Giri, and Shradha Mishra. Effect of polydispersity on the dynamics of active brownian particles. *Physical Review E*, 104(2):024601, 2021.

[16] Pablo de Castro and Peter Sollich. Phase separation dynamics of polydisperse colloids: a mean-field lattice-gas theory. *Phys. Chem. Chem. Phys.*, 19:22509–22527, 2017.

[17] Joakim Stenhammar, Raphael Wittkowski, Davide Marenduzzo, and Michael E Cates. Activity-induced phase separation and self-assembly in mixtures of active and passive particles. *Physical Review Letters*, 114(1):018301, 2015.

[18] Pablo de Castro, Francisco M Rocha, Saulo Diles, Rodrigo Soto, and Peter Sollich. Diversity of self-propulsion speeds reduces motility-induced clustering in confined active matter. *Soft Matter*, 17(43):9926–9936, 2021.

[19] Thomas Kolb and Daphne Klotsa. Active binary mixtures of fast and slow hard spheres. *Soft Matter*, 16(8):1967–1978, 2020.

[20] Christian Hoell, Hartmut Löwen, and Andreas M Menzel. Multi-species dynamical density functional theory for microswimmers: Derivation, orientational ordering, trapping potentials, and shear cells. *The Journal of Chemical Physics*, 151(6):064902, 2019.

[21] Raphael Wittkowski, Joakim Stenhammar, and Michael E Cates. Nonequilibrium dynamics of mixtures of active and passive colloidal particles. *New Journal of Physics*, 19(10):105003, 2017.

[22] Pablo de Castro and Peter Sollich. Phase separation of mixtures after a second quench: composition heterogeneities. *Soft Matter*, 15(45):9287–9299, 2019.

[23] Sho C Takatori and John F Brady. A theory for the phase behavior of mixtures of active particles. *Soft Matter*, 11(40):7920–7931, 2015.

[24] AI Curatolo, N Zhou, Y Zhao, C Liu, A Daerr, J Tailleur, and J Huang. Cooperative pattern formation in multi-component bacterial systems through reciprocal motility regulation. *Nature Physics*, pages 1–6, 2020.

[25] Berend van der Meer, Vasileios Prymidis, Marjolein Dijkstra, and Laura Filion. Predicting the phase behavior of mixtures of active spherical particles. *The Journal of Chemical Physics*, 152(14):144901, 2020.

[26] Pritha Dolai, Aditi Simha, and Shradha Mishra. Phase separation in binary mixtures of active and passive particles. *Soft Matter*, 14(29):6137–6145, 2018.

[27] Friederike Schmid and NB Wilding. Wetting of a symmetrical binary fluid mixture on a wall. *Physical Review E*, 63(3):031201, 2001.

[28] Pablo de Castro and Peter Sollich. Critical phase behavior in multi-component fluid mixtures: Complete scaling analysis. *The Journal of Chemical Physics*, 149(20):204902, 2018.

[29] Stephen Williams, Raphaël Jeanneret, Idan Tuval, and Marco Polin. Confinement-induced accumulation and de-mixing of microscopic active-passive mixtures. *Nature Communications*, 13(1):1–8, 2022.

[30] Gabriel S. Redner, Michael F. Hagan, and Aparna Baskaran. Structure and dynamics of a phase-separating active colloidal fluid. *Physical Review Letters*, 110:055701, 01 2013.

[31] René Wittmann, Claudio Maggi, Abhinav Sharma, Alberto Scacchi, Joseph M Brader, and U Marini Bettolo Marconi. Effective equilibrium states in the colored-noise model for active matter i. pairwise forces in the fox and unified colored noise approximations. *Journal of Statistical Mechanics: Theory and Experiment*, 2017(11):113207, 2017.

[32] Raphael Wittkowski, Adriano Tiribocchi, Joakim Stenhammar, Rosalind J Allen, Davide Marenduzzo, and Michael E Cates. Scalar φ 4 field theory for active-particle phase separation. *Nature Communications*, 5(1):1–9, 2014.

[33] In other self-clustering problems, binary mixtures were shown to behave similarly to fully polydisperse systems [14, 16, 18, 22, 28, 43]. Changing our δ is a proxy for changing the standard deviation of a continuous distribution of speeds.

[34] Translational diffusion is included to facilitate (future) theoretical developments and comparisons but it does not affect the qualitative behavior.

[35] Ryan C Maloney, Guo-Jun Liao, Sabine HL Klapp, and Carol K Hall. Clustering and phase separation in mixtures of dipolar and active particles. *Soft Matter*, 16(15):3779–3791, 2020.

[36] Also to facilitate (future) theoretical developments, the modified WCA potential used here has a smooth second derivative.

[37] Kenneth W. Desmond and Eric R. Weeks. Random close packing of disks and spheres in confined geometries. *Physical Review E*, 80:051305, Nov 2009.

[38] Rodrigo Soto and Ramin Golestanian. Run-and-tumble dynamics in a crowded environment: Persistent exclusion process for swimmers. *Physical Review E*, 89(1):012706, 2014.

[39] See Supplemental Material for concentration profiles in the steady state.

[40] Adam Patch, David Yllanes, and M Cristina Marchetti. Kinetics of motility-induced phase separation and swim pressure. *Physical Review E*, 95(1):012601, 2017.

[41] Michael E Hibbing, Clay Fuqua, Matthew R Parsek, and S Brook Peterson. Bacterial competition: surviving and thriving in the microbial jungle. *Nature reviews microbiology*, 8(1):15–25, 2010.

[42] Leonardo Miele and Silvia De Monte. Aggregative cycles evolve as a solution to conflicts in social investment. *PLoS computational biology*, 17(1):e1008617, 2021.

[43] Peter Sollich. Predicting phase equilibria in polydisperse systems. *Journal of Physics: Condensed Matter*, 14(3):R79, 2001.

Fast and slow self-propelled particles interacting with asymmetric obstacles: Wetting, segregation, rectification, and vorticity

Mauricio Rojas-Vega and Rodrigo Soto
Departamento de Física, FCFM, Universidad de Chile, Santiago, Chile

Pablo de Castro*
ICTP South American Institute for Fundamental Research & Instituto de Física Teórica, Universidade Estadual Paulista - UNESP. Rua Dr. Bento Teobaldo Ferraz 271, 01140-070 São Paulo, Brazil.
(Dated: November 30, 2022)

We study a mixture of "fast" and "slow" self-propelled particles in the presence of a regular array of large asymmetric obstacles. For this purpose, simulations of active Brownian particles interacting with a half-disk obstacle are performed in 2D with periodic boundary conditions. The system has two particle types, each of them characterized by its own self-propulsion speed. To isolate the effects of such "speed diversity", the system-average self-propulsion speed is kept unvaried as the degree of speed diversity is tuned. Because of their persistent motion, particles accumulate around the obstacle in a wetting phenomenon. Stationary segregation arises since faster particles are more likely to occupy new available spaces. For degrees of speed diversity $\geq 40\%$, we observe a transition where the self-propulsion of the slower particles becomes too weak and thus these particles start to accumulate more easily over a "layer" of faster particles rather than near the wall. Also, particles traveling from the curved to the flat side of the obstacle spend less time trapped than in the opposite direction. As a result, directed motion emerges spontaneously. We find that the corresponding rectification current is amplified when the degree of speed diversity is increased. In the passive-active limit, the passive particles still undergo directed motion dragged by the active ones. Due to rectification, segregation profiles are different between the curved and flat sides. Near the obstacle corners, pairs of vortices that further contribute to rectification are observed. Their vorticities also increase with speed diversity. Our results provide useful insights into the behavior of active matter in complex environments.

I. INTRODUCTION

Self-propelled particles—such as bacteria, tissue cells, and autophoretic colloids—have the ability to spontaneously accumulate around obstacles even in the absence of attractive forces [1]. Similarly to motility-induced phase separation (MIPS) [2], such *active wetting* arises because active particles have a direction of motion that evolves stochastically but slowly, i.e., their direction of motion is *persistent* [3–5]. For sufficiently large persistence times or densities, particles do not have time to find an escape route and thus become trapped between obstacles and other particles [6]. Active wetting helps control surface adhesion and capillary properties of bacterial biofilms [7–9], whose formation makes bacterial colonies more resilient against antibiotics [10].

In the case of *asymmetric* obstacles, simulations and experiments show that active particles undergo directed motion [11], in addition to accumulation. The spontaneous emergence of net particle transport due to environmental asymmetries, i.e., "rectification" currents, has constituted a central topic in both conceptual and technological contexts for decades [12]. More recently, research on rectification of self-propelled particles has gained momentum [13–23]. In Ref. [24], an initially homogeneous collection of active Brownian particles in 2D was simulated in a regular array of half-disk rigid obstacles oriented in the same fixed direction. The stationary average speed of the particles was found to be nonzero: instead, an effective rectification current emerges since particles traveling from the curved to the flat side of the obstacle spend less time trapped than those in the opposite direction. A similar behavior was observed for an irregular array of randomly-located obstacles oriented in the same fixed direction [25]. The sizes of the obstacles and accumulation layers directly affect the intensity of such rectification currents. Rectification by half-disk obstacles shows that no cavity is needed to trap particles [26], meaning that the existence of convex surfaces with distinct curvatures is sufficient to generate currents.

The authors of Ref. [24] considered identical active particles, i.e., particles with the same self-propulsion speed, rotational diffusion coefficient, and size. However, in natural colonies of bacteria and other microorganisms, a broad dispersion of motility parameters exists due to different ages, reproduction stages, shapes, sizes, and running

* pablo.castro@ictp-saifr.org;
Mostly performed at Universidad de Chile

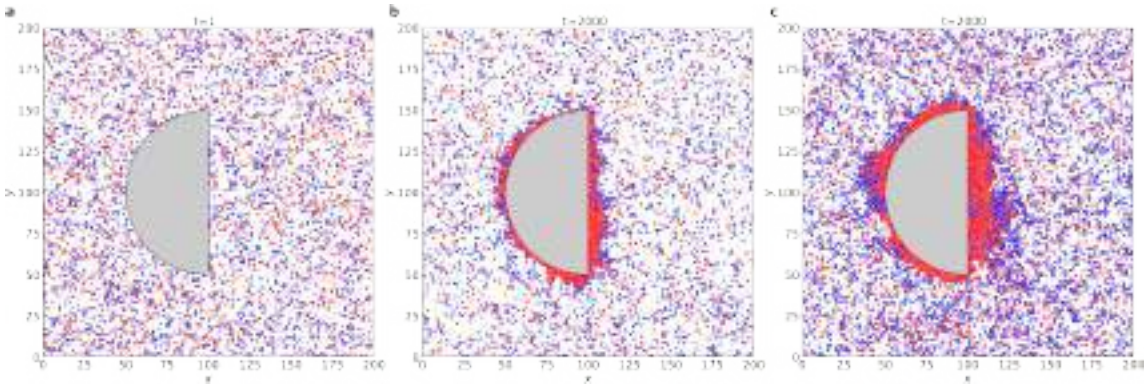

FIG. 1. Snapshots of the system for $\delta = 0.8$, with the faster particles in red and the slower ones in blue. The gray area corresponds to the obstacle. (a) Homogeneous initial state for $\phi = 0.13$. Configurations within the steady state for (b) $\phi = 0.13$ and (c) $\phi = 0.26$.

modes [26–29]. For either passive or active fluids, it is known that "diversity" of some particle attribute generates several new collective behaviors, including changing the nature and loci of phase diagram boundaries and introducing particle-type spatial segregation [4, 30–54]. Still, it remains unclear what are the effects of particle diversity on active rectification by convex asymmetric obstacles. This is important because, in complex biological environments, active matter commonly interacts with obstacles like that, as for example bacteria swimming around the internal structures of the host body where they live [55].

In this work, we use 2D simulations to investigate a *mixture* of "fast" and "slow" active Brownian particles in a regular array of half-disk obstacles. No external fields, hydrodynamic effects, or imposed alignment rules are present. Our main motivation is to understand how "self-propulsion speed diversity" (hereafter just *speed diversity*) couples with the presence of asymmetric convex obstacles and thus alters rectification currents as well as accumulation profiles. In particular, we discuss how these effects are connected with the emergence of segregation [51, 56] and vortices [57, 58] near the obstacle corners.

This paper is organized as follows. In Section II our model and simulation setup is laid out. In Section III, we present our results for wetting and spatial segregation. In Section IV, we turn our attention to rectification effects and how they are connected with the appearance of circulating currents. Section V brings our concluding remarks.

II. MODEL

We consider a binary mixture in 2D composed of N active Brownian disks labeled by i, where $N/2$ of them are "fast" particles, with self-propulsion speed $v_i = v_\mathrm{f} \equiv v_0(1+\delta)$, and the other $N/2$ are "slow" particles, with $v_i = v_\mathrm{s} \equiv v_0(1-\delta)$. The parameter $\delta \in [0,1]$ thus corresponds to the degree of speed diversity. For $\delta = 0$, all particles have identical self-propulsion speed and the system is called "monodisperse". In the opposite limit, when $\delta = 1$, the mixture is passive-active. For simplicity, global compositions other than 50-50% are not considered, but generalization is straightforward. On varying δ, the system-average self-propulsion speed is kept at v_0, which is constant and independent of δ. By doing so, the effects of speed diversity can be isolated. To avoid undesired artificial crystallization [59], each particle is randomly assigned one of two diameters, $d_\mathrm{small} = d_0$ and $d_\mathrm{large} = 1.4d_0$, uncorrelated with speed diversity, where d_0 is the scale that fixes particle diameters. Therefore, there are actually *four* particle types, but we focus on the effects of speed diversity since both particle sizes are similar. The system is said to be just binary or "bidisperse".

The dynamics of each particle's position $\boldsymbol{r}_i$ is governed by the equations

$$\partial_t \boldsymbol{r}_i = v_i\,\hat{\boldsymbol{\nu}}_i + \mu \boldsymbol{F}_i, \quad \partial_t \theta_i = \eta_i(t), \tag{1}$$

where $\hat{\boldsymbol{\nu}}_i = (\cos\theta_i, \sin\theta_i)$ determines the self-propulsion force direction and μ is the mobility, which we take equal to one, meaning that forces are expressed in units of velocity. Also, $\boldsymbol{F}_i = \sum_{j\neq i} \boldsymbol{F}_{ij} + \boldsymbol{F}_i^\mathrm{obst}$ is the net force on particle i due to interactions with other particles and with a half-disk obstacle, of radius $D/2$. The noise term $\eta_i(t)$ is Gaussian and white, with mean $\langle \eta_i(t) \rangle = 0$ and

correlation $\langle \eta_i(t)\eta_j(t')\rangle = 2\eta\delta_{ij}\delta(t-t')$, where η is the rotational diffusion coefficient.

The interparticle interactions are taken as a soft repulsive WCA-like potential [60] defined in terms of the interparticle distance r_{ij} as [61]

$$U = \begin{cases} 2^{\frac{3}{2}}\left(\frac{\sigma_{ij}}{r_{ij}}\right)^3 - 3\left(\frac{\sigma_{ij}}{r_{ij}}\right)^6 + \left(\frac{\sigma_{ij}}{r_{ij}}\right)^{12} - \frac{3}{4}, & r_{ij} \le 2^{\frac{1}{6}}\sigma_{ij}, \\ 0, & r_{ij} > 2^{\frac{1}{6}}\sigma_{ij} \end{cases} \tag{2}$$

with $\sigma_{ij} \equiv \frac{1}{2}(d_i + d_j)$, where d_i is the particle diameter of particle i. For the particle-obstacle interaction between particle i and the curved side, d_j is replace by D. For the interaction with the flat side, d_j is replaced by zero. Finally, there is no torque on the particles, and the directors $\hat{\boldsymbol{\nu}}_i$ evolve only by rotational diffusion [Eq. (1)].

The parameter distinguishing the particle types is the self-propulsion speed. We choose units and fixed parameters such that $v_0 = 1$ and the diameter scale is $d_0 = 1$. For the rotational diffusion coefficient and simulation time step, we take $\eta = 5 \times 10^{-3}$ and $\Delta t = 10^{-3}$, respectively. Initially, particles are distributed homogeneously at random positions with random velocity directions, independent of their types. The simulation is performed in a square box of side $L = 200$ (such that $D = L/2$) and with periodic boundary conditions, simulating therefore an infinite regular array of identical obstacles. The centers of the flat side and of the simulation box coincide. The average free-particle persistence length is $\ell \equiv v_0/\eta = 200$, which is comparable to the system and obstacle sizes. The occupied area fraction ϕ is defined as the total area occupied by particles divided by the area of the simulation box minus the obstacle, i.e.,

$$\phi = \frac{N}{2} \times \frac{\pi\left(d_{\text{small}}^2 + d_{\text{large}}^2\right)/4}{L^2 - \frac{\pi}{2}\left(\frac{D}{2}\right)^2}. \tag{3}$$

III. WETTING AND SEGREGATION

Movie 1 of the Supplementary Material shows the dynamics between the initial state and the stationary state ($t \ge 2000$) for $\phi = 0.13$ and $\delta = 0.8$. Snapshots of the initial and stationary states are shown in Figs. 1a and b. After particles quickly accumulate around the obstacle, the average thickness of the wetting layer stabilizes once the concentration of the "gas" (i.e., outside the layer) becomes sufficiently low that absorption and emission rates for the layer are equal. Because available spaces are more likely to be occupied by the faster particles (as they arrive there typically before the slower ones), segregation emerges. For larger area fractions, the wetting layer increases in size, as shown in Fig. 1c for $\phi = 0.26$. In all cases studied below ($\phi = 0.08$, 0.13, and 0.26 for various values of δ), the stationary gas concentration is sufficiently low such that no stationary clusters appear in the gas. That is, the residual gas density after the wetting layer has been formed is smaller than the necessary to produce MIPS [2]. Also, in the transient regime, the condensation by heterogeneous nucleation on the obstacle is faster than an eventual MIPS. Hence, the only condensed phase in the system is the wetting layer on the obstacle. Movies 2 and 3 of the Supplementary Material show, respectively, the transient and the steady state for $\phi = 0.26$ with $\delta = 0.8$.

Due to crowding, the dynamics inside the wetting cluster is much slower than that in the gas. Movie 1 also shows that the interface between the wetting layer and the gas fluctuates strongly. Presumably, this is a consequence of active capillary-like effects [62, 63] enhanced by the fact that particles can escape from the cluster not only by rotational diffusion but also by reaching the end of the obstacle wall.

Fig. 2 shows the stationary concentration fields for the total, "slow", and "fast" particles concentrations, denoted respectively by $n(\boldsymbol{r})$, $n_{\text{s}}(\boldsymbol{r})$, and $n_{\text{f}}(\boldsymbol{r})$, for selected values of ϕ and δ. They are defined similarly to the area fraction ϕ but are calculated locally using coarse-graining square boxes of side 2.5. We counted the number of particle centers in each box, multiplied by the area of the corresponding particle, and then divided the result by the area of the coarse-graining box. For boxes that include a fraction of the obstacle, the available area was calculated using standard Monte Carlo integration.

Fig. 2a shows the monodisperse ($\delta = 0$) scenario studied in Ref. [24]. The stationary accumulation is more pronounced for higher ϕ and decays smoothly towards the gas. For $\delta > 0$, we observe that $n_{\text{s}}(\boldsymbol{r})$ and $n_{\text{f}}(\boldsymbol{r})$ are significantly different from each other as the faster particles dominate the occupation closer to the obstacle, whereas the slower particles accumulate less sharply.

Concentration profiles were obtained by averaging the concentration fields along the direction parallel to each wall. For the curved side, the concentration is plotted against the radial distance to the wall. The concentration of faster particles decays monotonically towards the gas irrespective of δ, for both the curved and flat sides (data not shown). Near the walls, the accumulation of faster particles becomes more pronounced for higher δ as their incoming flux is naturally higher and also because a stronger self-propulsion means that the particle can open the way towards the obstacle by displacing other particles. Figure 3 shows concentration

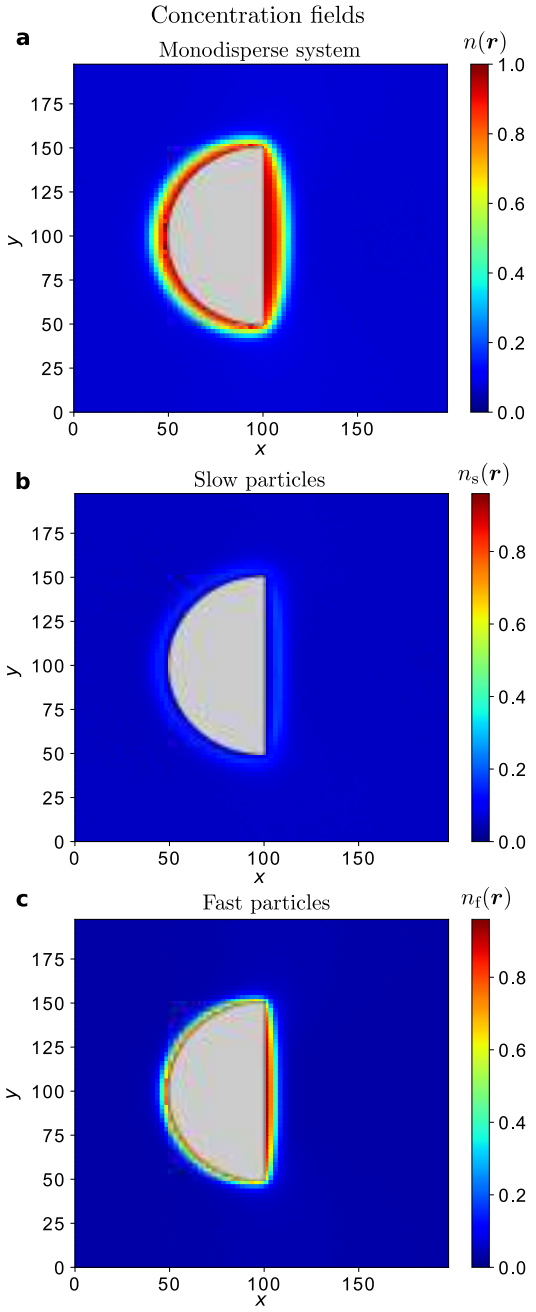

FIG. 2. Stationary concentration fields for $\phi = 0.13$. (a) Monodisperse system ($\delta = 0$). (b) Slow and (c) fast particles for mixture case with $\delta = 0.8$.

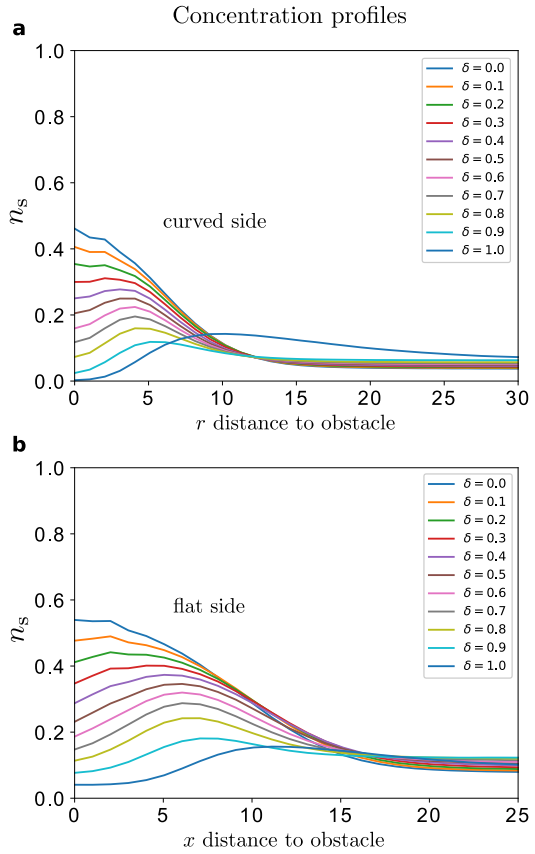

FIG. 3. Stationary concentration profiles of slow particles for various δ values and $\phi = 0.13$. (a) Curved and (b) flat side.

profiles of the slower particles for both sides and several values of δ. In this case, a peak located further away from the obstacle wall is clearly observed for $\delta \geq 0.4$. This transition occurs when the slower particles become sufficiently slow that they accumulate more easily on the boundary of the "layer" of faster particles than closer to the obstacle wall. Notice that the peak is less pronounced on the curved side.

To measure the degree of spatial segregation, we calculate [56]

$$\zeta = 1 - \frac{\int n_s(\boldsymbol{r}) n_f(\boldsymbol{r})\, dx\, dy}{\sqrt{\int n_s^2(\boldsymbol{r})\, dx\, dy \int n_f^2(\boldsymbol{r})\, dx\, dy}}, \qquad (4)$$

a segregation parameter which takes into account the overlapping between the concentration profiles. As such, $\zeta = 1$ implies complete segregation and $\zeta = 0$ means complete mixing, which in turn occurs only if $n_s(\boldsymbol{r}) \propto n_f(\boldsymbol{r})$. Fig. 4a shows that the degree of segregation increases with speed diversity, but complete segregation is never obtained, not even in the passive-active limit. This has two causes. Firstly, not all active particles participate in the wetting cluster, as it stops increasing once the gas concentration is sufficiently low. Secondly, some passive particles remain trapped inside the wetting layer by the active ones. Furthermore, Fig. 4a

shows that the degree of segregation in the low global concentration limit is almost independent of ϕ.

The segregation can also be quantified by the ratio between the slow and faster particles concentration profiles (Figs. 4b and c for the curved and flat side, respectively). For $\delta = 1$, there are almost no passive particles near the wall and the curved side concentration ratio is more than one order of magnitude bigger than for $\delta = 0.9$. This reveals that the case $\delta = 0.9$ is not as close to a passive-active mixture as one might expect. In fact, Fig. 3 shows a significant difference in the behavior of the concentration profile between $\delta = 0.9$ and $\delta = 1.0$. This can be understood by noticing that for $\delta = 0.9$ the slow particles persistence length $v_s/\eta = v_0(1-\delta)/\eta = 20$ is still comparable to other relevant length scales such as the wetting layer thickness, the obstacle size, and the system size. We also notice that there is more segregation on the curved side than on the flat side as particles are less capable to penetrate and settle inside that layer. For slow particles, such "expulsion" becomes more pronounced. In fact, it is almost impossible for a particle with weak self-propulsion to remain near the wetting interface without being wiped out into the gas by the rectification "wind" (see Section IV below); conversely, particles on the flat side can accumulate closer to the wall since the particle current on the flat side near the interface is not sufficient to wipe them out. This can be confirmed by looking once again at the passive particles profile ($\delta = 1$) in Fig. 3, where the concentration near the wall is practically zero on the curved side but not so on the flat side.

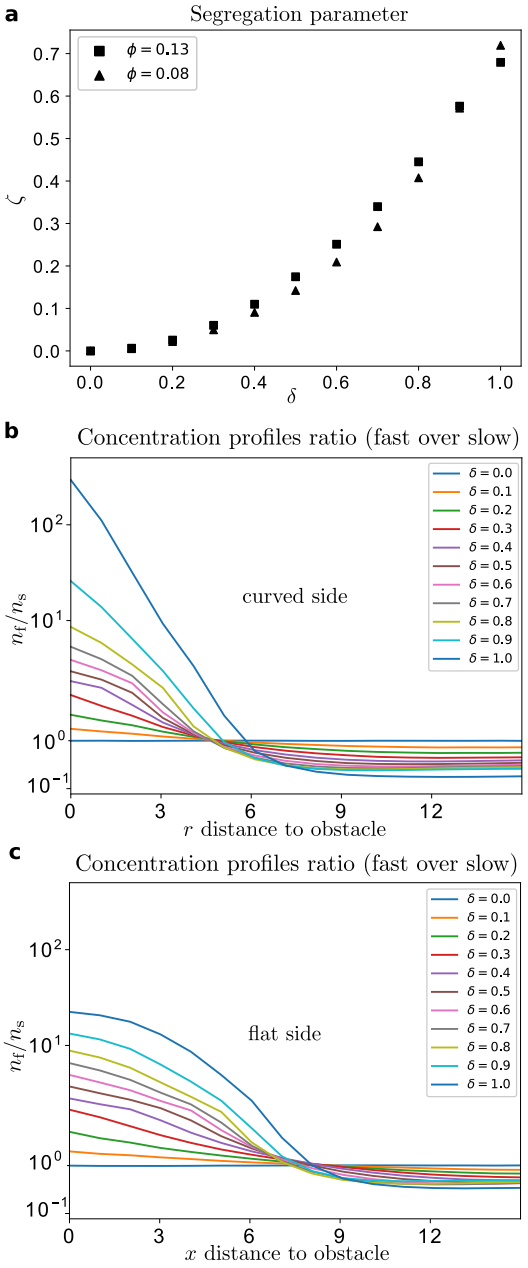

FIG. 4. (a) Global segregation parameter for $\phi = 0.08$ and $\phi = 0.13$ versus δ. (b) Curved and (c) flat side concentration profiles ratios (fast over slow) for $\phi = 0.13$ and various values of δ.

IV. RECTIFICATION AND VORTICITY

The asymmetric shape of the obstacle implies that particles traveling from the curved to the flat side will spend less time to overcome it than those in the opposite direction. In the monodisperse case ($\delta = 0$), a rectifications current arises in the stationary state [24]. We now focus on the behavior for $\delta > 0$. Fig. 5 shows the total stationary current (vector) field $\boldsymbol{j}(\boldsymbol{r}) \equiv n(\boldsymbol{r})\,\boldsymbol{v}(\boldsymbol{r})$, where $\boldsymbol{v}(\boldsymbol{r})$ is the actual velocity field (not the self-propulsion velocity field). Global rectification along the $+x$ direction is indicated by the fact that most current arrows point to the right or have a large $+x$ component. Particles slide on the curved side towards the right and are subject to higher current than in the gas. In fact, the highest local current is observed near the corners. For the flat side, the local current is in the opposite direction, i.e., the $-x$ direction (reflecting the appearance of vortices, as discussed below), but near the obstacle it is constrained to the y-axis only. Far from the obstacle, the current field changes to the $+x$ direction again.

To investigate how rectification is affected by speed diversity, we show in Fig. 6a the mean velocity in x, $\langle v_x \rangle$, averaged over particles and time instants within the steady state, as a function of

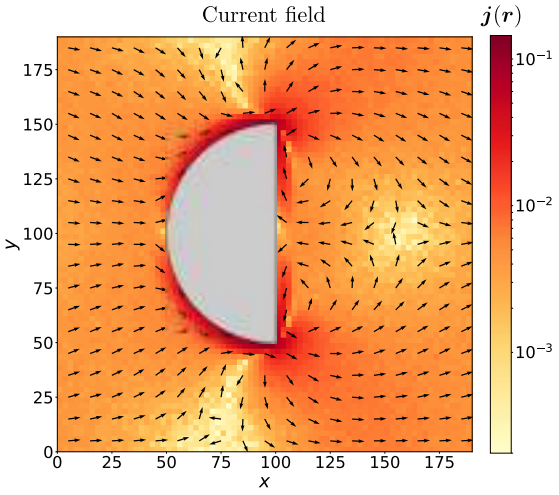

FIG. 5. Total stationary current field $\boldsymbol{j}$ for $\phi = 0.13$ and $\delta = 0.8$. For clarity, the arrows have all the same size and only indicate the direction of the current, while the magnitude of $\boldsymbol{j}$ is given via the color legend.

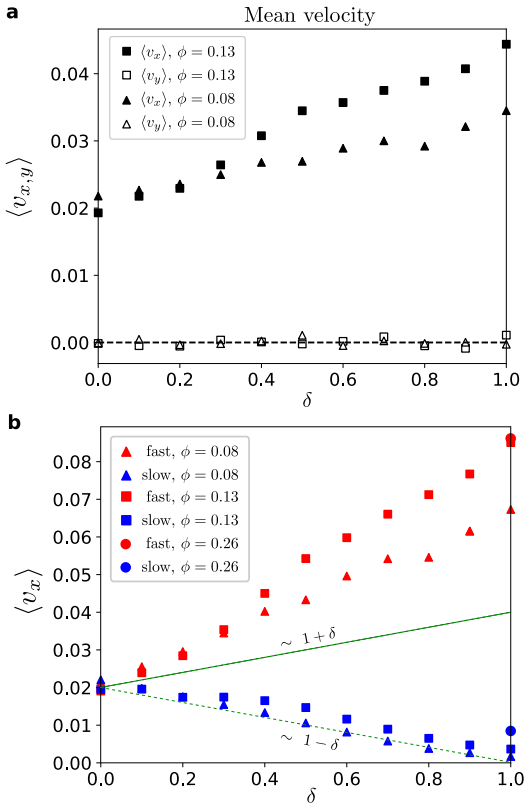

FIG. 6. Stationary mean (actual) velocity averaged over particles and realizations as a function of δ for $\phi = 0.08$ and 0.13. (a) Total mean velocity in x and in y. (b) Mean velocity in x for slow and for fast particles. The case $\phi = 0.26$ has been included only for $\delta = 1$, avoiding an overcrowding of the figure. The dashed lines present the naïve dependence for the mean velocity of the fast and slow particles.

δ. As a control, we also show that $\langle v_y \rangle$ is essentially zero, as expected. More importantly, $\langle v_x \rangle$ increases with δ, indicating an *amplification* of rectification currents that is induced solely by speed diversity (remember that each type corresponds to 50% of all particles and the system-average self-propulsion speed does not change with δ). By looking at $\langle v_x \rangle$ for each particle type in Fig. 6b, we see that, indeed, as δ increases, the faster particles undergo a rectification *increase* which is larger than the rectification *decrease* of the slower particles, even though their self-propulsion speeds were varied by the same amounts, in magnitude. Indeed, the average speed of fast particles is larger than the naïve dependence proportional to $1+\delta$, a manifestation of significant interaction effects. The slow particles for low ϕ do follow the naïve dependence proportional to $1-\delta$, but as the density increases interactions take over and their rectified velocity increases.

This rectification amplification induced by speed diversity can be understood as follows. First, $\langle v_x \rangle(\delta)$ must be an even function of δ since $\delta \to -\delta$ just relabels particle types and thus should have no physical consequence. Now, consider the monodisperse case of Ref. [24]. Fig. 3a therein suggests that the rectification current $\langle v_x \rangle \sim \exp(-\eta d_0/v_0)$, where we remind that η is the rotational diffusion coefficient and we incorporated the self-propulsion speed v_0 and the particles' diameter by dimensional analysis,. This makes sense: by increasing the active speed v_0, activity-induced rectification ought to increase as well. We now assume that the *qualitative* behavior of $\langle v_x \rangle(\delta)$ can be obtained simply from an arithmetic average between $\exp(-\eta d_0/v_\mathrm{s})$ and $\exp(-\eta d_0/v_\mathrm{f})$ (On the other hand, the *quantitative* behavior should require a more complicated analysis, as indicated, for example, by the δ-dependence of motility-induced cluster sizes in a system of slow and fast run-and-tumble particles studied in Ref. [64].) Expanding in δ, indeed no linear δ dependence survives, as anticipated. Also, for sufficiently high η, $\langle v_x \rangle(\delta)$ indeed increases with δ as observed numerically. (The same qualitative analytical examination indicates that a transition for much lower η *might* exist in the simulations, through which $\langle v_x \rangle(\delta)$ would become a decreasing function of δ. That is beyond our scope because the corresponding persistent lengths would be extremely large.)

Furthermore, Fig. 6b shows that $\langle v_x \rangle$ for the slower particles does not vanish completely at the active-passive limit $\delta = 1$. In fact, the passive

particles continue to contribute positively to the total $\langle v_x \rangle$. Such behavior where the motion of passive particles is "enhanced" by active ones has been previously reported in the context of motility-induced phase separation: the presence of active particles in fact induces *clustering* for the passive ones [34, 36, 65]. Here, what we find is that the active particles induce a finite degree of *rectification* for the passive ones, which increases with ϕ.

Revisiting the current field for the active-active mixture case, we notice that the flat side has a nonvanishing total local current moving away from the obstacle center along the y-axis. This behavior is connected to the appearance of vortices. We define

$$\boldsymbol{\omega}(\boldsymbol{r}) \equiv \nabla \times \boldsymbol{j}(\boldsymbol{r}) \tag{5}$$

as a vorticity-like field (not exactly the vorticity since it is the curl of the current field, not of the velocity field) and plot its z component in Fig. 7. We observe that one pair of vortices is formed around each obstacle corner.

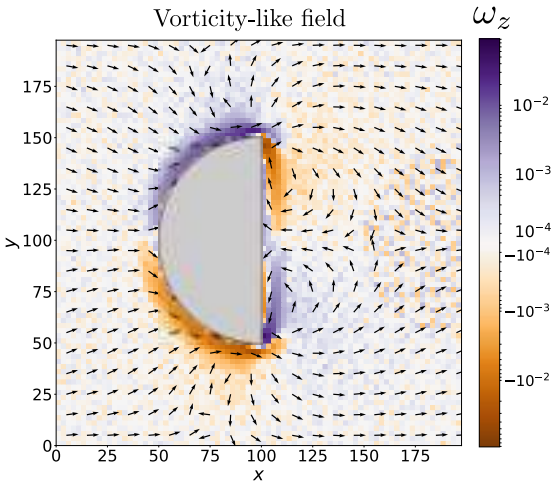

FIG. 7. Vorticity-like field defined by the z-component of $\boldsymbol{\omega}(\boldsymbol{r}) \equiv \nabla \times \boldsymbol{j}(\boldsymbol{r})$, i.e., ω_z, for $\delta = 0.8$ and $\phi = 0.13$, with positive (negative) values meaning counterclockwise (clockwise) rotation. The color scheme is shown on the right in symmetric logarithmic scale. The arrows, as in Fig. 5, show the direction of the total particle current field.

For each pair, one of the vortices is produced by the particles that slide on the curved side and the other by those that slide on the flat side. The latter particles move away from the obstacle center, along the y-axis. For each side, once the obstacle wall ends, the particles start to interact directly with those that were sliding on the other side. As a consequence, velocities become reoriented, thus generating the corresponding vortices.

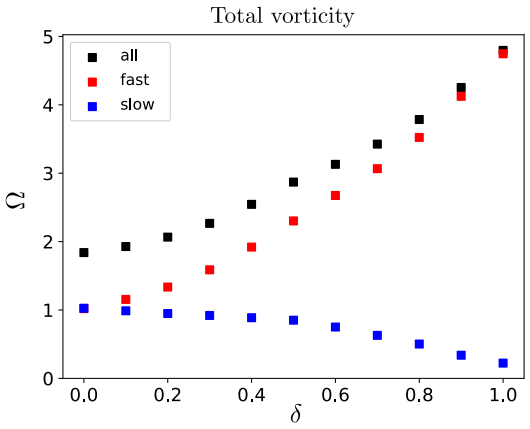

FIG. 8. Total global magnitude of vorticity-like field as a function of δ for $\phi = 0.13$. The partial vorticities, for fast and slow particles, are obtained from the partial current fields $\boldsymbol{j}_{\mathrm{f/s}}(\boldsymbol{r}) \equiv n_{\mathrm{f/s}}(\boldsymbol{r})\, \boldsymbol{v}_{\mathrm{f/s}}(\boldsymbol{r})$.

To see how vorticity changes with speed diversity, Fig. 8 shows the global vorticity magnitude, defined as $\Omega \equiv \int \omega_z(\boldsymbol{r})\, dx\, dy$, where we keep the signs in ω_z. The intensity of the vorticity also increases with δ: the particles that participate more in the vortices are those close to the obstacle and, as discussed above, these correspond to the faster particles.

V. CONCLUSIONS

Here we considered an active mixture of fast and slow swimmers in the presence of asymmetric obstacles (with a curved and a flat side). We identified wetting, segregation, rectification and vorticity. As such, this problem arises as an interesting playground for studying several phenomena. Using simulations, we showed how the degree of diversity of self-propulsion speeds alters these phenomena, both quantitatively and qualitatively.

The segregation profiles for speed diversity parameter $\delta = 0.9$ are significantly different from the $\delta = 1$ passive-active case. Also, for $\delta \geq 0.4$ a peak in the concentration profiles of the slower particles arises far from the wall and over the faster particles "layer", as their self-propulsion becomes too "weak" to allow for accumulation near the wall.

Regarding rectification, our results complement the explanation given in Ref. [24] for monodisperse systems: particles coming from the left side become rectified when sliding along the curved side of the obstacle, whereas those coming from the right side are reoriented due to the formation of vortices which rotate favorably to the global current near the corners. Also, in the passive-active case, we

observe that complete segregation is not achieved and that the passive particles continue to rectify as they are pushed by the active ones.

The present work provides a number of insights into the behavior of more realistic active matter systems such as bacterial fluids interacting with real surfaces. In the future, the effects of other active matter features and ingredients as well as distinct obstacle shapes would constitute an interesting research avenue.

ACKNOWLEDGMENTS

This research is supported by Fondecyt Grant No. 1180791 (RS) and ANID – Millennium Science Initiative Program – NCN19_170D (MR-V, RS and PdC), Chile. PdC was supported by a Postdoctoral Fellowship from São Paulo Research Foundation (FAPESP), grant 2021/10139-2, and FAPESP grant ICTP-SAIFR 2016/01343-7, Brazil.

[1] Néstor Sepúlveda and Rodrigo Soto, "Wetting transitions displayed by persistent active particles," Physical Review Letters **119**, 078001 (2017).

[2] Michael E Cates and Julien Tailleur, "Motility-induced phase separation," Annu. Rev. Condens. Matter Phys. **6**, 219–244 (2015).

[3] René Wittmann and Joseph M Brader, "Active brownian particles at interfaces: An effective equilibrium approach," EPL (Europhysics Letters) **114**, 68004 (2016).

[4] Pablo de Castro, Saulo Diles, Rodrigo Soto, and Peter Sollich, "Active mixtures in a narrow channel: Motility diversity changes cluster sizes," Soft Matter **17**, 2050–2061 (2021).

[5] Francesco Turci and Nigel B Wilding, "Wetting transition of active brownian particles on a thin membrane," arXiv preprint arXiv:2111.02492 (2021).

[6] Néstor Sepúlveda and Rodrigo Soto, "Universality of active wetting transitions," Physical Review E **98**, 052141 (2018).

[7] Rodrigo Soto and Ramin Golestanian, "Run-and-tumble dynamics in a crowded environment: Persistent exclusion process for swimmers," Physical Review E **89**, 012706 (2014).

[8] Pin Nie, Francisco Alarcon, Iván López-Montero, Belén Orgaz, Chantal Valeriani, and Massimo Pica Ciamarra, "In-silico modeling of early-stage biofilm formation," Soft Materials , 1–13 (2021).

[9] Giordano Fausti, Elsen Tjhung, Michael Cates, and Cesare Nardini, "Capillary interfacial tension in active phase separation," arXiv preprint arXiv:2103.15563 (2021).

[10] Iago Grobas, Marco Polin, and Munehiro Asally, "Swarming bacteria undergo localized dynamic phase transition to form stress-induced biofilms," bioRxiv (2020).

[11] CJ Olson Reichhardt and Charles Reichhardt, "Ratchet effects in active matter systems," Annual Review of Condensed Matter Physics **8**, 51–75 (2017).

[12] Peter Reimann, "Brownian motors: noisy transport far from equilibrium," Physics reports **361**, 57–265 (2002).

[13] Peter Galajda, Juan Keymer, Paul Chaikin, and Robert Austin, "A wall of funnels concentrates swimming bacteria," Journal of bacteriology **189**, 8704–8707 (2007).

[14] Pulak K Ghosh, Vyacheslav R Misko, Fabio Marchesoni, and Franco Nori, "Self-propelled janus particles in a ratchet: Numerical simulations," Physical Review Letters **110**, 268301 (2013).

[15] Andrey Pototsky, Aljoscha M Hahn, and Holger Stark, "Rectification of self-propelled particles by symmetric barriers," Physical Review E **87**, 042124 (2013).

[16] Joakim Stenhammar, Raphael Wittkowski, Davide Marenduzzo, and Michael E Cates, "Light-induced self-assembly of active rectification devices," Science Advances **2**, e1501850 (2016).

[17] Wei-jing Zhu, Teng-Chao Li, Wei-rong Zhong, and Bao-quan Ai, "Rectification and separation of mixtures of active and passive particles driven by temperature difference," The Journal of chemical physics **152**, 184903 (2020).

[18] Caleb G Wagner, Michael F Hagan, and Aparna Baskaran, "Steady states of active brownian particles interacting with boundaries," arXiv preprint arXiv:2109.06353 (2021).

[19] Caleb G Wagner, Michael F Hagan, and Aparna Baskaran, "Steady-state distributions of ideal active Brownian particles under confinement and forcing," Journal of Statistical Mechanics: Theory and Experiment **2017**, 043203 (2017).

[20] Jean-François Derivaux, Robert L Jack, and Michael E Cates, "Rectification in a mixture of active and passive particles subject to a ratchet potential," arXiv preprint arXiv:2112.12437 (2021).

[21] Bao-quan Ai, "Ratchet transport powered by chiral active particles," Scientific reports **6**, 1–7 (2016).

[22] Sergey Savel?ev, F Marchesoni, and Franco Nori, "Controlling transport in mixtures of interacting particles using brownian motors," Physical review letters **91**, 010601 (2003).

[23] Sergey Savel?ev, Fabio Marchesoni, and Franco Nori, "Manipulating small particles in mixtures far from equilibrium," Physical review letters **92**, 160602 (2004).

[24] Fabricio Q Potiguar, GA Farias, and WP Ferreira, "Self-propelled particle transport in regular arrays of rigid asymmetric obstacles," Physical Review E **90**, 012307 (2014).

[25] AD Borba, Jorge LC Domingos, ECB Moraes, FQ Potiguar, and WP Ferreira, "Controlling the

transport of active matter in disordered lattices of asymmetrical obstacles," Physical Review E **101**, 022601 (2020).
[26] Iván Berdakin, Alejandro V Silhanek, Hernán N Moyano Cortéz, Verónica I Marconi, and Carlos A Condat, "Quantifying the sorting efficiency of self-propelled run-and-tumble swimmers by geometrical ratchets," Central European Journal of Physics **11**, 1653–1661 (2013).
[27] Emiliano Perez Ipiña, Stefan Otte, Rodolphe Pontier-Bres, Dorota Czerucka, and Fernando Peruani, "Bacteria display optimal transport near surfaces," Nature Physics **15**, 610–615 (2019).
[28] Howard C Berg, *E. coli in Motion* (Springer Science & Business Media, 2008).
[29] Javier Sparacino, Gastón L Miño, Adolfo J Banchio, and VI Marconi, "Solitary choanoflagellate dynamics and microconfined directed transport," Journal of Physics D: Applied Physics **53**, 505403 (2020).
[30] Pablo de Castro and Peter Sollich, "Phase separation dynamics of polydisperse colloids: a mean-field lattice-gas theory," Phys. Chem. Chem. Phys. **19**, 22509–22527 (2017).
[31] Pablo de Castro and Peter Sollich, "Critical phase behavior in multi-component fluid mixtures: Complete scaling analysis," The Journal of Chemical Physics **149**, 204902 (2018).
[32] Pablo de Castro and Peter Sollich, "Phase separation of mixtures after a second quench: composition heterogeneities," Soft Matter **15**, 9287–9299 (2019).
[33] Pablo Souza de Castro Melo, *Phase separation of polydisperse fluids* (King's College London, 2019).
[34] Joakim Stenhammar, Raphael Wittkowski, Davide Marenduzzo, and Michael E Cates, "Activity-induced phase separation and self-assembly in mixtures of active and passive particles," Physical Review Letters **114**, 018301 (2015).
[35] Naveen Kumar Agrawal and Pallab Sinha Mahapatra, "Alignment-mediated segregation in an active-passive mixture," Physical Review E **104**, 044610 (2021).
[36] Thomas Kolb and Daphne Klotsa, "Active binary mixtures of fast and slow hard spheres," Soft Matter **16**, 1967–1978 (2020).
[37] Christian Hoell, Hartmut Löwen, and Andreas M Menzel, "Multi-species dynamical density functional theory for microswimmers: Derivation, orientational ordering, trapping potentials, and shear cells," The Journal of Chemical Physics **151**, 064902 (2019).
[38] Raphael Wittkowski, Joakim Stenhammar, and Michael E Cates, "Nonequilibrium dynamics of mixtures of active and passive colloidal particles," New Journal of Physics **19**, 105003 (2017).
[39] Sho C Takatori and John F Brady, "A theory for the phase behavior of mixtures of active particles," Soft Matter **11**, 7920–7931 (2015).
[40] AY Grosberg and J-F Joanny, "Nonequilibrium statistical mechanics of mixtures of particles in contact with different thermostats," Physical Review E **92**, 032118 (2015).
[41] AI Curatolo, N Zhou, Y Zhao, C Liu, A Daerr, J Tailleur, and J Huang, "Cooperative pattern formation in multi-component bacterial systems through reciprocal motility regulation," Nature Physics , 1–6 (2020).
[42] Yan Wang, Zhuanglin Shen, Yiqi Xia, Guoqiang Feng, and Wende Tian, "Phase separation and super diffusion of binary mixtures of active and passive particles," Chinese Physics B **29**, 053103 (2020).
[43] Berend van der Meer, Vasileios Prymidis, Marjolein Dijkstra, and Laura Filion, "Predicting the phase behavior of mixtures of active spherical particles," The Journal of Chemical Physics **152**, 144901 (2020).
[44] Pritha Dolai, Aditi Simha, and Shradha Mishra, "Phase separation in binary mixtures of active and passive particles," Soft Matter **14**, 6137–6145 (2018).
[45] Andrea Villa-Torrealba, Cristóbal Chávez-Raby, Pablo de Castro, and Rodrigo Soto, "Run-and-tumble bacteria slowly approaching the diffusive regime," Phys. Rev. E **101**, 062607 (2020).
[46] Sameer Kumar, Jay Prakash Singh, Debaprasad Giri, and Shradha Mishra, "Effect of polydispersity on the dynamics of active brownian particles," Physical Review E **104**, 024601 (2021).
[47] Sudipta Pattanayak, Jay Prakash Singh, Manoranjan Kumar, and Shradha Mishra, "Speed inhomogeneity accelerates information transfer in polar flock," Physical Review E **101**, 052602 (2020).
[48] Vivek Semwal, Jay Prakash, and Shradha Mishra, "Dynamics of active run and tumble and passive particles in binary mixture," arXiv preprint arXiv:2112.13015 (2021).
[49] Jay Prakash Singh and Shradha Mishra, "Phase separation in a binary mixture of self-propelled particles with variable speed," Physica A: Statistical Mechanics and its Applications **544**, 123530 (2020).
[50] Friederike Schmid and NB Wilding, "Wetting of a symmetrical binary fluid mixture on a wall," Physical Review E **63**, 031201 (2001).
[51] Ricardo Brito, H Enríquez, S Godoy, and R Soto, "Segregation induced by inelasticity in a vibrofluidized granular mixture," Physical Review E **77**, 061301 (2008).
[52] Andrea Costanzo, Jens Elgeti, Thorsten Auth, Gerhard Gompper, and Marisol Ripoll, "Motility-sorting of self-propelled particles in microchannels," EPL (Europhysics Letters) **107**, 36003 (2014).
[53] Enys Mones, András Czirók, and Tamás Vicsek, "Anomalous segregation dynamics of self-propelled particles," New journal of physics **17**, 063013 (2015).
[54] Shradha Mishra, Kolbjørn Tunstrøm, Iain D Couzin, and Cristián Huepe, "Collective dynamics of self-propelled particles with variable speed," Physical Review E **86**, 011901 (2012).

[55] Willow R DiLuzio, Linda Turner, Michael Mayer, Piotr Garstecki, Douglas B Weibel, Howard C Berg, and George M Whitesides, "Escherichia coli swim on the right-hand side," Nature **435**, 1271–1274 (2005).

[56] Ricardo Brito and Rodrigo Soto, "Competition of brazil nut effect, buoyancy, and inelasticity induced segregation in a granular mixture," The European Physical Journal Special Topics **179**, 207–219 (2009).

[57] Jun-xing Pan, Hua Wei, Mei-jiao Qi, Hui-fang Wang, Jin-jun Zhang, Kang Chen, *et al.*, "Vortex formation of spherical self-propelled particles around a circular obstacle," Soft Matter **16**, 5545–5551 (2020).

[58] Lorenzo Caprini, U Marini Bettolo Marconi, and Andrea Puglisi, "Spontaneous velocity alignment in motility-induced phase separation," Physical Review Letters **124**, 078001 (2020).

[59] Kenneth W Desmond and Eric R Weeks, "Random close packing of disks and spheres in confined geometries," Physical Review E **80**, 051305 (2009).

[60] Ryan C Maloney, Guo-Jun Liao, Sabine HL Klapp, and Carol K Hall, "Clustering and phase separation in mixtures of dipolar and active particles," Soft matter **16**, 3779–3791 (2020).

[61] The modified WCA potential used here has smooth second derivative, allowing it to be more suitable for (future) theoretical developments.

[62] Ahmad K Omar, Zhen-Gang Wang, and John F Brady, "Microscopic origins of the swim pressure and the anomalous surface tension of active matter," Physical Review E **101**, 012604 (2020).

[63] Adam Wysocki and Heiko Rieger, "Capillary action in scalar active matter," Physical Review Letters **124**, 048001 (2020).

[64] Pablo de Castro, Francisco M. Rocha, Saulo Diles, Rodrigo Soto, and Peter Sollich, "Diversity of self-propulsion speeds reduces motility-induced clustering in confined active matter," Soft Matter , – (2021).

[65] Shreyas Gokhale, Junang Li, Alexandre Solon, Jeff Gore, and Nikta Fakhri, "Dynamic clustering of passive colloids in dense suspensions of motile bacteria," arXiv preprint arXiv:2110.02294 (2021).

The effect of preferred location on population persistence and spread

Vivian Dornelas,[1,*] Pablo de Castro,[1,*] William F. Fagan,[2]
Justin M. Calabrese,[3] and Ricardo Martinez-Garcia[1,†]

[1] *ICTP South American Institute for Fundamental Research & Instituto de Física Teórica, Universidade Estadual Paulista - UNESP, São Paulo, Brazil*

[2] *Department of Biology, University of Maryland, College Park, MD, USA*

[3] *Center for Advanced Systems Understanding (CASUS), Görlitz, Germany*

(Dated: October 14, 2022)

A central question in ecology is how the demographic and movement parameters of a population determine its spatial spread and the critical habitat size that can sustain it. Yet, most studies make oversimplifying assumptions about individual movement behavior, which may result in inaccurate predictions. Here, we study the persistence and spread of a population of individuals which experience an effective attraction towards a preferred location in space. Using explicit growth-dispersal models with advective terms, we show how biological populations may adjust to habitat destruction depending on how far from the preferred location the habitat is destroyed. We also incorporate a matrix escape response by turning on attraction towards habitat edges for individuals located in the harsh environmental matrix surrounding the habitat. In particular, our results show that increasing attraction strengths may not always be beneficial. When the attraction center is located near habitat edges, animals may spend too much time exposed to higher death rates, which decreases the total population. Also, for intermediate matrix escape response strengths, death by competition inside the habitat may win over the individual benefit of escaping away sooner from the matrix, leading to overall smaller populations. Our results constitute an important first step towards a more realistic understanding of preferred-location effects at the population level.

I. INTRODUCTION

The critical size of a patch or habitat that makes a population go extinct is a central problem in ecology. Habitat sizes are closely connected with population persistence, species interactions, and habitat fragmentation [1]. For habitat sizes larger than the critical habitat size, a related problem is how a biological population spreads in space. Assuming simple Brownian diffusion models of spatial dispersal for the individuals, as well as a completely non-viable deadly environmental matrix surrounding the habitat, population spread and persistence are well understood at the theoretical level [2].

* These two authors contributed equally.
† ricardom@ictp-saifr.org

However, advances in tracking devices and statistical methods enable us to better understand how animals move. In particular, the above model overlooks the fact that many species do not spread in space in a purely diffusive manner; rather, they are subject to range residency or somewhat similar preferred-location effects [3]. It has been shown using GPS-tracking data that these animals use space non-uniformly, occupying ranges substantially smaller than the population range [4]. The reason why animals may exhibit this kind of behavior has to do with the existence of attractive centers located at places with special properties or resources (including ponds, nests, and shelter), which usually assume a fixed position in time.

A successful way to model preferred-location effects is by introducing an "advection" or "attraction" contribution into a growth-dispersal diffusion-like model. This new term originates from an attractive spring-like force towards a preferred location [3, 5]. This generates a kind of motion equation called Ornstein-Uhlenbeck (OU) model, where the animal velocity is a combination of random noise and a restoration contribution that increases linearly with the distance to a preferred location. The OU model has been shown to be more accurate for animal movement at long time scales than pure Brownian motion [3]. Yet, theoretical development incorporating the long-term consequences of preferred location at the population and community level are rare [4, 5].

In this paper, we provide the first study quantifying how preferred-location attraction may impact critical habitat size as well as how the different individual-level movement parameters and different spatial patterns of habitat destruction may affect population persistence in heterogeneous landscapes. Importantly, such comparison is possible because, in the infinite habitat size case, OU movement leads to a stationary spatial distributions of population density with finite variance around a well-defined mean. In essence, we extend the definition of critical habitat size to account for the spatial location of the habitat edges relative to key resources in the environment that determine the area of occurrence of a given species. In our model, besides assuming that individual movement can be described with an OU movement term towards a preferred location (a point in space), we consider that individuals change their movement behavior once located in the harsh matrix by turning on an additional OU movement term that corresponds to a matrix escape response towards habitat edges. Also, we assume a logistic population growth and a harsh matrix in which individuals die after a characteristic time rather than instantaneously. We incorporate all these ingredients in a partial differential equation for the population density, which we analyze in a one-dimensional finite domain. These ingredient allows us to incorporate two additional layers of complexity and study how the total size and spatial pattern of a population respond to habitat destruction depending on how far from the preferred location the habitat is destroyed. Such questions have not been explored before and are the main focus of our analysis.

This paper is organized as follows. Section II defines our mathematical model and approach. Section

III brings our analytical and numerical results. In Section IV we present our conclusions.

II. MODEL

We consider a population where each individual moves following a one-dimensional Ornstein-Uhlenbeck (OU) model [5] equipped with, in principle, two attractive terms: (i) towards a preferred location and (ii), if the animal is outside the patch, towards the closer edge of the patch. That is, the habitat itself is a preferred *region*, existing besides the preferred point-like location. The corresponding equation of motion for the position x at time t is

$$\dot{x}(t) = -\tau^{-1}\left[x(t) - \lambda\right] - g_{\mathrm{M}}(x)\left[x(t) - \lambda_{\mathrm{E}}(x)\right] + \sqrt{2D}\xi(t), \tag{1}$$

where $\xi(t)$ is a zero-mean white noise with variance unity, D is the diffusion coefficient, τ^{-1} is the preferred-location attraction rate, with dimensions of inverse time, $g_{\mathrm{M}}(x)$ is the matrix escape response strength, or edge attraction rate, which is turned on only for x in the matrix, and $\lambda_{\mathrm{E}}(x)$ is the location of the corresponding habitat edge (left or right, depending on x). For simplicity, and without loss of generality, in the following we set the origin of coordinates at the preferred location, i.e., the position of the attraction center is $x = \lambda = 0$. We also define $x = -L_{\mathrm{L}}$ and $x = +L_{\mathrm{R}}$ for the locations of the left and right habitat edges, respectively. Thus, $\lambda_{\mathrm{E}}(x) = -L_{\mathrm{L}}$ for $x < -L_{\mathrm{L}}$ and $\lambda_{\mathrm{E}}(x) = L_{\mathrm{R}}$ for $x > L_{\mathrm{R}}$. Also, $g_{\mathrm{M}}(x) = \tau_{\mathrm{M}}^{-1}$ for $x < -L_{\mathrm{L}}$ or $x > L_{\mathrm{R}}$, and zero otherwise, with τ_{M}^{-1} constant. The total habitat size is $L = L_{\mathrm{L}} + L_{\mathrm{R}}$.

We further assume that all individuals within the population have the same preferred location, which is a good assumption for non-territorial species and/or scenarios in which the preferred location is determined by the presence of key resources.

For the population dynamics, we assume that the population follows a logistic growth model with net reproduction rate $r(x)$ and constant competition parameter γ (see below). To mimic the effects of a harsh matrix, we use that $r(x) = r_{\mathrm{in}}$ inside the habitat and $r(x) = -d_{\mathrm{out}}$ outside, with r_{in} and d_{out} positive constants. Logisitic growth coupled to OU movement leads to the following partial differential equation for the spatiotemporal dynamics of the population density $u(x,t)$:

$$\frac{\partial u(x,t)}{\partial t} = r(x)u(x,t) - \gamma u(x,t)^2 + D\frac{\partial^2 u(x,t)}{\partial x^2} + \tau^{-1}\frac{\partial}{\partial x}\left[(x-\lambda)u(x,t)\right] + g_{\mathrm{M}}(x)\frac{\partial}{\partial x}\left[(x-\lambda_{\mathrm{E}}(x))u(x,t)\right]. \tag{2}$$

Mathematically, Eq. (2) is an extension of the well-known Fisher-Kolmogorov equation (diffusion and logistic population growth) that includes two advection terms to account for the attractions to the preferred location and to the habitat.

III. RESULTS

To build intuition progressively, we start by presenting our results for the critical habitat size, spatial distribution, and total population in the case where the animal cannot survive in the matrix, i.e., $d_{\rm out}^{-1} = 0$, considering preferred-location attraction. Then, we turn on $d_{\rm out}^{-1}$, first without matrix escape response, i.e, $\tau_{\rm M}^{-1} = 0$, and finally with matrix escape response, i.e., $\tau_{\rm M}^{-1} \neq 0$.

A. Extremely harsh matrix: $d_{\rm out}^{-1} = 0$

For an extremely harsh matrix, i.e., $d_{\rm out} \to \infty$, since the individuals do not change their movement inside the habitat close to the habitat edges, the boundary conditions are absorbing and read $u(-L_{\rm L}, t) = u(L_{\rm R}, t) = 0$. In this case, it does not make a difference to have or not a matrix escape rate since individuals die there instantaneously. Because we are interested in determining the habitat configurations $(L_{\rm L}, L_{\rm R})$ that lead to the long-term extinction of the population, we perform a linear stability analysis of the solution $u(x, t \to \infty) \equiv u_{\rm s}(x) = 0$. By doing so, we can calculate the critical *total* habitat size L_c of the population. In what follows, we prefer to choose $L_{\rm L}$ and obtain the critical *right-hand side* habitat size $L_{\rm R,c}$, without loss of generality. To that end, we neglect the quadratic term in the logistic growth and take the $t \to \infty$ limit in Eq. (2), which means setting $\partial_t u(x,t) = 0$. In this limit, Eq. (2) becomes an ordinary differential equation with solution $u_{\rm s}(x)$ of the following form (shown here for completeness only):

$$u_{\rm s}(x) = \exp\left(-\frac{x^2}{2\tau D}\right)\left[aH_{r\tau}\left(\frac{x}{\sqrt{2D\tau}}\right) + b\ {}_1F_1\left(-\frac{r\tau}{2}; \frac{1}{2}; \frac{x^2}{2D\tau}\right)\right], \tag{3}$$

where a and b are constants to be determined by boundary conditions, H_n is the Hermite polynomial of order n, such that $H_0(x) = 1, H_1(x) = 2x, \ldots$, and ${}_1F_1$ is the confluent hypergeometric function of the first kind [6]. Imposing the boundary conditions to Eq. (3), one obtains a system of two equations for a and b. Because we do not know the value of $u_s(x)$ elsewhere other than at the edges, the equations for a and b can only be used to find out the shape of $u_s(x)$ and therefore the stability of the $u_s(x) = 0$ solution. This is done by noticing that, in order for this system of equations to have non-trivial solutions different than $a = b = 0$, its determinant has to be zero, with a and b being the variables. With this condition for the determinant and assuming that $L_{\rm L}$ is fixed, we obtain a transcendental equation in $L_{\rm R}$ that can be solved numerically to obtain the critical right-hand side habitat size $L_{\rm R,c}$. We compare the results from this semi-analytical method with those obtained from the numerical integration of the full nonlinear Eq. (2). We use a central Euler method to solve Eq. (2) starting from a random positive initial condition for u that obeys the absorbing boundary conditions. This allows $L_{\rm R,c}$ to be easily calculated:

by varying $L_{\rm R}$, the critical value is reached once the steady-state total population size transitions from non-zero to zero.

Before showing our results for the critical habitat sizes and total population, we start understanding the the impact of habitat destruction on the spatial spread of our population by looking into the stationary profiles of population density $u_{\rm s}(x)$. This is done via numerical integration of the full nonlinear Eq. (2) for three different combinations of $L_{\rm L}$ and $L_{\rm R}$ that result in population persistence (Fig. 1). That is, we consider three habitat spatial configurations such that $L_{\rm L} + L_{\rm R} > L_c$. We observe that when habitat destruction is not symmetric around the preferred location, i.e., $L_{\rm L} \neq L_{\rm R}$, the location of the maximum population density $x_{\rm p}$ deviates from the preferred location, resulting in a skewed or asymmetric population density distribution. Interestingly, we observe that survival is possible even if the preferred location is situated in the matrix (see Fig. 1c), a scenario that could arise if an important resource ended up being located in the matrix, e.g., a lake in a deforested region.

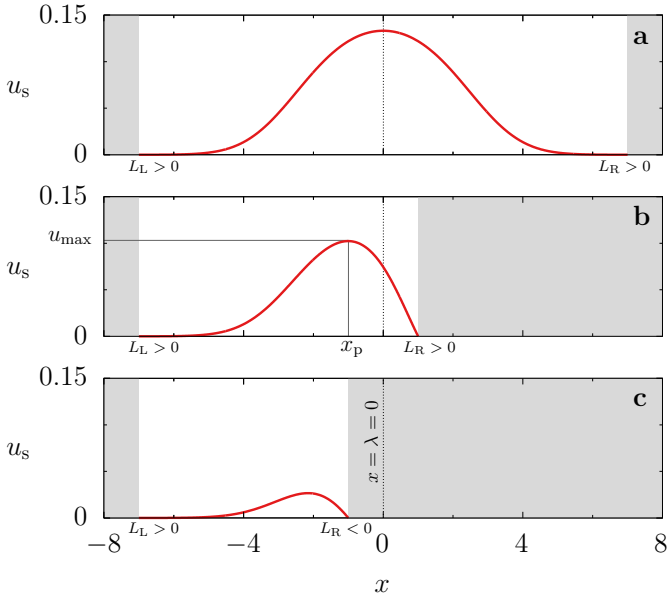

FIG. 1. Stationary population density distribution $u_{\rm s}(x)$ for (a) $L_{\rm R} = 7$ and $L_{\rm L} = 7$, (b) $L_{\rm R} = 1$ and $L_{\rm L} = 7$, and (c) $L_{\rm R} = -1$ and $L_{\rm L} = 7$, as calculated by numerically integrating Eq. (2). Other parameters: $r_{\rm in} = 0.1$, $d_{\rm out}^{-1} = 0$, $\gamma = 1$, $D = 0.1$, $\lambda = 0$, and $\tau^{-1} = 0.05$. $u_{\rm max}$ is the maximum population density and $x_{\rm p}$ its location. Gray regions represent the matrix.

We now explore the $L_{\rm R}$-$L_{\rm L}$ parameter space for different values of τ^{-1} (Fig. 2a-c). We can use numerical simulations of Eq. (2) to measure the total population fraction lost to deforestation (from $L \to \infty$ to finite $L_{\rm L}$ and $L_{\rm R}$). We actually plot the remaining total population fraction $\eta \equiv N_{\rm T}/N_{\rm T}^{\infty}$, where $N_{\rm T} \equiv \int u_{\rm s}(x)dx$ integrating over the entire range, and similarly for $N_{\rm T}^{\infty}$, for each parameter combination. The critical habitat size obtained via stability analysis from Eq. (3) as described above (solid line in Fig. 2a-c) shows an excellent agreement with the full numerical simulations. As expected, the behavior of

η is symmetric about the $L_R = L_L$ diagonal. Moreover, for sufficiently large L_R or L_L, further increasing habitat size does not change the population size because the flux of individuals through the habitat edges becomes negligible when these are very far from the population preferred location. This explains why the green solid lines in Fig. 2a-c are horizontal and vertical in the limits $L_L \to \infty$ and $L_R \to \infty$, respectively, and why they tend to this asymptotic behavior faster for higher τ^{-1}. Finally, Fig. 2a shows that the population can survive even when the preferred location lies within the matrix, as already observed in Fig. 1c. That is, the population can survive even when L_R and L_L have opposite signs (see Fig. 1a).

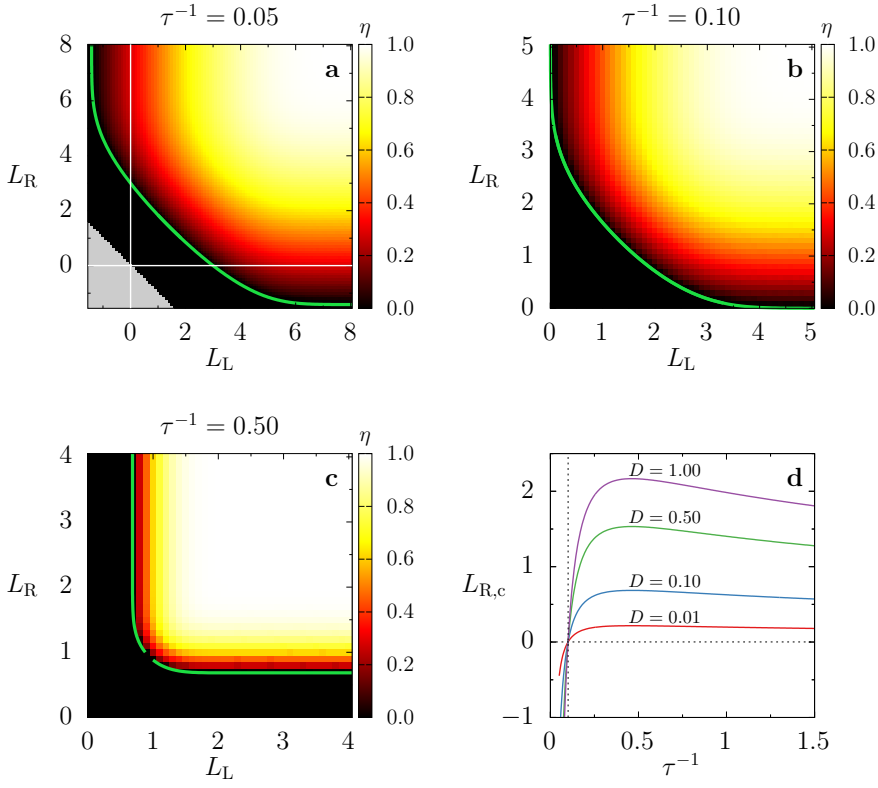

FIG. 2. (a)-(c): "Heat" map of total population (divided by the infinite-habitat population) η in the habitat sizes plane L_R versus L_L for (a) $\tau^{-1} = 0.05$, (b) $\tau^{-1} = 0.1$, and (c) $\tau^{-1} = 0.5$. Other parameters: $r_{in} = 0.1$, $d_{out}^{-1} = 0$, $D = 0.1$, and $\gamma = 1$. The solid line (green) shows the numerical solution from stability analysis for the critical habitat sizes line. In (a), the origin is marked to highlight the existence of survivability in a negative L_R and L_L region. The gray area is undefined as it would correspond to the "right" border being on the left and vice-versa. (d) Critical right habitat size $L_{R,c}$ as a function of τ^{-1} for distinct values of D, as indicated, $r_{in} = 0.1$, $d_{out}^{-1} = 0$, and $L_L = 100$.

The total population fraction lost to deforestation η can be plotted against the remaining fraction of habitat above the critical habitat size $\epsilon \equiv L/L_c$, as shown in Fig. 3 for $\lambda = 0$. For $\tau^{-1} = 0$, one would have $N_T^{\infty} \to \infty$ and thus $\eta \to 0$ since the population spreads homogeneously everywhere without borders and increases to a finite population size set by γ. By increasing τ^{-1}, the curve $\eta(\epsilon)$ moves up, indicating that a sharper decrease occurs towards extinction as one moves towards the critical habitat size. In other

words, close to the critical habitat size, lower-τ^{-1} centralized populations are more sensitive to the same relative habitat loss. In particular, Fig. 3 provides the percentage losses depending on such sensibility controlled by τ^{-1}. For instance, for $\tau^{-1} = 0.05$, even when the habitat size is still twice the critical habitat size ($\epsilon = 2$), the population goes down to about 50% of what it could be without deforestation or habitat limitations.

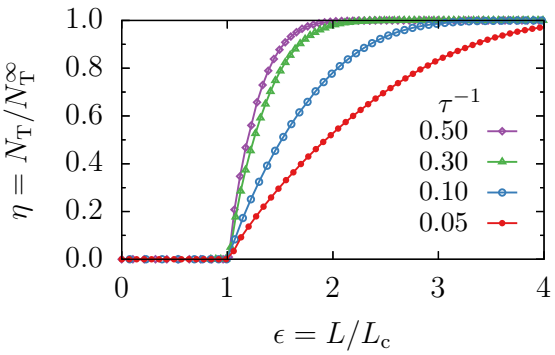

FIG. 3. Ratio between the total population for L and for $L \to \infty$, η, versus $\epsilon \equiv L/L_c$ for various τ^{-1} as indicated. Other parameters: $D = 0.1$, $\gamma = 1$, $r_{in} = 0.1$, $d_{out}^{-1} = 0$, and $\lambda = 0$.

To further investigate the behavior of the critical habitat size, we calculated the critical location of the right habitat edge $L_{R,c}$ in the case where death at the left one is negligible, obtained with $L_L \to \infty$. We conducted this analysis for several values of τ^{-1} and D. We identify three different regimes in the relationship between $L_{R,c}$ and τ^{-1} (see Fig. 2d). First, at intermediate values of τ^{-1}, $L_{R,c}$ is positive and increases with increasing τ^{-1} until it peaks at a value of τ^{-1} that depends on the intensity of the random component of movement, D. In this regime, individuals need a larger area to ensure population survival even if they would exhibit smaller home ranges in infinite habitats (higher values of τ^{-1} result in narrower distributions). This is due to the fact that the preferred location is located close to the habitat edges and, therefore, individuals need to spend more time away from it to minimize death risk and ensure population persistence. Then, for large values of τ^{-1}, $L_{R,c}$ decreases with increasing τ^{-1} because preferred-location attraction dominates individual movement; in this case, individual area requirements are small and the population is confined within a "safe", small region around the preferred location. Finally, at low values of τ^{-1} such that $\tau^{-1} < r_{in}$, one has that $L_{R,c}$ is negative, which means that the population can persist even if its preferred location is in the matrix. In this low-τ^{-1} regime, decreasing τ^{-1} (or increasing diffusion) leads to $L_{R,c}$ becoming more negative (i.e., the preferred location can be located further inside the matrix) because individuals are more spread around the preferred location, including towards the infinite side, and thus less individuals die crossing the edge attracted to the preferred location.

Next, we characterize the impact of different patterns of habitat destruction, represented by the locations of the habitat edges, on the spatial pattern of population density. As discussed in previous sections,

the distance between the spatial coordinate with maximum population density and the preferred location is a measure of the asymmetry of $u_s(x)$ (and also indicates skewness in this case). This distance quantifies how much the location of the maximum population density deviates from the expected valued in an infinite habitat and, because the preferred location is located at the origin of coordinates, this distance is equal to the location of the peak, x_p. Fig. 4a shows x_p as a function of the total habitat size $L = L_L + L_R$ for different levels of symmetry in habitat destruction. To implement asymmetry in habitat destruction systematically, we use L_L as a control parameter and define $L_R = \alpha L_L$. In the limit $\alpha = 1$, $L_R = L_L$ and habitat destruction is symmetric about the preferred location. As α decreases, habitat destruction becomes more asymmetric. We consider $\alpha = 0.25$, 0.5, 0.75, and 1.0. In the highest asymmetry case, $\alpha = 0.25$, x_p increases up to a certain value of L and then it has to decrease since, in the infinite habitat size limit, the maximum population density coincides with the OU home-range center [5]. For higher α, we see a similar behavior but with a progressively lower peak for $x_p(L)$. To validate our results, we check that, for symmetric habitat destruction, $x_p = 0$ for all values of the habitat size. The spread of $u_s(x)$, i.e., the standard deviation of x, is shown in Fig. 4b, confirming that the closer to a border the narrower the spatial distribution becomes.

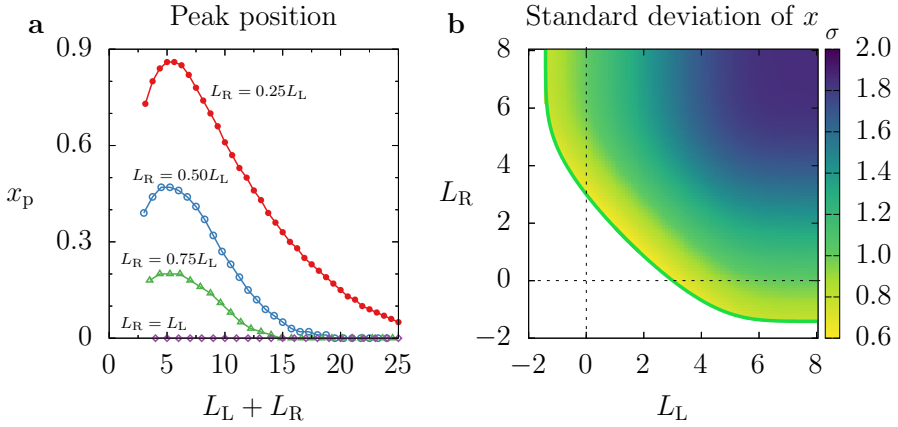

FIG. 4. (a) Peak position as a function of the total habitat size $L = L_L + L_R$ for $L_R = 0.25L_L$ (filled red disks), $L_R = 0.5L_L$ (empty blue circles), $L_R = 0.75L_L$ (empty green triangles), and $L_R = L_L$ (empty purple diamonds). (b) "Heat" map of the standard deviation of x. Other parameters: $r_{in} = 0.1$, $d_{out}^{-1} = 0$, $D = 0.1$, and $\tau^{-1} = 0.05$.

B. Partially harsh matrix with and without matrix escape response: $d_{out}^{-1} \neq 0$

Fig. 5 shows the stationary spatial distribution considering that the animal can now still survive for a time of the order $1/d_{out}$ outside the habitat, where $d_{out} > 0$ is thus the finite death rate in the matrix, and without matrix escape response ($\tau_M^{-1} = 0$). Our previous scenario corresponds to $d_{out} \to \infty$. The population now persists outside the matrix, which is best observed using a log scale for the u_s axis, as

shown on the right-hand side of Fig. 5. Notice the exponential tail indicated by a straight line when the u_s axis is in log scale. More importantly, the general qualitative behavior of the habitat size problem remains unaltered and therefore one can rely on our previous observations for the case with instantaneous death in the matrix.

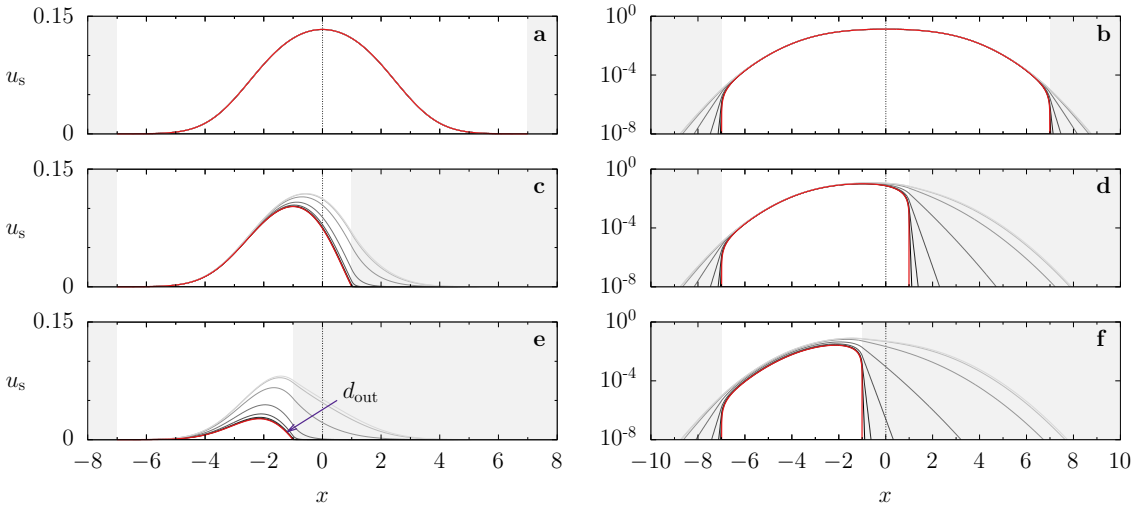

FIG. 5. Left: Stationary population density distribution $u_s(x)$ for the same parameters as in Fig. 1, with (a) corresponding to Fig. 1a, (c) to Fig. 1b, and (e) to Fig. 1c, but now with a finite negative net reproduction rate outside the habitat of magnitudes $d_{out} = 10^{-3}$, 10^{-2}, 10^{-1}, 10^0, 10^1, 10^2, and 10^3 increasing as indicated in (e). Right: Same as left side but with the u_s axis in log scale.

By turning on matrix escape response ($\tau_M^{-1} \neq 0$), the spatial distribution enters into the habitat, as shown in Fig. 6. In the symmetric case (Fig. 6a), as the individuals accumulate equally on both sides. For large enough τ_M^{-1}, the edges act as almost hard walls. Fig. 6 shows an asymmetric case where the preferred location is situated in the matrix. Even though the individuals are attracted to the matrix due to the preferred location attraction, for large enough matrix escape response, individuals will mostly accumulate at the habitat edge, in a highly asymmetric way.

Fig. 6 suggests a competition between two effects: the individual (and therefore populational) benefit of escaping from the matrix versus death by resource competition inside the habitat as more individuals dwell in it due to the matrix escape response. To understand that, we plot the total population (divided by the infinite habitat population) η versus τ_M^{-1}. For simplicity, we consider only the symmetric case. For sufficiently low d_{out}, a minimum in η versus τ_M^{-1} is observed. This is related to the balance between the spatial distribution mass outside versus inside as τ_M^{-1} is changed. In simple terms, by increasing τ_M^{-1}, resource competition inside the habitat increases more than the population gain obtained by individual escape since d_{out} is low. By further increasing τ_M^{-1}, the matrix escape response is so high that only a small amount of individuals enter (and potentially die in) the matrix and thus this effect now wins over the population loss that arises from additional resource competition inside the habitat.

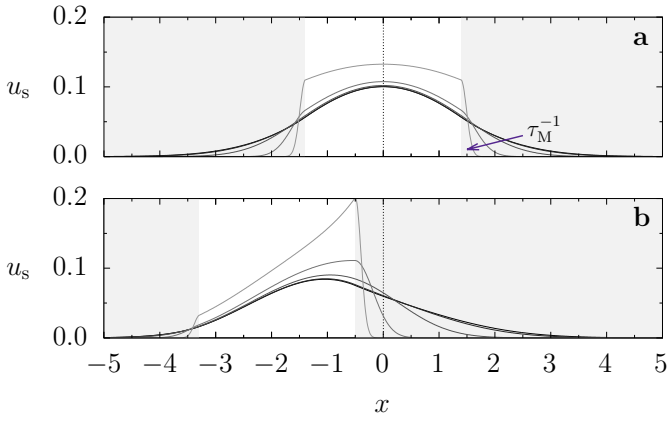

FIG. 6. Stationary population density distribution $u_s(x)$ for $L = 2.8$, smaller than the L_c of the extremely harsh matrix symmetric case, $\tau^{-1} = 0.05$, $d_{out} = 10^{-3}$, and $\tau_M^{-1} = 10^{-3}$, 10^{-2}, 10^{-1}, 10^0, and 10^1 increasing as indicated in the figure. (a) $L_R = L_L = 1.4$ and (b) $L_R = -0.5$ and $L_L = 3.3$. Other parameters as in Fig. 1.

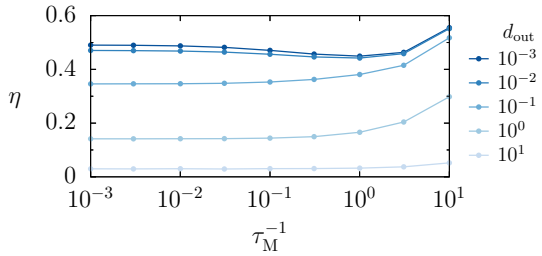

FIG. 7. Ratio between the total population for L and for $L \to \infty$, η, versus τ_M^{-1}. $L_R = L_L = 1.4$ and $d_{out} = 10^{-3}$, 10^{-2}, 10^{-1}, 10^0, and 10^1, with lighter colors corresponding to larger d_{out}.

IV. CONCLUSIONS

Here we addressed the movement ecology question of how preferred-location effects alter spatial spread at the population level. A growth-dispersal model with advective currents is introduced and solved to show how the populations adjust to habitat destruction depending on the position of the preferred location with respect to habitat edges. A matrix escape response has been incorporated (also as an advective/attraction term) and is turned on only for individuals located in the matrix. We have shown that the population size depends non-monotonically on attraction strengths. For an attraction center located near habitat edges, animals live around higher death rates and thus the total population decreases. For intermediate matrix escape response, death by competition inside the habitat is more important than the individual benefit of escaping from the matrix. This also leads to a decrease in total population.

Our findings highlight the importance of considering preferred location effects into individual movement behavior and its consequences to the populations. In particular, our calculation shows that, for the same habitat size, different levels of preferred-location (and/or matrix escape response) strengths lead to significantly different population fractions of the corresponding infinite-habitat population. This is

expected to motivate new observational and theoretical work to further understand the role of several kinds of non-Brownian movement aspects in the persistence and spread of biological populations, including applications to conservation biology.

ACKNOWLEDGMENTS

V.D. and P.d.C were supported by São Paulo Research Foundation (FAPESP, Brazil) postdoctoral fellowships #2020/04751-4 and #2021/10139-2, respectively. R.M.-G was supported by the FAPESP program Jovens Pesquisadores through grant no. 2019/05523-8, the ICTP through the Associates Programme, and the Simons Foundation through grant no. 284558FY19. V.D, P.C., and R.M.-G. were supported by FAPESP through ICTP-SAIFR grant no. 2016/01343-7. This research was supported by resources supplied by the Center for Scientific Computing (NCC/GridUNESP) of the São Paulo State University (UNESP).

[1] D. M. Debinski and R. D. Holt, A survey and overview of habitat fragmentation experiments, Conservation biology **14**, 342 (2000).

[2] H. Kierstead and L. B. Slobodkin, The size of water masses containing plankton blooms, J. mar. Res **12**, 141 (1953).

[3] C. H. Fleming, J. M. Calabrese, T. Mueller, K. A. Olson, P. Leimgruber, and W. F. Fagan, From fine-scale foraging to home ranges: a semivariance approach to identifying movement modes across spatiotemporal scales, The American Naturalist **183**, E154 (2014).

[4] M. J. Noonan, R. Martinez-Garcia, G. H. Davis, M. C. Crofoot, R. Kays, B. T. Hirsch, D. Caillaud, E. Payne, A. Sih, D. L. Sinn, *et al.*, Estimating encounter location distributions from animal tracking data, Methods in Ecology and Evolution **12**, 1158 (2021).

[5] R. Martinez-Garcia, C. H. Fleming, R. Seppelt, W. F. Fagan, and J. M. Calabrese, How range residency and long-range perception change encounter rates, Journal of theoretical biology **498**, 110267 (2020).

[6] G. B. Arfken and H. J. Weber, Mathematical methods for physicists (1999).

Contagion dynamics of self-propelled agents in narrow environments: Role of spontaneous agglomeration

Pablo de Castro* and Ricardo Martínez-García
ICTP-South American Institute for Fundamental Research - Instituto de Física Teórica da UNESP, Rua Dr. Bento Teobaldo Ferraz 271, 01140-070 São Paulo, Brazil.

Francisca Guzmán-Lastra
Department of Physics, Faculty of Sciences, Universidad de Chile, Santiago, Chile
(Dated: December 2, 2022)

Self-propelled agents can spontaneously agglomerate into clusters, provided that stochastic reorientation rates are low. In 1D, the stationary cluster size distribution follows a known exponential decay. Here we study how epidemics spread in spatially-structured scenarios. We develop a minimal lattice model for run-and-tumble particles which clusterize in narrow channels under a SIR (susceptible-infected-recovered) dynamics. A rich behavior controlled by motility-induced aggregation arises. The temporal evolution of the number of infected individuals shows a sequence of peaks resulting from individuals travelling between clusters. The final population fraction of ever-infected individuals depends non-monotonically on the single-individual parameters. Apart from simulations, we develop a mean-field theory for the SIR evolution and an individual-based kinetic theory for the final population fractions. Our work may lead to insights into viral phage therapy against bacterial infections, biochemical signaling between motile microorganisms, and social consensus.

I. INTRODUCTION

A central problem in epidemiology is how individual motion affects epidemic spread [1]. More broadly, this question concerns many dynamical contexts where individual states are transmitted by contact, whether among animals [2, 3], insects [4], microorganisms [5], or other sorts of agents [6]. Scenarios where individuals are not homogeneously distributed in space are particularly challenging [7]. Increasing attention has been paid to models of self-propelled particles where infection rates emerge from individual motion rules [8–14]. One example is the active Brownian particle (ABP) model, where the free-particle dynamics corresponds to a constant self-propulsion velocity whose direction undergoes rotational diffusion [15–17]. This model has been largely used to model animal movement, particularly bacteria [16]. ABPs spontaneously agglomerate into clusters even if subject to purely repulsive interactions [18]. Such motility-induced clustering arises as particles block each other due to low reorientation rate, i.e., persistent motion. A stationary cluster size distribution (CSD) is reached once the rates of particle absorption and emission from the clusters become equal [19]. The ratio between self-propulsion speed and reorientation rate can be interpreted as a proxy for the individual tendency of agglomerating.

Recently, assuming a susceptible-infected-recovered (SIR) scenario and two spatial dimensions (2D), the epidemic evolution of ABPs infecting each other by contact was considered [20]. For simplicity, a focus was given to parameters that do not allow for clustering. With recovery turned off, the critical density above which the entire system becomes infected was analytically calculated from individual-based (or "microscopic") considerations. More recently, the SIR contagion dynamics of self-propelled particles in 2D with repulsive interactions and polar alignment was investigated numerically [21]. Emerging spatial structures, such as bands and clusters, were shown to strongly affect the final fraction of ever-infected (recovered) individuals.

Another model, qualitatively similar to ABPs [22] but simpler, is the run-and-tumble particle (RTP), where the agent simply moves in a straight line ('run') up to a random time instant where a new random run direction is chosen ('tumble') [23, 24]. RTPs are also frequently used to model bacterial motion. For narrowly confined or one-dimensional (1D) systems, e.g., bacteria which live in long narrow soil or host pores, a number of theoretical difficulties are eliminated due to the fact that particle order is fixed [25]. In particular, the CSD of RTPs follows a known exponential decay dependent on motion parameters and density [26].

In the present work, we investigate how epidemics spread in spatially-structured systems of self-propelled particles in narrowly confined spaces. Besides simulations, we develop two kinds of theories. A computationally cheap model of RTPs on a 1D discrete lattice is used [26]. Particle alignment is absent, isolating the role of motility-

* pablo.castro@ictp-saifr.org

induced clustering. Tackling the 1D version of this problem is important in two fronts. First, it models real-world narrowly confined systems. Secondly, it eases the trajectory towards the intricate 2D version, generating intuition on which features to expect or not. In this direction, recently, 2D simulations were used to study clustering effects on the contagion dynamics of RTPs [27]. Differently than there, here we focus on the role of individual motion parameters, density, and recovery rate in the evolution and final fraction of ever-infected individuals as well as in the effects of cluster-cluster travels. Finally, in the 1D case studied here we can explain simulation data analytically, a crucial distinction from previous works.

Additional motivation includes the study of (i) viral phage therapy against bacterial infections [28–30], (ii) biochemical signaling between microorganisms [31, 32], and (iii) social consensus [33, 34]. Also, as we shall see, in our model the epidemics is mostly controlled by an interplay between recovery time and the reorientation plus travel time between clusters. If individuals do not recover quick enough, the epidemics continues. This resembles the spread of human diseases across villages separated by distances covered in large amounts of time [35, 36].

This paper is organized as follows. Section II defines our RTP model and reviews analytical CSD results, without contagion. Section III introduces the SIR dynamics and presents simulation results plus a mean-field explanation for them. Section IV derives and validates a microscopic theory for the final fraction of ever-infected individuals. Finally, Section IV brings conclusions.

II. RUN-AND-TUMBLE CLUSTERING

We start by reviewing the clustering model (without contagion) used below [26]. A discrete periodic lattice in 1D is considered, with $N = 2000$ sites, M particles, and maximal occupancy of one particle per site. Each particle has a director (self-propulsion direction), towards left or right. The dimensionless concentration is $\phi \equiv M/N$. Within each time step, M particles are selected randomly and sequentially (particle repetition is allowed but rare). With probability ν, the director is redrawn. If the director points to an empty neighboring site, the particle moves into it. The initial state corresponds to random positions and directors. The free-particle self-propulsion speed fluctuates around $v = 1$. The resulting stationary clustering behavior is shown in Fig. 1.

The CSD, defined as the average number of clusters of size l, is denoted by $F_c(l)$. Within the approximation $\nu/v \ll \phi$, the distributions of cluster and 'gas' region (i.e., empty region) sizes have been shown to follow[26]

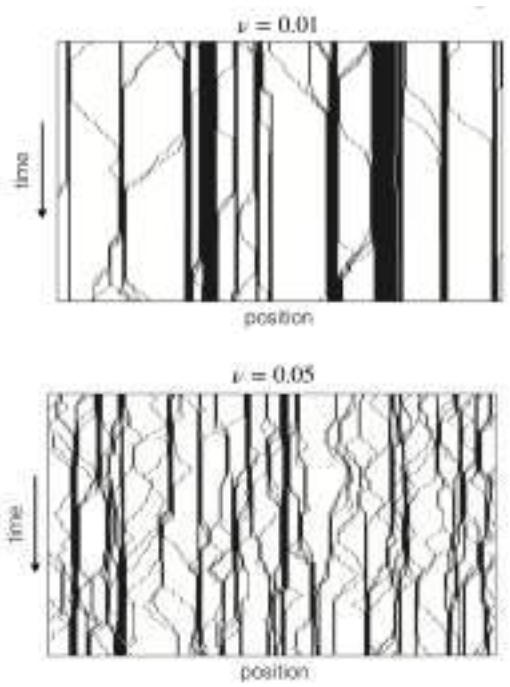

FIG. 1. Stationary clustering for $\phi = 0.2$ for (top) $\nu = 0.01$ and (bottom) $\nu = 0.05$, showing 300 time steps after time step 10^7 and 500 sites.

$$F_c(l) = A_c \exp(-l/L_c), \quad F_g(l) = A_g \exp(-l/L_g), \tag{1}$$

where the average cluster and gas region sizes are

$$L_c = \sqrt{\frac{2v\phi}{\nu(1-\phi)}}, \quad L_g = \sqrt{\frac{2v(1-\phi)}{\nu\phi}}, \tag{2}$$

and the prefactors are

$$A_c = \frac{N\nu\,(1-\phi)}{2v}, \quad A_g = \frac{N\nu\phi}{2v}. \tag{3}$$

For the purpose of this work, it has been checked that the above expressions still give sufficiently satisfactory results even without $\nu/v \ll \phi$.

III. SIR DYNAMICS

We now introduce and simulate the SIR dynamics. A particle is randomly selected, at time step 10^7 , to become infected, that is, after stationary clustering has been reached. Within the same time step, a new particle selection occurs. If it is infected, its susceptible neighbors become infected

(high transmissibility limit). With probability $r_{\rm rec}$, the selected particle recovers. If it is susceptible and any of its neighbors is infected (this is obviously never the case when the total number of infected particles is one), the selected particle becomes infected. As before, a new director may be drawn. After that, if the director points to an empty site, the particle moves. Random particle selections continue until M particles are selected within the same time step. The whole procedure is repeated for the subsequent time steps until the epidemics ends, i.e., the number of infected individuals becomes zero. The global SIR variables are denoted as S, I, and R, with $S+I+R=M$, the total number of particles. The population fractions are therefore $f_{\rm X}\equiv X/M$, where $X=S,I,R$, with $f_{\rm S}+f_{\rm I}+f_{\rm R}=1$.

Fig. 2 shows the temporal evolution of the spatial configurations, affected by the clustering-epidemic coupling. The space-time cone of infection corresponds to an epidemic spread whose speed is determined by the tumbling plus travel time between clusters and the time needed for the infection to spread within a cluster. The latter increases linearly with cluster size. The smaller the average gas region size, the easier to perceive the cone becomes. As time progresses, recovered particles start to appear within the cone.

The evolution of the population fractions is shown in Fig. 3. The susceptible fraction $f_{\rm S}$ decreases in a sequence of jumps resulting from particles arriving in susceptible clusters and infecting its individuals. The infected fraction $f_{\rm I}$ shows a corresponding series of peaks, with $f_{\rm I}$ relaxing after each peak while particles travel between clusters, until a new susceptible cluster is hit. This relaxation is a result of the exponential temporal decay arising from recovered individuals. (Actually, this picture gets averaged over right and left sides.) The recovered fraction $f_{\rm R}$ always increases as particles cannot become re-infected.

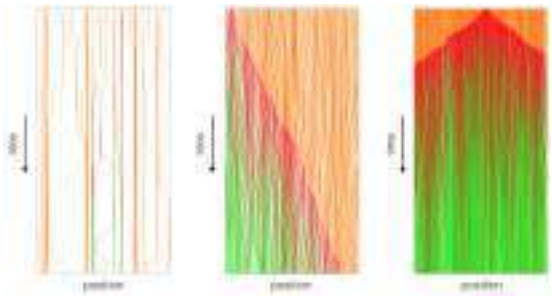

FIG. 2. From left to right: $\phi=0.1$, 0.5, 0.9, $\nu=0.005$, 0.5, 0.5 and $r_{\rm rec}=0.001$ for all. Color scheme in the next figure.

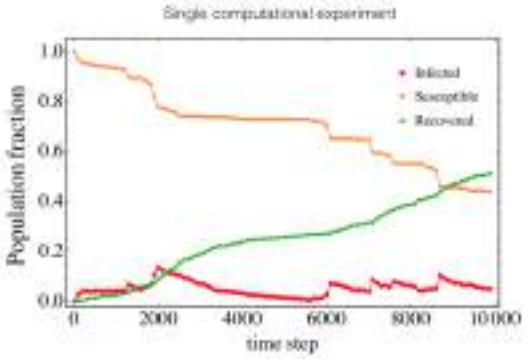

FIG. 3. Parameter choice is irrelevant: 1D nature leads to same general qualitative population fraction evolution for all parameter sets.

The realization averages $\langle f_{\rm X}\rangle$ is shown in Fig. 4. It is obtained by averaging $f_{\rm X}$ over 10^3 numerical experiments starting from random homogeneous position configurations. That is, in each experiment the clusters end up forming in different positions, meaning that the travels and thus the epidemic peaks will mostly occur in different time instants. As a result, the dynamics gets smoothed out, and only a single averaged peak arises, corresponding to the average instance of cluster-cluster travels during which the particle becomes recovered before reaching a new cluster. From now on, we drop the brackets in the notation for the realization averages, i.e., their notation are replaced according to $\langle X\rangle\to X$ and $\langle f_{\rm X}\rangle\to f_{\rm X}$.

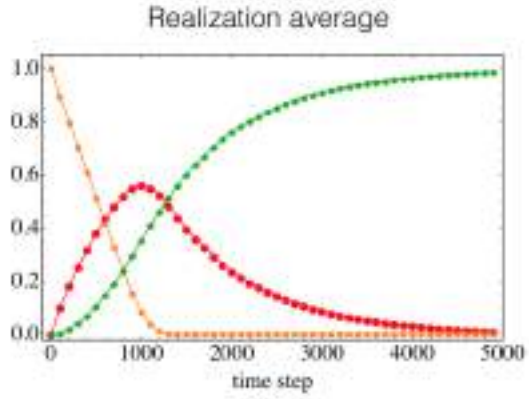

FIG. 4. Realization average of population fractions. As in the above figure, parameters choice is irrelevant.

A phenomenological mean-field theory explains the data in Fig. 4. It can be framed in terms of either X of $f_{\rm X}$, reading

$$\frac{dS}{dt}=-\beta\tanh\left[a(S-S_\infty)\right], \qquad (4)$$

$$\frac{dI}{dt} = \beta \tanh\left[a(S - S_\infty)\right] - r_{\rm rec} I \tag{5}$$

$$\frac{dR}{dt} = r_{\rm rec} I \tag{6}$$

where time t is measured in time step units (but taken as continuous in the theory), $X_\infty \equiv X(t \to \infty)$ for $X = S, I, R$, and a, β, and S_∞ are positive constants. In Eq. (4), if $S - S_\infty$ is high, i.e., far from the final saturation, then $\tanh\left[a(S - S_\infty)\right] \approx 1$. As a consequence, dS/dt is negative and constant. This is because (i) even though the infection may be detained in some realizations because the (right and left) infection-front leading particles will have not yet reached a new cluster, in other ones it will have reached and the infection will be advancing, and (ii) the 1D nature of the problem means that the size of the infection-front is constant, i.e., the increase of I does not lead to an increase in the effective infection rate as all infected particles but two (the leading ones) cannot be in contact with susceptible particles, by definition. The $\tanh\left[a(S - S_\infty)\right]$ corresponds to the final saturation process where, once S approaches its final value S_∞, the derivative dS/dt has to go to zero to avoid negative S. The first term on the right-hand side of Eq. (5) gives the corresponding increase in I whereas the second term gives a simple exponential decay of infected individuals into recovered ones. Finally, the opposite of the latter term appears in Eq. (6), concluding the set of equations.

The analytical solution of Eqs. (4)-(6) is

$$S(t) = S_\infty + \text{csch}^{-1}\left(e^{a\beta t}\,\text{csch}\left[a(M - S_\infty)\right]\right)/a,$$

$$I(t) = \frac{\beta}{r_{\rm rec}}\left[{}_2f_1\left(\frac{r_{\rm rec}}{2a\beta}; -e^{2a\beta t}\,\text{csch}^2\left[a(M - S_\infty)\right]\right)\right.$$

$$\left. - e^{-r_{\rm rec} t}\,{}_2f_1\left(\frac{r_{\rm rec}}{2a\beta}; -\text{csch}^2\left[a(M - S_\infty)\right]\right)\right],$$

$$R(t) = M - S(t) - I(t), \tag{7}$$

where ${}_2f_1\left(\frac{r_{\rm rec}}{2a\beta}; x\right) \equiv {}_2F_1\left(\frac{1}{2}, \frac{r_{\rm rec}}{2a\beta}; \frac{r_{\rm rec}}{2a\beta} + 1; x\right)$ and ${}_2F_1$ is the Gauss hypergeometric function [37]. Such phenomenological theory gives excellent results (see Fig. 4). The constants β, a, and S_∞ can be treated as fitting parameters, although here S_∞ is derived from the microscopic theory in Section IV.

IV. MICROSCOPIC THEORY

We now derive a microscopic theory for the (realization average) total amount of ever-infected (recovered) particles at the end, R_∞, where we remind that $X_\infty \equiv X(t \to \infty)$ for $X = S, I, R$. This will allow us to understand how the microscopic parameters, namely ν, ϕ, and $r_{\rm rec}$, affect the aftermath impact of the epidemics. By definition, $I_\infty = 0$ and thus $S_\infty + R_\infty = M$. We calculate R_∞ within the approximation where all clusters have the average size $L_{\rm c}$. Since the epidemics starts mostly likely within a cluster, at least one cluster becomes infected entirely, that is, the final number of ever-infected particles R_∞ is at least $L_{\rm c}$. Once the infection has reached a particle at the cluster border, that particle has to flip and travel to the neighbouring cluster in order for the epidemics to continue. Let us denote as $\tau_{\rm b}$ the flip plus travel time. If during $\tau_{\rm b}$ the particle recovers, the infection does not proceed. The infection will therefore proceed with probability $(1 - r_{\rm rec})^{\tau_{\rm b}}$ for the left and right sides. Assuming it has reached those clusters, another $2L_{\rm c}$ particles will be infected. The infection may then keep going, but only if the two first right and left clusters, with respect to the the "central", initial cluster, had become infected. Thus, the probability that a third and a fourth cluster become infected (one on the left and the other on the right) is $(1 - r_{\rm rec})^{\tau_{\rm b}} \times (1 - r_{\rm rec})^{\tau_{\rm b}} = (1 - r_{\rm rec})^{2\tau_{\rm b}}$. In summary, a geometric series arises, and R_∞ can be written as

$$R_\infty = L_{\rm c} + 2L_{\rm c}(1 - r_{\rm rec})^{\tau_{\rm b}} + 2L_{\rm c}(1 - r_{\rm rec})^{2\tau_{\rm b}} + \cdots$$

$$= L_{\rm c}\left[1 + 2\sum_{k=1}^{(N_{\rm c}-1)/2}(1 - r_{\rm rec})^{k\tau_{\rm b}}\right], \tag{8}$$

where, on the right-hand-side of Eq. (8), there are $(N_{\rm c} - 1)/2$ terms after the first one, $N_{\rm c}$ being the global amount of clusters, known analytically from Eqs. (1) and (3).

Using the geometric series formula, the resulting expression for R_∞ is too long to be written here but depends only on microscopic parameters, except for the time to tumble and travel between clusters $\tau_{\rm b}$ which is yet to be derived. In a first approximation, $\tau_{\rm b}$ can be calculated as $\tau_{\rm b} \equiv 2/\nu + L_{\rm g}/v$, considering the time for a direction redrawn to give a new direction (flip time) and assuming ballistic motion between clusters. However, the non-monotonic behavior of $f_{\rm R}^\infty(\nu)$ shown in Fig. 5 cannot be captured with the ballistic approximation, where $f_{\rm X}^\infty \equiv f_{\rm X}(t \to \infty)$. Initially, by increasing ν, one has that particles flip more frequently and thus escape more easily from the cluster. At the same time, the average cluster size decreases but the average gas region size too. For higher ν, $f_{\rm R}^\infty(\nu)$ increases less strongly with ν. By further increasing ν, $f_{\rm R}^\infty(\nu)$ starts to decrease with ν. This is because particles travel diffusively between clusters,

due to stochastic tumbling, and therefore will typically flip midway, detaining the advance of the infection. The mean-squared displacement of a RTP in 1D, that is, the MSD(t) expression in terms of ν and v [38], can be inverted and used to calculate the associated diffusive travel time $\mathrm{MSD}^{-1}(L_\mathrm{g}^2)$, replacing the ballistic travel time in the calculation of τ_b above, i.e., $\tau_\mathrm{b} = 2/\nu + \mathrm{MSD}^{-1}(L_\mathrm{g}^2)$. Such correction is indeed sufficient to capture the non-monotonic behavior of $f_\mathrm{R}^\infty(\nu)$, as shown in Fig. 5, whereas the ballistic approximation gives only a monotonic behavior.

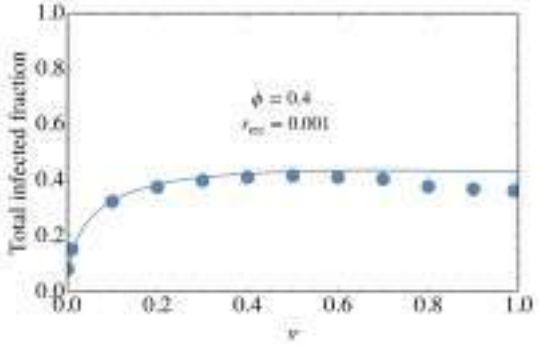

FIG. 5. Total fraction of infected versus ν.

The density dependence $f_\mathrm{R}^\infty(\phi)$ is also captured by the microscopic theory, as shown in Fig. 6. Counterintuitively, the final fraction of ever-infected individuals may decrease with ϕ in a range of low to intermediate ϕ. To understand this behavior, let us look into the dependence on ϕ of the factors in Eq. (8), divided by $M\phi$ to give f_R^∞. For $\phi < 0.5$, increasing ϕ increases the number of clusters N_c, up to a maximum at $\phi = 0.5$. Beyond that, the number of clusters decreases as particles attach to exiting clusters rather than forming new ones. If it was possible to increase N_c alone keeping ν, v, and ϕ fixed, the effect would be to decrease R_∞ since more clusters would correspond to more chances for the just-infected particle to recover while flipping plus travelling between between clusters. Since ν, v, and ϕ parameters determine N_c as well as the other factors of Eq. (8), namely τ_b and L_c, a complex set of non-monotonic dependences arises. Considering that ϕ increases N_c for $\phi < 0.5$ contributing to reducing R_∞, we will focus on whether the other ϕ dependences corroborate with such decrease. This is because $f_\mathrm{R}^\infty(\phi) \sim L_\mathrm{c}(\phi)/\phi$. As expected, the theory also shows that $f_\mathrm{R}^\infty(\phi = 0) = 0$ and $f_\mathrm{R}^\infty(\phi = 1) = 1$.

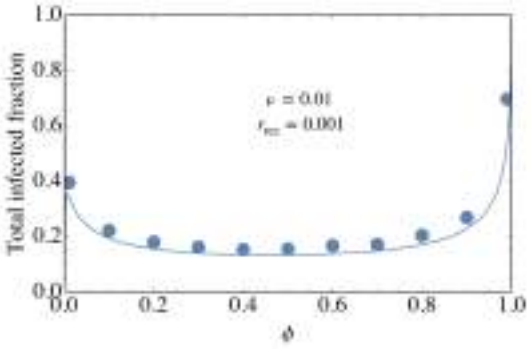

FIG. 6. Total final fraction of infected versus ϕ.

V. CONCLUSIONS

In this work, we studied the contagion of spontaneously agglomerating self-propelled particles in narrowly-confined scenarios. At first, by decreasing motion persistence, v/ν, the total final fraction of infected particles increases. That is because particles leave clusters sooner and then infect other clusters. However, by further decreasing persistence, the total final fraction of infected particles decreases. The reason why is that particles move more diffusively, flipping back towards their "original" clusters, before infecting other clusters.

In principle, additional improvements could be made in the theoretical approaches. In the phenomenological approach, all three constants may, in principle, be derived microscopically. The microscopic theory itself could use the entire distributions rather than only the average cluster and gas sizes. These improvements, however, are not necessary to capture the essence of th clustering-epidemic coupling, as shown above.

On the other hand, more relevant future directions include incorporating 2D effects as well as other SIR-like processes such as exposure, reinfection and death [3]. Our results provides insights into how active clustering plays distinct roles in the efficiency of epidemics.

VI. ACKNOWLEDGEMENTS

PdC is supported by grant #2021/10139-2, São Paulo Research Foundation (FAPESP), Brazil. RM-G was supported by the FAPESP program Jovens Pesquisadores through grant no. 2019/05523-8, the ICTP through the Associates Programme, and the Simons Foundation through grant no. 284558FY19. PdC and RM-G were supported by FAPESP through ICTP-SAIFR grant no. 2016/01343-7. This research was sup-

ported by resources supplied by the Center for Scientific Computing (NCC/GridUNESP) of the São Paulo State University (UNESP).

[1] M. M. Conner and M. W. Miller, Movement patterns and spatial epidemiology of a prion disease in mule deer population units, Ecological Applications **14**, 1870 (2004).

[2] C. Cosner, J. C. Beier, R. S. Cantrell, D. Impoinvil, L. Kapitanski, M. D. Potts, A. Troyo, and S. Ruan, The effects of human movement on the persistence of vector-borne diseases, Journal of theoretical biology **258**, 550 (2009).

[3] G. L. Vasconcelos, A. A. Brum, F. A. Almeida, A. Macêdo, G. C. Duarte-Filho, and R. Ospina, Standard and anomalous waves of covid-19: A multiple-wave growth model for epidemics, Brazilian Journal of Physics **51**, 1867 (2021).

[4] J. J. Brown, J. R. Mihaljevic, L. Des Marteaux, and J. Hrček, Metacommunity theory for transmission of heritable symbionts within insect communities, Ecology and evolution **10**, 1703 (2020).

[5] X. Li, F. Gonzalez, N. Esteves, B. E. Scharf, and J. Chen, Formation of phage lysis patterns and implications on co-propagation of phages and motile host bacteria, PLoS computational biology **16**, e1007236 (2020).

[6] M. Paoluzzi, M. Leoni, and M. C. Marchetti, Information and motility exchange in collectives of active particles, Soft Matter **16**, 6317 (2020).

[7] M. Martcheva, Spatial heterogeneity in epidemiological models, in *An Introduction to Mathematical Epidemiology* (Springer, 2015) pp. 387–414.

[8] J. P. Rodríguez, F. Ghanbarnejad, and V. M. Eguíluz, Particle velocity controls phase transitions in contagion dynamics, Scientific reports **9**, 1 (2019).

[9] S. Ghosh, A. Chakraborty, and S. Bhattacharya, How surface and fomite infection affect contagion dynamics: a study with self-propelled particles, The European Physical Journal Special Topics , 1 (2022).

[10] J. P. Rodríguez, M. Paoluzzi, D. Levis, and M. Starnini, Epidemic processes on self-propelled particles: continuum and agent-based modelling, arXiv preprint arXiv:2203.12355 (2022).

[11] D. Kim and A. Quaini, Coupling kinetic theory approaches for pedestrian dynamics and disease contagion in a confined environment, Mathematical Models and Methods in Applied Sciences **30**, 1893 (2020).

[12] D. Kim, K. O'Connell, W. Ott, and A. Quaini, A kinetic theory approach for 2d crowd dynamics with emotional contagion, Mathematical Models and Methods in Applied Sciences **31**, 1137 (2021).

[13] S. Namilae, A. Srinivasan, A. Mubayi, M. Scotch, and R. Pahle, Self-propelled pedestrian dynamics model: Application to passenger movement and infection propagation in airplanes, Physica A: Statistical Mechanics and its Applications **465**, 248 (2017).

[14] D. Levis, A. Diaz-Guilera, I. Pagonabarraga, and M. Starnini, Flocking-enhanced social contagion, Physical Review Research **2**, 032056 (2020).

[15] M. Rojas-Vega, P. de Castro, and R. Soto, Fast and slow self-propelled particles interacting with asymmetric obstacles: Wetting, segregation, rectification, and vorticity, arXiv preprint arXiv:2111.05952 (2021).

[16] P. Romanczuk, M. Bär, W. Ebeling, B. Lindner, and L. Schimansky-Geier, Active brownian particles, The European Physical Journal Special Topics **202**, 1 (2012).

[17] E. F. Teixeira, H. C. Fernandes, and L. G. Brunnet, A single active ring model with velocity self-alignment, Soft Matter **17**, 5991 (2021).

[18] G. S. Redner, M. F. Hagan, and A. Baskaran, Structure and dynamics of a phase-separating active colloidal fluid, Physical Review Letters **110**, 055701 (2013).

[19] F. Peruani, L. Schimansky-Geier, and M. Baer, Cluster dynamics and cluster size distributions in systems of self-propelled particles, The European Physical Journal Special Topics **191**, 173 (2010).

[20] A. Norambuena, F. J. Valencia, and F. Guzmán-Lastra, Understanding contagion dynamics through microscopic processes in active brownian particles, Scientific Reports **10**, 1 (2020).

[21] Y. Zhao, C. Huepe, and P. Romanczuk, Contagion dynamics in self-organized systems of self-propelled agents, Scientific reports **12**, 1 (2022).

[22] M. E. Cates and J. Tailleur, When are active brownian particles and run-and-tumble particles equivalent? consequences for motility-induced phase separation, EPL (Europhysics Letters) **101**, 20010 (2013).

[23] A. Villa-Torrealba, C. Chávez-Raby, P. de Castro, and R. Soto, Run-and-tumble bacteria slowly approaching the diffusive regime, Physical Review E **101**, 062607 (2020).

[24] P. de Castro, F. M. Rocha, S. Diles, R. Soto, and P. Sollich, Diversity of self-propulsion speeds reduces motility-induced clustering in confined active matter, Soft Matter **17**, 9926 (2021).

[25] P. de Castro, S. Diles, R. Soto, and P. Sollich, Active mixtures in a narrow channel: Motility diversity changes cluster sizes, Soft Matter **17**, 2050 (2021).

[26] R. Soto and R. Golestanian, Run-and-tumble dynamics in a crowded environment: Persistent exclusion process for swimmers, Physical Review E **89**, 012706 (2014).

[27] P. Forgács, A. Libál, C. Reichhardt, N. Hengartner, and C. J. O. Reichhardt, Using active matter to introduce spatial heterogeneity to the susceptible infected recovered model of epidemic spread-

ing, Scientific Reports **12**, 11229 (2022).
[28] R. A. Rodriguez-Gonzalez, C. Y. Leung, B. K. Chan, P. E. Turner, and J. S. Weitz, Quantitative models of phage-antibiotic combination therapy, MSystems **5**, e00756 (2020).
[29] E. W. Meynell, A phage, ϕ_X, which attacks motile bacteria, Microbiology **25**, 253 (1961).
[30] J. Marchi, *Statistical mechanics of viral-immune co-evolution*, Ph.D. thesis, Université Paris sciences et lettres (2020).
[31] S. Van Vliet, F. J. Hol, T. Weenink, P. Galajda, and J. E. Keymer, The effects of chemical interactions and culture history on the colonization of structured habitats by competing bacterial populations, BMC microbiology **14**, 1 (2014).
[32] K. M. Simpson Alfaro, Spatial biology of ising-like synthetic genetic networks, (2021).
[33] N. Crokidakis and F. L. Forgerini, Consequence of reputation in the sznajd consensus model, Physics Letters A **374**, 3380 (2010).
[34] V. Dornelas, M. Ramos, and C. Anteneodo, Impact of network randomness on multiple opinion dynamics, Physica A: Statistical Mechanics and its Applications **506**, 197 (2018).
[35] P. Richards, J. Amara, M. C. Ferme, P. Kamara, E. Mokuwa, A. I. Sheriff, R. Suluku, and M. Voors, Social pathways for ebola virus disease in rural sierra leone, and some implications for containment, PLoS neglected tropical diseases **9**, e0003567 (2015).
[36] A. Rotinsulu and W. Sulistyo, Spatial autocorrelation in the spread of sars-cov-2 (covid-19) among villages (study case: The city of tomohon), The IJICS (International Journal of Informatics and Computer Science) **5**, 199 (2021).
[37] G. B. Arfken and H. J. Weber, Mathematical methods for physicists (1999).
[38] K. Malakar, V. Jemseena, A. Kundu, K. V. Kumar, S. Sabhapandit, S. N. Majumdar, S. Redner, and A. Dhar, Steady state, relaxation and first-passage properties of a run-and-tumble particle in one-dimension, Journal of Statistical Mechanics: Theory and Experiment **2018**, 043215 (2018).

Optimal random searches with chemotaxis

Pablo de Castro* and Ricardo Martínez-García†
ICTP-South American Institute for Fundamental Research - Instituto de Física Teórica da UNESP, Rua Dr. Bento Teobaldo Ferraz 271, 01140-070 São Paulo, Brazil.
(Dated: November 17, 2022)

We investigate how different levels of chemotaxis can alter the optimal movement strategy in random searches such as animal foraging. Lévy walkers are studied in 1D in the presence of a near and a far target. Each target produces a stationary concentration of scent molecules, exponentially decaying with distance. The concentration gradient is used by the searcher to increase its probability of choosing the near-target direction. Without scent, by employing very long steps in the far-target direction, finding a target is guaranteed, but at the cost of a long walk. Conversely, by employing very small steps, the searcher may get stuck in between targets for a long time. The optimal strategy corresponds to a certain superdiffusive balance between short and long steps. At intermediate scent spread length, however, a discontinuous transition occurs, over which the optimal strategy becomes completely Brownian since large steps would risk placing the searcher too far from where the scent is useful. At even higher scent spread length, a second discontinuous transition occurs, now "backwards": the scent profile becomes so flat that, despite far reaching, it cannot be useful. Our results shine a light on how the degree of external information sampling changes optimal foraging strategies for searchers in scarce environments.

I. INTRODUCTION

A multitude of biological species search for crucial ecological resources—such as food, water and mates—by effectively performing a random walk whose distribution of displacement lengths is similar to that of a Lévy walker [1, 2]. The most commonly studied distribution of displacement lengths characterizing a Lévy walker (LW) is the power-law or Lévy/Pareto distribution:

$$p(\ell) \sim \ell^{-\mu} \qquad \text{for} \qquad \ell \in [\ell_{\min}, \ell_{\max}]. \quad (1)$$

In the LW model, each new displacement has a length drawn from distribution (1), with μ being the only parameter of the distribution, whereas the direction of the move is completely random [3]. Within this model, the average travelled distance to find an item has a global minimum for $\mu \approx 2$. This optimal foraging result is consistent with experimental data for bees and deer, among other species [4].

Based on a one-dimensional (1D) analysis, it can be shown that the mechanism by which a Lévy random walker can optimize target encounters in the presence of a "near" and a "far" target, under information-deprived scenarios, consists of combining an optimal diffusivity (optimally enhanced diffusion) with a minimal diffusion constant [5]. The search dynamics adequately balances between finding near and far targets, while, at the same time, shifts the optimal balance towards relatively larger near-to-far target encounter ratios.

Here we model random searches under the effects of a scent concentration profile emitted by a target and processed by the olfactory system of the searcher. This is incorporated by introducing a directional bias whose intensity depends on the distances to the targets. Instead of performing the search "in the dark", useful information is available at each new random choice of direction, which in turn becomes biased towards the near-target direction. That is, the (gradient of the) concentration of scent molecules is used to improve the probability of choosing the best direction. In particular, we study how optimal motion strategies may change in the presence of such chemotaxis-like information sampling [6, 7].

This paper is organized as follows. In Section II we lay down the mathematical details and assumptions of our model. Section III shows our main results obtained from simulations plus a theoretical validation of them. In Section IV we discuss our results and conclude with future directions.

II. MODEL

A. Landscape configuration

. We consider a search process in 1D in which the searcher moves to the right with probability p_+ and to the left with probability p_-. The searcher starts each search at a distance x_0 from a target (the "near" target) and $\lambda - x_0$ from the other (the "far" target). Both targets emit signal cues that, when sensed by the searcher, bias its movement towards the nearest target. We treat each emitting target as a punctual sources of odor cues. Cues

* pablo.castro@ictp-saifr.org
† ricardom@ictp-saifr.org

are emitted at constant rate γ_{emission}, decay with constant rate γ_{decay} and diffuse with diffusion constant D. The combination of these three processes leads to a stationary profile of cues concentration that decays exponentially with the distance from the target [8]:

$$C(x) = \frac{\gamma_{\text{emission}}}{2\sqrt{\gamma_{\text{decay}} D}} \exp\left(-\sqrt{\frac{\gamma_{\text{decay}}}{D}}|x - x_{\text{target}}|\right), \tag{2}$$

where x is the position of the searcher (see Fig. 1). For simplicity, we set $\gamma_{\text{emission}} = \gamma_{\text{decay}} = 1$, and use the square root of the diffusion constant, that is, the scent spread length $\lambda_s \equiv \sqrt{D/\gamma_{\text{decay}}}$, as the only parameter that controls the range of the interaction between the target and the searcher. See Fig. 2 for a schematics of the model.

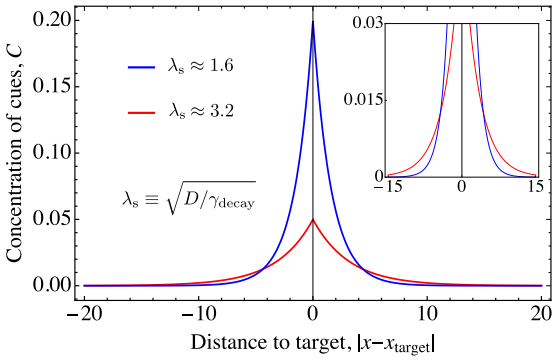

FIG. 1. Cues concentration profile around target for different levels of signal spread length $\lambda_s \equiv \sqrt{D/\gamma_{\text{decay}}}$: higher peak (blue): $\lambda_s = 1.58$; lower peak (red): $\lambda_s = 3.16$. Inset: zoom-in to show the two curves crossing each other either side of the target.

B. Search strategy

. We consider search strategies as the combination of gathering information from the environment and moving. At every time step, the individual decides whether to sample the *gradient* of cues or not and then makes a displacement of length ℓ. Information gathering occurs with probability s, mimicking a cost involved in processing cues. If the searcher does not measure the concentration of cues, then $p_\pm(x) = 1/2$; if it decides to evaluate the concentration of cues, the probabilities of moving to the right or the left are, respectively,

$$p_\pm(x) = \frac{1}{2} \pm \alpha \left[C'_-(x) + C'_+(x)\right], \tag{3}$$

provided that the RHS is between 0 and 1 since these are probabilities; otherwise the probability

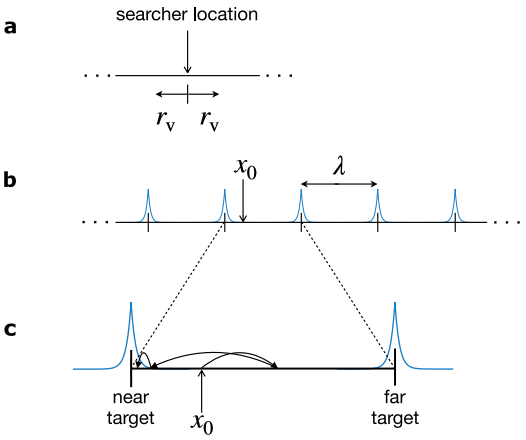

FIG. 2. Schematics of model. More in the main text. (a) Radius of vision. (b) Initial position at distance x_0 from near target. The dynamics can be interpreted as being performed in a periodic distribution of fixed targets with spatial period λ where the searcher resumes searching, after finding a target, at a distance x_0 again, either side of the found target. (c) Sketch of search dynamics between two targets, defined as near and far target based on the initial position. Similar to figure in Ref. [5] without scent concentration profile.

assumes the saturated values 0 or 1 accordingly. In Eq. (3), the effect of the gradient of the total concentration of cues is to bias the movement of the searcher in the direction in which the gradient of cues increases, which has to be the direction of the nearest target. That is, the LW undergoes chemotaxis. Here α is a sensitivity to the cues parameter that regulates the strength of the bias. In simple terms, animals such as dogs would have high α whereas humans would have low α.

Once the direction is randomly chosen, the length of the displacement is drawn from a Lévy distribution (1) and thus depends on the individual pattern of movement characterized by the μ parameter. Different types of movement represent different ways of combining short and long-range displacements and thus of alternating between exploitative and explorative modes of searching. We can therefore define a search strategy in terms of its movement and the probability of processing the concentration of cues, (μ, s), where $\mu \to \infty$ recovers Brownian motion and $\mu \to 0$ a uniform distribution of displacement lengths. A search is considered finished once the searcher hits a position within a distance r_v (radius of vision) of the target. If the last drawn length makes the searcher cross the closest point defined by the radius of vision or even the target position, the actual displacement length is registered as being only up to the radius

of vision point. A new search then starts at a distance x_0 from the found target. Mid-search resetting, where the searcher gives up and starts the search over after a certain amount of time without finding any items, is not considered here [9]. A summary of the used parameters can be found in Table I. Also, we use $\ell_{\min} = 1$ and $\ell_{\max} = 10^4$ to truncate the Lévy distribution.

Parameter class	Symbol	Meaning	Value
Environment	λ	Size of the landscape	1000
	λ_s	Scent cues spread length	variable
	x_0	Initial position	variable
Search strategy	μ	Type of movement	variable
	s	Probability of info sampling	variable
Physiological	α	Accuracy in gradient sensing	variable
	r_v	Radius of vision	1

TABLE I. Parameters table.

C. Measuring search efficiency

. Because we assume that the forager moves at constant speed $v = 1$ (our time step is $\Delta t = 1$), optimal search strategies will be characterized by a minimum average travelled distance to a target, $\langle L\rangle$. Additionally, we also measure the probability of finding the near target, which in turn is denoted by a "0", or the far target, denoted by a "λ", that is, p_0 and p_λ, which obey $p_0 + p_\lambda = 1$. The average travelled distance corresponding to each type of target are $\langle L_0\rangle$ and $\langle L_\lambda\rangle$. All these observables are related to each other through

$$\langle L\rangle = p_0\langle L_0\rangle + (1 - p_0)\langle L_\lambda\rangle. \tag{4}$$

III. RESULTS

Fig. 3a shows our results for $\langle L\rangle(\mu)$ for different values of λ_s (whereas Fig. 3b shows other representations of the data). For small λ_s, the behavior is similar to that of the case without scent effects. A global minimum is observed around $\mu \approx 2$. This can be explained as follows. By employing very long steps in the far-target direction, finding a target is guaranteed, but at the cost of a long walk. Conversely, by employing very small steps, the searcher may get stuck in between the two targets for a long time since there is no strong directional bias towards the nearest target. The optimal strategy corresponds to a superdiffusive balance between short and long steps. Although the derivative of $\langle L\rangle(\mu)$ decays with μ at high μ until eventually becoming negative, this is not enough to make the Brownian case (calculated by restricting all displacements to have length $\ell = 1$, corresponding to $\mu \to \infty$) more efficient than the superdiffusive $\mu \approx 2$ minimum.

At intermediate λ_s, a discontinuous transition occurs. In fact, by increasing λ_s from low to intermediate values, the high μ part of the $\langle L\rangle(\mu)$ curve lowers until it becomes lower than the now local minimum around $\mu \approx 2$. Unlike Ref. [5], here we also present data for $\mu > 3$ in order to properly understand the global behavior across the range of λ_s. The argument in Ref. [5] is that $\mu \geq 3$ corresponds to a finite variance and therefore the walker is no longer a LW, effectively converging to a Brownian walker due to the Central Limit Theorem. We do not use that argument here since the time duration to converge to Brownian motion may change wildly by varying our parameters.

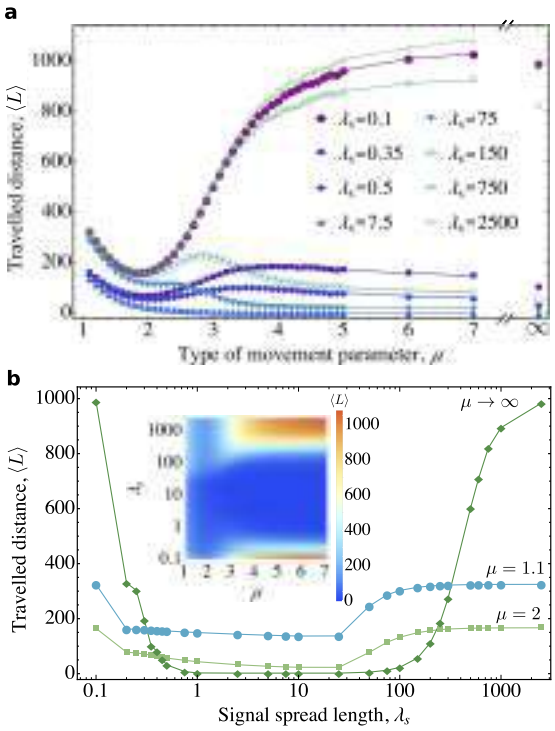

FIG. 3. (a) Average travelled distance $\langle L\rangle$ versus Lévy walk exponent μ for various values of the scent spread length λ_s (increasing from purple to blue to green). The higher the μ, the more "Brownian". Other parameters: the total number of items found or searches is $N_{\text{found}} = 10^7$, $s = 0.5$, $x_0 = 2$, and $\alpha = 10^3$. (b) Same data as in (a) but now plotting $\langle L\rangle$ versus λ_s for fixed μ as indicated. Inset: merging data in (a) and (b) into a "heat map".

The optimal $\mu_{\text{opt}}(\lambda_s)$ is summarized in Fig. 4a. The superdiffusive-to-Brownian and Brownian-to-superdiffusive discontinuous transitions of optimality define three regions. As expected, the limits

$\lambda_s \to 0$ and $\lambda_s \to \infty$, i.e., no chemotactic gradient, lead to the same optimal μ. To show the robustness of these transitions, we plot the effective persistence length $\ell_p^{\rm eff}$, defined as the average displacement between actual changes of direction (measured over many item findings and considering that the last displacement ends when the item is found). (Similarly, an effective $\mu_{\rm eff}$ that incorporates directional bias could be defined.) This quantity does not "know" about chemotactic sampling: it only sees the trajectories. Still, Fig. 4b shows that similar superdiffusive-Brownian transitions are found in $\ell_p^{\rm eff}$ versus λ_s, where, for each λ_s, it is used $\mu = \mu_{\rm opt}(\lambda_s)$. The same qualitative behavior is found for initial positions $x_0 = 5$, 10, and 20, with similar quantitative values for $\ell_p^{\rm eff}$ in each optimality range (data not shown). Fig. 4c shows a single trajectory, from the initial position up until the searcher finds the target, for each optimality region, with corresponding λ_s and $\mu_{\rm opt}$ in each case. These simulated trajectories are shown for merely illustrative purposes since our optimality statements refer to the average travelled distance and are therefore statistical properties.

Changing other parameters can change the sizes of the optimality regions shown in Fig. 4a. As illustration, Fig. 5a shows $\mu_{\rm opt}$ vs λ_s for distinct values of chemotactic sensitivity α. For smaller α, the region where Brownian is the optimal strategy shrinks. For $\alpha = 10$, it is already absent. That is, even though the searcher can perform chemotaxis, this feature is so weak that it does not change the kind of motion pattern qualitatively, that is, Brownian never becomes optimal no matter the value of λ_s. For $\alpha < 1$ (data not shown), the curve is essentially flat, meaning that chemotaxis play no role in determining the optimal μ, not even quantitatively. A similar behavior occurs for decreasing signal sampling probability s (data not shown).

The effect of increasing the search initial position is to decrease $\mu_{\rm opt}$ (more ballistic) in the region where superdiffusive strategy is optimal—see Fig. 5b. This is because the searcher starts farther from the near target and thus it needs to take more long steps since it cannot reach the near target as frequently and quickly as before (on the other hand, the far target distance does not change much, in relative terms). The transition values of λ_s change as well. The low-λ_s transition occurs at higher λ_s than before since the cues concentration profile needs to reach farther now to start affecting the searcher around its initial position. The high-λ_s transition occurs at higher λ_s for $x_0 = 5$ and at lower λ_s for $x_0 = 10$, compared to the case $x_0 = 2$. Presumably, this non-monotonic effect kicks in once the distance to the near target is large enough that the cues concentration profile

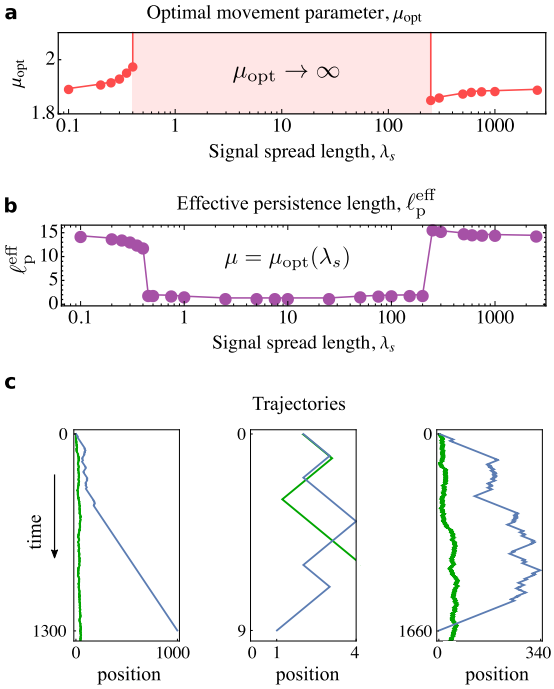

FIG. 4. (a) Optimal μ versus λ_s in linear-log scale. (b) Effective persistence length $\ell_p^{\rm eff}$ versus λ_s in linear-log scale. For each λ_s, it is used $\mu = \mu_{\rm opt}(\lambda_s)$ from (a). (c) In blue, three single trajectories (time is shown along the vertical and the position along the horizontal direction) for $\lambda_s = 0.1, 7.5, 750$, from left to right. The values of μ for each trajectory are $\mu_{\rm opt}(\lambda_s)$, i.e., $\mu_{\rm opt} \approx 2$, $\mu_{\rm opt} \to \infty$, and, again, $\mu_{\rm opt} \approx 2$, respectively, as given in (a). Notice the different temporal and spatial scales across the three figures. In green, three single trajectories for the same values $\lambda_s = 0.1, 7.5, 750$ from left to right but for the "wrong" μ, i.e., $\mu_{\rm opt} \to \infty$, $\mu_{\rm opt} \approx 2$, and, again, $\mu_{\rm opt} \to \infty$, respectively. Other parameters as in Fig. 3.

from the *far* target affects the search more significantly, which can occur if λ_s is large enough. Notice that for $x_0 = 10$, the superdiffusive exponent already becomes the most ballistic possible, $\mu_{\rm opt} = 1$. Increasing x_0 beyond $x_0 = 10$ is computationally expensive since the total travelled distance increases exponentially with x_0.

To obtain further insight into the influence of chemotaxis, Fig. 6a shows the fraction of near targets p_0 versus λ_s. For $\mu \to \infty$, the motion is Brownian and therefore almost all targets that end up being found are near targets. This makes sense since the searcher performs small steps and thus it is likely to find the near target before moving too far, even if this occurs only after travelling a large distance composed of many small steps. This is the case when Brownian motion is not the optimal strategy. For highly ballistic motion such as with

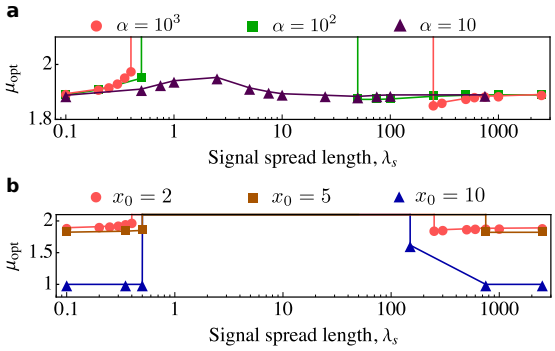

FIG. 5. (a) Optimal μ versus λ_s in linear-log scale for various values of α. The region where Brownian is the optimal behavior shrinks with decreasing chemotactic sensitivity and vanishes completely at finite α. (b) Same as (a) but for fixed α and varying x_0. Other parameters as in Fig. 3.

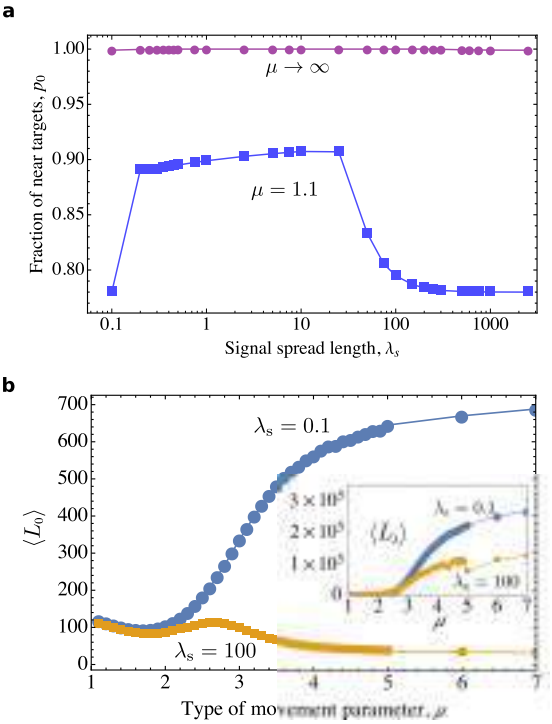

FIG. 6. (a) Fraction of near targets p_0 versus λ_s for $\mu = 1.1$ ("ballistic", blue squares) and $\mu \to \infty$ (Brownian, purple filled circles). (b) Travelled distance for (main figure) near and (inset) far targets versus μ for $\lambda_s = 0.1$ (blue filled circles) and $\lambda_s = 100$ (yellow squares). In the inset, the "noise" in the data for high μ is a consequence of having only a few instances where the far target is found. Other parameters as in Fig. 3.

$\mu = 1.1$, the searcher can perform long steps in the "wrong" direction, moving away from the near target, and therefore there are many instances in which the found target is the far target, hence why p_0 is smaller. For intermediate λ_s, the searcher becomes strongly biased towards the near target and thus p_0 increases. To confirm this picture, Figs. 6b shows the travelled distance versus μ for each type of target for small and intermediate λ_s.

IV. DISCUSSION AND CONCLUSIONS

In some specific ecological scenarios, optimality may involve other considerations than the ones present here. For instance, an equilibrium between near versus far target encounters may be necessary to avoid overexploitation of the near target, that is, that the near target becomes incapable of providing resources, thus forcing the searcher to walk longer distances. As we have seen, for a range of intermediate values of λ_s, $\mu \to \infty$ is the optimal strategy for minimizing the travelled distance. However, we have found that increasing μ leads to an increase in the frequency of near-target findings p_0 (data not shown).

Our qualitative results are expected to hold for any kind of persistent-motion random walker, e.g., the run-and-tumble dynamics used to model bacterial motion [10, 11]. The same principle would apply: by increasing chemotactic bias, the walker is better off being less persistent in order to be able to "use" the bias around a target and avoid moving away from it "accidentally". Our results indicate that in more applied scenarios such as sperm navigation [6] and bacterial chemotaxis towards nutrients [7], or even T-cells searching for bacteria [12], by increasing the spread of concentration profile of the signalling molecules too much, the searcher may become overwhelmed and not be able to detect large gradients that could help guide it. These are questions for future research.

V. ACKNOWLEDGEMENTS

PdC is supported by grant #2021/10139-2, São Paulo Research Foundation (FAPESP), Brazil. RM-G was supported by the FAPESP program Jovens Pesquisadores through grant 2019/05523-8, the ICTP through the Associates Programme, and the Simons Foundation through grant 284558FY19. PdC and RM-G were supported by FAPESP through ICTP-SAIFR grant 2016/01343-7. This research used resources of the Center for Scientific Computing (NCC/GridUNESP) at UNESP.

[1] Gandhimohan M Viswanathan, "Fish in lévy-flight foraging," Nature **465**, 1018–1019 (2010).

[2] Gandhimohan M Viswanathan, Vsevolod Afanasyev, Sergey V Buldyrev, Eugene J Murphy, Peter A Prince, and H Eugene Stanley, "Lévy flight search patterns of wandering albatrosses," Nature **381**, 413–415 (1996).

[3] Alex James, Michael J Plank, and Andrew M Edwards, "Assessing lévy walks as models of animal foraging," Journal of the Royal Society Interface **8**, 1233–1247 (2011).

[4] Gandimohan M Viswanathan, Sergey V Buldyrev, Shlomo Havlin, MGE Da Luz, EP Raposo, and H Eugene Stanley, "Optimizing the success of random searches," nature **401**, 911–914 (1999).

[5] Frederic Bartumeus, Ernesto P Raposo, Gandhimohan M Viswanathan, and Marcos GE da Luz, "Stochastic optimal foraging: tuning intensive and extensive dynamics in random searches," PloS one **9**, e106373 (2014).

[6] Justus A Kromer, Steffen Märcker, Steffen Lange, Christel Baier, and Benjamin M Friedrich, "Decision making improves sperm chemotaxis in the presence of noise," PLoS computational biology **14**, e1006109 (2018).

[7] Roman Stocker and Justin R Seymour, "Ecology and physics of bacterial chemotaxis in the ocean," Microbiology and Molecular Biology Reviews **76**, 792–812 (2012).

[8] Benoit Cushman-Roisin, "Lecture notes in environmental transport and fate," (2012).

[9] Benjamin De Bruyne, Satya N Majumdar, and Grégory Schehr, "Optimal resetting brownian bridges via enhanced fluctuations," Physical Review Letters **128**, 200603 (2022).

[10] Andrea Villa-Torrealba, Cristóbal Chávez-Raby, Pablo de Castro, and Rodrigo Soto, "Run-and-tumble bacteria slowly approaching the diffusive regime," Physical Review E **101**, 062607 (2020).

[11] Pablo de Castro, Francisco M Rocha, Saulo Diles, Rodrigo Soto, and Peter Sollich, "Diversity of self-propulsion speeds reduces motility-induced clustering in confined active matter," Soft Matter **17**, 9926–9936 (2021).

[12] Matthew F Krummel, Frederic Bartumeus, and Audrey Gérard, "T cell migration, search strategies and mechanisms," Nature Reviews Immunology **16**, 193–201 (2016).